Advanced geometric calibration and control for medical X-ray systems

Citation for published version (APA):
van der Maas, R. J. R. (2016). *Advanced geometric calibration and control for medical X-ray systems*. [Phd Thesis 1 (Research TU/e / Graduation TU/e), Mechanical Engineering]. Technische Universiteit Eindhoven.

Document status and date:
Published: 03/03/2016

Document Version:
Publisher's PDF, also known as Version of Record (includes final page, issue and volume numbers)

Please check the document version of this publication:

• A submitted manuscript is the version of the article upon submission and before peer-review. There can be important differences between the submitted version and the official published version of record. People interested in the research are advised to contact the author for the final version of the publication, or visit the DOI to the publisher's website.
• The final author version and the galley proof are versions of the publication after peer review.
• The final published version features the final layout of the paper including the volume, issue and page numbers.

[Link to publication](#)

ADVANCED GEOMETRIC CALIBRATION AND CONTROL FOR MEDICAL X-RAY SYSTEMS

RICK VAN DER MAAS

Advanced Geometric Calibration and Control for Medical X-ray Systems

Rick van der Maas

disc

Advanced Geometric Calibration and Control for Medical X-ray Systems

PROEFSCHRIFT

ter verkrijging van de graad van doctor aan de
Technische Universiteit Eindhoven, op gezag van de
rector magnificus, prof.dr.ir. F.P.T. Baaijens, voor een
commissie aangewezen door het College voor
Promoties, in het openbaar te verdedigen
op dinsdag 3 maart 2016 om 16.00 uur

door

Richard Jacobus Rudolf van der Maas

geboren te Vlissingen

Dit proefschrift is goedgekeurd door de promotoren en de samenstelling van de promotiecommissie is als volgt:

voorzitter:	prof.dr. L.P.H. de Goey
promotor:	prof.dr.ir. M. Steinbuch
copromotor:	dr.ir. A.G. de Jager
leden:	prof.dr.ir. N. van de Wouw
	prof.dr.ir. T. Singh (State University of New York at Buffalo)
	prof.dr.ir. J. Schoukens (Vrije Universiteit Brussel)
adviseurs:	dr.ir. T.A.E. Oomen
	ir. J.J. Dries (Philips Healthcare)

Het onderzoek dat in dit proefschrift wordt beschreven is uitgevoerd in overeenstemming met de TU/e Gedragscode Wetenschapsbeoefening.

Contents

Chapter 1

Introduction

1.1 From X-ray imaging to high-definition 3D reconstruction

With the discovery of X-ray by Wilhelm Conrad Röntgen in 1895 [1], a first breakthrough towards modern medical imaging was achieved. X-ray radiation is a electromagnetic radiation, in the wavelength range of 0.01 - 10 nanometers. Many natural sources emit X-ray, e.g., cosmic radiation and specific materials, in fact, on average, humans are exposed to twice as much radiation during a live time due to environmental sources than due to medical applications [2]. X-ray is used for many purposes, e.g., quality checks, security, and in medical sciences. In this thesis, the focus is on medical applications, typically used for interventional/minimal invasive surgery, e.g., stent placement or catheter guidance in the vascular system. The main focus is on improving geometric calibration procedures for medical X-ray systems that lead to reduced calibration times and improved image qualities for the next generation imaging systems.

1.1.1 Fundamentals of X-ray imaging and reconstruction

X-rays are generated using an *X-ray tube* (Fig. 1.1, ①), which is a vacuum tube that contains a cathode and anode. By heating the cathode, free electrons are accelerated and collide at high speed with the positively charged anode. When the electrons strike a nucleus, energy is released in the form of X-ray radiation. By modification of the voltage between the anode and cathode the energy, i.e., penetrating power, of the obtained X-rays is controlled. By adjusting the current applied to the filament, the amount of dose can be controlled [3, Chap. 2].
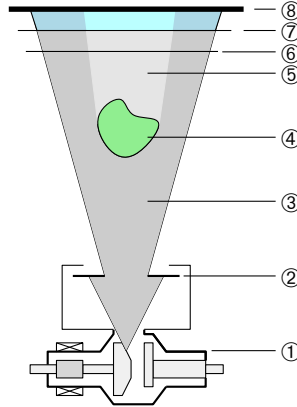
Fig. 1.1. Schematic representation of the X-ray imaging process, where ①: X-ray tube, ②: collimator (shutters), ③: radiated X-ray photons, ④: object of interest, ⑤: attenuated X-ray photons, ⑥: anti-scatter grid, ⑦: scintillation layer, and ⑧: detection layer (photo-diodes).

To avoid unnecessary exposure for the patient and medical staff, the generated X-ray beam first passes through the *collimator* (②). Inside the collimator, movable shutters are placed such that specific parts of the beam can be blocked, i.e., to avoid exposure that is not captured by the detector or to focus on a specific part of the patients anatomy.

The attenuation coefficient is an important material property which forms the fundamental of X-ray imaging, it reflects the ratio between the *radiated* (③) photons by the X-ray tube and the *attenuated* (⑤) X-ray photons by the object of interest. The attenuation coefficient is closely related to the material density, i.e., the denser the material, the higher the attenuation coefficient. Moreover, part of the photons is deflected in arbitrary directions by the atoms of the object of interest, leading to scattered radiation. Hence, an *anti-scatter grid* (⑥) is placed before the detector to preserve the direct X-rays from tube to detector and filter out scattered rays.

By detecting the attenuated photons after passing through the patient and anti-scatter grid, an X-ray image is obtained. The detection of X-ray has developed from the traditional "wet" process, similar to the development of photographic film, to a fully digitized image. The detection of digital X-ray images contains two steps, first a *scintillation layer* (⑦) is passed that converts the X-ray photons to visible light. Second the visible light is detected and converted to electronic signals by photo-diodes in the *detector* (⑧).

Where early medical applications typically aimed at the visualization of high-density structures, e.g., bone-structures, modern techniques such as 3D rotational Angiography (3DRA) aim at the visualization of the vascular system as

well by means of contrast fluids. By injecting the patient with a contrast fluid that has a high attenuation coefficient, irregularities or blockages of the vascular system can be visualized. XperCT is the interventional equivalent of CT, where slices of the object of interest are visualized, with the main focus on the visualization of "soft" tissue without the use of contrast fluids. Traditional CT systems enable a full circular revolution of the X-ray detector and source, where XperCT is limited to a semi-circular motion range.

Nowadays, medical imaging has developed towards high-definition digital images and three-dimensional (3D) *reconstructions*. With the introduction of the Radon transform [4], the fundamentals for state-of-the-art computed tomography (CT) and magnetic resonance imaging (MRI) are laid. The projection of a single X-ray is representing the attenuation of the object, i.e., the ratio between the radiated and detected amount of X-ray. By the acquisition of multiple X-rays simultaneously, a two-dimensional (2D) image is obtained. When multiple 2D images are obtained from various positions and orientations over a sufficient range, typically a (semi-)circular trajectory, the intersections of the individual line integrals represents a value for a point in 3D space. Hence, a 3D reconstruction is obtained, see [5, Sec. 5.11], [3, Chap. 3], and [6] for more details.

1.1.2   Image-guided interventions

Over the past decades, an increased interest of the medical society to make surgical procedures faster, safer and more efficient, in combination with modern technological advances, has led to a significant increase of *minimally invasive* and *image-guided* interventions. In sharp contrast to traditional surgical procedures, these "interventions" allow for minimal collateral damage to the patient during surgery, e.g., only small incisions, leading to less postoperative complications and faster patient recovery times. Using specialized surgical instruments, treatments are performed inside the patient guided by real-time imaging.

The natural pathways of the vascular system are more and more exploited to reach the location of interest with surgical instruments, e.g., by progressing through the femoral artery to reach the coronary vessels. Catheter placement, which is used for a variety of purposes, e.g., fluid drainage and delivery, but also cauterization of selected locations of the hearth muscle (cardiac ablation), is often performed through the vascular system. Other applications are the placements of a stent, which essentially are hollow flexible tubes, that expand after placement to keep vessels open and prevent bleeding. To navigate such a device in the interior of the human body without direct visual contact, 2D images often do not provide sufficient information. By overlaying an X-ray fluoroscopy image, which is a low-dose continuous imaging mode, over a pre-generated 3D reconstruction, a more complete visualization of the situation is provided to the user. Such an overlay procedure is typically referred to as 3D roadmapping [7], [8].

In addition, early detection and surgery/interventions on aneurysms requires high definition 3D reconstructions. An aneurysm is a local weakness of the vascular system that, depending on the location, potentially is life threatening. Typically catheters are used to place custom made endografts designed to relieve pressure. Alternatively, the aneurysm is filled with thin coils to cause blood coagulation (cerebral aneurysms). For these procedures, 3D information can provide insight in the complexity of the aneurysm and surrounding systems, which is crucial for successful interventions [9].

Alternative currently existing imaging methods such as ultrasound, MRI, and CT, have several advantages from an imaging perspective, e.g., higher contrast due to larger pixel sizes. However, overall they do not provide the image resolution, speed and flexibility for the same cost as can be achieved using interventional X-ray imaging.

1.1.3   Influence of system imperfections

A vast amount of calibrations is performed on medical X-ray systems to ensure an optimal reconstruction and image quality. Calibration of the image acquisition components, e.g., detector calibration to compensate for nonlinearity and non-uniformity and calibrations related to polychromaticity (wavelength disturbances) of X-rays are indispensable to obtain images of high quality with a minimum dose exposure. Moreover, *geometric calibrations*, which are the main focus in this thesis are performed. Since any physical system suffers from (mechanical) imperfections, the true (motion) behavior will deviate from the design specifications.

For medical imaging purposes, the pose of the image acquisition components with respect to the patient are key. The detection surface is assumed a rigid surface of known dimensions and is fully defined in 3D space by six degrees-of-freedom, i.e., three translations and three orientations, both defined with respect to a fixed reference. The X-ray source, typically assumed a point source [10], [11], is defined by three translational degrees of freedom only, bringing the total to nine degrees-of-freedom, in this thesis referred to as *geometric parameters*. Note that this is the case regardless of the mechanical configuration of the system, e.g., various types of interventional X-ray systems or CT systems.

Focusing on interventional X-ray systems, typical configurations exist of a chain of interconnected kinematic links, ending in the detector and X-ray source. Note that the structure is similar to many designs in industrial robotics where positioning of the end effector is essential for performance. Typical effects that lead to deviations from the user-defined (ideal) trajectory are given by, but not limited to,

- system imperfections due to limited production and assemblage accuracies, e.g., offsets and misalignments,

- finite stiffness' of mechanical elements, e.g., finite construction stiffness but also flexibilities in the drive-train components leading to quasi-static (position-dependent) deformations and dynamical effects,

- external disturbances from, e.g., other systems or thermal variations, and

- slowly time-varying behavior due to wear of components.

As a result of mechanical imperfections of the system, leading to deviations from the expected (ideal) poses of the image acquisition components, each individual 2D projection is shifted and rotated in an unknown manner. As argued in Sec. 1.1.1, the reconstruction of a 3D object is based on the mapping of multiple 2D projections, i.e., the intersections of the line-integrals represent points in 3D space. The problem of defining the true poses of the image acquisition components, i.e., the aforementioned geometric parameters, when a specific reference signal is applied, is referred to as *geometric calibration*. When the true trajectory is identified, the 3D reconstruction procedure can be performed with high accuracy.

Common practice for the considered class of systems is a geometric calibration where, using an off-line external measurement, the trajectory is calibrated, see, e.g., [12, Sec. 2.11]. For the validity of the off-line calibration measurements during normal operation of the system, a strict reproducibility condition is imposed.

1.2 Next generation interventional imaging

Cost awareness in the development and production of medical systems has grown over the last decades due to rising costs of health care in many countries all over the world. With the development of minimally invasive procedures, increased requirements in terms of image quality and reduced X-ray dose usage, limitations of the currently used imaging systems and procedures are becoming apparent. Moreover, from a mechatronic point-of-view on the design of next generation interventional X-ray systems, the following developments are envisioned:

1. lightweight system design, and

2. extended scan possibilities.

Although these developments are desired in terms of usability and cost effectiveness, a significant amount of new and increased mechatronic challenges are introduced. In the remainder of this section, the advantages and consequences of these developments on image quality and systems calibrations are explored.

Lightweight system design

Lightweight system design has several advantages over the current systems. By virtue of Newton's law, $F = ma$, with F the required force to achieve an acceleration a given a mass m, it is highlighted that by reducing the mass of the system the required forces are reduced. Hence, less restrictive conditions are placed on the actuators, gearboxes and guidings of the system. Moreover, transportation costs can be reduced and ease and safety of installations can be increased. Since interventional medical X-ray systems typically operate in a crowded environment, i.e., medical staff, the patient on the table, and equipment are present, safety is crucial. Often current-based collision detection methods are exploited where deviations from the predicted current with respect to the measured current applied to the actuators indicate a collision. For lightweight systems, forces required for acceleration and deceleration, but also impact forces are typically smaller.

Besides advantages, lightweight system design imposes at least two main challenges:

- a reduction of mass is often also resulting in a reduction of stiffness. However, the ratio between stiffness and mass typically does not remain the same, often leading to a change of flexible modes to lower frequencies, and

- the relation between the input and non-collocated performance variables, i.e., the nine degrees-of-freedom defined as the geometric parameters as argued in Sec. 1.1.3, are described by geometric (kinematic) relations and an increasing dynamical component. As a result of the combination of fixed and changing (external) forces and a lower stiffness, dynamical deflections increase.

Due to these effects, dynamics will play a significant role for future systems, complicating the geometric calibration of the system. Moreover, the quality of individual 2D images is endangered due to possible increased amplitudes of system vibrations during a single exposure.

Extended scan possibilities

Due to a growing number of minimal invasive surgeries, and thus more crowded clinical environments, there is an increasing demand from the medical community on scan and positioning freedom of interventional imaging systems. See Appendix A for an overview of the current systems. Allowing access to the patient while obtaining accurate images is important and can be achieved by over-actuation, i.e., by using multiple joints during a scan or even increasing the number of joints of the system. An example of such an innovative development is the Siemens Artis Zeego where a C-arc is mounted on an industrial robot with 7 degrees-of-freedom [13]. An increase in actuated motions leads to an increase

in possible error sources, which complicates the geometric calibration of the system. Also by increasing the number of scan options, the number of required calibrations increases significantly.

1.3 Problem statement

Throughout this thesis, interventional X-ray systems are considered. However, the proposed approaches can also be exploited to other configurations of X-ray based imaging systems that exploit the imaging structure as depicted in Fig. 1.1. Taking into account the expected future developments and the current limitations in geometric calibrations, the general research goal of this thesis can be summarized as follows:

> *Develop a framework to deal time-efficiently with (non)reproducible geometric system imperfections to guarantee high-definition imaging, given the current and expected (future) challenges in medical X-ray applications.*

By exploiting developments in modeling, estimation, and control of mechatronic systems, solutions are desired for multiple limiting factors in the system design. The main limiting factors for the current geometric calibrations of medical X-ray systems are given in I-IV.

I Geometric calibrations using external measurements or tools require time-consuming experimentations [11]. For the current generation interventional X-ray systems the semi-annual calibration times take up to four hours for each individual system depending on the configuration and available options.

II Reproducibility of the system is crucial for successful application of existing geometric calibration approaches. It is expected that future developments lead to larger contributions of the dynamical behavior to the geometric parameters, therefore the susceptibility to external disturbances and initial operating conditions endanger the required reproducibility condition.

III Only predefined trajectories can be used for reconstruction purposes. The true trajectory that the system follows is a result of a combination of the systems kinematics, compliances, and dynamics where only the resulting output is calibrated. Without additional system knowledge, the measured output can not be extrapolated to other scan trajectories.

IV Geometric calibrations have to be repeated over fixed time-intervals, typically six months. Also, when the system mechanics are minimally changed, e.g., due to a moderate collision or component replacement, the calibration has to be repeated.

Besides the imperative geometric calibrations, many calibrations are required to guarantee a desired image quality, see [14] for a detailed overview. For the results presented in this thesis, the following assumption should hold:

Assumption 1.1. *It is assumed throughout this thesis that all calibrations, e.g., detector and source calibrations, are performed. Also, the detector and X-ray source are assumed ideal, i.e.,*

1. *the detector is assumed a rigid body, perfectly aligned on a rectilinear grid, and*

2. *the X-ray source can be described by a point-source from which the deviations from the ideal position can be neglected.*

In view of modern developments towards the next generation imaging systems, the following research questions are formulated.

Research Challenge I. *Design a framework for geometric calibrations of interventional X-ray systems, that overcomes the aforementioned limitations I to IV.*

Research Challenge II. *Investigate whether additional sensors, smart sensing technology, and (model-based) sensor fusion techniques can be used to render periodic calibrations, as stated in limitation IV, unnecessary. Using these technologies, design a fully automated (data-driven) geometric calibration approach that facilitates enhanced performance for the current and next-generation of X-ray systems.*

Research Challenge III. *Investigate the influence of (feedback/feedforward) control strategies on the geometric calibrations to limit the effects of increased dynamics on the system behavior as stated in limitations II and III.*

In the next section, existing geometric calibration approaches applied in medical imaging applications are presented. The advantages and limitations with respect to the problem statement are given and novel approaches are proposed.

1.4   Current geometric calibration approaches

As presented in the previous sections, due to inherent imperfections in the mechanical structure, geometric calibrations are imperative to avoid reconstruction artifacts, see, e.g., [15], [16], and [17, Chap. 7] for a detailed analysis. Multiple approaches to perform geometric calibrations on medical X-ray systems and industrial robotic systems are reported in literature. In this section, an overview of some approaches is provided and a comparison in view of the general research goal in Sec. 1.3 is given.
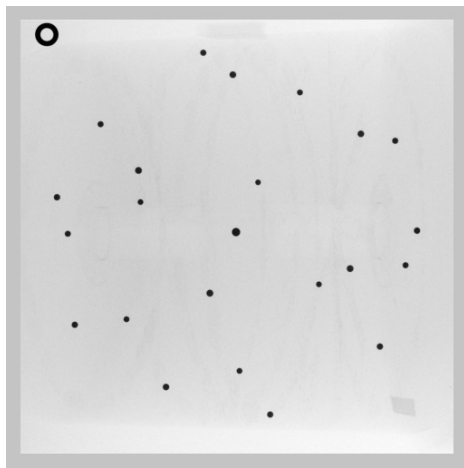
Fig. 1.2. 2D image fluoroscopy image of a generally used phantom for geometric calibrations

Phantom-based geometric calibration

In the medical imaging community, phantom-based calibrations are widely applied. By placing an object with accurately known size and shape within the line of sight, i.e., within the exposure of an X-ray projection, the pose of the image acquisition components is reconstructed. Each projection must contain sufficient information to determine the geometric parameters, e.g., a homogeneous sphere of known radius does not provide sufficient information to estimation all parameters due to the rotational symmetry. Therefore, a (calibration) phantom is typically used that consists of multiple bullets spread uniformly in 3D space. A single projection of the phantom is shown in Fig. 1.2, where the dark bullets show the markers. Early research in the use of calibration phantoms show that 8 bullets, positioned in the corners of a cube, in theory provides sufficient information. However, due to overlapping bullets in specific projections, typically a significant larger amount of bullets is introduced in the phantom. The distribution of the bullets in 3D space is typically based on the corners of regular polyhedra, which are three-dimensional objects bounded by identical and regular surfaces (polygons), with each edge shared by exactly two polygons. Based on practical experience, the dodecahedron often is used, where 20 bullets are distributed over the corners and an additional center bullet and two alignment bullets are introduced, leading to accurate results even if several bullets are lost due to overlaps. Moreover, a dodecahedron is relatively easy to produce with high accuracy. Three layers of an X-ray opaque (low-density) material are used, in which bullets of a high-density material, e.g., bronze, are pressed. Due to the large difference in densities of the material, the contrast within X-ray images is

large. See [18], [19], [20], and [21] for additional information on commonly used bullet-patterns. After performing a bullet search, e.g., using the Hough transformation [5, Chap. 10], the projected coordinates are mapped to the poses of the system using a projection matrix (pinhole camera model), see [9, Sec. 4.3.1], and [3, Chap. 1].

Depending on the type of system, the size of the calibration phantom may vary. By placing the phantom on the patient table, a fixed (world) reference is obtained from which the poses of the X-ray detector and source can be derived. For accuracy, it is desired to spread the bullets as far as possible, however, the phantom should remain within the projection. Hence, the size of the used phantom is heavily depending on the detector size and distance from the X-ray source.

Recovering the pose of the system based on a 2D projection leads to a highly nonlinear optimization problem [22]. Assuming the system imperfections lead to relatively small deviations from the ideal trajectory, initial estimates are available, however, practical results show that global convergence is not always guaranteed [23]. Approximative approaches, based on the estimation of parameters of ellipsoids are presented in [10], which recasts the nonlinear estimation problem in a linear least-squares problem, see also [11] and [24] for further developments. The main drawback of these approaches is the required assumption that at least one out-of-plane rotation of the detector is assumed to be zero. In practice this results to small estimation errors, see, e.g., [25] for an analysis on the sensitivity of image quality for variations of geometric parameters.

Even though accurate results are obtained using phantom-based calibrations, the procedure has some major drawbacks.

1. The method is based on a single (off-line) measurement, i.e., after the calibration scan, reproducibility is assumed such that the obtained geometric parameters can be used for future reconstructions. When the reproducibility condition is violated, there are no guarantees on the obtained reconstruction qualities. For the current generations of interventional X-ray systems, this implies that recalibration is required to deal with

   - changes to the system behavior, e.g., (ex)change of components or the effects of collisions, and
   - to compensate for (slowly) time-varying behavior of the system.

2. The obtained geometric parameters are highly dependent on the pose and the dynamical behavior of the system. No extrapolation of the data is possible to other scan types, velocities, or positions. When purely static calibrations are considered, geometric parameters are estimated over a uniformly distributed grid while between the grid points the values are obtained by interpolation, see e.g., the 3D roadmapping calibration [7]. Resulting from the large number of required calibrations, the calibration times are significant.

Image-based geometric calibration

To overcome the strict reproducibility condition imposed by phantom-based calibration approaches, research has focused on the use of the obtained images during the actual performed (patient) scan. A possible approach is to place markers within the exposure volume during patient imaging, e.g., by strategically placing the markers on the patient or in the patient table [26]. The main drawback of such an approach is the loss of information within the projection due to the possible occlusion of interesting anatomy by high-density, i.e., X-ray absorbing, markers. After obtaining the 2D X-ray projections, interpolation based reconstruction of the expected anatomy occluded by the marker can be performed at the cost of a localized increase of noise within the image. Although the signal-to-noise ratio (SNR) of an X-ray image can be increased by increasing the X-ray dose, regulations concerned with X-ray exposure to the patient and staff limit this option.

Alternative approaches, purely based on detection points within the anatomy of the patient, e.g., specific predefined points of the human bone-structure, are proposed in, e.g., [27], [28] with successful results. Although the geometric parameters can be estimated using these procedures, (involuntary) patient motions pose a serious challenge for 3D reconstruction mappings, particularly when imaging is required of the vascular system. In [29] an iterative restoration algorithm is proposed that, based on entropy minimization optimizes the 3D reconstruction. Since the approach is purely based on the obtained images, patient motions again introduce a significant uncertainty.

External measurements

Modern developments in imaging and computer vision enable fast processing of camera images. By placing visual markers on the X-ray detector and source, direct measurements are performed of the geometric parameters. Similar approaches are widely applied using both vision as well as laser trackers for geometric calibrations of industrial robotic systems, see, e.g., [30], [31], and [32].

Although direct measurements do not require reproducibility of the system it is challenging to guarantee a direct line-of-sight to the system at all times. During surgery, intervention rooms are typically very crowded with medical staff, screens, and additional required tools. In addition, the patient and table is typically covered with sheets that (partly) covers the system. This issue can be overcome by the addition of more cameras, or other measurement instruments, leading to additional costs.

Towards geometric calibration for next generation interventional X-ray systems

Although the presented existing approaches lead to satisfactory results, the design of the next generation interventional X-ray systems is significantly limited, both functional as well as financial, by the limitations I to IV presented in Sec. 1.3. The importance of advanced solutions for fast and accurate geometric calibration of (interventional) X-ray systems is underlined by the vast amount of recent publications on the topic.

In sharp contrast to pre-existing approaches, in this thesis the geometric calibration problem is evaluated from a mechatronic model-based point-of-view. The (mechanical) causes and imperfections that lead to deviations of the geometric parameters from the user-defined trajectory are analyzed. Based on developments in the field of industrial robotic systems, advanced modeling, estimation, and control approaches are exploited to overcome the currently existing limitations as presented in Sec. 1.3.

The proposed approaches in this thesis can be roughly divided in two main directions.

1. Estimation-based approaches where the actual behavior of the system is estimated.

2. Design and control based approaches where the actual behavior of the system is modified such that the behavior approximates the ideal behavior more closely.

For the current generation (interventional) X-ray systems, the time-consuming geometric calibration and the predefined scan trajectories, as described in point I and III in Sec. 1.3, are the main limiting factors. The phantom-based approaches are widely applied with satisfactory results in terms of 3D reconstruction qualities, at the cost of significant calibration times. This leads to the first contribution of this thesis.

Contribution I. *A new model-based framework for geometric calibrations for interventional X-ray systems that recasts the extensive calibration problem in a model parameter identification problem.*

The main advantage of the proposed approach over existing methods is the significant reduction in calibration times by exploiting the predictive properties of a physics based model.

Although the model-based approach in contribution I has significant advantages over pre-existing methods, dynamical effects are not included in the modeling approach. The dynamics of a robotic systems are often highly pose dependent and can typically be approximated by a linear parameter varying (LPV) model where the actuation angles are chosen as the scheduling parameters [33]. The second contribution of this thesis is based on the identification of local nonparametric frequency response functions (FRF) of an LPV system.

Contribution II. *A novel approach for the measurement of frequency response functions for linear parameter varying systems is proposed. Based on the local polynomial method (LPM) [34] and the local rational method (LRM) [35], which are developed for linear time-invariant (LTI) systems, a new approach that uses the smoothness over the scheduling parameter is proposed leading to significant reduction in measurement times and enhanced estimation accuracy.*

Accurate estimations of system behavior is typically obtained by sensor-fusion techniques, e.g., Kalman or particle filters. Based on model-based predictions and measurements, accurate estimations of unmeasured states of the system can be obtained. This leads to the third contribution in this work.

Contribution III. *A fully data/model-driven geometric calibration approach is proposed. Based on accurate dynamic and quasi-static modeling of the system, in combination with additional sensors and advanced state-observer designs, geometric parameters are estimated. Due to the use of measured data, the imposed reproducibility condition on the system, as described in point II in Sec. 1.3, can be relaxed. Moreover, the proposed approach allows for adaptation of the model parameters. leading to increased time-intervals between re-calibrations described in point IV in Sec. 1.3.*

The final aim of the geometric calibration is the estimation of geometric parameters, which includes parameters of both the X-ray detector as well as the tube. A relative displacement between the X-ray detector and tube directly influences the projected image. The proposed approach in Contribution III leads to independent estimations of the geometric parameters corresponding to the X-ray detector and source. In Contribution IV a novel measurement approach is proposed that extends the approach in Contribution III.

Contribution IV. *A new image-based measurement technique is proposed that uses the X-ray images obtained during a patient scan by virtue of a small mechanical addition to the system. Relative displacements between the X-ray detector and tube are directly measured and used within an observer to obtain an improved accuracy in the estimation of the geometric parameters.*

With this contribution, the estimation based approaches are concluded. An alternative approach to ease or avoid the geometric calibration procedure is to force the system to follow the ideal trajectory. For point-to-point motions, input-shaping techniques lead to significant improvements for lightly-damped motion systems. For the interventional X-ray system application, it is desired to track the behavior during the scan, leading to the final contribution.

Contribution V. *A novel design approach for time-delay filters is introduced that enables tracking of dynamic references with lightly-damped motion systems.*

Using the proposed input-shaping approach, the dynamic excitation of the system is reduced, increasing the reproducibility of the system, as described in point II in Sec. 1.3.

1.5　　Outline of the thesis

In this section, it is described how the research challenges formulated in Sec. 1.3 are related to the contributions and an outline is provided. The individual chapters of this thesis are submitted for journal publication.

Chapter 2
Published as: R. van der Maas, B. de Jager, M. Steinbuch, and J. Dries, "Model-based geometric calibration for medical X-ray systems", Medical Physics, 42(11), pp. 6170 - 6181, 2015.

Chapter 3
Submitted for journal publication as: R. van der Maas, A. van der Maas, J. Dries, and B. de Jager, "Efficient Non-Parametric Identification of Multi-Axis Medical X-ray Systems".

Chapter 4
Submitted for journal publication as: R. van der Maas, A. van der Maas, R. Voorhoeve, and T. Oomen, "Accurate FRF Identification of LPV Systems: nD Local Parametric Modeling with Application to a Medical X-ray System".

Chapter 5
Prepared for journal publication as: R. van der Maas, J. Dries, and B. de Jager, "Data-Driven Geometric Calibration for Medical X-ray Systems".

Chapter 6
Prepared for journal publication as: R. van der Maas, R. Gaasbeek, M. den Hartog, and B. de Jager, "Image-Based Pose Estimation using Mechanical Markers for Enhanced Geometric 3D X-ray Calibrations".

Chapter 7
Submitted for journal publication as: R. van der Maas, T. Singh, and M. Steinbuch, "Periodic Signal Tracking for Lightly Damped Systems".

Each of the chapters in this thesis is related to a specific research challenge and a corresponding contribution. An overview of these relations is provided in Fig. 1.3.

Geometric System Calibrations	Chapter 1	Introduction
Research Challenge I: Geometric Calibrations	Chapter 2	Contribution I: Model-based geometric calibration framework that recasts the calibration problem in a model parameter identification problem.
Research Challenge II: Additional Measurements	Chapter 3 Chapter 4	Contribution II: Nonparametric system identification approaches enable fast and accurate modeling of the system dynamics. Additionally, a novel approach is proposed for the identification of linear parameter varying systems.
	Chapter 5	Contribution III: Fully data/model-driven geometric system calibrations, enabling the relaxation of the reproducibility condition.
	Chapter 6	Contribution IV: Enable the use of actual X-ray images in the geometric calibration process. Extends the geometric calibrations from Contribution III with additional measurements.
Research Challange III: Control Strategies	Chapter 7	Contribution V: A novel design approach for time-delay filters enabling tracking of dynamic references.
	Chapter 8	Conclusions

Fig. 1.3. Overview of the thesis

1.6 Research results beyond this thesis

During the course of the PhD project that has led to the presented results in this thesis, several lines of research have been explored that have not been included in this work.

First, the geometric calibration problem has been analyzed from a mechatronic perspective, resulting in renewed insights in the system. The effects of (mechanical) imperfections, disturbances, and design choices on the obtained reconstruction qualities has been thoroughly investigated.

Second, explorations towards image-based measurements led to new insights on the application of filtering approaches. Dose control, which is considered outside the scope of this thesis, is essential for accurate imaging. An average gray value of an image is computed, and based on that value the dose in adjusted for the next image. Large homogeneous objects of X-ray opaque material, e.g., surgical tools, lead to a significant disturbance in the measurement (average gray value) and as such to a non-optimal X-ray dose exposure for the visualization of the patients anatomy. An approach based on morphologic filtering has been developed leading to significant improvements in image quality. The results has been published as [36] and the approach is practically implemented as a software

update.

Third, the use of advanced (feedback/feedforward) control approaches is investigated. The use of iterative learning control (ILC) to achieve enhanced non-collocated tracking performance of the trajectories of the X-ray detector and tube has been reported in [37].

Fourth, the image-based measurement approach is introduced for relative pose measurements using a specifically designed marker. Additional results are achieved by using the shutters located within the collimator of the system as a reference. Relative X-ray detector and tube rotations are estimated with high accuracy, without additional mechanical modifications. Ongoing research focuses on increased usage of the images for various purposes.

Fifth, an approach to quantify 3D image quality is developed. Using active contour models, reconstruction artifacts, i.e., systematic reconstruction errors leading to shape errors in the reconstructed object, are quantified by evaluation of a cross-section of a thin wire. Moreover, the quality of the reconstruction in terms of contrast and sharpness is expressed using well established approaches, which has a strong equivalence to linear system theory, available for 2D images. The results has been reported in [38].

To conclude, as part of the PhD an experimental medical X-ray system has been placed in the laboratory at the Eindhoven University of Technology to facilitate future research on mechatronic challenges.

Chapter 2

Model-Based Geometric Calibration

A model-based approach for geometric system calibrations of medical X-ray systems is presented. Currently applied calibration approaches lead to satisfying 3D reconstruction qualities, however, the required calibration times are extensive. The aim of this chapter is the introduction of a novel model-based approach for geometric system calibrations, leading to a significant reduction of calibration times. By exploiting the predictive properties of a physics based model, the geometric calibration parameters can be estimated. It is presented how physical model parameters, e.g., misalignments and link lengths, can be estimated using phantom-based measurement data. Effectively, the calibration procedure is recast to a parameter identification experiment. The potential of the proposed approach is illustrated by virtue of a benchmark object, successful reconstruction of a clinical phantom, and comparisons to the current phantom-based accuracies. Accurate (kinematic) models are required to achieve the desired accuracies. Based on the results in this chapter, the approach seems to be feasible for practical applications. However, the development of models with enhanced accuracies is required to meet future specifications.

2.1   Introduction

Advancing techniques in the medical society increasingly rely on high quality images of the interior of the human body. Minimal invasive surgery aims at reduced collateral damage during surgery, leading to less postoperative complications and faster patient recovery times. Accurate imaging is key for successful application of minimal invasive surgeries. X-ray Computed Tomography (CT) and three-dimensional rotational angiography (3DRA) enable the generation of high quality 3D reconstructions, based on a large number of 2D X-ray images each taken from a different point-of-view with respect to the patient [39]. Beside diagnostics, 3D reconstructions are typically used for 3D roadmapping where real-time 2D fluoroscopy images are projected on a pregenerated 3D reconstruction [7, 8]. Interventional C-arm based X-ray systems, as indicated in Fig. 2.1, are well suited for both described applications [24]. Due to the combination of the open kinematic structure of the system and a finite stiffness of the systems' mechanical components, the performance is significantly influenced by internal and external disturbances, e.g., gravitational and Coriolis forces, leading to position dependent, quasi-static deformations and inherent multivariable dynamic behavior [21].

Accurate calibrations are crucial to guarantee simultaneously a desired 3D quality and a sufficiently accurate overlay of the 2D fluoroscopy image over the 3D reconstruction for roadmapping. Due to system imperfections, e.g., manufacturing and assembly tolerances and the effects of external influences, the true geometry of the systems' image acquisition components, the detector, and X-ray source typically vary from the desired trajectory over the full scanning range. Assuming reproducibility of the system, phantom-based calibration procedures are widely applied in practice [10,11,18,22,40]. By performing a calibration scan of a specifically designed object with accurately known size and shape (phantom), the true behavior of the system is estimated using the obtained images. The resulting values for each pose are stored in a database and can be used for future reconstruction scans. The described procedure must be repeated for each scan trajectory, type, and velocity, leading to significant calibration times. In addition, the reproducibility condition imposes strict limitations on the systems' design from an engineering point-of-view. A relaxation of the reproducibility condition can be obtained using the images of the actual 3D reconstructions, e.g., using markers positioned in the patient table [26], or more advanced (markerless) techniques [27–29].

The 3D reconstructions are performed during system movements and are considered *dynamic* calibrations, while calibrations for 3D roadmapping are performed at *static* locations. Hence, independent measurements are required. Due to the finite density of the roadmapping calibration grid, interpolations are required to match the calibration data with actual physical system poses.

In this chapter, a model-based approach is introduced for system calibra-
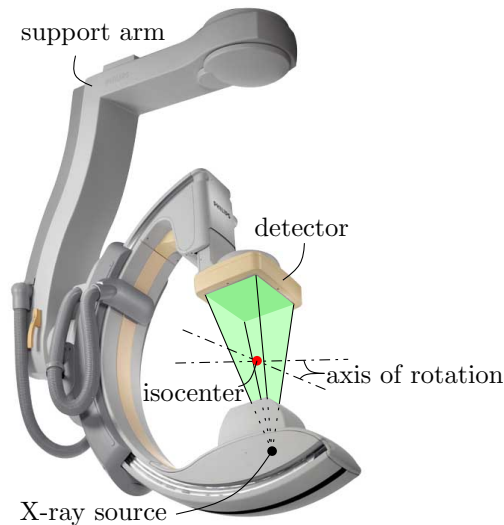
Fig. 2.1. Philips Xper Allura FD20 with indication of the exposure volume $\mathcal{V}_E$ (green pyramid).

tions, with application to 3D reconstructions and 3D roadmapping. The main contributions are

1. a model-based procedure that enables fast and reliable estimations of geometric parameters by exploiting the predictive properties of a physical model and reducing the required amount of calibration scans, and

2. an improved overlay for roadmapping applications, by utilizing the same model as used for the 3D reconstruction, which renders the additional interpolations unnecessary.

The emphasis is on the potential of the introduced approach. Basic *a priori* knowledge of the system is utilized and a parameter identification procedure is provided that can be applied on a limited amount of data obtained using a phantom-based approach.

This chapter is structured as follows, first, the fundamental relation between the calibration values and system geometry is illustrated in Sec. 2.2 concluding with a description of the proposed approach. Next, the modeling and identification approach is introduced in Sec. 2.3 which leads to the experimental results discussed in Sec. 2.4. The chapter concludes in Sec. 2.5 with the conclusions.

2.2 Preliminaries and proposed procedure

A basic understanding of the theory behind 3D reconstructions and roadmapping applications and the effects of the systems' geometry on the resulting quality is key for the design of a predictive model. Based on a pure vector notation, as is typical for (industrial) robotic systems [12, Chap. 2], [41], the relation between physical system parameters and the resulting 3D quality is illustrated. It should be noted that other representations, e.g., using the pinhole camera model, can be applied as well.

The results presented are based on a ceiling mounted Philips Xper Allura FD20 system, however, the approach can be applied to any system with 3D and/or roadmapping capabilities.

2.2.1 Influence of physical system parameters on 3D reconstruction quality

To illustrate the effect of mechanical imperfections and external influences on the acquired 3D quality, the definition of a reconstruction volume $\mathcal{V}_R$ is required. In order to define $\mathcal{V}_R$, first, the definition of the exposure volume $\mathcal{V}_E$ is introduced. In Fig. 2.2 the exposure volume for a single 2D image is illustrated, which is a detailed representation of the exposure volume depicted in green in Fig. 2.1. The exposure volume is defined as the volume spanned by the X-ray source and the detecting surface Ω_d of the system. Under the assumption that the detecting surface is of known shape and size, rigid, and the X-ray source being a point source, the relative vector $\underline{\nu}_s^d \in \mathbb{R}^3$ is defined as in Fig. 2.2. The vector $\underline{\nu}_s^d$ describes the relative position of the X-ray source with respect to the origin of the local coordinate system at the center of the detector, denoted by the superscript d. As a result, $\underline{\nu}_s^d$ and Ω_d fully define the size and shape of the exposure volume $\mathcal{V}_E(k)$, for a specific image k, as defined in Definition 2.1. The attenuation coefficients of the matter included in the exposure volume, which is a measure of the rate of quanta absorption, directly lead to the projected 2D image, see, e.g., [3].

Definition 2.1. (Exposure volume)
The exposure volume $\mathcal{V}_E$ is defined as all points that are exposed to X-ray quanta during a single exposure k and as such contribute to the acquired 2D image as indicated in Fig. 2.1 and 2.2.

Radon [4] showed that it is possible to reconstruct a 2D slice from a set of 1D projection images. This theory is generalized for 3D reconstructions based on a mapping of multiple 2D images [3, 6]. Under the assumption that Tuy-Smith's condition is fulfilled by the trajectory [42], the reconstruction is generated accurately for all points, or a subset, that are included in the intersection of all exposure volumes, defined as the reconstruction volume $\mathcal{V}_R$ in Definition 2.2. A graphical interpretation is shown in the middle of Fig. 2.2 for two images.
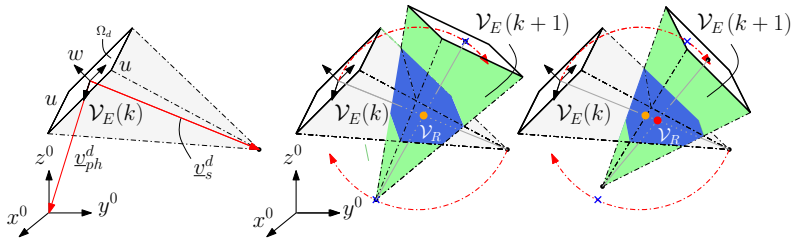
Fig. 2.2. Left: exposure volume $\mathcal{V}_E$ (green); reconstruction volume $\mathcal{V}_R$ (blue), based on two images. Middle: ideal situation; right: result due to the influence of deviations from the ideal trajectory (red dashed-dotted line).

Definition 2.2. (Reconstruction volume)
The reconstruction volume $\mathcal{V}_R$, depicted in Fig. 2.2, is mathematically defined by

$$\mathcal{V}_R = \bigcap_{k=1}^{N} \mathcal{V}_E(k), \tag{2.1}$$

with k a specific image and N the total number of images used for the generation of the 3D reconstruction.

Note that points close to the reconstruction volume that are included in almost all $\mathcal{V}_E$ can theoretically also be used for reconstructions, however, the quality degrades rapidly. In Fig. 2.2, both the ideal situation without any perturbations from the ideal reference trajectory and the perturbed situation are indicated. A change in the geometry of the system directly leads to a different size and shape of the reconstruction volume.

By virtue of the pinhole camera model, see, e.g., [3, Chap. 1], the acquisition geometry for flat-panel cone-beam systems can be described by a projection matrix in combination with a rotation matrix and translation vector. The projection of an arbitrary point within the exposure volume is highly correlated to the kinematic position and orientation of the detector, the position of the focal spot, and the relative position of the object with respect to the image-acquisition components. Hence, (mechanical) deviations from the ideal acquisition geometry lead to perturbed projections resulting in artifacts for (quasi-static) deterministic offsets and blur for zero-mean dynamical effects as indicated in Fig. 2.3. Hence, knowledge of the absolute exposure volumes with respect to each other is crucial.

In order to achieve an absolute reference, a fixed coordinate frame is required. This coordinate frame is typically chosen at the center of the phantom, however, in theory can be chosen arbitrary. To fully describe the position of each exposure volume, an additional vector, defined by $\underline{\nu}_{ph}^d$ as depicted in Fig. 2.2, is required.

increasing quasi-static error

increasing dynamic error
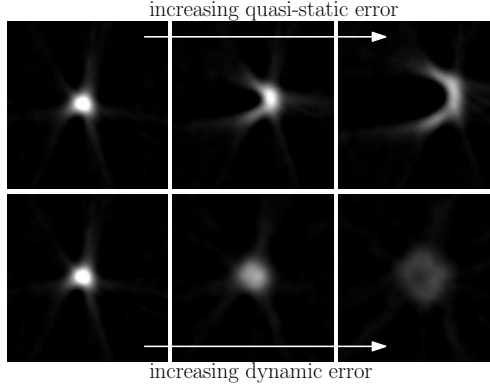
Fig. 2.3. Cross section of a thin wire for introduced geometric errors; top: simulated detector misalignment; bottom: dynamic offsets in calibration parameter; from left to right an increasing offset amplitude.

Three additional angular parameters $\underline{\theta}_w$ are required to describe the orientation of the detection plane Ω_d with respect to the fixed reference frame. This leads to a total of nine parameters for each projection k,

$$\underline{\xi}(k) = \left[\underline{\nu}_s^{d^T}(k)\ \underline{\nu}_{ph}^{d^T}(k)\ \underline{\theta}_w^T(k) \right], \qquad (2.2)$$

enabling the definition of the full cone-beam in the phantom coordinate system, e.g., $\underline{\nu}_s^{ph} = R_d^{ph}(\underline{\theta}_w)\underline{\nu}_s^d + \underline{\nu}_d^{ph}$. The advantage of the use of a vector notation as in (2.2), compared to, e.g., the pinhole camera model, is the direct relation toward available modeling approaches for robotic systems as presented in Sec. 2.3. However, alternative representations of the system can be applied as well. The aim of the calibration is to obtain the misalignments with respect to the parameters in (2.2), described by offsets on the vectors and an additional rotation matrix describing the rotational offsets.

Assuming knowledge of the deviations from the ideal trajectories, compensations are applied to the 2D images, e.g., shifts and rotations can be counteracted at the cost of a small amount of image information loss at the edges of the projections.

The calibration parameters in (2.2) can be separated in a known reference part $\underline{\xi}_r(k)$ and an unknown (offset) part due to system imperfections and disturbances $\Delta\underline{\xi}(k)$, leading to

$$\underline{\xi}(k) = \underline{\xi}_r(k) + \Delta\underline{\xi}(k). \qquad (2.3)$$

Typically, the ideal behavior $\underline{\xi}_r(k)$ is known from the design specifications, however, calibrations are required to compensate for the unknown part $\Delta\underline{\xi}(k)$. In Sec. 2.2.2 and 2.2.3 the currently applied calibration procedure and a novel
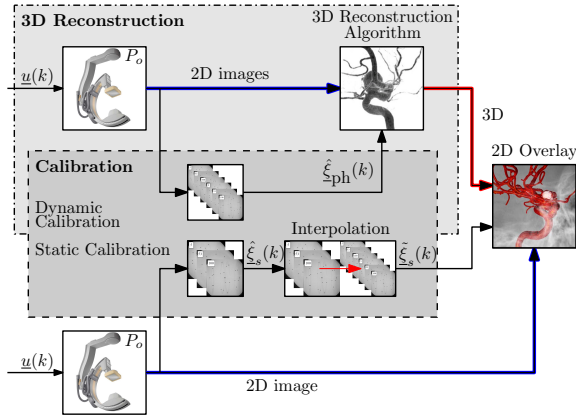
Fig. 2.4. Currently used calibration procedure for 3D reconstructions and 3D roadmapping applications with P_o indicating the true physical system.

model-based calibration procedure are presented respectively. In the remainder of this chapter, the term *geometric calibration* implies obtaining the geometric parameters as described in (2.2) either by *measurement* or *estimation*.

2.2.2 Currently applied calibration procedure

To illustrate the currently applied procedure, a schematic representation is provided in Fig. 2.4. It should be noted that separate calibration procedures are required for 3D reconstruction and 3D roadmapping applications. The use of a calibration phantom is common for both approaches. In this section, both existing procedures for 3D calibration and roadmapping applications are explained in detail.

Calibration for 3D reconstruction

A general relation between the accuracy of the obtained geometric calibration parameters and the quality of the obtained 3D reconstructions or 3D roadmapping applications is introduced in the previous section. The assumption is made that artifacts uncorrelated to the mechanics of the system are relatively small or already reduced in an image pre-processing step. A calibration phantom consists of multiple markers, typically circular objects of a high density material [10, 22]. Using a marker search algorithm, multiple marker positions of the phantom, are found in each obtained image. The marker positions are denoted

by $\tilde{\underline{\rho}}(\underline{\xi}) = \underline{\rho}(\underline{\xi}) + \underline{v}$ with $\underline{\rho}(\underline{\xi})$ the real position of the markers given the parameters $\underline{\xi}$ as defined in (2.2) and $\underline{v} \in \mathcal{N}(0, \sigma_v^2)$, indicating a zero-mean, normally distributed measurement noise with (co)variance σ_v^2. The reasons for the use of more markers then minimally required are twofold. First, to guarantee a sufficient number of markers within the line-of-sight while occlusions may occur. Second, a large quantity of marker positions enables an averaging effect for the computed geometric calibration. The cost function,

$$\mathcal{J} = \arg \min_{\hat{\underline{\xi}}_{\text{ph}}} \|\tilde{\underline{\rho}}(\underline{\xi}) - F(\hat{\underline{\xi}}_{\text{ph}})\|_2^2, \tag{2.4}$$

with $F(\hat{\underline{\xi}}_{\text{ph}})$ an estimation of the marker positions based on the estimated pose of the system $\hat{\underline{\xi}}_{\text{ph}}$, is defined. The parameter $\hat{\underline{\xi}}_{\text{ph}}$ is an approximation, indicated by $\hat{\cdot}$, of the true system poses described in (2.3), where the subscript ph indicates the estimation is obtained using a phantom-based approach. Note that the optimal solution is $\underline{\xi} = \hat{\underline{\xi}}_{\text{ph}}$ assuming the phantoms geometry is accurately described by a (calibrated) phantom model F. The estimated calibration parameters $\hat{\underline{\xi}}_{\text{ph}}$ are used for compensation in the 3D reconstruction algorithm as indicated in Fig. 2.4. Depending on the capabilities of the system, the number of calibration scans increases significantly, e.g., if the system allows for a detector shift, all acquisition types and velocities have to be calibrated for all usable detector positions to guarantee accurate 3D reconstruction. Hence, the total required calibration might take up to several hours for modern systems, including 3D roadmapping calibrations as presented in detail in the next section. Typically, the geometric calibrations are repeated every six months to compensate for system variations over time, e.g., wear of bearings or actuators, and after replacements or enhancements of (mechanical) components.

Accurate knowledge of the total of nine required calibration parameters in (2.2) guarantees optimal reconstruction qualities. However, this often leads to numerical difficulties imposed by non-convexity of the nonlinear optimization in (2.4). A large amount of approximative approaches is available in literature, see, e.g., [10], proposing a reduction of the number of estimated calibration parameters while introducing minimal reduction of reconstruction qualities.

Based on the mechanical structure of the system, it is known that the dominant structural flexibilities are located in joints, i.e., bearings and transmissions, and the support (arm) of the system to the ceiling, while the C-arc can be assumed rigid. Hence, the vector $\underline{v}_s^d(k)$, describing the position of the source with respect to the detector as presented in Sec. 2.2.1, is considered a constant, i.e., $\underline{v}_s^d(k) = [0, \ 0, \ -\text{SID}]^T \ \forall \ k$, with SID (source image distance) the distance between the focal spot and the center of the detecting surface. It should be noted that the remaining six estimated parameters include a small bias with respect to the true poses of the system as in (2.2).
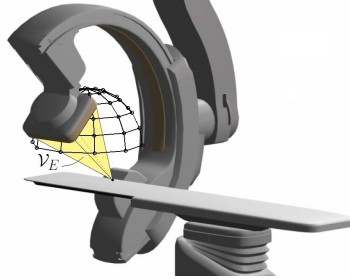
Fig. 2.5. Philips Xper Allura FD20 with indication of the exposure volume $\mathcal{V}_E$ (yellow pyramid) and a possible roadmapping calibration grid (black hemisphere).

Roadmapping calibration

A static 2D fluoroscopy provides only limited information to the user, however, it can be obtained from various directions using a C-arm based system. Particularly for procedures where potentially harmful contrast media are required, time-saving procedures are desired to minimize negative effects to the patients health. The 3D roadmapping technique allows for the overlay of live obtained 2D images over a predefined 3D reconstruction, reducing the prolonged exposure to contrast fluids while still visualizing the relevant part of the interior of the patient. In order to achieve accurate overlay in combination with the freedom of system positioning available to the user, an extensive calibration is required to match the 2D fluoroscopy images to the predefined 3D reconstruction for the full operating range of the system. As a result, a purely *static* calibration is required over a large number of system poses, in practice performed on a predefined grid as indicated in Fig. 2.5. The procedure to obtain $\underline{\xi}(k)$, $\forall\,k$ is equal to the phantom-based approach described in the previous section. To emphasize the difference between the 3D roadmapping and 3D calibration, the acquired geometric parameters can be denoted by

$$\hat{\underline{\xi}}_{\mathrm{ph}}(k) = \hat{\underline{\xi}}_s(k) + \hat{\underline{\xi}}_d(k),\tag{2.5}$$

with the subscripts s and d representing *static* and *dynamic* respectively. For the 3D roadmapping calibration $\hat{\underline{\xi}}_d(k) = 0$, which is not the case for 3D calibrations.

When the system is used between calibrated points, an interpolation step is required leading to the estimated geometric parameters $\tilde{\underline{\xi}}(k)$ as indicated in Fig. 2.4.

2.2.3 Proposed model-based calibration estimation

Although the calibrations presented in the previous sections lead to accurate results, the large number of calibrations for 3D reconstructions and calibrated grid

points for roadmapping applications lead to undesired long calibration times.

C-arm based X-ray systems represent a subclass of (industrial) robotic systems. Modern developments in modeling and control of (industrial) robotics allow for reliable predictions of (dynamical) system behavior [43, 44]. Using a model to obtain estimations of the systems' behavior given a specific input signal, i.e., dynamic responses (3D reconstructions) or static responses for a given motor angle (3D roadmapping), has the potential to reduce calibration times. By *a priori* defining the mechanical structure, i.e., the kinematics leading to the geometric parameters $\underline{\xi}(k)$, a finite set of physical parameters $\underline{\theta}$ can be identified that describes the system up to a desired accuracy. The system should satisfy the following two assumptions for the proposed model-based calibration procedure.

Assumption 2.1. (Assumptions for Model-Based Calibration)

1. *The system should allow for high repeatability in system motions.*

2. *A priori physical knowledge of the system is available.*

Note that for successful application of the current phantom-based calibration approach, Assumption 1 should also be satisfied. Assumption 2 leads to a trade-off between system knowledge and the requirement of performing a large number of system calibrations. In Fig. 2.6 a graphical representation of the proposed approach is given. An additional advantage of the proposed procedure is the elimination of the interpolation step in the 3D roadmapping calibration. A modeling approach often used for industrial robotic systems is suggested, however, any modeling approach leading to a prediction of the geometric parameters suffices. Also, the presented Philips Allura C-arm system under consideration is used in the upcoming sections to illustrate the potential of the proposed approach. However, the approach can be applied on any other system for which *a priori* information is available on the kinematic structure.

2.3 Modeling and parameter identification

The Philips C-arm based X-ray system under investigation is a serial link robotic system. The assumption that the movement of the source with respect to the detector has a minimal effect as introduced in Sec. 2.2.2 is maintained in this section, which allows for modeling of the detector position only.

Remark 2.1. Note that the proposed approach in Sec. 2.2.3 can be applied in combination with any geometric parameter reduction approach. However, if the bias with respect to the true system poses increases significantly, the physical effects imposed by assumptions or estimations should be included in the model.
◁
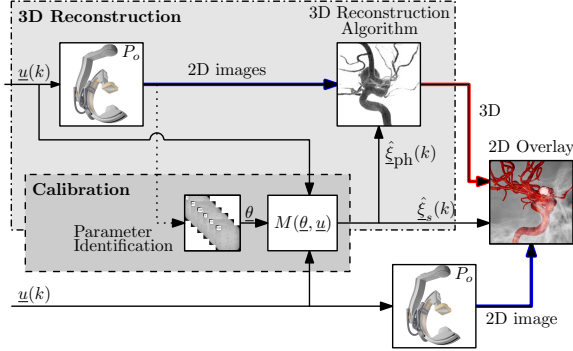
Fig. 2.6. Proposed approach to combine 3D reconstruction and roadmapping calibrations

The position and orientation of the detector are defined by three main contributions,

$$\hat{\underline{\xi}}(k) = \hat{\underline{\xi}}_k(k) + \hat{\underline{\xi}}_c(k) + \hat{\underline{\xi}}_{flex}(k) \tag{2.6}$$

where $\hat{\underline{\xi}}_k(k)$ describes a kinematic contribution, $\hat{\underline{\xi}}_c(k)$ a joint compliance contribution, and $\hat{\underline{\xi}}_{flex}(k)$ a contribution of flexible elements. First, the modeling approach for the three contributions in (2.6) is discussed in Sec. 2.3.1 through 2.3.3, followed by a parameter identification procedure in Sec. 2.3.4.

2.3.1   Kinematic modeling

For robotic systems, often the Denavit-Hartenberg (DH) convention is used [12, Sec. 2.8.2], [41, Sec. 3.2], which enables the description of kinematic poses of a serial link system with a minimal number of parameters. Any other parametrization might be chosen, however the DH-convention provides a minimal realization, which is beneficial for the identification of the parameters as is presented in Sec. 2.3.4. Many practical applications of the DH-convention are available in literature, see, e.g., [30, 32, 44]. The coordinate transformation, used to describe the displacement of each link, is defined by four parameters, according to the homogeneous transformation matrix

$$^jT = \begin{bmatrix} \cos(\theta_j) & -\sin(\theta_j)\cos(\alpha_j) & \sin(\theta_j)\sin(\alpha_j) & a_j\cos(\theta_j) \\ \sin(\theta_j) & \cos(\theta_j)\cos(\alpha_j) & -\cos(\theta_j)\sin(\alpha_j) & a_j\sin(\theta_j) \\ 0 & \sin(\alpha_j) & \sin(\alpha_j) & d_j \\ 0 & 0 & 0 & 1 \end{bmatrix}, \tag{2.7}$$

with j indicating the corresponding joint, a_j, α_j, d_j and θ_j generally denoted as the *link length*, *link twist*, *link offset*, and *joint angle* respectively [12, 41]. An extension of the original theory is applied where

$$\theta_j = \theta_{\delta_j} + \theta_j^* \beta_j, \tag{2.8}$$

with θ_{δ_j} a constant joint offset, θ_j^* the actuated joint angle, and β_j an offset in transmission ratio from the design specifications. The total homogeneous transformation matrix T of a serial link system is given by

$$T = {}^1T\,{}^2T \dots {}^{N_j}T = \prod_{j=1}^{N_j} {}^jT, \tag{2.9}$$

with N_j the total number of links, facilitating the total kinematic description,

$$\begin{bmatrix} \nu_{ph}^d \\ 1 \end{bmatrix} = \begin{bmatrix} f(\underline{q}) \\ 1 \end{bmatrix} = T \begin{bmatrix} \nu^w \\ 1 \end{bmatrix}, \tag{2.10}$$

with $f(\underline{q})$ a nonlinear expression in $\underline{q} = [\underline{a}, \underline{\theta_\delta}, \underline{\alpha}, \underline{d}, \underline{\beta}]^T$, a vector of physical unknown parameters, and $\underline{\nu}^w$ a vector expressing the center of the phantom, expressed in the phantom coordinate system, i.e., $\underline{\nu}^w = [0, 0, 0]^T$. Recall that the estimated output $\underline{\nu}_{ph}^d$ of the model contains three of the total of six required geometric parameters as defined in (2.2). The remaining three parameters are defined by the angles included in the rotational matrix defined as the upper left 3×3 elements of T in (2.9), i.e.,

$$T = \left[\begin{array}{c|c} R(\underline{\theta}_w) \in \mathbb{R}^{3\times3} & \nu_{\mathrm{ph}}^d \in \mathbb{R}^{3\times1} \\ \hline \underline{0} \in \mathbb{R}^{1\times3} & 1 \in \mathbb{R}^{1\times1} \end{array} \right]. \tag{2.11}$$

Hence, when the physical parameters q are known, estimations of all six required geometric parameters as described in Sec. 2.2.1 are available.

Remark 2.2. The same procedure can also be applied for nine parameters, however, an additional model describing the source position with additional DH-parameters should be derived. ◁

The definition of the DH-parameters and assignments of coordinate systems is straightforward and thoroughly covered in literature with practical applications [12, 30, 32, 41, 44]. In Fig. 2.7 a graphical representation of the DH-description of the system under investigation is given with the nominal parameters provided in Table 2.1. Note that in contrast to the standard definitions, the detector coordinate frame is chosen as the first frame instead of a fixed world frame, enabling a direct comparison to the measured calibration parameters $\underline{\nu}_{ph}^d$, introduced in Sec. 2.2.1 and indicated in Fig. 2.2, which is also defined in the local detector coordinate frame. Where for modeling of most robotic systems the main interest is on endpoint *position*, the *orientation* of the detector
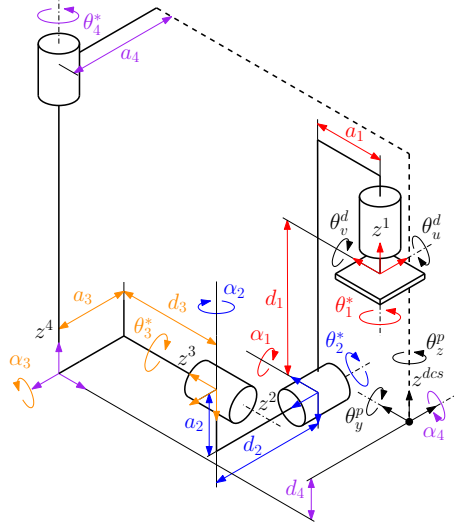
Fig. 2.7. Definition coordinate systems and DH-parameters of the Philips Xper Allura FD20

Table 2.1. DH-parameters of the Philips Xper Allura FD20

	a [mm]	$\delta\theta$ [rad]	α [rad]	d [mm]	β [-]
1	0	$\pi/2$	$-\pi/2$	-385	1
2	0	$\pi/2$	$\pi/2$	0	1
3	0	$\pi/2$	$-\pi/2$	0	1
4	0	π	0	0	1

is not uniquely defined due to the limited number of parameters used in the DH-convention. To compensate for this, two additional rotations of the detection plane and two additional rotations of the fixed phantom coordinate frame are introduced. The detector plane can be uniquely described as indicated in Fig. 2.7, for which ideally,

$$\underline{\theta}_f = \begin{bmatrix} \theta_u^d & \theta_v^d & \theta_y^p & \theta_z^p \end{bmatrix}^T = \begin{bmatrix} 0 & 0 & 0 & 0 \end{bmatrix}^T \text{[rad]}, \qquad (2.12)$$

with the subscript u and v indicating the orthogonal detector coordinates in the imaging plane as indicated in Fig. 2.7. In addition to the kinematic model, joint compliance, e.g., limited transmission stiffness and bearing flexibilities, is important in most robotic systems and is presented in Sec. 2.3.2.

2.3.2   Modeling of joint compliance

The compliance contribution at the detector for each joint can be described by [30, 31]

$$\hat{\underline{\xi}}_c = \frac{\partial f(\underline{q})}{\partial \Delta \underline{\theta}_c} \Delta \underline{\theta}_c = J_\theta \Delta \underline{\theta}_c, \qquad (2.13)$$

with $\Delta \underline{\theta}_c$ a rotation of the joint axis due to an external load at the endpoint of the kinematic chain and J_θ the Jacobian of the nonlinear expression $f(\underline{q})$ as given in (2.10). The effective joint torques due to the end-effector load are given by [30]

$$\underline{\tau} = J_\theta^T \underline{F}. \qquad (2.14)$$

The compliance of a joint can be modeled by a linear torsion stiffness according to

$$\Delta \underline{\theta}_c = C_\theta \underline{\tau}, \qquad (2.15)$$

with C_θ a diagonal matrix describing the individual torsion stiffness of each joint. Combining (2.13), (2.14) and (2.15) leads to

$$\hat{\underline{\xi}}_c = J_\theta C_\theta J_\theta^T \underline{F}, \qquad (2.16)$$

which can be rewritten as a set of equations linear in the stiffness parameter [45, 46].

2.3.3   Flexible element modeling

Link flexibility of the support arm, connecting the system to the ceiling, and the finite stiffness of the ceiling have a significant influence on the calibration parameters and can as a result not be neglected. By defining flexible links based on physical insight and first order flexible link models [47] of the dominant flexible elements, a model is defined. Small perturbations in the stiffness parameters lead to small variation in the predicted output. Hence, the nominal design parameters can be used for modeling of the flexible elements without introducing large errors. As a result, the flexible elements are excluded from the parameter identification procedure introduced in the following section.

2.3.4   Parameter identification

The unknown physical system parameters $\underline{q}$ in the nonlinear expression $f(\underline{q})$, as defined below (2.10), are estimated in this section based on measured data. Although the compliance and flexible contributions as described in Sec. 2.3.2 and Sec. 2.3.3 can be added to the set of unknown parameters, for improved readability the procedure is shown for the kinematic parameters only.

For the identification of nonlinear parameters in the model, an iterative least-square estimation is proposed. The least-square estimation is an intuitive approach for the identification of the parameters, it should however be noted that

other parameter identification approaches are available. Accurate initial parameters are crucial for convergence since the optimization problem is typically non-convex [12]. The first-order Taylor series expansion of $f(\underline{q})$, leads to

$$\Delta\hat{\underline{\xi}} = \frac{\partial f(\underline{q})}{\partial \underline{a}}\Delta\underline{a} + \frac{\partial f(\underline{q})}{\partial \underline{\theta}_\delta}\Delta\underline{\theta}_\delta + \frac{\partial f(\underline{q})}{\partial \underline{\alpha}}\Delta\underline{\alpha}\dots \tag{2.17}$$
$$+ \frac{\partial f(\underline{q})}{\partial \underline{d}}\Delta\underline{d} + \frac{\partial f(\underline{q})}{\partial \underline{\beta}}\Delta\underline{\beta} + \frac{\partial f(\underline{q})}{\partial \underline{\theta}_f}\Delta\underline{\theta}_f,$$

with $\Delta\hat{\underline{\xi}} = \hat{\underline{\xi}}_{\text{ph}} - \hat{\underline{\xi}}_{\text{m}}$ the difference between the model-based prediction $\hat{\underline{\xi}}_{\text{m}}$ and the phantom-based acquired geometric parameters $\hat{\underline{\xi}}_{\text{ph}}$. The set of equations,

$$\Delta\hat{\underline{\xi}} = \left[\frac{\mathrm{d}f(\underline{q})}{\mathrm{d}\underline{q}} \ \frac{\mathrm{d}f(\underline{q})}{\mathrm{d}\underline{\theta}_f} \right] \left[\begin{array}{c} \Delta\underline{q} \\ \Delta\underline{\theta}_f \end{array} \right] = J(\underline{q}) \left[\begin{array}{c} \Delta\underline{q} \\ \Delta\underline{\theta}_f \end{array} \right], \tag{2.18}$$

can be defined where $J(\underline{q})$ denotes the Jacobian of $f(\underline{q})$ with respect to the parameters $\underline{q}$ and $\underline{\theta}_f$. By introducing multiple measurement points, the set of equations,

$$\Delta\bar{\underline{\xi}} = \left[\begin{array}{c} \Delta\underline{\xi}_1 \\ \vdots \\ \Delta\underline{\xi}_{N_i} \end{array} \right] = \left[\begin{array}{c} J(\underline{q})_1 \\ \vdots \\ J(\underline{q})_{N_i} \end{array} \right] \left[\begin{array}{c} \Delta\underline{q} \\ \Delta\underline{\theta}_f \end{array} \right] = \bar{J}(\underline{q}) \left[\begin{array}{c} \Delta\underline{q} \\ \Delta\underline{\theta}_f \end{array} \right], \tag{2.19}$$

with N_i indicating the number of acquired measurement points, can be defined. Solving the set of equations in (2.19), assuming a zero-mean Gaussian distributed measurement noise on

$$\underline{\xi}(k) = \xi_0(k) + \eta, \tag{2.20}$$

with $\xi_0(k)$ the true set of parameters, $\underline{\xi}(k)$ the measured set and $\eta \in \mathcal{N}(0, C^\xi)$ with C^ξ a covariance matrix describing the Gaussian distributed measurement noise included in $\underline{\xi}(k)$, a least-squares estimation problem can be considered [48]. Assuming a global optimum of (2.19) is obtained, by increasing N_i the decreasing of the covariance on the estimated parameters can be approximated by

$$C^q = \frac{C^\xi}{N_i}. \tag{2.21}$$

As an additional condition, the matrix $\bar{J}(\underline{q})$ should be full rank to enable the computation of the least-square solution. This can be achieved by using a minimal realization of the system, e.g., using the DH-convention, and using sufficiently exciting reference signals during the identification experiment. By virtue of the obtained values for $\Delta\underline{q}$, an updated nominal parameter set can be obtained by $\underline{q}_{l+1} = \underline{q}_l + \Delta\underline{q}_l$ for iteration l. The same holds for the parameters in $\Delta\underline{\theta}_f$. By using the updated parameters to define a new nominal model $f(\underline{q}_{l+1})$, a new Jacobian can be computed using (2.17), resulting in an iterative procedure.

2.4 Experimental results

The modeling and parameter identification procedure as described in Sec. 2.3 is applied to a ceiling suspended Philips Xper Allura FD20 system, as depicted in Fig. 2.5. The results are presented for

1. a 3D reconstruction, and

2. multiple benchmark positions for the 3D roadmapping calibration.

First, the parameter identification results are presented.

2.4.1 Parameter identification experiment

In order to identify all model-parameters, the excitation signal should be persistently exciting, i.e., all actuation signals should be used while covering as many positions as possible within the operating space of the system [49]. In Fig. 2.8, the estimation errors are shown, as defined in (2.17), i.e., $\Delta \underline{\xi} = \hat{\underline{\xi}}_{\text{ph}} - \hat{\underline{\xi}}$, with $\hat{\underline{\xi}}_{\text{ph}}$ obtained from (2.4) and $\hat{\underline{\xi}}$ from (2.6). After five iterations, the result has converged to the physical parameters as indicated in Table 2.2. Due to safety limitations, simultaneous actuation of multiple joints is not possible on the system under consideration, leading to the data set of geometric parameters corresponding to a consecutive set of actuator movements. It should be noted that as a result infeasible jumps are present that might, in some cases, lead to identification difficulties, i.e., convergence issues. In addition, the systems' movements are limited by the patient table supporting the calibration phantom, possible other objects within the room, and the fact that the calibration phantom should be within the light of sight for each image. Only slow movements are used, reducing the dynamical contributions within the measurement set to a minimum, which corresponds best to the used *static* model, i.e., $\hat{\underline{\xi}} \approx \hat{\underline{\xi}}_s$.

Standard deviations of the estimation errors are shown to provide a quantitative measure for each geometric parameter. Note that clear outliers are present in the estimation errors. It should be noted that not all actuated motions are directly relevant for 3D reconstruction scans. Some actuated motions are only used to place the system in a specific pose, e.g., head- or nurse side, from which a standardized reconstruction movement is started. Estimation errors, particularly constant offsets in these motions, are often less critical for 3D reconstruction qualities. Although, for 3D roadmapping all offsets are problematic, the same model is used for the 3D reconstruction and the 3D roadmapping calibration, resulting in the same translational and rotational offsets are present in the reconstruction and the overlay calibration. Hence, the overlay remains accurate. The obtained physical parameters in Table 2.2 are feasible and within the given systems production specifications.
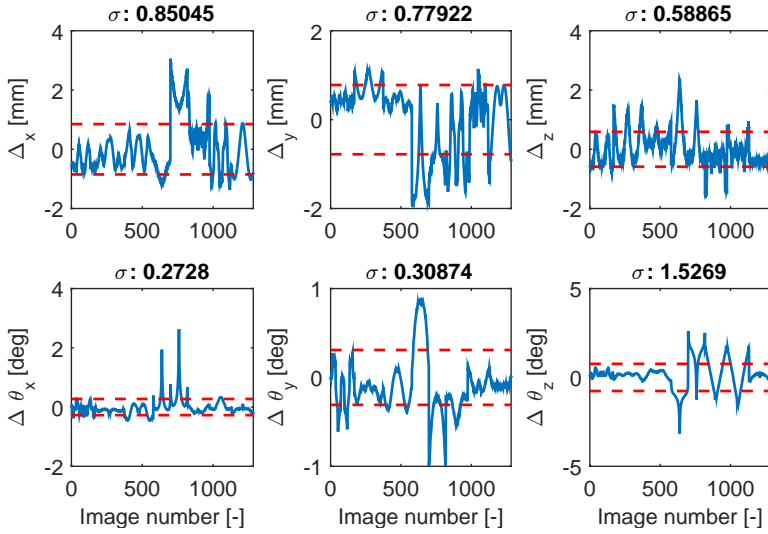
Fig. 2.8. Residual errors of identification data set after parameter identification (blue); $\pm$ standard deviation (σ) (red).
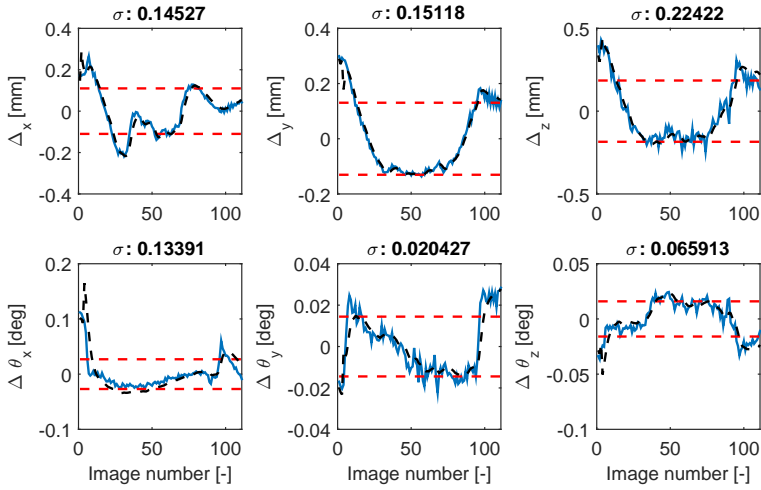
Fig. 2.9. Estimation errors of high-speed 3DRA calibration; $\underline{\xi}_{ph} - \hat{\underline{\xi}}_m$ (blue); $\underline{\xi}_{ot} - \hat{\underline{\xi}}_m$, with $\underline{\xi}_{ot}$ geometric parameters measured using the optical tracker (black-dashed); $\pm$ standard deviation of the estimation error (σ) (red)

Table 2.2. Identified DH-parameters of the Philips Xper Allura FD20

	a [mm]	$\delta\theta$ [rad]	α [rad]	d [mm]	β [-]
1	-0.6888	1.5789	-1.5668	-390.0287	0.9995
2	0.8832	1.5786	1.5769	-0.2988	0.9978
3	-0.3489	1.5655	-1.5774	5.4242	0.9981
4	3.7129	3.1908	0.0129	1.6914	0.9876

$$\underline{\theta}_f = \left[\, 2e^{-4},\ 1.5e^{-4},\ 11e^{-4},\ 14e^{-4} \,\right]^T \text{[rad]}$$

As a final remark it should be noted that the identification measurement contains 1200 images, acquired with a framerate of 7 fps., leading to a theoretical measurement time of approximately 3 minutes. Including the time required to set up the measurement and assuming predefined calibration movements, the required time for the identification experiment remains significantly smaller then the time required for all calibration motions for modern systems required by the phantom-based geometric calibrations as indicated in Sec. 2.2.2.

2.4.2   3D Reconstruction validation

The definition of required estimation accuracies for 3D reconstructions is not unique since it is highly dependent on the type of examined tissue, the desired scan type, e.g., 3DRA (high resolution) or CT, and the preference of the user. It can be stated that 3DRA scans, primarily used for high density imaging, e.g., visualization of arteries and aneurysms, and high-resolution CT, e.g., used for imaging of the inner ear, require the most demanding accuracies, i.e., high spatial resolutions are desired. Recall that not all estimation errors lead to a degraded 3D reconstruction quality, i.e., constant offsets in the geometric parameters over all images typically lead to a shift of the total reconstruction within the reconstruction volume without degrading the quality. Standard deviations are again used to quantify the estimation accuracy for each geometric parameter. The resulting estimation errors for a high-speed 3DRA scan are shown, in Fig. 2.9 indicating the difference between the model-based prediction and a phantom-based calibration set. An additional (external) measurement is performed using a NDI PRO CMM optical tracker which enables high-speed, high-accuracy (20μm) validation measurements. In Fig. 2.9, a small difference between the phantom-based approach and the external validation measurement is visible. Hence, the assumption leading to the reduced number of estimated geometric parameters in Sec. 2.2.2 is valid, since the modeling errors are dominant.

After identification of the physical parameters of the system, the resulting model-based predictions can be used for the reconstruction of benchmark ob-
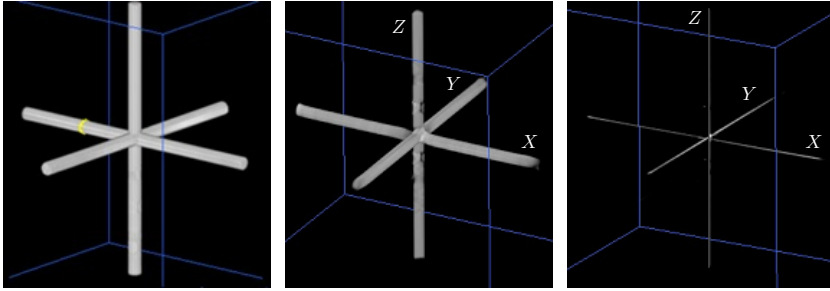
Fig. 2.10. 3D reconstruction results of a cross-wire; left: phantom-based calibration; axis Ø1 mm, middle: model-based calibration; axis Ø1 mm, right: model-based calibration; axis Ø0.2 mm

jects, consisting of multiple thin wires with diameters of ≈ 1 and ≈ 0.2 mm respectively. In Fig. 2.10 a reconstruction of such a benchmark object is illustrated for an ideal calibration and using the model-based calibrations. The reconstruction quality is not optimal, however, the structure of the cross-wire is clearly visible. Blur effects due to (unmodeled) dynamical effects can be observed, although they are not dominant. In Fig. 2.11, the corresponding 2D intensity profiles are shown where it can clearly be observed that reasonable results are obtained for 2 directions, i.e., the axis in the X and Z directions. In the Y direction, residual artifacts are visible, which is a clear indication that the model is not sufficiently accurate. Finally, in Fig. 2.12, the reconstruction of a clinically relevant phantom of an aneurysm is shown. The general structure of the reconstruction is of a similar quality as the phantom-based approach. Only for small veins, details are missing.

2.4.3   3D Roadmapping overlay validation

As indicated in (2.5), the geometric parameters consist of static- and dynamic contributions. The 3D roadmapping calibration is a purely static calibration, which is in line with the proposed quasi-static model. The overlay accuracy is typically not constant over the full imaging plane, which leads to multiple measures; at the image center, $1/3$ of the image and $2/3$ of the image. A benchmark data set, consisting of a random set of calibration positions, is used to validate the approach. For these positions, the maximum error, the maximum error of the best 90% estimated points, i.e., 10% outliers are discarded, and the average error over all data are compared to average phantom-based results indicated in Table 2.3. It should be mentioned that the maximum errors do not meet the specified values. However, comparable results to the average phantom-based approach, which requires interpolations, are obtained after outlier removal. From
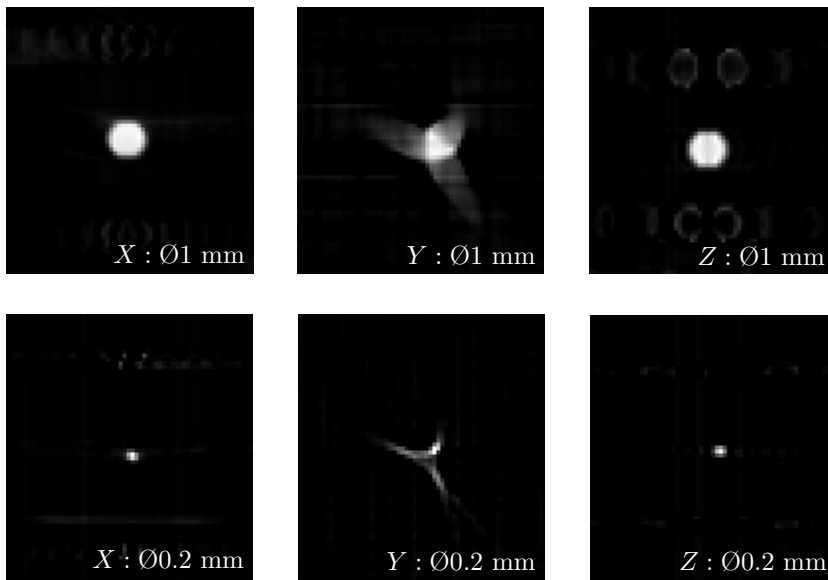
Fig. 2.11. 2D intensity profiles of wire frame indicated in Fig. 2.10; from left to right x, y, and z axis respectively; upper: Ø1 mm; lower: Ø0.2 mm.
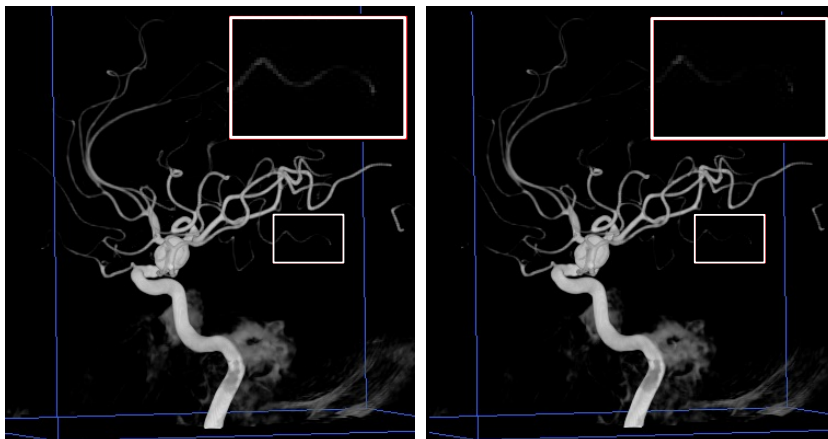
Fig. 2.12. 3D reconstruction of an aneurysm (phantom); left: phantom-based approach; right: model-based approach; in red square a detail zoom.

these results, the conclusions can be drawn that the results are of sufficient accuracy for practical usage.

Table 2.3. Overlay errors for (random) benchmark points; all values are in mm.

	max	max 90%	average	phantom-based 90%
Image center	0.814	0.593	0.212	0.477
1/3 image	0.842	0.611	0.313	0.523
2/3 image	0.867	0.647	0.514	0.683

2.5 Conclusions

A model-based approach for system calibrations for medical X-ray systems is proposed. A direct relation between the mechanical components of the system and the obtained 3D reconstruction quality is illustrated by virtue of the geometric parameters. The fundamentals behind the phantom-based calibration are highlighted and it is proposed to use the phantom-based approach for model-parameter identification experiments. By exploiting the predictive properties of a model, the required time for a geometric calibration can be reduced significantly with approximately a factor 10 to 15, which is the main goal in this chapter. Since the time-interval between geometric calibrations is prescribed by external circumstances, i.e., wear, collisions, or upgrades of the system, it is infeasible that the proposed approach increases these time-intervals. However, using state-of-the-art techniques available for robotic systems future extensions include data-driven learning of the model-parameters, enabling an increase in time-intervals between calibrations, possibly leading to automatic calibration. A modeling approach for quasi-static behavior of the system is proposed based on industrial robotic systems and a parameter identification approach is discussed followed by experimental results. The experimental results show that for 3D roadmapping applications, satisfying results can be obtained by the proposed approach, however, for 3DRA calibrations, the results are not optimal yet, which can be improved by using a more complete model, e.g., by extending the model with dynamical behavior. It should be noted that a trade-off is made between the model complexity and the accuracy of the estimations. More dynamical effects can be modeled, however, more complex models are not always desired. Investigations toward combinations with alternative existing approaches, e.g., markerless estimation of geometric parameters based on projection images [28], are interesting due to the combination of reliable model-based estimations of predictable system effects and the estimation of unpredictable effects, e.g., patient motions.

Driven by the desire for faster, more accurate measurements, and production-

and transportation cost reductions, trends in modern design of high-tech mecha-
tronic systems and robotics emphasize lightweight system design. Lightweight
systems typically have an increased sensitivity for internal and external dis-
turbances which pressures the reproducibility condition which is key for the
currently applied phantom-based approaches. Using an extended model that
includes the dynamical behavior of a system, possibly in combination with addi-
tional sensors, the estimation of geometric parameters can be performed during
normal system operation. Developments in Micro-ElectroMechanical Systems
(MEMS) technology allow for relatively cheap, accurate measurements of linear
accelerations, and angular velocities directly located at the detector and X-ray
source. A vast amount of research for robotic applications that exploits these
developments can be applied on medical systems. The model-based approach
proposed in this chapter might be a first step in that direction.

Chapter 3

Nonparametric Identification of a Medical X-ray System

.

The need for accurate knowledge of complex dynamical behavior for high-performance mechatronic systems led to the development of a vast amount of nonparametric system identification approaches over the recent years. The aim of this chapter is to compare several proposed methods based on experiments on a physical complex mechanical system to bridge the gap between identification theory and practical applications in industry, where basic identification approaches are often the norm. Typical practical implications such as operation under closed-loop control, multivariable coupled behavior and nonlinear effects are included in the analysis. Finally, a possible approach for fast and reliable identification is illustrated based on measurement results of an interventional medical X-ray system.

3.1   Introduction

Modern mechatronic systems are subject to increasing demands in terms of accuracy and throughput [50]. Model-based control design is a structured approach to deal with complex and multivariable dynamical systems, see [51], [52], and [53]. Particularly for positioning- and robotic systems, the estimation of unmeasured states, e.g., using Kalman filters, is increasingly important for accurate control, [43], [54]. Obtaining accurate models is key for achieving optimal results. Nonparametric identification is a well established intermediate step for parametric modeling of dynamical systems [48], [55].

High performance systems which are produced in (relatively) large volumes, e.g., (industrial) robotic systems such as interventional medical X-ray systems [39], typically have to deal with a tradeoff between production costs and accuracies. Larger uncertainties and increasing demands on the system lead to the desire for individual identification of each system. For many systems, like the medical X-ray system example, the mounting location is typically a significant factor in the relevant performance measures, i.e., identification experiments *in situ* at the customers location are desired. Complex mechatronic systems, such as robotic systems, typically exhibit highly coupled multivariable flexible behavior including nonlinearities, e.g., friction, hysteresis, and parameter varying behavior, see [44], [56], and [57]. For stability reasons, many systems operate only in closed-loop settings. For multiple-input multiple-output (MIMO) systems, traditional methods require multiple experiments for accurate identification of the frequency response matrix (FRM). For large volumes of produced systems, the relative cost of parts increases, typically leading to a decreased signal to noise ratio (SNR) due to imperfect sensors. As a result, undesirable long experiments are necessary to enable sufficient averaging.

For identification of (linear) parameter varying systems, which is a generally used approach to describe a specific class of nonlinear systems [33], two main approaches can be found in literature. On the one hand a global approach that aims at the identification of an LPV model in one shot, [58], [59]. On the other hand, local experiments, which is often referred to as using "frozen" parameters can be performed, i.e., performing workpoint depending identification experiments [60]. On this local domain, linear time invariant (LTI) behavior is assumed, which will be validated through an estimate of the nonlinear distortions as is presented in Sec. 3.4. The local nonparametric models are typically used as a basis for interpolation, leading to a parametric LPV model, see [33], [61] or for specific applications on robotic systems [62].

A vast amount of post-processing methods is developed to obtain nonparametric models. The best linear approximation (BLA) as introduced in [48] is a well established approximation for systems that exhibit a limited amount of nonlinear behavior. In [48, Chap. 3] it is argued that periodic excitation signals have advantageous properties, e.g., making a distinction possible between vari-

ances due to nonlinear contributions and to noise. Periodic multisine excitations allow the user more freedom in the selection of excited frequencies which can be exploited to optimize the SNR.

Local parametric approaches for non-periodic excitation signals, e.g., the local polynomial method (LPM) [63] and the local rational method (LRM) [35], [64], enable a simultaneous estimation of system dynamics and estimation of transient (or leakage) effects, rendering the removal of data due to transient effects unnecessary. As a result, the required measurement time can be reduced for each system. The LPM is extended for multisine excitation signals in [48, Sec. 7.3].

Although many approaches are available in literature, experimental results on complex mechatronic and mechanical systems are scarce. First results of the estimation of nonlinear distortions of complex robotic systems are presented in [65] in a closed-loop element-wise MIMO setting. Full MIMO identification in an open-loop setting is presented in [66].

In this chapter, the aim is to illustrate an approach for experiment design which leads to efficient experiments for accurate and fast nonparametric identification of a complex interventional medical X-ray system. The main contributions in this chapter are,

1. an efficient procedure in terms of measurement times and accuracy for obtaining frequency response functions of complex mechanical systems, by exploiting *a priori* system knowledge to optimize the excitation signal,

2. the implementation of the local rational method as introduced in [35] and the evaluation of the advantageous properties in closed-loop, for MIMO systems, and for periodic, e.g., multisine excitation signals,

3. a quantitative comparison in terms of time-efficiency and accuracy of multiple state-of-the-art nonparametric and local parametric identification approaches, based on experimental results from an interventional medical X-ray system, and

4. an illustration of the exploitation of a robustly obtained BLA to verify the LTI identification for each operating point.

Contribution 4. includes a check for both the LTI assumption and the quality of the used excitation signal using the nonlinear variance on the BLA.

In Sec. 3.2 a system description of the interventional X-ray system is provided and the identification objective is presented. In Sec. 3.3, the experiment design approach is described, including the design of the excitation signals. In Sec. 3.4 the theory behind the compared post-processing approaches is presented. The experimental results are presented in Sec. 3.5 followed by conclusions and recommendations in Sec. 3.6.

3.2   System description and identification objective

3.2.1   Interventional X-ray system

The interventional medical X-ray system in Fig. 2.1 is considered in this chapter. The system consists of two main parts; the C-arc which can be actuated over two orthogonal principal axis and the static, but flexible, support arm mounting the system to the ceiling for which all joints are on a mechanical break. The actuators are current driven electrical motors with inputs $\underline{u}(t) = \begin{bmatrix} u_1(t) & u_2(t) \end{bmatrix}^T$. The measured and controlled outputs are collocated encoders, measuring the angular rotations of both actuators. In addition, acceleration measurements are available in 3 orthogonal directions at the X-ray detector, leading to the total measurement vector $\underline{y}(t) = \begin{bmatrix} \ddot{y}_u(t) & \ddot{y}_v(t) & \ddot{y}_w(t) & y_1(t) & y_2(t) \end{bmatrix}^T$, where $\ddot{y}$ stands for the second derivative of y and the subscripts u, v, and w indicate the principal directions of the local coordinate system with the origin at the center of the detector plane. It should be noted that the acceleration measurements typically are used for estimation purposes and are not used for feedback control.

3.2.2   Measurement and identification objective

To stabilize a system or achieve a desired (tracking) performance, most systems operate in closed-loop conditions as depicted in Fig. 3.1. The open-loop system is denoted by G_{uy}, which describes the mapping,

$$y_0 = G_{uy} * u_0 \tag{3.1}$$

with $*$ indicating the convolution, the time-domain signal $u_0 \in \mathbb{R}^{n_u}$ the open-loop unperturbed input of the system with n_u inputs entering the plant and $y_0 \in \mathbb{R}^{n_y}$ the unperturbed output of dimension n_y. The signal $w \in \mathbb{R}^{n_u}$ is used to apply a user-defined excitation signal to the system and $r \in \mathbb{R}^2$ is a reference signal, which is typically used to enforce a jog mode, i.e., an additional motion to overcome stick-slip friction in the system. The matrix $T_y \in \mathbb{R}^{2 \times n_y}$ is used to select the feedback signals only, i.e.,

$$\begin{bmatrix} y_1 \\ y_2 \end{bmatrix} = T_y \, y. \tag{3.2}$$

The DFT of a signal is defined by

$$X(k) = \frac{1}{\sqrt{N}} \sum_{n=0}^{N-1} x(nT_s) e^{-i2\pi nk/N}, \tag{3.3}$$
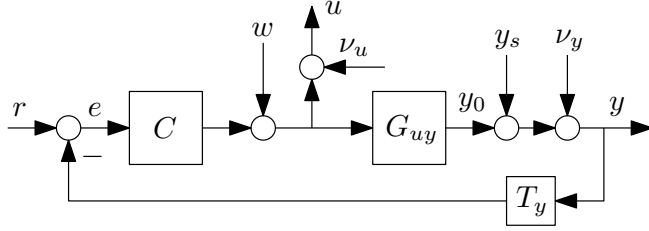
Fig. 3.1. Closed-Loop Measurement Setup

with N the number of samples, i the complex operator, T_s the sampling time, and k the discrete time index. The time domain signal $x(t)$ can be replaced by either $u(t)$ or $y(t)$, leading to the DFTs $U(k)$ and $Y(k)$ respectively.

The measured signals, assuming $r(t) = 0$, are given by

$$U(k) = W(k) - CT_y\big(Y_s(k) + V_y(k)\big) + V_u(k), \tag{3.4}$$

$$Y(k) = Y_0(k) + Y_s(k) + V_y(k), \tag{3.5}$$

where C is the controller, V_u and V_y are measurement noise of appropriate dimensions, and $U_s(k) = CT_yY_s$ and Y_s are stochastic nonlinear distortions. It should be noted that the plant input U is correlated to the measurement noise and nonlinear distortion on Y, as a result of the feedback structure.

The fundamental equation corresponding to the indirect method is given by

$$Z(k) = G_{wz}(\Omega_k)W(k) + T_{wz}(k) + Z_s(k) + V_z(k), \tag{3.6}$$

see e.g., [48, Sec. 3.8], since for closed-loop settings, direct (open-loop) approaches lead to biased results [67]. The notation Ω_k is adopted from [48] and denotes a generalized transform variable evaluated at DFT frequency k, i.e., in the Laplace domain $\Omega_k = j\omega_k$ and in the Z-domain $\Omega_k = e^{-j\omega_k T_s}$, with T_s the total sampling period. The indirect output equation in (3.6) is used throughout this chapter, with

$$Z(k) = \begin{bmatrix} Y(k) \\ U(k) \end{bmatrix}, \tag{3.7}$$

the DFT of the measured input- and output signals, G_{wz} indicating the mapping $w \mapsto z$, i.e., $G_{wz} = \begin{bmatrix} G_{wy} & G_{wu} \end{bmatrix}^T$, T_{wz} represents a transient response or leakage term, Z_s a stochastic nonlinear distortion, and V_z the measurement noise on the measured signals.

The objective for the identification experiment is to obtain an accurate nonparametric estimation of G_{uy}, and additionally obtain an estimation of the noise variances and estimations of nonlinear distortions. The measurement time is desired to be as short as possible, to enable measurements for each individual system during *in situ* installation.

3.3   Experiment design

The approaches in this chapter are based on periodic excitation signals. A multisine signal is defined by

$$w(t) = \sum_{k=1}^{N} A_k \sin(2\pi kt/N + \phi_k), \tag{3.8}$$

with N the number of samples in a single multisine period, A_k the amplitude of excitation bin k, and ϕ_k is a uniformly distributed phase on $[0, 2\pi)$ such that $\mathbb{E}\{e^{i\phi_k}\} = 0$. The interventional X-ray system, as described in Sec. 3.2, has multiple inputs, which means MIMO identification experiments are required. A full random orthogonal multisine input matrix is described by

$$\mathbf{W}(k) = D_W(k)TD_\phi(k), \tag{3.9}$$

where $D_W(k)$ and $D_\phi(k)$ are both diagonal matrices containing the multisines and additional phases for each excitation bin k respectively. The matrix T is an orthogonal (Hadamard) matrix, see [48, Sec. 3.7] and [68]. By obtaining the input matrix $\mathbf{W}(k) \in \mathbb{R}^{n_u \times n_u}$, n_u experiments can be performed on the system where each column of $\mathbf{W}(k)$ is used as input for the corresponding experiment. For purely linear systems, the orthogonality imposed by the matrix T is sufficient to identify the system behavior. For systems that exhibit (weakly) nonlinear behavior the additional randomness of the phases in $D_\phi(k)$ is desired for optimal estimation of the covariances due to nonlinear distortions, as will be presented in detail in Sec. 3.4. In addition, for the local parametric approaches presented in Sec. 3.4.2 the additional phase randomness is even required to avoid singular matrices during the least-squares estimations.

For MIMO systems, the frequency response matrix (FRM) describes a linear approximation of the systems dynamics. Since any physical system exhibits some measure of nonlinear behavior, the best linear approximation (BLA) of the systems' dynamics is desired [48]. Input characteristics, e.g., DC gains and RMS values, heavily determine the resulting BLA for nonlinear systems due to the power dependency of nonlinearities. Hence, the characteristics of the input signal should be chosen as close to operating conditions of the system as possible, to obtain a relevant BLA. Similar reasoning holds for multivariable systems. If the system usually operates under single joint movements, full MIMO identification may yield undesired coupled behavior, which does not correspond to normal operating conditions, and the system should therefore be identified using single-input multiple-output experiments.

Since the X-ray system typically moves in a single direction during operation, the effect of stick-slip friction is limited to the begin and end of the trajectories. Hence, a jog mode is chosen to reduce the effect of stick-slip behavior in the nonlinear distortion estimation. By choosing a periodic jog mode such that an

integer number of periods fits in a single multisine period without exceeding the mechanical limits of the system, there are no additional leakage distortions.

The choice of the excitation signal heavily depends on the systems dynamical behavior. Mechanical systems typically exhibit lightly-damped resonances, which requires a dense excitation grid. The spectral distance Δf linearly depends on the measurement length by $\Delta f = f_s/N$, with f_s the systems sampling rate and N the number of samples within a single period. By increasing the spectral density Δf, measurement times increase rapidly. In addition, due to hardware limitations, the total power of the excitation signal is typically bounded. Hence, an increase of the number of harmonics in $w(t)$ from (3.8) leads to a decreased SNR. To optimize the SNR, it might be desired to select the excitation frequencies manually, e.g., a logarithmic distribution or the selection of a dense grid around resonances, while reducing the number of excitations in other frequency regions. The latter approach requires *a priori* knowledge on the system. To optimize the experiment, a three step procedure is introduced,

1. perform a (long) measurement using multiple periods, multisine realizations, and experiments [48, Sec. 4.3.1] to estimate the system behavior, preferably on multiple systems,

2. optimize the excitation signal such that a dense grid is selected in a nonconservative band around the resonances and/or other frequencies of interest, and

3. perform *in situ* identification experiments on each individual system, using the newly obtained excitation signal.

The following section introduces various approaches that enable nonparametric identification of complex dynamical systems.

3.4 Nonparametric identification approaches using periodic excitations

Nonparametric estimation of the best linear approximation can be performed fully based on data or using a local parametric estimation. Both approaches are briefly introduced in the current section.

3.4.1 Best linear approximation by averaging

First the robust method is introduced, which is based on multiple realizations of multisine signals, followed by a fast approach which only requires a single realization. The methods assume the general experimentation structure in (3.6).

Robust method

The robust method is based on averaging over various periods, realizations, and experiments of the periodic signal.

By computing the DFT of (3.7) and averaging for each realization and experiment over the periods,

$$\bar{Z}^{[m,e]} = \frac{1}{P} \sum_{p=1}^{P} Z^{[m,e,p]}(k), \tag{3.10}$$

the effect of the noise term $V_z(k)$ is reduced. Throughout this thesis, the realizations m, experiments e, and periods p are indicated by the superscript $[m,e,p]$ when they are individually evaluated, where the notation is adopted from [48]. Note that depending on the length of a single period and the dynamics of the system, determined by the pole locations, a set of initial periods should be removed for each realization and each experiment to reduce the transient and leakage effects $T_{wz}(k)$, i.e., the remaining $T_{wz}(k) \approx 0$. In (3.10) it is assumed that $p = 1$ is the first period where the transient effects have faded out. The total number of periods remaining after transient removal is denoted by P.

To quantify the uncertainties on the estimations, typically the sample covariance over multiple DFT vectors is used, a more detailed explanation is given in, [48, Chap. 16]. The noise covariance for the output is given by the sample covariances over the periods,

$$^{\mathrm{n}}\hat{C}_{\bar{Z}}^{[m,e]}(k) = \frac{1}{P(P-1)} \sum_{p=1}^{P} e_Z(k) e_Z^H(k), \tag{3.11}$$

with $^{\mathrm{n}}\hat{C}_{\bar{Z}}^{[m,e]}$ the noise covariance, P the number of periods after the transient effects have been removed, and $e_Z(k) = Z^{[m,e,p]}(k) - \bar{Z}^{[m,e]}(k)$ the deviation of each period compared to its average. The output matrix for each realization is obtained by stacking the data such that the measurement of each experiment forms a single column according to

$$\mathbf{Z}^{[m]}(k) = \left[\, \bar{Z}^{[m,1]}(k) \, \ldots \, \bar{Z}^{[m,n_u]}(k) \,\right]. \tag{3.12}$$

For a meaningful averaging over the realizations, a correction for the random phase is required. The input matrix $\mathbf{W}^{[m]}(k)$ can be written according to

$$\mathbf{W}^{[m]}(k) = D_{|W|}^{[m]}(k) T_{\angle W}^{[m]}(k), \tag{3.13}$$

with $D_{|W|}^{[m]}(k)$ a diagonal matrix including the amplitudes of the multisine signal, i.e., the singular values of $\mathbf{W}(k)$, at frequency bin k, and $T_{\angle W}^{[m]}(k)$ a unitary matrix that describes the orthogonality and phase of the multisine, i.e., $T_{\angle W}^{[m]^{-1}} =$

$T_{\angle W}^{[m]^H}$, with the superscript H indicating the Hermitian transpose. Note that the separation in (3.13) is different from the structure in (3.9). The matrix $T_{\angle W}^{[m]}(k)$ can be obtained from (3.13), i.e., $T_{\angle W}^{[m]}(k) = D_{|W|}^{[m]^{-1}}(k)\mathbf{W}^{[m]}(k)$. After computation of the orthogonal phase matrix, the output matrix can be corrected for the random phases,

$$\mathbf{Z}_c^{[m]}(k) = \mathbf{Z}^{[m]}(k)T_{\angle W}^{[m]^H}(k), \tag{3.14}$$

enabling averaging over the realizations according to

$$\bar{\mathbf{Z}}_c(k) = \frac{1}{M}\sum_{m=1}^{M}\mathbf{Z}_c^{[m]}(k), \tag{3.15}$$

with M the total number of realizations. Note that $\bar{\mathbf{Z}}_c(k)$ is still similar to (3.7), with the phase corrected $\bar{\mathbf{Y}}_c$ and $\bar{\mathbf{U}}_c$. The total output noise covariance can be computed by averaging over the sample noise covariances (3.11),

$$^{\mathrm{n}}\hat{C}_{\bar{Z}}(k) = \frac{1}{n_u}\frac{1}{M^2}\sum_{e=1}^{n_u}\sum_{m=1}^{M}{}^{\mathrm{n}}\hat{C}_{\bar{Z}}^{[m,e]}(k), \tag{3.16}$$

where the average sample covariance over the realizations is obtained, see Sec. C.1 for an explanation of the sample (co)variance. The sample mean is calculated over the realizations, since only a finite set of realizations is measured. The averaging over the experiments is a normal mean, since this is the full set of experiments required for the estimation. The BLA can be computed by

$$\begin{aligned}\hat{G}_{uy}(\Omega_k) &= \left(\bar{\mathbf{Y}}_c(k)D_{|W|}^{-1}(k)\right)\left(\bar{\mathbf{U}}_c(k)D_{|W|}^{-1}(k)\right)^{-1}\\ &= \bar{\mathbf{Y}}_c(k)\bar{\mathbf{U}}_c^{-1}(k), \end{aligned} \tag{3.17}$$

where it should be noted that the amplitude distribution is by design identical for each realization. The noise covariance on the plant is obtained from [48, Sec. 2.7.2] modified according to [48, Sec. 7.3.3.3],

$$^{\mathrm{n}}\hat{C}_G(k) = \overline{\left(\bar{\mathbf{U}}_c(k)\bar{\mathbf{U}}_c^H(k)\right)}^{-1}\otimes\left(Q(k)\,{}^{\mathrm{n}}\hat{C}_{\bar{Z}}(k)Q^H(k)\right) \tag{3.18}$$

with $\otimes$ indicating the Kronecker product, $Q(k) = \begin{bmatrix} I_{n_y} & -\hat{G}_{uy} \end{bmatrix}$ to map the covariance on $\bar{\mathbf{Z}}$ to $\bar{\mathbf{Y}}$, where I_{n_y} is an identity matrix of dimension $n_y \times n_y$, and where $\hat{G}_{uy}$ follows from (3.17).

The total covariance, e.g., due to noise, nonlinearities, and residual transient or leakage effects, is given by

$$\hat{C}_{\bar{Z}}(k) = \frac{1}{n_u}\sum_{e=1}^{n_u}\hat{C}_{\bar{Z}}^{[e]}(k), \tag{3.19}$$

where $\hat{C}_{\bar{Z}}^{[e]}(k)$ follows from a similar computation as in (3.11), calculating the sample mean over M and defining $e_Z(k) = \bar{Z}_c^{[m,e]}(k) - \bar{Z}_c^{[e]}(k)$. The obtained result in (3.19) can be mapped to the plant estimation using (3.18), resulting in $\hat{C}_G(k)$. The final step is the computation of the stochastic nonlinear distortions, which can be defined *element-wise* for each frequency and input-output combination by

$$
{}^{\mathrm{s}}\hat{C}_G(k) = \begin{cases} \hat{C}_G(k) - {}^{\mathrm{n}}\hat{C}_G(k) & \text{if } \hat{C}_G(k) \geq {}^{\mathrm{n}}\hat{C}_G(k) \\ 0 & \text{if } \hat{C}_G(k) < {}^{\mathrm{n}}\hat{C}_G(k) \end{cases} \tag{3.20}
$$

indicating that the stochastic nonlinear distortions are only defined when the total covariance exceeds the noise covariance. In [48, Chap. 4.3], the BLA by averaging is described in detail. The nonlinear analysis of the method relies on the principle that a periodic input signal results in a periodic output signal (PISPO), including all nonlinear effects in the system. This assumption results in the separation between the nonlinearities in the measurement and the measurement noise and hence enables Eq. (3.20). Besides that, only information about nonlinear contributions acting on frequencies that are excited are distinguishable. The BLA of a system is an approximation of the systems dynamics given a certain input signal. A different input signal will typically result in a different BLA of the system and consequently a different covariance due to the stochastic nonlinearities. It is crucial for the usability of the identified plant dynamics that the identification experiment is performed with an input signal as close to the true application as possible. The effects of the stochastic nonlinearities to the BLA can be minimized by increasing the number of realizations.

Fast method

The fast method to obtain the BLA is based on multiple measured periods and experiments of a single realization. Estimations on the stochastic nonlinear distortion are obtained by evaluation of the non-excited frequencies. To achieve good results, the selection of sufficient detection lines, i.e., unexcited harmonics, typically chosen 1 in 2, 3, or 4 consecutive excited frequencies, [48, Sec. 4.3.2], is key for accurate estimations of stochastic nonlinear distortions. The plant estimation is recovered from the robust method by evaluation of a single realization, however, performing n_u experiments is still required for MIMO systems. Both the input and output signals are averaged over the periods, similar to (3.10), to reduce the influence of noise, resulting in the output matrix as in (3.12). Since only a single realization is used, there is no need for the mapping of the phase of W since this is identical for Y and U and would be undone in the plant estimation. The plant estimation is obtained similar to (3.17). The key difference with the robust method from the previous section is in the computation of the total covariance. The computation of the noise covariance is done equivalent

to (3.11), (3.16), and (3.18). Note that for closed-loop settings, an additional correction step is required to compensate for correlation on the detection lines with the measured output of the system, i.e.,

$$\bar{\mathbf{Y}}_{\mathrm{cl}}(k_{\mathrm{det}}) = \bar{\mathbf{Y}}(k_{\mathrm{det}}) - \hat{G}_{uy}(\Omega_{k_{\mathrm{det}}})\bar{\mathbf{U}}(k_{\mathrm{det}}), \tag{3.21}$$

with k_{det} indicating the detection frequency bin and $\hat{G}_{uy}(\Omega_{k_{\mathrm{det}}})$ obtained from a linear interpolation between the excited frequency bins k_{ex} around the evaluated detection bin, i.e.,

$$\hat{G}_{uy}(\Omega_{k_{\mathrm{det}}}) = \frac{(k_2 - k_{\mathrm{det}})\hat{G}_{uy}(\Omega_{k_1}) + (k_{\mathrm{det}} - k_1)\hat{G}_{uy}(\Omega_{k_2})}{k_2 - k_1}, \tag{3.22}$$

with $k_1 < k_{\mathrm{det}} < k_2$, where k_1 and k_2 are the neighboring excited frequencies of k_{det}. The covariance on the output is computed by

$$\hat{C}_{\bar{\mathbf{Y}}_{\mathrm{cl}}}(k_{\mathrm{ex}}) = |\bar{\mathbf{Y}}_{\mathrm{cl}}(k_{\mathrm{det}})\bar{\mathbf{Y}}_{\mathrm{cl}}^H(k_{\mathrm{det}})|. \tag{3.23}$$

This covariance estimation requires an additional interpolation to compute (3.23) at k_{ex}. Using (3.18), the output covariance is mapped to the plant, however, it should be noted that $Q(k)$ is equal to an identity matrix since the output covariance is already known for $\bar{\mathbf{Y}}$. Obtaining the covariance due to stochastic nonlinearities is performed using (3.20).

3.4.2 Local parametric approach

Besides the robust and fast approach for the computation of the BLA presented in Sec. 3.4.1, local parametric approaches are available. The LPM for arbitrary (non-periodic) excitation signals is presented in [63]. Current developments tend to local approximations using rational function, leading to the LRM, see, e.g., [35], [64]. A robust and fast implementation of the LPM for periodic excitation signals is described in [48, Sec. 7.3] and [69]. In the current section the derivation is provided for both a robust and fast implementation of the LRM using periodic excitation signals. It should be noted that the LPM is recovered by replacing the rational functions by polynomials. The main advantage of the local parametric approaches over the approaches in Sec. 3.4.1 is the estimation of transient effects which renders the removal of acquired measurement data unnecessary. Hence, no measurement time is lost which is desired to achieve the objective described in Sec. 3.2.2, i.e., short measurement times to enable individual identification of each system. The local parametric approaches using periodic excitation signals are performed in two steps. First, the transient is estimated and the measured in- and output DFT are corrected. Second, the plant is estimated using averaging over multiple realizations in the robust method, or using a second local parametric estimation step for the fast method.

Robust method

In the first step, in contrast to the approach in Sec. 3.4.1, the aim is to estimate the transient based on non-excited frequency bins. Where in the previous section the DFT is computed over a single period, here the DFT is computed over the full measurement, resulting in P times as many frequency bins in the signals, which results in $P - 1$ non-excited lines between every excited frequency for a full multisine signal. This approach is similar to [48, Sec. 7.3], assuming similar periodicity for nonlinear contributions as the system behavior. See also Fig. 3.2 for a graphical interpretation.

The rational function describing the local estimation of the transient is given by

$$T_{wz}(\Omega_k) = D^{-1}(r)M(r), \tag{3.24}$$

$$D(r) = I_{n_z} + D_1 r + D_2 r^2 + \ldots + D_{N_d} r^{N_d} \qquad \in \mathbb{C}^{n_z \times n_z}, \tag{3.25}$$

$$M(r) = M_0 + M_1 r + M_2 r^2 + \ldots + M_{N_m} r^{N_m} \qquad \in \mathbb{C}^{n_z \times 1}, \tag{3.26}$$

where r is defined in (3.29). N_m and N_d are user-defined orders of the numerator and denominator polynomials respectively. $T_{wz}(\Omega_k)$ represents the full frequency response matrix of the transient. The individual matrices D_i and M_i contain all unknown parameters to describe the local approximation. It should be noted that the constant term in the denominator polynomial is enforced $D_0 = I_{n_z}$, with $n_z = n_y + n_u$ the number of closed-loop outputs. By enforcing the constant denominator matrix to be non-singular, the matrix $D(r)$ will be non-singular and additionally, the parametric identification will not result in a trivial solution.

The general equation in (3.6) reduces for the non-excited frequency bins to

$$Z^{[m,e]}(\alpha P + r) = T_{wz}^{[m,e]}(\alpha P + r) + V_z^{[m,e]}(\alpha P + r). \tag{3.27}$$

After substitution of (3.24), neglecting the noise contribution, and rewriting (3.27) results in,

$$Z^{[m,e]}(\alpha P + r) = M_z^{[m,e]}(r) - \tilde{D}_z^{[m,e]}(r)Z^{[m,e]}(\alpha P + r), \tag{3.28}$$

where $D_z^{[m,e]}(r) = I_{n_z} + \tilde{D}_z^{[m,e]}(r)$ in (3.24),

$$r = \left[-(P-1) \ \ldots \ -1 \ 1 \ \ldots \ (P-1) \right], \tag{3.29}$$

and αP the excited frequency bin as indicated in Fig. 3.2. Note that r can be extended to a larger frequency window, however, it should be guaranteed that no excited frequency bins are included, i.e., $\alpha P \notin r \ \forall \ \alpha \in \mathbb{Z}$.

Given the measurements $Z^{[m,e]}$, a by design overdetermined set of linear equations is defined by

$$Z^{[m,e]}(\alpha P + r) = \Theta^{[m,e]}(\alpha P)K^{[m,e]}(\alpha P + r), \tag{3.30}$$
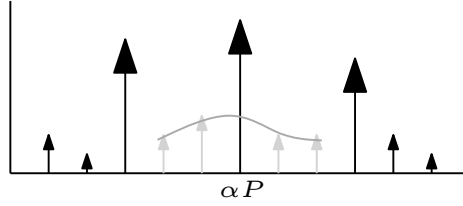
Fig. 3.2. Indication of excited frequency bin αP and non-excited frequency bins $\alpha P + r$ indicated by the red arrows; local estimation of transient indicated in blue; example for P = 3. Assuming the system is PISPO, the non-excited frequency bins only contain noise and transient effects.

with,

$$\Theta^{[m,e]}(\alpha P) = \begin{bmatrix} M_0 & M_1 & \dots & M_{N_m} & D_1 & \dots & D_{N_d} \end{bmatrix}, \tag{3.31}$$

where $M_0 = T_{wz}^{[m,e]}(\Omega_{\alpha P})$. It should be noted that the definition of the output equation (3.30) is enabled by the choice of $D_0 = I_{n_z}$. If none of the unknown parameters would be constraint $\hat{\Theta} = 0$ is a trivial solution. The solution can be computed by minimizing,

$$\hat{\Theta} = \arg \min_{\Theta} \| Z(\alpha P + r) - \Theta(\alpha P) K(\alpha P + r) \|_F^2, \tag{3.32}$$

with subscript F indicating the Frobenius norm, see [48, Chap. 15]. After minimization, the residual term,

$$\mathcal{R}^{[m,e]}(\alpha P) = Z(\alpha P + r) - \hat{\Theta}(\alpha P) K(\alpha P + r), \tag{3.33}$$

is obtained. Based on the residuals, the noise covariance on $Z^{[m,e]}(\alpha P)$ is estimated according to

$$^{\mathrm{n}}\hat{C}_{\bar{Z}}^{[m,e]}(\alpha P) = \gamma \mathcal{R}^{[m,e]}(\alpha P) \mathcal{R}^{[m,e]^H}(\alpha P), \tag{3.34}$$

with a scaling factor,

$$\gamma = \frac{1 + \| \Sigma^{-1} \mathcal{V}_{[1,:]}^H \|_2^2}{2(P-1) - (N_m + 1 + (n_u + n_y)N_d)}. \tag{3.35}$$

By exploiting the singular value decomposition, i.e., $K^H = \mathcal{U}\Sigma\mathcal{V}^H$, the required term $\Sigma^{-1}\mathcal{V}_{[1,:]}^H$ is obtained, where the subscript $[1,:]$ indicates the first row. Using the result of (3.34), the total noise covariance on the plant is estimated according to (3.16) and (3.18). Note that $\gamma \geq 0$ is ensured by the overdetermined least-squares problem, i.e., $2(P-1) \geq N_m + 1 + n_z N_d$.

After estimation of the transient effect $\hat{T}_{wz}^{[m,e]}(\alpha P)$, the measured signals can be compensated,

$$\bar{Z}^{[m,e]}(\alpha P) = Z^{[m,e]}(\alpha P) - \hat{T}_{wz}^{[m,e]}(\alpha P), \tag{3.36}$$

with $\hat{T}_{wz}^{[m,e]}(\alpha P) = \left[\hat{T}_{wy}^{[m,e]}(\alpha P) \; \hat{T}_{wu}^{[m,e]}(\alpha P) \right]^T$. Computation of the plant can be performed using averaging over the realizations, similar to (3.15), followed by the computation of the BLA as in (3.17) evaluated at all excited frequency bins αP.

The estimation of the total covariance is defined similar to (3.11), followed by the mapping to the plant as in (3.18), which follows the approach in [48, Sec. 7.3.6]. The stochastic nonlinear distortions are defined as in (3.20).

Fast method

The robust method in the previous section exploits multiple realizations to estimate the plant similar to the robust method presented in Sec. 3.4.1. In this section a fast method is presented, based on a measurement of multiple periods of a single multisine realization in a single experiment for both SISO and MIMO systems. The first part of the fast approach is identical to transient estimation for the robust method presented in the previous section. After the correction of the closed-loop output signal $Z(\alpha P)$ for the transient behavior in (3.36), the general output equation is given by

$$\bar{Z}(\alpha P) = G_{wz}(\Omega_{\alpha P})W(\alpha P) + \delta \mathcal{Z}(\alpha P), \qquad (3.37)$$

where $\delta \mathcal{Z}$ represents all unmodeled effects, e.g., nonlinearities, noise and estimation errors of the transient resulting from (3.32). For the estimation of the open-loop plant, only the excited lines are considered, selected by αP. Similar to (3.24), a rational function is given for the plant by

$$G_{wz}(\Omega_{(\alpha + \psi)P}) = D^{-1}(\psi)N(\psi), \qquad (3.38)$$

with $D(\psi)$ defined as in (3.25),

$$N(\psi) = N_0 + N_1\psi + N_2\psi^2 + \ldots + N_{N_n}\psi^{N_n} \in \mathbb{C}^{n_z \times n_u}, \qquad (3.39)$$

with N_n the order of the plant polynomials, and

$$\psi = \begin{bmatrix} -n_E & \ldots & 0 & \ldots & n_E \end{bmatrix}, \qquad (3.40)$$

with n_E a user defined value $n_E > 0$, and chosen such that the least-squares problem is overdetermined. After substitution of (3.38), (3.37) is rewritten to

$$\bar{Z}((\alpha + \psi)P) = N((\alpha + \psi)P)W((\alpha + \psi)P) - \tilde{D}((\alpha + \psi)P)\bar{Z}((\alpha + \psi)P). \quad (3.41)$$

The order N_d is chosen equal to the transient in (3.24), which can be explained by the fact that the poles of the system typically determine the transient. Similar to (3.32), a minimization problem is defined to estimate the system behavior,

$$\hat{\Psi} = \arg\min_{\Psi} \left\| \bar{Z}\left((\alpha + \psi)P\right) - \Psi(\alpha P)L(\alpha + \psi) \right\|_F^2, \qquad (3.42)$$

where all signals are evaluated at frequency bin $(\alpha + \psi)P$. The matrix Ψ is defined by

$$\Psi(kP) = \begin{bmatrix} N_0 & N_1 & \ldots & N_{N_n} & D_1 & \ldots & D_{N_d} \end{bmatrix}, \tag{3.43}$$

with $N_0 = G_{wz}(\alpha P)$. Computation of the plant is performed according to the indirect method,

$$\hat{G}_{uy}(\alpha P) = \hat{G}_{wy}(\alpha P)\hat{G}_{wu}^{-1}(\alpha P), \tag{3.44}$$

which is similar to (3.17).

The noise covariance on the output as in (3.34) is available for only a single experiment. Hence, the mapping to the plant according to (3.18) suffers from a singular term $\overline{\left(\bar{\mathbf{U}}_c(k)\bar{\mathbf{U}}_c^H(k)\right)}^{-1}$. In [48, Sec. 7.3.7.4] an alternative approach is proposed for the LPM, which can also be employed for the LRM. The mapping from total output to plant covariance is given by

$$^{\mathrm{n}}\hat{C}_G(\alpha P) = \tilde{G}\left(\overline{S^H S} \otimes {}^{\mathrm{n}}\hat{C}_{\bar{Z}}(kP)\right)\tilde{G}^H, \tag{3.45}$$

where,

$$\tilde{G} = \hat{G}_{wu}^{-T} \otimes \begin{bmatrix} I_{n_y} & -\hat{G}_{uy} \end{bmatrix}, \tag{3.46}$$

$$S = L^H \left(LL^H\right)^{-1} \begin{bmatrix} I_{n_u} \\ 0 \end{bmatrix}, \tag{3.47}$$

where I_{n_y} and I_{n_u} are identity matrices of dimensions $n_y \times n_y$ and $n_u \times n_u$ respectively. The total covariance is again based on the residuals of the minimization in (3.42), equivalent to (3.33) and (3.34), where γ is defined as,

$$\gamma = \frac{1}{2n_E + 1 - n_u(N_n + 1) - n_z N_d}. \tag{3.48}$$

The mapping of the total covariance to the plant can be done using (3.45), resulting in $\hat{C}_G(\alpha P)$. Similar to the previous methods, the covariance due to stochastic nonlinear distortions is computed element-wise according to (3.20).

Remark 3.1. Note that by replacing the rational functions in (3.24) and (3.38) by polynomial functions, i.e., $N_d = 0$, the robust and fast methods for the LPM are recovered as described in [48, Sec. 7.3.2.2]. See also Chap. 4 for an open-loop description of the LPM. ◁

3.5 Experimental results

Based on the theoretical methods presented in Sec. 3.4, experiments are performed on the closed-loop setup of the Philips Allura FD20 as illustrated in Fig. 3.1. The steps 1) - 3) presented in Sec. 3.3 are illustrated in Sec. 3.5.1 to 3.5.3 respectively.

3.5.1　Initial experiment

The initial experiment is analysed using the Robust method as presented in Sec. 3.4.1, using $P = 10$, $M = 7$ and $N = 10f_s$, with $f_s = 256$ Hz, resulting in $\Delta f = 0.1$ Hz. The main advantage of this approach is that no user-defined estimation errors, e.g., mismatches in order selections, are introduced, which could be the case using local parametric approaches, at the cost of typically longer experimental times. The excited frequencies are non-uniformly distributed over the frequency range, i.e., *a priori* information from finite element simulations and previous nonparametric identification experiments are exploited to distribute the excited frequencies. Note that $\Delta f = 0.1$ Hz still holds, however, A_k can be chosen zero for a selection of harmonics in (3.8). The applied distribution of excited frequencies can be recognized by the distribution of the noise covariances in Fig. 3.3 indicated by the red dots. In [70] is argued that frequencies up to approximately 40 Hz are relevant for imaging applications, see also [9] for a more detailed analysis. Experiments are performed for a total of 13 frozen parameters equally distributed over a full scan range of the system, i.e., the system is identified around selected angles ranging from -90 degrees to 90 degrees with intervals of 15 degrees. The jog mode is applied as a sinusoidal signal with an amplitude of 2 degrees and frequency 0.05Hz. A single FRM is illustrated in Fig. 3.3 by the blue line, where upper- and lower limits on the variations of the obtained BLAs are indicated by the gray area. The system can be characterized as a parameter varying system, as can be seen in the right column. The estimated stochastic nonlinear distortions are significantly lower then the plant estimation, leading to the conclusion that using the frozen parameters the LTI condition for each operating point can be assumed. A violation of the LTI condition would result in a positive bias on the estimated variance due to stochastic nonlinearities. The amplitudes of the excitation signal is chosen maximal for good SNR, however, such that actuator saturations are avoided.

3.5.2　Excitation signal optimization

Based on the results obtained in the previous section, an optimization of the excitation signal can be performed. Recall that the previous excitation signal is obtained using *a priori* system information. Results in Fig. 3.3 allow the optimization of the excitation signal even further. It can be observed, particularly for the element P_{31}, that the resonance around 14 Hz does not change over frequencies for different operating points, which allows for a local dense grid selection. A closer observation of the resonance around 8 Hz shows a shift in frequency, which requires a more conservative excitation grid around this frequency to be able to include the true lightly damped behavior. Note that for local parametric approaches, a minimum amount of excited frequencies within a certain magnitude band is required to guarantee maximum bounded errors on the estimation, see [71]. Using an optimal excitation signal, the SNR at the excited frequencies
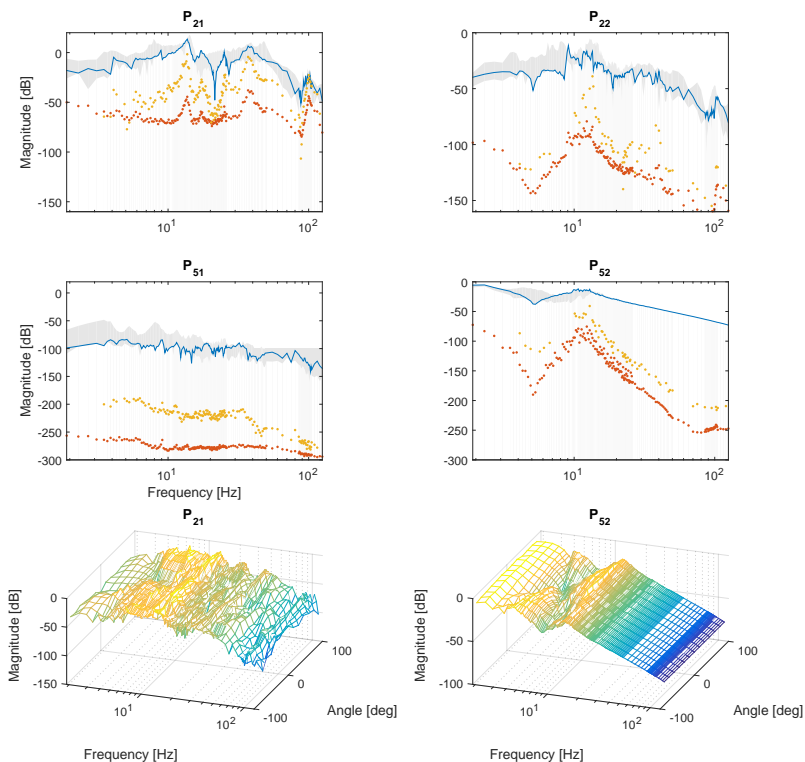
Fig. 3.3. Results using the robust method from Sec. 3.4.1; BLA (blue), variance on BLA due to noise (red-dotted), variance on BLA due to nonlinear distortions (yellow-dotted); Grey area indicates the set of all LTI models, i.e., the angle of system described by offset on u_1 as described in Sec. 3.2; For clarity only the mapping $[u_1, u_2]^T \mapsto [\ddot{y}_v, y_2]^T$ is illustrated, which are indicated by P_{xz} with x the corresponding output, i.e., the 3-rd and 5-th output respectively, and z indicating the corresponding input. A 3D representation of the parameter varying behavior of the diagonal terms of the considered mapping are depicted in the right column.

can be increased without loosing crucial information. Based on the estimations of the covariances due to stochastic nonlinear distortions it can be concluded that LTI conditions are satisfied for each operating point. Hence, an optimal excitation signal can be made for only a single realization with a larger number of periods.

3.5.3   Final experimental results

Using an optimized excitation signal, based on the conclusions drawn in Sec. 3.5.2, new experiments are performed. The fast method and parametric estimation approaches, as presented in Sec. 3.4.1 and 3.4.2 respectively, are used to post-process the data, where the results shown in Sec. 3.5.1 are used for comparison. In Fig. 3.4, the comparison is shown. The local parametric robust methods are processed using $P = 10$ periods, $M = 7$ realizations, and $n_u = 2$ experiments. In sharp contrast, the fast local parametric methods are based on a single experiment and realization and 10 periods, leading to a reduction in measurement time by a factor 14. Comparing the estimation results, it can be observed that the global and most dominant behavior is captured accurately, however, the overall estimation error is larger for the fast methods compared to the robust BLA. The overall estimations of the system dynamics are similar for the LPM and LRM, however, the covariance estimation due to stochastic nonlinearities for the LPM tends to be an underestimation compared to the robust BLA. The numerator polynomials for both the LPM and LRM for plant and transient estimations have been chosen $N_n = N_m = 2$, while the denominator for the LRM has been chosen $N_d = 1$. The quality of the estimated plants using the local parametric approaches depends on the chosen orders for the polynomials. Rules-of-thumb are available in literature, see e.g., [48, Chap. 7], [64], however, some optimization might be required for optimal results. Using the initial, extensive measurements, a guideline is available to tune the parameters. For the individual C-arc X-ray systems, the orders can be chosen similar, since the overall dynamical behaviour will be comparable.

3.6   Conclusion

In this chapter, multiple state-of-the-art post-processing approaches for non-parametric identification are evaluated. The main objective is to obtain insight in the dynamical behavior, which can be used for parametric modeling of an interventional medical X-ray system. Since the mounting conditions of the system are crucial for the system dynamics, resulting in the first flexible mode, fast identification experiments are desired, such that it can be performed in hospitals. Local parametric approaches, such as the local polynomial and rational methods, have the advantage that transient behavior is estimated, which enables compensation without the need to neglect data. Hence, all measured data is effectively
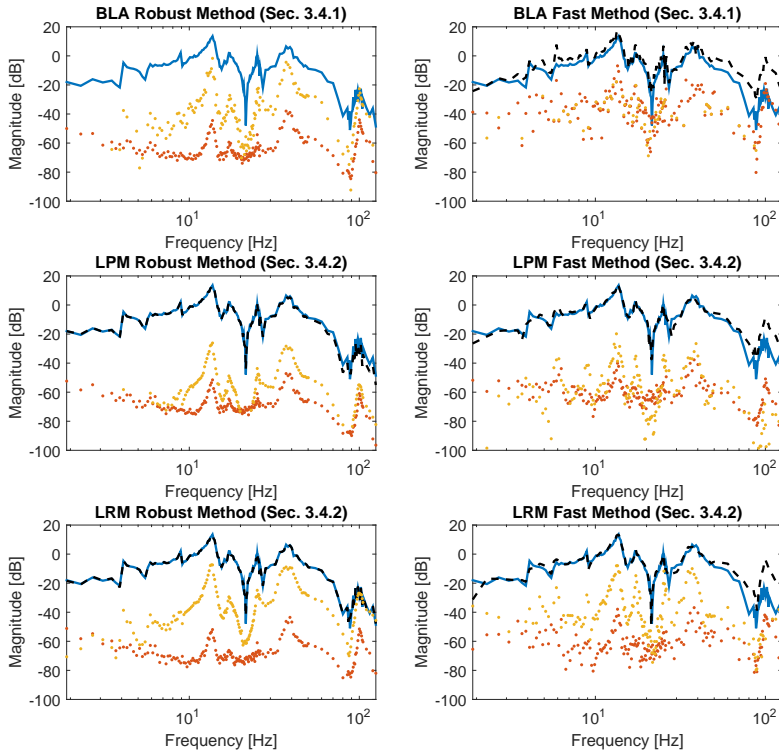
Fig. 3.4. Results for a single operating point ($u_1 \approx 30$) after optimizing of the excitation signal; estimation BLA robust method (blue); estimation of alternative post-processing methods (black-dashed); variance on BLA due to noise (red-dotted); variance on BLA due to nonlinear distortions (yellow-dotted); for clarity only the mapping $u_1 \mapsto \ddot{y}_v$ is illustrated.

used for obtaining a nonparametric estimation. Periodic excitation signals have specific advantages, e.g., covariances due to stochastic nonlinear distortions can be estimated and the user can focus the energy of the excitations signals over specific frequencies of interest. The local parametric approaches in combination with measurements performed on a physical system are presented, where the main (theoretical) focus is on the LRM. A three step procedure is presented, which includes extensive pre-testing of the system, or multiple systems, to obtain *a priori* insight of the system behavior, optimization of the excitation signal, and performing dedicated *in situ* experiments. The result show that the local parametric approaches are able to estimate the system behavior. The results

of the fast methods do not achieve the same accuracies as the robust methods, however, they allow for a significant measurement time reduction since only a single realization and experiment is required. By increasing the number of measured periods, the quality of the fast methods increases significantly due to an increased noise averaging.

Chapter 4

Nonparametric Identification of Parameter Varying Systems

Linear parameter varying (LPV) controller synthesis is a systematic approach for designing gain-scheduled controllers. The advances in LPV controller have spurred the development of system identification techniques that deliver the required models. The aim of this chapter is to present an accurate and fast frequency response function (FRF) identification methodology for LPV systems. A local parametric modeling approach is developed that exploits smoothness over frequencies and scheduling parameters. By exploiting the smoothness over frequency as well as over the scheduling parameters, increased time efficiency in experimentation time and accuracy of the FRF is obtained. Traditional approaches, i.e., the local polynomial method (LPM)/local rational method (LRM), are recovered as a special case of the proposed approach. The application potential is illustrated by a simulation example as well as real-life experiments on a medical X-ray system.

4.1   Introduction

Controller synthesis for linear parameter varying (LPV) systems is a systematic design approach for gain-scheduled control of nonlinear systems [72], [73]. Gain scheduled controllers are currently one of the most commonly applied and popular design methodologies for nonlinear systems such that a guaranteed global performance is obtained. Examples of LPV systems can be found in many application areas, ranging from mechanical positioning systems where a change of position lead to varying dynamics, see, e.g., [61], [74] for industrial applications, to electromagnetic actuators [75], shape memory alloy actuators [76], diesel engines [77], and wind turbine control [78].

   The development of LPV control design methodologies has spurred the research of system identification techniques that produce the required models, see [58], [79] for early results, and [33], [80], and [81] for an extensive overview of the present state of the art. The developments are roughly divided into two approaches. On the one hand, global approaches are used to identify an LPV model using a single global experiment. Examples of global LPV modeling approaches include [58], [59], and [82]. On the other hand, local approaches are based on the identification of a set of "frozen" parameters followed by interpolation leading to an LPV model [33]. Examples of local LPV modeling include [74], [83], [84], and [85].

   For both global or local LPV identification approaches, well-designed preliminary tests are extremely valuable when attempting to present real-life systems as parametric LPV models. Real-life systems are typically nonlinear and time-varying to a certain extend. The additional complexity and modeling costs that are associated with modeling a system as LPV have to be justified from the accuracy requirements that originate from the modeling goal. A typical approach for pre-testing in LPV systems is to estimate nonparametric LTI systems for certain frozen operating conditions, where the frozen parameters are the ones that are expected to induce the parameter dependent behavior. Note that preliminary pre-testing is quite standard in applications of system identification [86, Chap. 10].

   The identification of frequency response functions (FRF) has been significantly advanced over the recent years, see [48] for a recent overview of the state-of-the-art methods. For LTI systems, local parametric modeling approaches and extensions have recently been an important aspect in the developments of nonparametric identification approaches, see [34] for the local polynomial method (LPM) and [35] for the local rational method (LRM), see also [48, Chap. 7], and [87]. These methods exploit the smoothness of the FRF to reduce the variance and bias errors compared to alternative methods.

   Although both LPV and nonparametric identification have been significantly developed individually, the LPV behavior is not yet exploited during nonparametric FRF modeling. The aim of this chapter is to develop an accurate and

fast approach for the identification of nonparametric frozen LTI models of LPV systems. The main idea to exploit the fact that the behavior of an LPV system is typically a smooth function of the frequency as well as the scheduling variable. Direct application of the method include pre-testing and local LPV modeling.

The main contribution of this chapter is a new framework for nonparametric LPV modeling of systems with m scheduling parameters. Both open-loop and closed-loop operating conditions are described and multiple-input, multiple-output (MIMO) systems are considered. The approach is validated on a simulation example and the application potential is demonstrated on a real-life high performance medical X-ray system. This chapter aims to develop non-parametric identification techniques tailored for LPV systems, where the proposed approach has several advantages over pre-existing methods, including the following.

- The approach has an increased time efficiency in experimentation time and accuracy of the frequency response functions.

- The proposed method incorporates the advantage of LPM/LRM methods to use transient responses, i.e., in addition to data measured after the system achieved steady-state conditions, the transient response is used for the estimation of the FRF. Particularly for LPV systems, this property might lead to significant experimentation time reductions, since the scheduling variable has to be changed for each frozen frozen LTI measurement. For MIMO systems, local parametric approaches enable the estimation of the frequency response matrix (FRM) by virtue of a single experiment [88]. Hence, for multivariable systems, significant experimental time reductions are obtained.

- The approach is applicable to both multisine and noise excitation signals and a local quantification of the errors imposed by the frozen parameter compared to a true local LTI representation can be obtained via the best linear approximation (BLA).

Finally, it is pointed out that several related identification techniques have been developed in literature. The first step in obtaining a FRF is the conversion of data to the frequency domain by virtue of the Fourier transformation. In the proposed approach, the Fourier transform is taken for each data set separately, and subsequently processed using the proposed approach. An alternative approach is to extend the Fourier transform as in [89], [90] where higher-dimensional Fourier transforms are applied to reconstruct spatial acoustic fields in mechanical systems. Although higher order Fourier transforms potentially enable the direct global identification of the FRF, the proposed frozen parameter approach avoid issues arising from dynamic scheduling. Second, in the line of research [91], [92], [93], time-varying systems are investigated using related problems. Essentially, this relates to the LPV case by taking only time as scheduling variable, see [94, Sec. 1]. As a result, the extrapolation properties of the model

are much more restrictive, and the resulting model is not directly suitable for LPV controller synthesis algorithms.

This chapter is organized as follows. In Sec. 4.2 the considered class of systems is introduced and a problem description is presented. In Sec. 4.3 the traditional local polynomial method and the novel nD-LPM approach are presented. In Sec. 4.4, the proposed method is extended towards the local rational method (LRM) and in Sec. 4.5 application using arbitrary excitation signals is presented. In Sec. 4.7 and 4.8 simulation and experimental results of a medical X-ray system are presented respectively. In Sec. 4.9, the conclusions of this chapter are discussed.

4.2   Problem description

4.2.1   Linear parameter varying systems

Many systems exhibit, to a certain extent, parameter dependent behavior on non-stationary parameters, e.g., position or temperature. These systems fit into the LPV framework. Consider the MIMO parameter dependent state-space formulation [94, Chap. 1],

$$
\begin{aligned}
\dot{x}(t) &= A(\theta_1, \theta_2, \ldots, \theta_m)x(t) + B(\theta_1, \theta_2, \ldots, \theta_m)u(t) \\
y(t) &= C(\theta_1, \theta_2, \ldots, \theta_m)x(t) + D(\theta_1, \theta_2, \ldots, \theta_m)u(t)
\end{aligned},
\tag{4.1}
$$

with n_u inputs and n_y outputs, $x(t) \in \mathbb{R}^{n_x}$ the state vector, $u(t) \in \mathbb{R}^{n_u}$ and $y(t) \in \mathbb{R}^{n_y}$ the input and output vector respectively, and $A \in \mathbb{R}^{n_x \times n_x}$, $B \in \mathbb{R}^{n_x \times n_u}$, $C \in \mathbb{R}^{n_y \times n_x}$, and $D \in \mathbb{R}^{n_y \times n_u}$ the system matrices which depend on the m scheduling parameters $\theta_1, \ldots, \theta_m$. For a given set of scheduling parameters $\boldsymbol{\theta}$, which is assumed to be frozen, the transfer function is given by

$$
G(s, \boldsymbol{\theta}) = C(\boldsymbol{\theta})(sI - A(\boldsymbol{\theta}))^{-1}B(\boldsymbol{\theta}) + D(\boldsymbol{\theta}),
\tag{4.2}
$$

where the short notation $G(s, \boldsymbol{\theta})$ is defined by

$$
G(s, \boldsymbol{\theta}) := G(s, \theta_1, \theta_2, \ldots, \theta_m)
\tag{4.3}
$$

The trajectory of (a subset of) the scheduling parameters can also be a function of the states of the system, e.g., $\boldsymbol{\theta} = f(x(t))$, which directly implies that LPV systems can be used to represent a class of nonlinear systems. Throughout, it is assumed that the scheduling parameters can be frozen during the experiment, i.e., $\boldsymbol{\theta} = \boldsymbol{\theta}^*$, resulting in local LTI behavior of the system, which is a standard assumption in many local LPV approaches, including [61], [74], and [83]. In this case, for all possible $\boldsymbol{\theta}$, the description in (4.1) generates an infinite family of LTI models, where for each LTI model, Assumption 4.1 holds.

Assumption 4.1. *The FRF of the LTI dynamical behavior can be approximated locally by a polynomial of finite order.*

This assumption enforces smoothness of the approximation over frequencies, as in detail analyzed in [71]. The physical implementation of Assumption 4.2 is a restricted range of the scheduling parameters, i.e., $\boldsymbol{\theta}_{\min} \leq \boldsymbol{\theta} \leq \boldsymbol{\theta}_{\max}$. By limiting the rate of variation, i.e., $\dot{\boldsymbol{\theta}}_{\min} \leq \dot{\boldsymbol{\theta}} \leq \dot{\boldsymbol{\theta}}_{\max}$, second-order dynamics due to fast variations of the scheduling parameter are limited [33], [83]. Hence, smoothness over the scheduling parameter is imposed, as described in Assumption 4.2.

Assumption 4.2. *Smoothness over the scheduling degree-of-freedom is assumed.*

This assumption enables a smooth approximation of the dynamical behavior using finite order polynomial functions in multiple dimensions, as is in detail presented in Sec. 4.3.

4.2.2 Problem definition

The goal of this chapter is to obtain accurate local frequency response functions, using multiple LTI experiments, that approximate the true behavior of the LPV system. Parametric modeling of LPV systems, leading to parametric state-space descriptions as in (4.1), are typically obtained by the identification of multiple parametric LTI models followed by an interpolation step. Nonparametric identification often is an intermediate step in obtaining parametric models. Traditional approaches, e.g., the local polynomial method (LPM) or the local rational method (LRM), enable a combined estimation of dynamical system behavior and transient effects. Hence, measured data during a transient can be exploited for the estimation of the plant, enabling fast measurements for LTI systems. The current fast methods for the LPM and LRM address the shorter measurements by exploiting the transient period of a measurement and smoothen the dynamical behavior over the frequency direction, however, no smoothness between several LTI models is considered. By exploiting this smoothness, as described in (4.1), a more efficient and accurate method for the nonparametric identification of an LPV system is achieved.

4.3 nD-LPM for periodic excitation signals

In Sec. 4.3.1, the basis definitions and concepts are introduced, followed by the proposed nD-LPM approach for open-loop MIMO systems in Sec. 4.3.2. In Sec. 4.3.3, the proposed approach is extended for systems operating in closed-loop. In Sec. 4.4 an nD-LRM approach is presented. This section concludes with implementation aspects, including numerical conditioning and boundary effects over both the frequency direction as well as scheduling degrees-of-freedom.

### 4.3.1	Local polynomial method

The proposed local parametric approach exploits the LPM for LTI systems, e.g., $\boldsymbol{\theta} = \boldsymbol{\theta}^*$ as developed for arbitrary excitation signals in [63] and for periodic excitation signals in [48, Sec. 7.3] and [88]. The focus in this chapter is on periodic excitations signals due to the associated advantages, see [55, Sec. 2.6]. The approach can be directly extended towards arbitrary excitation signals, see [95] and Sec. 4.5. The LPM is based on a local approximation of the dynamical systems behavior as well as the transient effects using a polynomial function of finite order.

The discrete Fourier transform (DFT) is defined as

$$X(k, \boldsymbol{\theta}^*) = \frac{1}{\sqrt{PN}} \sum_{n=0}^{PN-1} x(nT_s, \boldsymbol{\theta}^*) e^{-i2\pi nk/PN}, \tag{4.4}$$

with P the number of measured periods of a periodic excitation signal, N the number of samples per period, and T_s the sampling rate in seconds. For periodic signals without external disturbances, $X(k \neq \alpha P, \boldsymbol{\theta}^*) = 0 \ \forall \ \alpha = 1, \ \ldots, \ N/2$. Note that nonlinear contributions are assumed periodical and therefore are not present on the intermediate frequencies. All intermediate frequencies, i.e., $k = \alpha P + r$, with

$$r = -(P-1), \ -(P-2), \ \ldots, \ -1, \ 1, \ \ldots, \ (P-2), \ (P-1), \tag{4.5}$$

which satisfy $X(k = \alpha P + r, \boldsymbol{\theta}^*) = 0$, see also [96] for an analysis of this property.

At the excited frequencies $k = \alpha P$, the open-loop output spectrum is given by

$$Y(\alpha P) = G(\Omega_{\alpha P}) U(\alpha P) + T_y(\Omega_{\alpha P}) + V(\alpha P), \tag{4.6}$$

with $V(\alpha P)$ a band-limited zeros-mean measurement noise, $U(\alpha P)$ and $Y(\alpha P)$ the input and output DFT spectra respectively, $G(\Omega_{\alpha P})$ the local dynamical behavior of the system, and $T_y(\Omega_{\alpha P})$ the local transient effects. This notation is in line with [48, Sec. 7.3] and Sec. 3.4.2. The input signal is a full random orthogonal multisine signal with random phase, see [48, Sec. 3.7] for a more detailed description. For MIMO systems it is crucial that all inputs are excited with independent multisine signals, which is guaranteed by the aforementioned class of input signals. Exploiting the properties of periodic excitation signals, i.e, $U(\alpha P + r) = 0$, it follows that,

$$Y(\alpha P + r) = T_y(\Omega_{\alpha P + r}) + V(\alpha P + r). \tag{4.7}$$

Based on the difference between (4.6) and (4.7), a two step procedure is generally persued and discussed extensively in [48, Sec. 7.3]. First, based on (4.7) the leakage effects are estimated. Second, the leakage effects are compensated for in (4.6) enabling a more accurate estimation of $G(\Omega_{\alpha P})$.

Step 1

In the LPM, the leakage effects $T_y(\Omega_{\alpha P+r})$ are approximated by a Taylor series expansion around the frequencies αP, i.e.,

$$T_y(\Omega_{\alpha P+r}) = T_y(\Omega_{\alpha P}) + \sum_{x=1}^{N_m} \frac{1}{x!} \frac{\partial^x T_y(\Omega_{\alpha P})}{\partial \Omega^x} r^x,$$

$$= T_y(\Omega_{\alpha P}) + \sum_{x=1}^{N_m} t_x r^x, \tag{4.8}$$

with N_m a design variable that specifies the order of the polynomial and t_x the complex coefficients to be estimated. Substitution of (4.8) in (4.7) results in the linear system,

$$Y(\alpha P + r) = T_y(\Omega_{\alpha P}) + \sum_{x=1}^{N_m} t_x r^x + V(\alpha P + r),$$

$$= \Theta_t K_t(r) + V(\alpha P + r), \tag{4.9}$$

with,

$$\Theta_t = \begin{bmatrix} T_y(\Omega_{\alpha P}) & t_1 & \dots & t_{N_m} \end{bmatrix} \in \mathbb{C}^{n_y \times (N_m+1)}, \tag{4.10}$$

and,

$$K_t(r) = \begin{bmatrix} 1 \\ r \\ \vdots \\ r^{N_m} \end{bmatrix} \in \mathbb{R}^{(N_m+1) \times 2(P-1)}. \tag{4.11}$$

unknown in the parameters included in Θ_t. By defining the cost function,

$$\mathcal{J} = \arg\min_{\hat{\Theta}_t} \|Y(\alpha P + r) - \hat{\Theta}_t K_t(r)\|_F^2, \tag{4.12}$$

solving of the unknown parameters in (4.9) is recast in a least-squares problem which can be solved accurately.

Step 2

After obtaining the estimated $\hat{T}_y(\Omega_{\alpha P})$, the output spectrum at the excited frequency bins given in (4.6) is compensated according to

$$Y_c(\alpha P) = Y(\alpha P) - \hat{T}_y(\Omega_{\alpha P}), \tag{4.13}$$

resulting in,

$$Y_c(\alpha P) = G(\Omega_{\alpha P})U(\alpha P) + V(\alpha P). \tag{4.14}$$

The estimation of $\hat{G}(\Omega_{\alpha P})$ is obtained by a similar procedure. By defining a new frequency window,

$$\psi = [-n, \ -(n-1), \ \ldots, \ 0, \ \ldots, \ (n-1), \ n], \tag{4.15}$$

with n a user-defined number of frequencies, a window of excited frequencies is selected by $G(\Omega_{(\alpha+\psi)P})$. The Taylor series expansion of the plant is given by

$$G(\Omega_{(\alpha+\psi)P}) = G(\Omega_{\alpha P}) + \sum_{x=1}^{N_n} \frac{1}{x!} \frac{\partial^x G(\Omega_{\alpha P})}{\partial \Omega^x} \psi^x,$$

$$= G(\Omega_{\alpha P}) + \sum_{x=1}^{N_n} g_x \psi^x, \tag{4.16}$$

with N_n again a design variable that specifies the order of the polynomial. Substitution of (4.16) in (4.14) results in,

$$Y_c((\alpha+\psi)P) = \left(G(\Omega_{\alpha P}) + \sum_{x=1}^{N_n} g_x \psi^x \right) U((\alpha+\psi)P) + V((\alpha+\psi)P),$$

$$= \Theta_g K_g(\psi) + V((\alpha+\psi)P), \tag{4.17}$$

with,

$$\Theta_g = \begin{bmatrix} G(\Omega_{\alpha P}) \ g_1 \ \ldots \ g_{N_n} \end{bmatrix} \in \mathbb{C}^{n_y \times n_u(N_n+1)}, \tag{4.18}$$

where $g_x \ \forall \ x$ are defined as t_x in step 1, and

$$K_g(\psi, U) = \begin{bmatrix} 1 \\ \psi \\ \ldots \\ \psi^{N_n} \end{bmatrix} \otimes U\left((\alpha+\psi)P\right), \tag{4.19}$$

with $K_g(\psi, U) \in \mathbb{C}^{n_u(N_n+1)\times(2n+1)}$ and $\otimes$ indicating the Kronecker product, which is recast in a least-squares problem similar to (4.12), [96].

The above two-step procedure can be followed to identify frozen frequency response functions of LPV systems. In the next section, a more efficient procedure is developed that exploits the scheduling directions in addition to smoothness over the frequencies.

4.3.2   nD local parameteric approach for LPV systems

An intuitive approach to identify LPV systems is using the local LPV modeling techniques. In the local LPV approaches, several LTI experiments are performed and the system is identified independently for each of these poses. This approach is graphically indicated in Fig. 4.1a, in which it is observed that there is no relation between the individual models.

The main contribution in this chapter is the identification approach for LPV systems using higher-dimensional functions that extends local parametric methods to exploit smoothness in the scheduling variables. The proposed method is to exploit a combination of Assumptions 4.1 and 4.2, i.e., smoothness over both the frequency as well as the scheduling degree of freedom. In Fig. 4.1b, a graphical interpretation of the idea is presented for a single scheduling parameter. A smooth surface is used rather than individual functions to identify the behavior of the plant as a smooth function of both the frequency and the scheduling parameter.

Exploiting the LPM as presented in Sec. 4.3.1 with higher-dimensional functions, local estimations over multiple LTI measurements can be obtained. A typical approximation of a smooth function is a Taylor series expansion. The Taylor series expansion of a higher-dimensional function is used in this chapter to describe the systems' dynamics, resulting in a linear least-squares optimization to obtain a local parametrization of an LPV system.

The output spectrum at the non-excited frequency bins $k = \alpha P + r$ of the full LPV system is given by

$$Y(\alpha P + r, \boldsymbol{\theta}_\beta) = T_y(\Omega_{\alpha P + r}, \boldsymbol{\theta}_\beta) + V(\alpha P + r, \boldsymbol{\theta}_\beta). \qquad (4.20)$$

For each frozen set of scheduling parameters, i.e., each LTI measurement, step 1 from Sec. 4.3.1 is repeated to estimate the leakage effects. Since it typically cannot be guaranteed that the initial states of the system are the same for each individual LTI experiment, it is assumed that there is no correlation between the transient effects of the individual LTI experiments. Hence, leakage is considered a frequency effect only.

The proposed approach follows the local frequency window as defined in (4.15) from step 2 in Sec. 4.3.1. Furthermore, additional local windows are employed over the scheduling directions, which are spanned by the vectors of dimensions $2p_i + 1$,

$$z_i = [-p_i, \ -(p_i - 1), \ \ldots, \ 0, \ \ldots, \ (p_i - 1), \ p_i], \qquad (4.21)$$

$\forall i = 1, 2, \ldots, m$, which can be user-defined independently for each scheduling parameter. Similar to the short notation in (4.3), a local frequency and scheduling domain is denoted by

$$G(\Omega_{(\alpha+\psi)P}, \boldsymbol{\theta}_\beta + \mathbf{z}) := G(\Omega_{(\alpha+\psi)P}, \theta_1 + z_1, \ldots, \theta_m + z_m), \qquad (4.22)$$

where the subscript β indicates a specific frozen set of scheduling parameters and $\mathbf{z}$ the local window for all scheduling parameters, defined similar to $\boldsymbol{\theta}$. The pink plane in Fig. 4.1b spans the domain $(\alpha + \psi)P$ and $\boldsymbol{\theta}_\beta + \mathbf{z}$.

The corresponding nD-Taylor series expansion for multiple variables, each

(a) The LPM on several LTI poses

(b) The 2D-LPM over several LTI poses
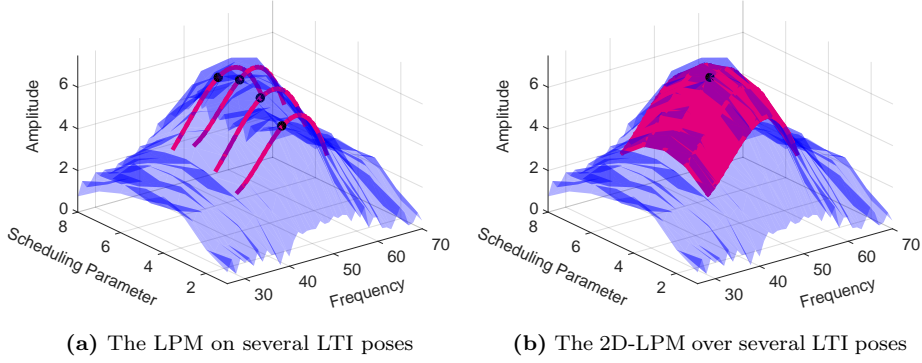
Fig. 4.1. Graphical interpretation of the approaches. In blue, the perturbed plant is shown; in pink, the estimated models; in black dots, the estimated plant dynamics is indicated.

with a user-defined order, is given by [97],

$$G(\Omega_{(\alpha+\psi)P}, \boldsymbol{\theta}_\beta + \mathbf{z}) = \tag{4.23}$$

$$\sum_{i_1=0}^{N_n} \sum_{i_2=0}^{Q_{z_1}-i_1} \cdots \sum_{i_n=0}^{Q_{z_m}-\sum\limits_{x=1}^{m} i_x} \left(\frac{\psi^{i_1} \prod\limits_{x=1}^{m} z_x^{i_{x+1}}}{\prod\limits_{x=1}^{n} i_x!} \frac{\partial^{\sum\limits_{x=1}^{n} i_x} G(\Omega_{\alpha P}, \boldsymbol{\theta}_\beta)}{\partial \Omega^{i_1} \prod\limits_{x=1}^{m} \partial \theta_x^{i_{x+1}}} \right),$$

with N_n and Q_{z_i} $\forall i = 1, 2, \ldots m$ indicating user-defined variables that enables the order selection over frequencies and each scheduling parameter respectively. Note that the approximation orders as indicated in (4.23) should satisfy $N_n \leq Q_{z_1} \leq \ldots \leq Q_{z_m}$. The inequality constraint on the orders is flexible up to an interchange of the summations, resulting in an arbitrary choice for each scheduling parameter and the frequency axis. The only hard constraint is the fact that the upper limit of each of the summations should remain positive.

Substitution of the desired approximation order from (4.23) into the compensated output spectrum at the excited frequency lines as given in (4.14), results again in a linear set of equations. Note that the order selection is not necessarily identical over the frequencies or over the various scheduling directions. Furthermore, if no scheduling parameters are included, i.e., $\boldsymbol{\theta}$ is again chosen as a single frozen set of scheduling parameters, the LPM as presented in Sec. 4.3.1 is recovered.
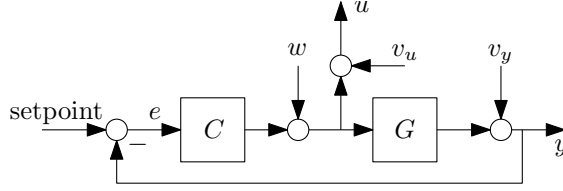
Fig. 4.2. Simplified feedback interconnection.

4.3.3 Closed-loop operating conditions

Many systems are operating in closed-loop as indicated in Fig. 4.2 for stabilization or to achieve an increased performance. The closed-loop output can again be defined as, [48, Sec. 7.3],

$$Z(k, \boldsymbol{\theta}) = \begin{bmatrix} Y(k, \boldsymbol{\theta}) \\ U(k, \boldsymbol{\theta}) \end{bmatrix} \in \mathbb{C}^{n_u + n_y}, \tag{4.24}$$

with $Y(k, \boldsymbol{\theta})$ and $U(k, \boldsymbol{\theta})$ the DFT of the measured plant input and output, in line with Chap. 3. The output spectra for the closed-loop are given by

$$Z(k, \boldsymbol{\theta}) = G_{wz}(\Omega_k, \boldsymbol{\theta})W(k, \boldsymbol{\theta}) + T_{wz}(\Omega_k, \boldsymbol{\theta}) + V_z(k, \boldsymbol{\theta}), \tag{4.25}$$

with $W(k, \boldsymbol{\theta})$ a user-defined excitation signal, and $V_z(k, \boldsymbol{\theta})$ a noise term. The transfer function $G_{wz}(\Omega_k)$ is given by the mapping,

$$G_{wz} : w \mapsto z := \begin{bmatrix} G_{wy} \\ G_{wu} \end{bmatrix} = \begin{bmatrix} G \\ I \end{bmatrix} (I + CG)^{-1}. \tag{4.26}$$

Similarly, $T_{wz}(\Omega_k)$ in (4.25) is the transient corresponding to the mapping $w \mapsto z$.

The closed-loop output spectrum in (4.25) is, after substitution of $Y(s)$ by $Z(s)$, directly applicable for the LPM as described in Sec. 4.3.1 for each frozen scheduling set or the proposed nD-LPM approach in Sec. 4.3.2. After obtaining an estimation for G_{wz}, the open-loop plant estimation is obtained by [48, Sec. 2.6],

$$\hat{G}(\Omega_k) = \hat{G}_{wy}(\Omega_k)\hat{G}_{wu}^{-1}(\Omega_k). \tag{4.27}$$

for all Ω_k for which G_{wu} is nonsingular.

4.3.4 Covariance analysis

To quantify the quality of the obtained frequency response measurement, a variance analysis is presented in the current section for the closed-loop situation. The open-loop covariance is obtained by replacing the closed-loop output signals Z, (4.25), by the open-loop output signals Y, (4.6). The use of periodic

excitation signals enables a distinction between external noise disturbances and (periodic) nonlinear distortions within the system. The estimation of the covariance as a result of noise is fully based on the estimation of the transient, i.e., on the non-excited frequency bins only a combination of leakage effects as well as external disturbances is present, see also [48] for details. By defining the residuals of the least-squares problem by

$$\mathcal{R}_t = Z(\alpha P + r, \boldsymbol{\theta}_\beta) - \hat{\Theta}_t K_t(r), \tag{4.28}$$

the variance due to measurement noise is given by

$$ {}^{\mathrm{n}}\hat{C}_z(\alpha P, \boldsymbol{\theta}_\beta) = \frac{\mu}{q} \mathcal{R}_t \mathcal{R}_t^H, \tag{4.29}$$

with $\mu = 1 + \|\Sigma \mathcal{V}_{[1,:]}^H\|_F^2$, as is defined in [48, Sec. 7.3.2.2], where Σ and $\mathcal{V}$ are obtained from the singular value decomposition $K_t^H = \mathcal{U}\Sigma\mathcal{V}^H$, with the subscript $[1,:]$ indicating the first row, and

$$q = 2(P - 1) - \mathrm{rank}(K_t). \tag{4.30}$$

After the correction of the output signal for the transient effects, the remaining disturbance sources are measurement noise and (periodic) nonlinear distortions, [48]. The residuals of the plant estimations are therefore used for the estimation of the total covariance on the output signal. The total covariance is defined by

$$ {}^{\mathrm{t}}\hat{C}_z(\alpha P, \boldsymbol{\theta}_\beta) = \frac{1}{q} \mathcal{R}_g \mathcal{R}_g^H, \tag{4.31}$$

where the residual $\mathcal{R}_g$ is defined as,

$$\mathcal{R}_g = Z_c((\alpha + \psi)P, \boldsymbol{\theta}_\beta + \mathbf{z}) - \hat{\Theta}_g K_g(\psi, \mathbf{z}, U, \boldsymbol{\theta}_\beta), \tag{4.32}$$

which follows from (4.17) and the nD result as presented in Sec. 4.3.2 for the open-loop situation, i.e., $Z_c = Y_c$, or the closed-loop equivalent with Z_c, and

$$q = (2n + 1) \prod_{x=1}^{m} (2p_i + 1) - \mathrm{rank}(K_g). \tag{4.33}$$

The covariances related to the output spectra, i.e., ${}^{\mathrm{n}}\hat{C}_z$ as well as ${}^{\mathrm{t}}\hat{C}_z$, are mapped to a covariance on the estimated closed-loop plant dynamics according to

$$\hat{C}_{G_{wz}}(\Omega_{\alpha P}, \boldsymbol{\theta}_\beta) = S^{\bar{H}} S \otimes \hat{C}_z(\alpha P, \boldsymbol{\theta}_\beta), \tag{4.34}$$

with $\otimes$ the kronecker product, and

$$S = K^H (K K^H)^{-1} \begin{bmatrix} I_{n_u} \\ O_{\mathrm{dim}(K,1) - n_u \times n_u} \end{bmatrix}, \tag{4.35}$$

where I_{n_u} is a square identity matrix of dimensions n_u and $O_{\dim(K,1)-n_u \times n_u}$ a zero matrix where $\dim(K,1)$ indicates the number of rows of the K matrix. A final mapping from the covariances of the closed-loop transfer functions included in G_{wz} to the open-loop plant G is done according to [48, Sec. 7.2.7],

$$\hat{C}_G = (\hat{G}_{wu} \otimes [I_{n_y}, \ -\hat{G}])\hat{C}_{G_{wz}}(\hat{G}_{wu} \otimes [I_{n_y}, \ -\hat{G}])^H. \qquad (4.36)$$

Note that for the open-loop case the computation of the covariances is equivalent, however, the final mapping in (4.36), which corresponds to (4.27), is not required since $G_{qz} = G$ for open-loop systems. By computation of the difference between the total covariance, (4.31), and the noise covariance, (4.29), an estimation for the stochastic nonlinear distortions is obtained. A detailed analysis of the covariances for the LPM can be found in [48, Sec. 7.3.7] and [88]. Extensive literature is available on the analysis of covariances on FRF measurements. BLA analysis as discussed in [48, Sec. 4.3] can be used to validate the obtained covariances on, however, this requires extensive experiment times.

4.3.5 Implementation aspects

Border effects

For both the transient estimation as well as the plant estimation, described in step 1 and 2 of Sec. 4.3.1 respectively, border effects at the edges of the frequency grid are present. Recall that for the transient estimation, only unexcited frequencies are evaluated. The DC-term of a periodic excitation signal is typically chosen zero, allowing for a full definition of the local frequency window r as defined in (4.5) for the lower frequency range. However, typically the Nyquist frequency is excited, leading to a degenerate local window for $k \geq (N/2)P$. For the plant estimation, only the excited frequencies are evaluated, leading to a degenerate local window ψ as in (4.15) for $k \leq nP$ and $k \geq (N/2-n)P$.

To deal with the edges of the frequency grid, the use of an asymmetric window around the evaluated frequency k is presented in [63]. An alternative approach that exploits the periodicity of the DFT over the frequency is presented in [35].

A similar phenomenon is encountered when local windows over the scheduling parameters are evaluated. The edges of the scheduling domain, i.e., $\theta_i \leq \theta_i^{\min}+p_i$ and $\theta_i \geq \theta_i^{\max} - p_i$, lead also to a degenerate local window. In addition to the asymmetric window and exploiting the periodicity of the DFT, an adaptive window size in the scheduling domain can be implemented such that at $\theta_i = \theta_i^{\min}$ or $\theta_i = \theta_i^{\max}$ the LPM for LTI systems is recovered, i.e., $p_i = 0$. Depending on the system properties and the users preference, a suitable approach is selected.

Numerical stability

If the least-squares problems are poorly conditioned, numerical difficulties may arise. In [63] is an approach presented for enhanced conditioning, which can

be applied in both step 1 and 2 as presented in Sec. 4.3.1 as well as for the alternative step 2 exploiting the proposed nD-LPM. In particular, let

$$\tilde{K} = D^{-1}K, \tag{4.37}$$

with,

$$D(i,i) = \begin{cases} \|K(i,:)\|_2 & \text{if } \|K(i,:)\|_2 \neq 0 \\ 1 & \text{if } \|K(i,:)\|_2 = 0 \end{cases}, \tag{4.38}$$

where : indicates all items in row i, and scale the least-squares solution as $\hat{\Theta} = \tilde{\Theta}D^{-1}$.

4.4   nD-LRM for periodic excitation signals

Modern developments in local parametric approaches for the identification of frequency response functions tend toward the use of rational functions, leading to the local rational method (LRM), see, e.g., [35]. In [64] it is presented that the LRM is a powerful approach for systems with lightly damped poles. Given the closed-loop output spectrum as in (4.25), the transfer functions G_{wz} and T_{wz} are replaced by

$$G_{wz}(\Omega_{(\alpha+\psi)P}, \boldsymbol{\theta}_\beta + \mathbf{z}) = D^{-1}(\psi, \mathbf{z})N(\psi, \mathbf{z}), \quad \text{and,} \tag{4.39}$$

$$T_{wz}(\Omega_{\alpha P+r}, \boldsymbol{\theta}_\beta + \mathbf{z}) = D^{-1}(r, \mathbf{z})M(r, 0), \tag{4.40}$$

respectively with,

$$N(\psi, \mathbf{z}) = n_0 + n_1\psi + n_2\mathbf{z} + n_3\psi\mathbf{z} + \dots, \tag{4.41}$$

$$M(r, 0) = m_0 + m_1 r + m_2 r^2 \dots, \tag{4.42}$$

from which the unknown parameters n_i and $m_i, \forall i = 0, 1, 2, \dots$ follow from the nD Taylor series expansion in (4.23) and r is defined in (4.5) and ψ in (4.15). The definition of $D(r, \mathbf{z})$ also follows from (4.23), however, the parameters are scaled such that d_0 is unity [35], i.e.,

$$D(r, \mathbf{z}) = 1 + d_1 r + d_2 \mathbf{z} + d_3 r\mathbf{z} + \dots \qquad := 1 + \tilde{D}(r, \mathbf{z}), \tag{4.43}$$

Recall that the transient typically is dominated by the poles of the system. Hence, the local estimation of the poles of the transient is equal to the estimation of the plant while the numerator is exploited to compensate for errors due to varying initial conditions over different frozen experiments.

Remark 4.1. Note that it is not strictly required scale D_0 in (4.43) to unity. Other choices can be made as well, however, D_0 is an intuitive choice since the estimations for $G(\alpha P, \boldsymbol{\theta}_\beta)$ and $T(\alpha P, \boldsymbol{\theta}_\beta)$ are directly obtained by the parameters n_0 and m_0 respectively. The selection of a normalized parameter in (4.43) is required to enforce a nontrivial solution of the least-squares as in (4.12), i.e., $\Theta \neq 0$.   ◁

Substitution of (4.39) and (4.40) in the closed-loop output spectra and evaluation of the unexcited frequencies results in,

$$\left(1 + \tilde{D}(r, \mathbf{z})\right) Z(\alpha P + r, \boldsymbol{\theta}_\beta) = M(r, 0) + D(r, \mathbf{z}) V(\alpha P + r, \boldsymbol{\theta}_\beta), \qquad (4.44)$$

which can be stacked according to

$$Z(\alpha P + r, \boldsymbol{\theta}_\beta) = \begin{bmatrix} M(r, 0) & \tilde{D}(r, \mathbf{z}) \end{bmatrix} \begin{bmatrix} I \\ -Z(\alpha P + r, \boldsymbol{\theta}_\beta) \end{bmatrix} + D(r, \mathbf{z}) V(\alpha P + r, \boldsymbol{\theta}_\beta),$$

$$= \Theta_t K_t(r, Z) + D(r, \mathbf{z}) V(\alpha P + r, \boldsymbol{\theta}_\beta), \qquad (4.45)$$

for which estimations can be obtained using the least-squares cost function in (4.12).

After obtaining an estimation for the transient, the output spectrum at the excited frequencies can be compensated as in (4.14). Substitution of (4.39) in the compensated output spectrum results in,

$$\left(1 + \tilde{D}(\psi, \mathbf{z})\right) Z((\alpha + \psi)P, \boldsymbol{\theta}_\beta + \mathbf{z}) = N(\psi, \mathbf{z}) W((\alpha + \psi)P, \boldsymbol{\theta}_\beta + \mathbf{z}) +$$

$$D(\psi, \mathbf{z}) V((\alpha + \psi)P, \boldsymbol{\theta}_\beta + \mathbf{z}), \qquad (4.46)$$

which can again be rewritten according to

$$Z((\alpha + \psi)P, \boldsymbol{\theta}_\beta + \mathbf{z}) = \begin{bmatrix} N(\psi, \mathbf{z}) & \tilde{D}(\psi, \mathbf{z}) \end{bmatrix} \begin{bmatrix} W((\alpha + \psi)P, \boldsymbol{\theta}_\beta + \mathbf{z}) \\ -Z((\alpha + \psi)P, \boldsymbol{\theta}_\beta + \mathbf{z}) \end{bmatrix}$$

$$+ D(\psi, \mathbf{z}) V((\alpha + \psi)P, \boldsymbol{\theta}_\beta + \mathbf{z}),$$

$$= \Theta_g K_g(\psi, \mathbf{z}, Z) + D(\psi, \mathbf{z}) V((\alpha + \psi)P, \boldsymbol{\theta}_\beta + \mathbf{z}), \quad (4.47)$$

for which again a least-squares solution can be obtained. Note that when the orders of all directions of the Taylor expansions of D in (4.43) are chosen 0, the nD-LPM as in Sec. 4.3.2 is recovered. The 2D-LRM is in detail presented including application results on a medical X-ray system in [98].

Remark 4.2. Note that the measurement noises V for both estimations are weighted by the denominator. In [99] and [100] a detailed analysis is provided on the effects of noise and the effectiveness of both the LPM and LRM. ◁

4.5   Arbitrary excitation signals

The local parametric methods can also be exploited in combination with arbitrary excitation signals, see e.g., [35], [63]. The DFT of arbitrary, non-periodic excitation signals, e.g., a (zero-mean) band-limited white noise signal, contain system dynamics as well as transient effects over all frequency bins. Hence, the output spectrum in (4.25) is defined $\forall k$. In sharp contrast to the periodic

excitation signal situation, the system dynamics and the transient effects are estimated simultaneously.

The Taylor series expansion of the transient term is given by (4.8) by replacing αP with k, i.e.,

$$T_y(\Omega_{k+\psi}, \boldsymbol{\theta}_\beta + \mathbf{z}) = T_y(\Omega_k, \boldsymbol{\theta}_\beta + \mathbf{z}) + \sum_{x=1}^{N_m} t_x \psi^x. \tag{4.48}$$

For the system dynamics, the Taylor series expansion in (4.23) is exploited, again by replacing αP with k, leading to

$$G(\Omega_{k+\psi}, \boldsymbol{\theta}_\beta + \mathbf{z}) = G(\Omega_k, \boldsymbol{\theta}_\beta) + g_1 \psi + g_2 \mathbf{z} + g_3 \psi \mathbf{z} + g_4 \psi^2 \ldots, \tag{4.49}$$

with ψ defined as in (4.15). Similar to Sec. 4.4, the system dynamics and transient are described using rational functions as defined in (4.39) and (4.40) respectively.

The closed-loop output spectrum is given by

$$\left(1 + \tilde{D}(\psi, \mathbf{z})\right) Z(k+\psi, \boldsymbol{\theta}_\beta + \mathbf{z}) = N(\psi, \mathbf{z}) W(k+\psi, \boldsymbol{\theta}_\beta + \mathbf{z}) + M(\psi, 0) +$$
$$D(\psi, \mathbf{z}) V(k+\psi, \boldsymbol{\theta}_\beta + \mathbf{z}), \tag{4.50}$$

which leads to

$$Z(k+\psi, \boldsymbol{\theta}_\beta + \mathbf{z}) = \begin{bmatrix} N(\psi, \mathbf{z}) & M(\psi, 0) & \tilde{D}(\psi, \mathbf{z}) \end{bmatrix} \begin{bmatrix} W(k+\psi, \boldsymbol{\theta}_\beta + \mathbf{z}) \\ I \\ -Z(k+\psi, \boldsymbol{\theta}_\beta + \mathbf{z}) \end{bmatrix}$$
$$+ D(\psi, \mathbf{z}) V(k+\psi, \boldsymbol{\theta}_\beta + \mathbf{z}),$$
$$= \Theta K(\psi, \mathbf{z}, Z) + D(\psi, \mathbf{z}) V(k+\psi, \boldsymbol{\theta}_\beta + \mathbf{z}), \tag{4.51}$$

for which again a least-squares solution can be obtained.

In [95] the results of the LPM for arbitrary excitation signals is presented for a 2D situation based on a simulation example of a wafer stage model. Note that similar to the periodic excitation case, the LPM is recovered by selecting the order of the denominator of the rational functions equal to zero. Also note that the LPM for arbitrary excitation signals is essentially a special case of the periodic excitation signals, where the number of periods $P = 1$.

4.6　System description: medical X-ray system

To illustrate the potential of the proposed approach, a simulation example and real-life experiments are performed on an interventional C-arc based medical X-ray system as indicated in Fig. 4.4. Interventional X-ray systems are typically used to obtain high-definition 3D reconstructions of the interior of the human
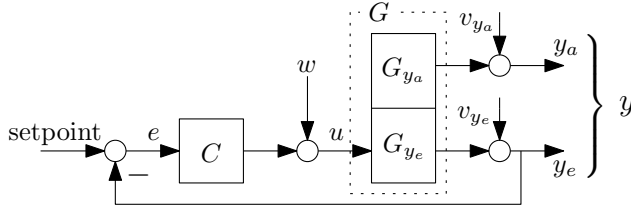
Fig. 4.3. Simplified feedback interconnection; y indicates the total output of the system, with $y_e = [\theta_1, \ \theta_2]^T$ indicating the encoder measurements and $y_a = [\ddot{x}, \ \ddot{y}, \ \ddot{z}]^T$ indicating the acceleration measurements.

body and enable imaging during minimal invasive procedures. The system has two actively controlled motion axis, indicated by the input currents u_1 and u_2 corresponding to the angles θ_1 and θ_2 in Fig. 4.5 respectively. The motions of the system are measured using collocated incremental encoders on the motor axis, indicated by $y_e = [\,\theta_1 \ \theta_2\,]^T$, which are also used for feedback purposes. For imaging purposes, the system is equipped with acceleration sensors located at the X-ray detector, measuring three orthogonal local degrees of freedom, indicated by $y_a = [\,\ddot{x} \ \ddot{y} \ \ddot{z}\,]^T$. These measurements are not exploited in the feedback/control loop as indicated in Fig. 4.3.

The system under consideration exhibits inherent linear parameter varying behavior. A changing pose of the system, of which an example is indicated in Fig. 4.5, results in different stiffness and damping properties between the actuator and the measured position. Additionally, the center of gravity of the system is not located in the center of rotation, resulting in position depending dynamics, even in the collocated measurements.

To enhance readability, only a single scheduling parameter is evaluated in this chapter, which is a semi-circular motion of θ_2 ranging from -90 to 90 degrees as indicated in Fig. 4.5. Due to the geometric change of the system, the dynamical behavior is a direct function of the angle θ_2. Hence, the system exhibits typical LPV behavior due to changing mass distributions, hence due to pole variations. Additionally, the non-collocated positioning of the acceleration sensors, results in additional varying zero locations.

Input u_1 corresponding to θ_1 is only used to apply periodic excitation signals to the system, but is considered frozen as a scheduling parameter.

The goal of the measurement is to identify the plant G indicated in Fig. 4.3. Note that a subset of the outputs is used for feedback, hence the closed-loop approach as presented in Sec. 4.3.3 is adopted. By defining $y(t) = [y_a(t), \ y_e(t)]^T$, the situation in Fig. 4.2 is recovered, i.e., the closed-loop transfer function

$$G_{wy} : w \mapsto y := \begin{bmatrix} G_{y_a} \\ G_{y_e} \end{bmatrix} (I + CG_{y_e})^{-1} = G(I + CG_{y_e})^{-1} \qquad (4.52)$$
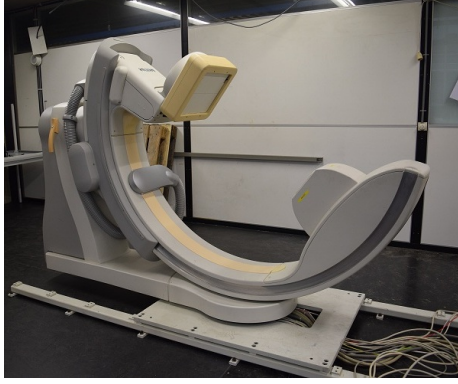
Fig. 4.4. Philips Allura Centron interventional X-ray system.

enables a direct computation of the plant G by post-multiplication with G_{wu}^{-1} as in (4.27) where $G_{wu} : w \mapsto u := (I + CG_{y_e})^{-1}$.

Finally, note that the dynamical behavior of the system is symmetric when the scheduling range for θ_1 is extended, i.e., $-90 \geq \theta_1 \geq 90$ degrees, as a result of the semi-circular motion. Hence, also over the scheduling direction symmetry can be exploited to deal with the border effects.

Since only a single scheduling parameter is considered, a 2D-LPM approach is obtained. The nD Taylor series expansion of the plant in (4.23) reduces to

$$G(\Omega_{(\alpha+\psi)P}, \theta_1 + z) = G(\Omega_{\alpha P}, \theta_1) + \sum_{i_1=1}^{Q_z} \sum_{i_2=1}^{N_n - i_1} g_{i_1,i_2} \psi^{i_2} z^{i_1}, \qquad (4.53)$$

where,

$$g_{i_1,i_2} = \frac{\partial^{i_1+i_2} G(\Omega_{\alpha P}, \theta_1)}{\partial \psi^{i_2} z^{i_1}}, \qquad (4.54)$$

with N_n and Q_z user-defined variables to select the order of the approximation over the frequency and scheduling direction respectively.

4.7   Simulation results

In this section, the potential of the proposed approach is illustrated using a simulation model of a medical X-ray system in Sec. 4.6.

The main goal of the simulation example is to present a comparison between the LPM and the nD-LPM in terms of bias and variance. It should be noted that the system is MIMO, even though only a single scheduling parameter is exploited, in the sense of a single degree of freedom of the system. A simplified

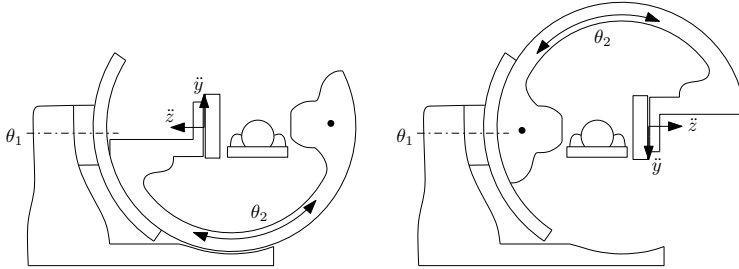**Fig. 4.5.** Schematic representation of geometrical effect of scheduling variable θ_2.

model with input $u = [u_1, \ u_2]^T$ and output $y = [y_{a,1}, \ y_{e,2}]^T = [\ddot{x}, \ \theta_2]^T$ is used for the simulations.

Numerical experiments are performed using a multisine excitation signal with a period length of 10 seconds leading to a spectral distance of 0.1 Hz. The experiments have identical excitation frequencies and a flat spectrum. Each period is repeated 6 times leading to a measurement time of 60 seconds for each of the frozen scheduling parameter sets. Over the full scheduling domain, 25 frozen positions are defined, leading to a total measurement time of 25 minutes. An additive measurement noise is included such that the SNR for the acceleration and encoder measurement are 30dB and 20dB respectively. The simulated measurements, obtained in a closed-loop situation as in Sec. 4.3.3, are processed using the standard approach as in Sec. 4.3.1 and using the proposed nD-LPM approach as presented in Sec. 4.3.2, where for the single scheduling parameter the Taylor series expansion as in (4.53) is used.

The resulting plant estimations are shown in Fig. 4.8 for the LPM and the 2D-LPM where the parameters indicated in Table 4.1 are used. It is observed by

Table 4.1. Local estimation parameters

Tuning parameters	N_n	N_m	Q_z	n	p_i
LPM	3	2	−	8	−
2D-LPM	3	2	1	8	2

comparing 4.6a to 4.7a, 4.6b to 4.7b, etc., that the plant estimations from the proposed 2D approach appear less noisy and take the underlying dynamical behavior into account better compared to the LPM. Looking at the diagonal terms of the systems dynamics, i.e., G_{11} and G_{22}, the overall behavior over the entire frequency-scheduling domain appear smoother using the 2D approach. Looking at G_{12}, the systems dynamics remain relatively noisy using both approaches, however, the anti-resonance using the 2D-LPM approach is more clearly than using the LPM. The effects of measurement noise on the estimations has been

(a) LPM: $G_{11} := u_1 \mapsto \ddot{x}$

(b) LPM: $G_{21} := u_1 \mapsto \theta_2$

(c) LPM: $G_{12} := u_2 \mapsto \ddot{x}$

(d) LPM: $G_{22} := u_2 \mapsto \theta_2$
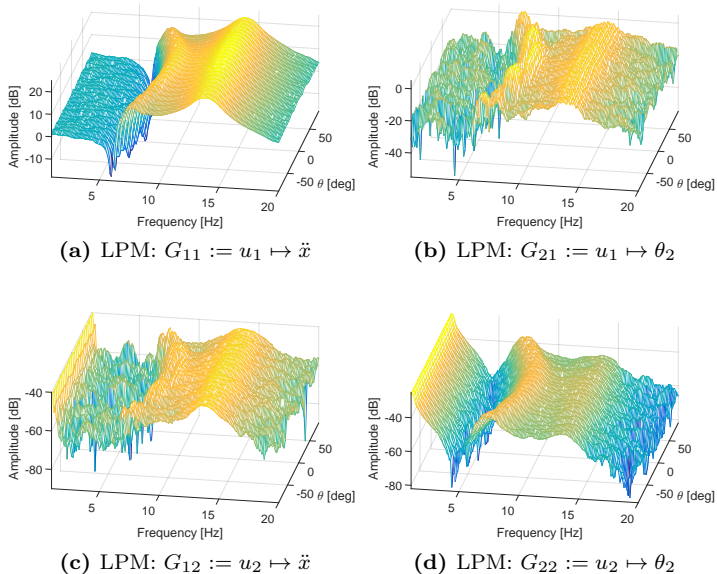
Fig. 4.6. Simulation results. Estimated using the LPM on each LTI position as in Fig. 4.1a.

(a) 2D-LPM: $G_{11} := u_1 \mapsto \ddot{x}$

(b) 2D-LPM: $G_{21} := u_1 \mapsto \theta_2$

(c) 2D-LPM: $G_{12} := u_2 \mapsto \ddot{x}$

(d) 2D-LPM: $G_{22} := u_2 \mapsto \theta_2$

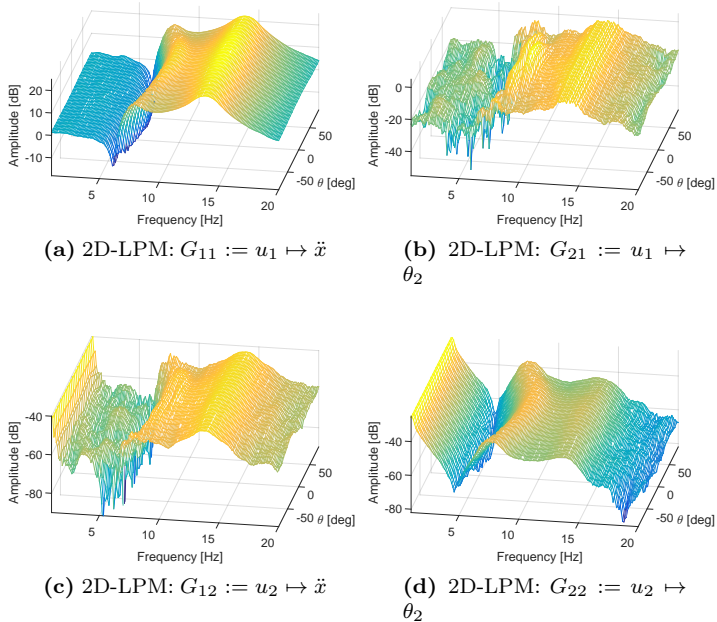**Fig. 4.7.** Simulation results. Estimated using the 2D-LPM as in Fig. 4.1b.
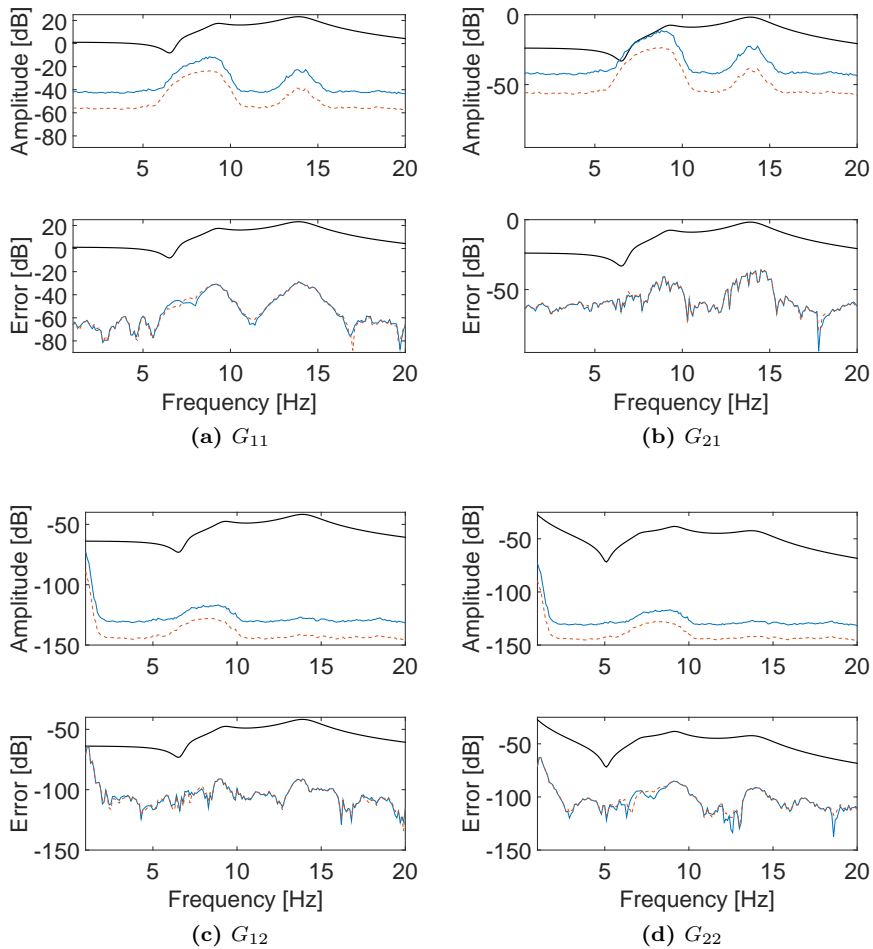
Fig. 4.8. Indication of the performance of the method. The actual plant, averaged over the scheduling parameters (black) is compared to the total covariance (top figures) and the absolute estimation error (bottom figures). The LPM (blue) and the 2D-LPM (red-dashed) are compared in these figures.

reduced significantly.

To enable a quantitative comparison, the estimation bias and variance are evaluated. Since an estimation bias is only available when the true system is known, the simulation model is exploited for this analysis. For each frozen scheduling parameter set, the LTI plant is determined. In Fig. 4.8, a qualitative measure for the performance of the two methods is shown. The LPV plant dynamics are averaged over the scheduling parameters per frequency such that the global performance can be observed. The absolute estimation errors, defined by,

$$ e = \frac{1}{n_\theta} \sum_{i=1}^{n_\theta} (G - G_x)(G - G_x)^H, \tag{4.55} $$

with n_θ the total number of scheduling parameters, G the true system, G_x represents any estimated system, with G_{2DLPM} the plant dynamics obtained using the 2D-LPM approach and G_{LPM} the plant dynamics from the LPM approach per LTI. The total variance follows from (4.31) after mapping to the plant using (4.34). Note that the estimation error is not a general quality measure, since for physical systems, the true system dynamics underlying the identification experiment are unknown. The estimation error is similar for both approaches, while the variance of the proposed approach is significantly lower for all frequencies. This leads to the conclusion that the nD-LPM approach enables an accurate and efficient estimation of the plant dynamics without necessarily introducing additional estimation errors.

4.8   Experimental results

Next, the proposed approach is applied to the experimental medical X-ray system in Fig. 4.4. Similar experiments are performed as described in Sec. 4.7. However, due to the presence of significant nonlinear effects as a result of friction, the measurement time is increased. The friction in the system leads to significant nonlinearities, making the non-parametric identification a challenging task. By increasing the measurement times with a sufficiently exciting input signal, promising results can be obtained despite the effects of the friction. A multisine excitation signal is used using a period length of 30 seconds. The excitation signal is repeated 10 times, leading to a total measurement time for each frozen scheduling parameter of 5 minutes. A total of 13 LTI measurements is performed, leading to a total measurement time of 65 minutes.

The resulting plant estimations for the diagonal elements are illustrated for the LPM and the nD-LPM approach in Fig. 4.9. The parameter varying dynamics of the system are clearly visible in the obtained FRFs, resulting in shifting resonance and antiresonance frequencies and changing damping coefficients for the different measurements. It is observed that the plant estimation using the

(a) G_{11}: traditional LPM approach

(b) G_{11}: proposed 2D-LPM approach

(c) G_{22}: traditional LPM approach

(d) G_{22}: proposed 2D-LPM approach
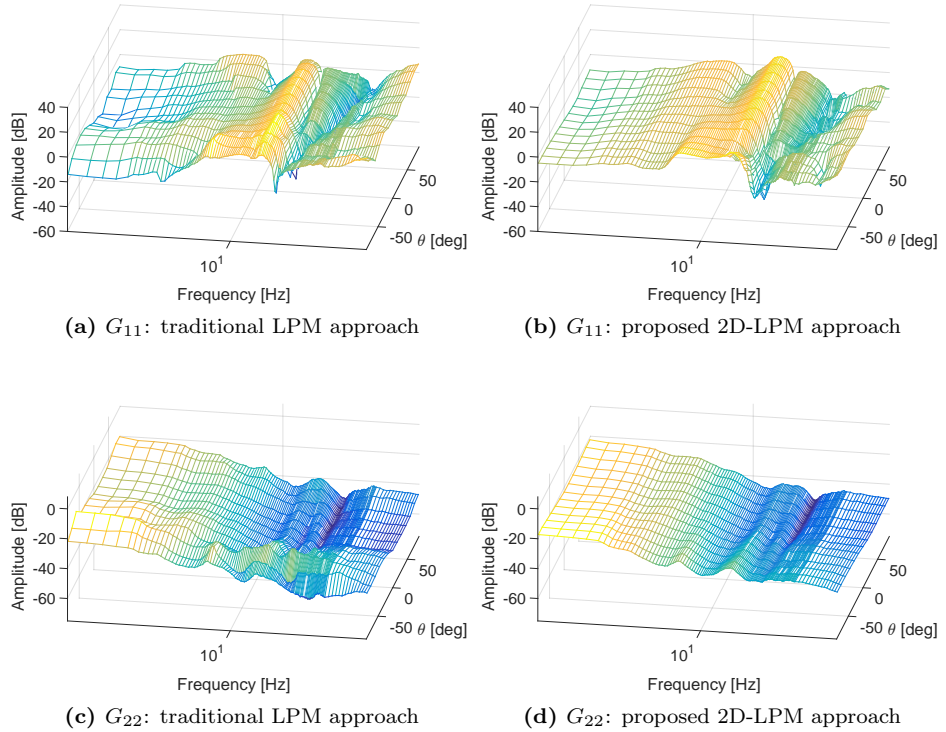
Fig. 4.9. Experimentation results. On te left, the diagonal plant elements G_{11} and G_{22} are shown using the traditional approach. On the right, the same elements are shown using the proposed 2D-LPM approach.

proposed approach is smoother than using the LPM. In Fig. 4.10, the corresponding variances and estimation of stochastic nonlinearities are shown. Similar to the approach in Sec. 4.7, the results are averaged over the scheduling parameters. The variances as a result of the noise contributions are again significantly lower using the 2D-LPM than using the LPM, since more closely neighboring frequencies are exploited to estimate the smooth function on. The difference in the estimation of the variance due to stochastic nonlinearities is explained by the definition of the best linear approximation (BLA) [48]. It can be seen that over the entire frequency range, the variance of the 2D-LPM is significantly lower than using the LPM for each LTI position. This result has been obtained using the exact same measured data.

The selection of the multisine signal is critical. For large excitation magnitudes, dynamical behavior in the neighborhood of the desired local LTI is

included in the measurement due to the inherently larger output signal. Hence, a local averaged LTI estimation is obtained. As a result, the estimation of the stochastic nonlinear distortions is increasing. Depending on the rate of variation of the dynamical behavior as a function of the scheduling parameter, the amplitude of the multisine should be chosen sufficiently small to approximate the LTI behavior with the BLA accurately. The stochastic nonlinearities give an indication if the frozen operating condition is satisfied throughout the experiment. In Fig. 4.10 it is shown that the estimation of the stochastic nonlinearities is significantly smaller than the estimated plant amplitude, leading to confidence in the chosen multisine amplitude, i.e., the estimation is not dominated by nonlinearities.

Looking at the FRF of the system, obtained using the LPM and the 2D-LPM approach, it can be concluded that the obtained results appear significantly more smooth using the proposed approach. Additionally, the obtained covariances corresponding to the identified systems dynamics show a significant desirable reduction of approximately 20 dB for all frequencies.

The result in Fig. 4.9 show shifts of (anti)resonances and a change of gain over the scheduling domain which can be directly related to the physics of the system. The dominant frequency at approximately 14 Hz is directly related to a natural frequency induced by the non-rigid connection of the detector to the C-arc, which is constant over the scheduling domain. However, other frequencies are typically related to changes in relative stiffness' as a result of a change in the mechanical structure as indicated in Fig. 4.5. The obtained nonparametric frequency response functions can directly be applied for local LPV modeling and controller analysis.

4.9   Conclusions

In this chapter, an nD-LPM approach for nonparametric frequency response functions modeling of LPV systems is presented. Based on recent advances in local parametric approaches for FRF identification, an approach that exploits smoothness over the scheduling parameter is introduced. The theory is developed and the potential of the approach is illustrated on a simulation example and experiments on a medical X-ray system.

Based on the simulation and real-life experimental results, it is shown that the proposed approach has several advantages over existing local parametric methods. Due to the use of local parametric approximations, all data, including the data obtained before reaching steady-state, is used. This is a significant improvement, particularly for LPV systems where multiple experiments over multiple scheduling parameter sets are required in a local approach. Local parametric approaches only require a single realization and experiment reducing the required measurement time significantly compared to classical methods with multiple experiments for MIMO systems, [48, Sec. 3.7]. Finally, the proposed ap-
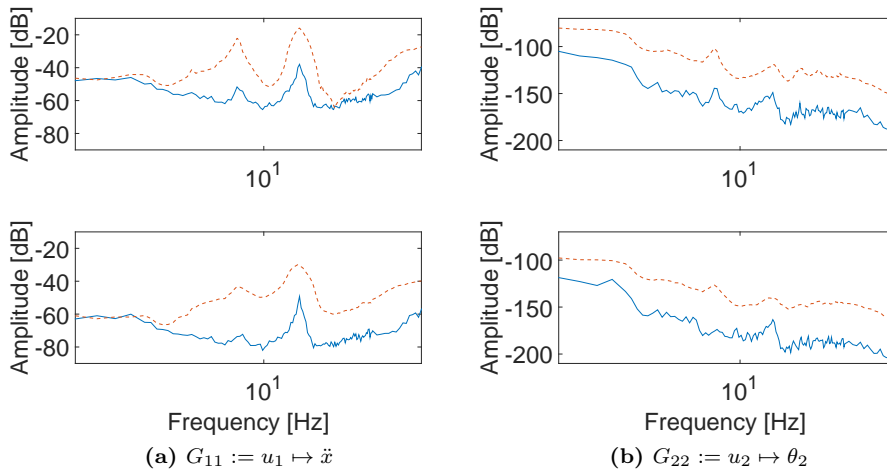
Fig. 4.10. Variance as a result of nonlinearities and measurement noise. For comparison, the plant dynamics are included in black. Top figures: noise variance; bottom figures: variance due to nonlinearities. Left figures: mapping $u_1 \mapsto \ddot{x}$; right figures: mapping $u_2 \mapsto \theta_2$. The variances on the LPM are indicated in blue, the 2D-LPM in red.

proach exploits smoothness over the scheduling parameters, leading to enhanced averaging of noise effects. Hence, shorter measurements can be performed for similar accuracy in terms of variance.

Chapter 5

Data-Driven Geometric Calibration

Currently applied calibration approaches for medical X-ray systems lead to satisfying 3D roadmapping overlay and 3D reconstruction accuracies, however, the required calibration times are extensive and the approaches are limited to systems that exhibit reproducible behavior. The aim of this chapter is to introduce a novel data-driven approach for geometric system calibrations aiming at overcoming the strict reproducibility conditions and leading to reduced calibration times. By using a physical model in combination with additional measurements and observer techniques, e.g., Kalman filters, geometric calibration parameters are estimated based on measured data during normal system operation. This is in sharp contrast to existing approaches where a calibration measurement is performed, which is used for future compensations, without a patient present. The proposed approach is demonstrated using a simplified simulation model and additional experimental results on an real interventional X-ray system, where the estimated calibration parameters are compared to both phantom and model-based calibration approaches. By combining accurate models, additional measurements and state-of-the-art state-estimation techniques, estimations of the geometric parameters required for imaging applications with high accuracy are obtained.

5.1   Introduction

Developments in the medical society increasingly rely on high quality imaging of the interior of the human body. Interventional X-ray systems are important to enable modern minimal invasive surgeries, where the aim is to minimize collateral damage during surgery, leading to less postoperative complications and faster patient recovery times. X-ray computed tomography (CT) and three-dimensional rotational angiography (3DRA) enable the generation of high quality 3D reconstructions, based on a large number of two-dimensional (2D) X-ray images each taken from a different point-of-view with respect to the patient [39]. Beside diagnostics, 3D reconstructions are typically used for roadmapping applications where real-time 2D fluoroscopy images are projected on a pregenerated 3D reconstruction [7], [8].

C-arc based X-ray systems enable relatively free access to the patient, which is desired during minimal invasive surgeries. Due to the combination of the open-kinematic structure of the system and a finite stiffness of the systems' mechanical components, the performance is significantly influenced by internal and external disturbances, e.g., gravitational forces. For C-arc based X-ray systems, which can be compared to industrial robotic systems, the behavior is subject to quasi-static deformations and inherent multivariable dynamic behavior [21].

Independent of the type of imaging system, geometric calibrations are important for successful imaging, see e.g., [101] for calibrations of magnetic resonance imaging (MRI) systems and [24] for interventional C-arc based X-ray systems. Phantom-based calibration approaches are widely applied in practice, see e.g., [10,11,18,22,40]. For each obtained 2D image, the geometric calibration parameters are given by the pose of the system, i.e., six degrees of freedom and three degrees of freedom describing the position and orientation of the detection plane and the position of the X-ray source respectively. By performing a calibration scan of a specifically designed object with accurately known size and shape (phantom), the geometric calibration parameters are reconstructed. The procedure is repeated for each possible variation on the scan, leading to significant calibration times. In [102], a model-based approach where the systems imperfections are characterized is introduced, leading to significant reductions in calibration times.

Although the aforementioned calibration approaches lead to the desired reconstruction qualities, a reproducibility condition is imposed on the system behavior. Regular recalibration is typically required to maintain the desired output over longer periods of time as a result of time-varying system behavior, e.g., wear of the system or (mechanical) changes as a result of accidental collisions. The reproducibility requirement typically translates to heavy systems, which is undesired from a cost and safety point-of-view. Motivated by Newtons law, the design of high-performance mechatronic systems is typically tending to lightweight system design. At the cost of an increased sensitivity to internal and external

(dynamical) disturbances, faster movements, reduced costs, and enhanced safety is achieved.

The aim of this chapter is to present a novel approach that exploits obtained measurements of the system, e.g., incremental encoder data and acceleration measurements, to estimate the desired geometric calibration parameters. The proposed approach has several advantages over existing approaches.

1. Using measured data during reconstruction scans of the patient to estimate the geometric parameters, increased estimation qualities are obtained, i.e., variances due to non-reproducible dynamical behavior are compensated to a certain extent. Hence, the proposed approach enables a relaxation of the reproducibility condition.

2. Phantom-based and model-based calibration approaches require regular recalibration to compensate for time-varying system behavior. By considering the model parameters, e.g., damping ratios, natural frequencies or masses/inertias, in the considered models as variable states, (slowly) time-varying system parameters are updated by using algorithms as introduced in Sec. 5.2.4. Hence, the intervals between recalibration can be increased significantly.

3. The proposed approach enables a fully automated, data-driven calibration. Hence, no extensive (time-consuming) manual calibration procedures have to be performed.

The main contribution of this chapter is the development of a flexible data-driven approach that exploits *a priori* system knowledge in models in combination with obtained measurements from the system to estimate geometric calibration parameters. The potential of the proposed approach is illustrated on a real-life medical X-ray system.

In this chapter the emphasis is on dynamical (scan) motions, e.g., 3D reconstruction scans. However, it should be noted that the approach can be extended to other types of systems and motions as well. In literature, alternative approaches are available that lead to a reduced reproducibility condition on the system. In [26] it is proposed to add markers in the patient table to provide a fixed reference to the patient. The main drawback of the approach is the possible occlusion of relevant anatomy and localized increased disturbance levels in the obtained X-ray images. In [29], an approach is presented that evaluates the image entropy to characterize the amount of artifacts induced due to geometric imperfections leading to improvement reconstruction qualities. However, the approach requires significant computation power and is sensitive to disturbances that have similar effects in the obtained images as geometric imperfections, e.g., patient motions. Based on the acquired images, image-based approaches are proposed in [27], [28] that uses features of the human anatomy to estimate the geometric parameters.
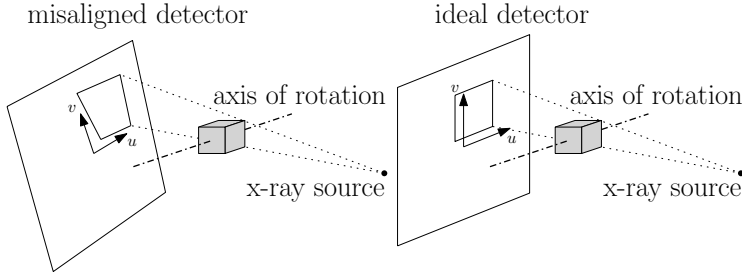
Fig. 5.1. Projection of an object with perfect alignment (right); and misaligned detector in orientations and translations (left).

This chapter is structured as follows, first, the existing fundamental approaches are highlighted and a problem description is provided in Sec. 5.2. In Sec. 5.3 the required theory on observer design is explained, followed by a proposed modeling and parameter estimation procedure in Sec. 5.4 that leads to the required models for Kalman filter based state estimations [103], which is in more detail introduced in Sec. 5.2.4. The potential of the proposed approach is illustrated on a real-life experimental X-ray system from which the results are shown in Sec. 5.5. This chapter concludes with conclusions and recommendations for future extensions in Sec. 5.6.

5.2   Preliminaries and proposed approach

5.2.1   Geometric calibration and parameters

By virtue of the pinhole camera model, see, e.g., [3, Chap. 1], the acquisition geometry for flat-panel cone-beam systems can be described by a projection matrix in combination with a rotation matrix and a translation vector. The projection of an arbitrary point within the X-ray exposed volume is highly correlated to the kinematic position and orientation of the detector, the position of the focal spot (X-ray source), and the relative position of the object with respect to the image-acquisition components [11].

An X-ray image is created by measuring the projected X-ray dose, which is a measure of quanta absorption by the material [3], of all matter included in a direct trajectory from the X-ray source to the detector. The mathematical description often used to model the projection for the $\mathbb{R}^3$-space to the $\mathbb{R}^2$-space, which is the projected image on the detector, is referred to as *projective geometry* [104].

In literature on geometric calibrations, typically the X-ray source is assumed a point source, [11], [40]. As a consequence, the projective space is formed by the intersection of all lines from the origin of $\mathbb{R}^3$, i.e., the X-ray source, to the

detection plane, as indicated in Fig. 5.1. Hence, every (projected) point on the detection plane corresponds to a line in $\mathbb{R}^3$ [104], [105]. Homogeneous transformation matrices are widely used in vision applications to describe projections of points in 3D space to 2D planes, i.e., the pinhole camera model.

For each acquired image nine degrees of freedom or "*geometric parameters*" are estimated, i.e., three translations and three orientations of the detector and three translational offsets only due to the point source assumption of the X-ray source. The geometric parameters are typically only known by approximation. For the ideal situation, design parameters can be used. However, any system in practice suffers from mechanical imperfections and (unknown) external disturbances. In practice widely applied phantom-based geometric calibration approaches focus on the measurement of the effects of these imperfections, i.e., the resulting actual trajectory of the detector and X-ray source. Since (a subset of) the geometric parameters appears in the argument of the homogeneous transformation matrices, the estimation of the actual parameters is a mathematically challenging nonlinear, non-convex optimization problem. A vast amount of approaches is proposed in literature, where in general a nonlinear optimization is performed on an approximative description (model) with enhanced global convergence properties, and/or where a reduction of the number of estimated parameters is proposed, see, e.g., [10], [11], and [106].

Typically, quasi-static offsets, as a result of (mechanical) misalignments or deterministic offsets in the system, lead to artifacts in reconstructions while zero-mean dynamical behavior result in blurring effects [102].

5.2.2 Model-based geometric calibration

An alternative calibration approach for C-arc based X-ray systems is presented in [102] where the underlying mechanical effects are modeled that lead to offsets of the geometric parameters with respect to the ideal situation. By exploiting the predictive properties of a physics based model, only a limited set of experiments is performed for the identification of physical parameters, leading to significant calibration time reductions with similar reconstruction qualities.

Based on modern modeling and parameter identification approaches widely used in the field of (industrial) robotic systems, [12, 31, 32, 44], quasi-static behavior is described as a function of a finite set of physical system parameters, e.g., misalignment (rotational or translational) offsets, deviations in gear ratios, and production imperfections leading to varying link lengths and masses, which is a significantly different approach then the estimation of geometric parameters directly. A typical mathematical modeling approach for robotic systems uses the Denavit-Hartenberg (DH) convention [12, Sec. 2.8.2], which describes the end-point position, e.g., X-ray source or detector, in terms of a minimal number of physical system parameters in combination with homogeneous transformation matrices, similar to the geometric calibration problem, see [102] for a detailed

implementation of the presented approach.

By performing a predefined identification measurement using a calibration phantom, the physical system parameters are estimated. Since the estimation problem remains nonlinear, a minimal realization is desired, which can be obtained using the DH-convention. Accurate initial parameter estimations, which is typically the case since the deviations are small with respect to the design parameters, are key for convergence of iterative parameter search approaches, e.g., by virtue of a Gauss-Newton algorithm. Under the strict assumption that the system behavior is reproducible, the calibration problem is recast in an parameter identification problem, which enables a significant reduction of calibration times.

5.2.3   Problem description

The key assumption for the phantom and model-based calibration approaches in Secs. 5.2.1 and 5.2.2 is reproducibility of the system, typically enforced by the mechanical design of the system, e.g., by heavy constructions with large stiffness' approximating rigid body behavior. Lightweight systems have multiple advantages over the current state-of-the-art designs.

- The system design can be more cost-efficient, e.g., less material costs, smaller actuators and gear-boxes, lower transportation costs, and less strict conditions on the supporting ceiling or floor base.

- Enhanced safety, e.g., faster (emergency) brake times and reduced (accidental) collision forces due to the lowered inertias.

- Quick and simplified in field installation.

The main disadvantage of lightweight system design is the increased sensitivity to internal, e.g., motion induced, and external disturbances, leading to a decreased reproducibility of the geometric parameters. Similar observations can be made when the scan velocities of the current generation of systems increase, i.e., higher accelerations. The dynamics of the system are significantly more excited while the initial states of the system are typically not guaranteed to be the same for each scan due to a wide variety of (external) situations.

Unrelated to lightweight system design, an alternative non-reproducible effect that can be observed is changing system behavior due to usage over time. Typically, geometric calibrations are repeated with time-intervals of six months for various reasons, e.g., wear of the system or small changes due to accidental collisions.

The proposed approach in this chapter enables a relaxation of the reproducibility condition imposed on the current generation of systems by exploiting accurate models in combination with measured data during actual patient scans. A general description is presented in Sec. 5.2.4 and the remainder of the chapter

deals with the technical details concluding with experimental results illustrating the potential of the proposed approach.

5.2.4 Proposed data-driven geometric calibration approach

To recap, the aim of this section is to introduce a data-driven approach that exploits available measurements to predict the system behavior during an actual patient scan. In the current section, the fundamental idea behind the proposed data-driven approach is explained.

The reconstruction algorithm is considered a given process,

$$\mathcal{I}^{\text{3D}} = f_R(\mathcal{I}^{\text{2D}}, \underline{\xi}_{\text{geo}}), \tag{5.1}$$

where $\mathcal{I}^{\text{3D}}$ denotes the obtained 3D reconstruction, $\mathcal{I}^{\text{2D}}$ a set of 2D images obtained during a full scan, and $\underline{\xi}_{\text{geo}}$ a set of geometric parameters that correspond to each 2D image. It should be noted that the quality of the individual 2D images is also influenced by the (lightweight) system design, however, this is considered out of the scope of this work. The objective is to obtain accurate estimations of $\underline{\xi}_{\text{geo}}$ such that the reconstruction process can be obtained with satisfying 3D results.

The (measured) output of a system can be roughly divided in two parts; a quasi-static, and a dynamical contribution. Dynamical models are often expressed in multi-input-multi-output (MIMO) discrete-time state-space formulations,

$$\begin{aligned} x_{k+1} &= f(x_k,\ u_k), \\ y_k &= h(x_k,\ u_k), \end{aligned} \tag{5.2}$$

with $x_k \in \mathbb{R}^{n_x}$ the state vector of length n_x, k the discrete-time index, and $u \in \mathbb{R}^{n_u}$ and $y \in \mathbb{R}^{n_y}$ the input and output vector respectively with n_u inputs and n_y outputs. The functions $f(x_k,\ u_k)$ and $h(x_k,\ u_k)$ are describing the state-equation and output-equation respectively. The state-equation is a dynamical description, while the output equation relates the states, that are not necessarily physically meaningful, to the measured outputs. In this work, the quasi-static components are included in the output equation, i.e.,

$$y_k = h_d(x_k,\ u_k) + h_{qs}(x_k) := h(x_k,\ u_k), \tag{5.3}$$

where $h_d(x_k,\ u_k)$ denotes the dynamic contributions and $h_{qs}(x_k)$ the quasi-static contributions. It should be noted that the quasi-static output is a function of the current state, e.g., absolute angular rotations of the actuators define the quasi-static offsets.

The output vector y_k can be a combination of measured outputs, such as incremental encoder measurements or acceleration and absolute velocity measurements. With the development of micro-electro-mechanical systems (MEMS),
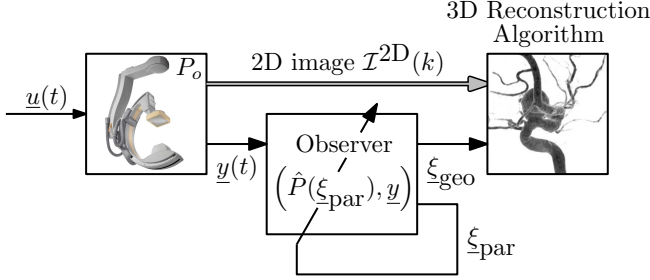
Fig. 5.2. Schematic representation of the proposed data-driven geometric calibration approach.

relatively cheap, accurate measurements of linear accelerations and angular velocities can be obtained, directly located at the positions of interest, i.e., the image acquisition components. The input vector is assumed user-defined, e.g., a predefined scan trajectory. State-estimators or observers aim at the estimation of the system states x_k which are typically not directly measured [103], [43].

To estimate the geometric parameters that do have a physical interpretation in terms of orientations and translations of the image acquisition components but are typically unmeasured, a model should be available to enable the derivation of the geometric parameters from the estimated states. A schematic representation of the proposed procedure is provided in Fig. 5.2.

The remainder of this work shows how observers can be exploited to obtain accurate estimations of the states of the system. It also presents how a modal state-space representation can be obtained from a standard Euler-Lagrange formulation that is the result of many modeling approaches, which has specific advantageous properties for the data-driven approach as well as in-field installation which will be presented in detail in Sec. 5.4. In addition, it is shown how the method can be exploited for the identification of the physical system parameters denoted by $\underline{\xi}_{\text{par}}$ included in the quasi-static model as presented in Sec. 5.2.2, rendering the identification procedure proposed in [102] unnecessary. As an additional advantage, an adaptive approach is obtained that is able to compensate for slowly time-varying behavior of the system.

In the remainder of this chapter, two approaches are presented.

1. A linear model of the system is available and the model parameters are assumed known and fixed. A linear Kalman filter is exploited to estimate the model states, i.e., the geometric parameters.

2. A model as in (5.2) is used where the model parameters are chosen as additional states in the observer design. Due to the typically nonlinear structure of the model, extended and unscented Kalman filters are exploited [107].

5.3 Observer design

A vast amount of observer design approaches is available in literature, e.g., the Kalman filter (KF) for linear systems [103], the Extended Kalman filter (EKF) for nonlinear systems [107], and the Unscented Kalman filter (UKF) [108], [109]. The principle of the discrete time Kalman filters, which forms the basis for the proposed approach in this chapter, is presented in the current section for three different filters, which each unique advantageous properties. In the following section (Sec. 5.4) more details are provided on how the underlying (non)linear models can be obtained.

5.3.1 Kalman filter

The Kalman Filter is optimal for linear systems, where the multivariable, discrete time, linear state-space approximative model of the true system P_0 is given by

$$\hat{P}: \quad \begin{aligned} x_{k+1} &= F_k x_k + G_k u_k + V_k v_k, \\ z_k &= H_k x_k + D_k u_k + W_k w_k, \end{aligned} \tag{5.4}$$

with $v_k \in \mathcal{N}(0, Q_k)$ and $w_k \in \mathcal{N}(0, R_k)$ zero-mean Gaussian noises with covariances Q and R respectively. Note that the system matrices F_k, G_k, H_k, D_k, V_k, and W_k might be time/parameter varying. The model output variable z_k represents a realization of the measured outputs of the system, which does not necessarily includes the geometric parameters.

Kalman filtering is a recursive procedure that is performed for each obtained discrete-time step. Given a (model-based) predicted state and covariance, the Kalman filter is performing a measurement and covariance P update according to

$$\hat{x}_{k|k} = \hat{x}_{k|k-1} + K_k(z_k - \hat{z}_k), \tag{5.5}$$

$$P_{k|k} = (I - K_k H_k)P_{k|k-1}, \tag{5.6}$$

where the notation is adopted from [110] with the subscript $\hat{x}_{k|k-1}$ denoting the estimation of x at time instant k given an estimation at time instant $k-1$, and z_k the measurement vector at k. The predicted states and outputs before update (5.5) are given by

$$\hat{x}_{k|k-1} = F_{k-1}\hat{x}_{k-1|k-1} + G_{k-1}u_{k-1}, \tag{5.7}$$

$$\hat{z}_k = H_k \hat{x}_{k|k-1} + D_k u_k. \tag{5.8}$$

The corresponding predicted covariance matrix is given by

$$P_{k|k-1} = F_{k-1}P_{k-1|k-1}F_{k-1}^T + V_{k-1}Q_{k-1}V_{k-1}^T. \tag{5.9}$$

The predicted states and covariance matrices in (5.7) and (5.9) respectively are fully model based predictions and heavily rely on the updated states and

covariances from the previous step. The Kalman gain K_k in (5.5) and (5.6) is selected such that an optimal balance between the measurements and model-based predictions in terms of a minimization of the covariance is obtained. For linear systems, the solution is given by the discrete algebraic Riccati equation (DARE) [110], see also Sec. C.2 for a discrete-time derivation, resulting in,

$$K_k = P_{k|k-1}H_k^T(H_kP_{k|k-1}H_k^T + W_kR_kW_k^T)^{-1}. \tag{5.10}$$

Typically estimation errors are characterized by a bias term and a covariance. The covariance is minimized by obtaining a Kalman gain according to (5.10), where the bias term is dominated by modeling errors which follow from (5.5), see also [110, Sec. 7.2.4]. Note that the zero-mean distributed noise assumption is key for the state and output prediction, i.e., $\mathbb{E}\{v_k\} = \mathbb{E}\{w_k\} = 0$. If the signal is not Gaussian, e.g., when there is a coloring of the noise, the system should be expanded with an appropriate exogenous model, see, e.g., [111] for more details on this so-called internal model principle. Typically, for an offset an additional integrator is required leading to an expanded F_k and corresponding state-vector x_k. The noise terms v_k and w_k remain assumed zeros-mean Gaussian distributed white noises, while the matrices V_k and W_k provide the intensity scaling. To minimize the estimation errors, accurate modeling is key. Since any system is nonlinear to a certain degree and when model parameters are considered additional states, the estimation problem becomes nonlinear. Hence, observers are desired that are able to deal with nonlinear models.

5.3.2   Extended Kalman filter

The EKF is based on local linearizations of a nonlinear system description and strongly related to the linear KF. Given a nonlinear model of the real system P_0,

$$\hat{P}: \quad \begin{aligned} x_{k+1} &= f(x_k, u_k, v_k), \\ z_k &= h(x_k, u_k, w_k), \end{aligned} \tag{5.11}$$

where in contrast to (5.2) only the measured outputs z_k are selected, with the state equation $f(x_k, u_k, v_k)$ and the output equation $h(x_k, u_k, w_k)$. The state prediction and output prediction as in (5.7) and (5.8) respectively are obtained by direct evaluation of the nonlinear equations in (5.11). However, the remaining steps require a linearization of the nonlinear expressions at each time step, i.e.,

$$\bar{F}_k = \left.\frac{\partial f(x_k, u_k, v_k)}{\partial x}\right|_{x=\hat{x}_{k|k}}, \bar{H}_k = \left.\frac{\partial h(x_k, u_k, w_k)}{\partial x}\right|_{x=\hat{x}_{k|k}}, \tag{5.12}$$

and,

$$\bar{V}_k = \left.\frac{\partial f(x_k, u_k, v_k)}{\partial v}\right|_{x=\hat{x}_{k|k}}, \bar{W}_k = \left.\frac{\partial h(x_k, u_k, w_k)}{\partial w}\right|_{x=\hat{x}_{k|k}}. \tag{5.13}$$

are required. By substitution of the linearized matrices $\bar{F}_k$, $\bar{H}_k$, $\bar{V}_k$, and $\bar{W}_k$, the procedure in Sec. 5.3.1 can be followed.

The main drawback of the Extended Kalman filter is that there are no guarantees on global convergence as a result of the local linearizations. However, in practical applications the ease of implementation in combination with in general satisfying results make the EKF a widely applied approach, [43, 112–114].

Remark 5.1. For the estimation of (a subset of) the states, observability of these states is required. A widely applied approach to test observability of a (linearized) system, the following should hold [55, Sec. 10.6],

$$\text{rank}\left(\begin{bmatrix} \bar{H}_k \\ \bar{H}_k \bar{F}_k \\ \vdots \\ \bar{H}_k \bar{F}_k^{n_x-1} \end{bmatrix}\right) = n_x, \tag{5.14}$$

with n_x the number of states and rank indicating the column rank. ◁

5.3.3 Unscented Kalman filter

An approach that is purely based on the evaluation of the nonlinear model as in (5.11) is the unscented Kalman filter, first introduced in [108], see also [109] for more details.

The UKF is based on the evaluation of the system by a limited number of data-points, which is in sharp contrast to the evaluation of the system using a single updated state estimation as in the (E)KF. The UKF is based on a similar principle as Monte-Carlo simulations, however, by making a specific selection of the data-points a reduced number of evaluations is required. Hence, the computation time is significantly smaller for the UKF then for Monte-Carlo based approaches. The data-points define the covariance region and are often referred to as sigma-points, denoted by

$$\chi_{k-1|k-1}^0 = \hat{x}_{k-1|k-1}, \tag{5.15}$$

$$\chi_{k-1|k-1}^i = \hat{x}_{k-1|k-1} \pm \sqrt{(n_x + \kappa)P_{k-1|k-1}}\,\Big|_{[i]}, \tag{5.16}$$

with $\sqrt{(n_x + \kappa)P_{k-1|k-1}}$ defining the principle axis of the covariance region and the subscript $[i]$ indicating the selection of the column of the principle axis matrix corresponding to the ith data-point. Note that each column of the principle axis matrix is used for the computation of two data-points according to the $\pm$ sign. The variable n_x represents the number of states of the model, κ a scaling factor and the index $i = 1, 2, \ldots, 2n_x$. The integer κ is typically used as an additional degree of freedom, e.g., typically chosen $n_x + \kappa = 3$ for Gaussian distributions.

Note that negative values for κ can be obtained [113]. All sigma-points are evaluated using the nonlinear state equation, resulting in,

$$\hat{\chi}_{k|k-1}^j = f(\chi_{k-1|k-1}^j, u_{k-1}), \tag{5.17}$$

with $j = 0, 1, \ldots, 2n_x$. By computation of the weighted average,

$$\hat{x}_{k|k-1} = \sum_{j=0}^{2n_x} \gamma_x^j \hat{\chi}_{k|k-1}^j, \tag{5.18}$$

with γ_x a weighting function, a state prediction is obtained, equivalent to (5.7) for the linear situation. Similarly, the weighted average over the covariances is computed according to

$$P_{k|k-1} = \sum_{j=0}^{2n_x} \gamma_p^j \text{cov}(\hat{\chi}_{k|k-1}^j), \tag{5.19}$$

leading to a prediction of the covariance for which the linear equivalent is given in (5.9).

Many proposals for the definition of the weighting factors γ_p are available in literature, see, e.g., [115], [116], and [109]. Virtually, any choice can be made, however,

$$\sum_{j=0}^{2n_x} \gamma_p^j = 1, \tag{5.20}$$

should always hold, to provide an unbiased estimate. In [117] an alternative approach for improved estimation accuracy is proposed, in particular for systems with a large number of states, using additional sigma points.

After the computation of the state and covariance estimations, the weighted output estimation is given by

$$\mathcal{Z}_k^j = h(\hat{\chi}_{k|k-1}^j, u_k), \tag{5.21}$$

$$\hat{z}_k = \sum_{j=0}^{2n_x} \gamma_x^j \mathcal{Z}_k^j, \tag{5.22}$$

from which the (cross-)covariance of the state and output estimations are computed by

$$P_{\text{xz}} = \sum_{j=0}^{2n_x} \gamma_p^j \text{cov}(\hat{\chi}_{k|k-1}^j, \mathcal{Z}_k^j), \tag{5.23}$$

$$P_{\text{zz}} = \sum_{j=0}^{2n_x} \gamma_p^j \text{cov}(\mathcal{Z}_k^j). \tag{5.24}$$

The Kalman gain is computed by

$$K_k = P_{xz}(P_{zz} + WRW^T)^{-1}, \tag{5.25}$$

which is again used to update the state similar to (5.5). Note that as a result of the direct estimation of the covariance due to the evaluation of the nonlinear function with the sigma-points, no information on the state-covariance is required. The update on the predicted covariance is given by

$$P_{k|k} = P_{k|k-1} - K_k(P_{zz} + WRW^T)K_k^T, \tag{5.26}$$

concluding the update step.

Due to the evaluation of the nonlinear equations, there are no linearization errors introduced which is the case for the EKF. As a result, the exploited model in the observer is close to the true system behavior, leading to a reduced estimation bias. Moreover, it is not required to provide a process noise covariance, i.e., Q from (5.4). The process noise is usually difficult to estimate, leading to an additional tuning parameter for (E)KF implementations. The UKF does not require the term due to a direct estimation of the state covariance by virtue of the sigma-points.

In Sec. 5.4, a possible modeling approach is proposed to obtain the underlying (non)linear models required for the estimation steps in the (E/U)KF, based on the nonparametric modeling methods as introduced in Chaps. 3 and 4.

5.4 Parametric modeling for state-estimations

5.4.1 Parametric modeling

A dynamical system can be denoted using a set of coupled differential equations, [118],

$$\begin{aligned} M\ddot{q} + D\dot{q} + Kq &= B_0 u \\ y &= C_0 q + M_{qs}(q) \end{aligned}, \tag{5.27}$$

with M, D, and K the mass, viscous damping, and stiffness matrices respectively, C_0 an output matrix, B_0 an input matrix, with $\ddot{q}$ and $\dot{q}$ indicating a double and single time-derivative of q respectively. The term $M_{qs}(q)$ indicates quasi-static and rigid body motions as obtained in Chap. 2. The mass matrix is positive definite and the stiffness matrix semi-positive definite. The vector $q \in \mathbb{R}^{n_s}$ represents the displacement of the nodes of the lumped parameter system where n_s represents the number of masses.

Typical for robotic systems is the parameter dependency of the dynamical behavior, e.g., due to changing link lengths or geometric poses the system compliances change, making the systems inherently nonlinear. In this thesis, Coriolis

and centrifugal forces are neglected since these only have a limited influence on the systems behavior. As a result, often complicated (parameter varying) dynamic models are obtained, which will be in more detail described in Sec. 5.4.2, resulting in $M(\boldsymbol{\theta})$, $D(\boldsymbol{\theta})$, $K(\boldsymbol{\theta})$, $B_0(\boldsymbol{\theta})$, and $C_0(\boldsymbol{\theta})$. In the current section a single LTI model is assumed for notational convenience, i.e., a single workpoint is considered $\boldsymbol{\theta} = \boldsymbol{\theta}^*$. As presented in Sec. 5.2.4, the system parameters are considered estimated variables by the observer. Hence, in this section a parametric modeling approach is introduced that 1) leads to a reduced number of estimated parameters for dynamic modeling, and 2) leads to physical parameters that have direct physical interpretations such that initial estimations can be obtained with relative ease, as will be presented in detail in Sec. 5.4.3. It is shown how an alternative parameterization is obtained which has equivalent input/output behavior as (5.27). To incorporate the geometric nonlinearity in the model, an approach based on model estimations for varying poses of the system is introduced in Sec. 5.4.2. By obtaining multiple LTI models for different workpoints, which are connection by virtue of an additional step interconnecting various system poses, a linear parameter varying (LPV) model is obtained.

In literature, several approaches are available to transform an LTI model in a state-space representation. In [74], a control canonical form is proposed as a state-space representation for SISO systems. Alternative canonical state-space representations are presented in [119], [120], and [121]. In [122], an approach based on balanced realizations of LTI models is suggested. In this chapter, a modal approach [118], [123] is applied. The main advantage of the approach is the limited number of required parameters and the direct relation to the mechanics/physics of the system in terms of natural frequencies and damping coefficients.

The first step in obtaining the modal form starting from (5.27) is solving the generalized eigenvalue problem [123],

$$K\phi = \omega_n^2 M\phi, \quad \phi \neq 0, \tag{5.28}$$

resulting in the natural frequencies ω_n and the mode shapes ϕ, see also [118]. By defining the modal matrix $\Phi = [\phi_1, \ \phi_2, \ \ldots, \ \phi_{n_s}]$, in which each column spans the direction of the mode shapes, the equations of motion in (5.27) can be expressed as,

$$\begin{aligned} M_m\ddot{\eta} + D_m\dot{\eta} + K_m\eta &= \Phi^T B_0 u \\ y &= C_0\Phi\eta \end{aligned}, \tag{5.29}$$

with the diagonal matrices $M_m = \Phi^T M \Phi$ and $K_m = \Phi^T K \Phi$. The matrix $D_m = \Phi^T D \Phi$ is diagonal for specific damping types, e.g., proportional or Rayleigh damping, where it is assumed that $D_m = \alpha M_m + \beta K_m$ with α and β nonnegative scalars [124]. Typically, lightly damped systems are modeled using damping models that lead to a diagonal form of D_m [118]. Hence, in the remainder of this work, D_m is considered diagonal. Pre-multiplication of (5.29) with M_m^{-1}

results in,

$$\ddot{\eta} + 2Z\Omega\dot{\eta} + \Omega^2\eta = B_m u \\ y = C_m\eta , \qquad (5.30)$$

with the diagonal matrices $\Omega^2 = M_m^{-1}K_m$, $Z = \text{diag}\{\zeta_i\}, i = 1, 2, \ldots, n_s$, and $C_m = C_0\Phi$, and $B_m = M_m^{-1}\Phi^T B_0$. As a result of the diagonal structure of the matrices, there is no coupling between the independent natural frequencies In addition, input/output related scalings are defined using the matrices B_m and C_m. The corresponding state-space realization is given by

$$\dot{\nu} = \begin{bmatrix} 0 & 1 \\ -\Omega^2 & -2Z\Omega \end{bmatrix}\nu + \begin{bmatrix} 0 \\ B_m \end{bmatrix}u, \\ y = C_m\nu , \qquad (5.31)$$

with $\nu = [\eta, \ \dot{\eta}]^T$. The poles of the system are independent of the measurement locations. By selecting a sufficient number of modes, e.g., modes that lie in a frequency range and have a large enough magnitude to disturb the 3D reconstructions, the dynamical behavior over multiple degrees of freedom can be obtained by proper selection and scaling of the B_m and C_m matrices, and the damping constants in Z.

When acceleration sensors are included, i.e., $y = C_a\ddot{\eta}$, the acceleration signal is expressed as a linear combination of the position and velocity components in ν that follows directly from (5.31), i.e.,

$$y = \begin{bmatrix} C_m \\ -C_a \begin{bmatrix} \Omega^2 & 2Z\Omega \end{bmatrix} \end{bmatrix}\nu + \begin{bmatrix} 0 \\ C_a B_m \end{bmatrix}u. \qquad (5.32)$$

Note that the feed-through term $C_a B_m$ is proportional to the output and is zero when the accelerometer location matrix C_a and B_m are orthogonal. Typically this is for the modal form the case when the acceleration sensor and the excitation forces are not collocated [118]. A physical interpretation of this property is that there are always dynamics present in the non-collocated situation between the excitation and measurement. Hence, a change in the input has a filtered effect on the output. Note that this modeling approach is limited to (strictly) proper systems.

Here it is shown that a model satisfying the formulation in (5.27) can be re-cast in the modal state-space form in (5.31). Due to the diagonal structure of the model parameters included in Ω^2 and $2Z\Omega$, which directly relate to the natural frequencies and the damping of the system, initial estimations can be obtained according to multiple approaches, e.g., modal analysis or more informative frequency response measurements, which is further emphasized in Sec. 5.4.3.

5.4.2   Modeling geometric nonlinearities

For the description of the dynamics of open-chain robotic systems, often the Euler-Lagrange formulation used, see, e.g., [125, 126], and [12],

$$\underbrace{M(q,\dot q)\ddot q}_{\text{inertia}} + \underbrace{C(q,\dot q)\dot q}_{\text{centrifugal + coriolis}} + \underbrace{P_g(q)}_{\text{gravity}} = \underbrace{f_n}_{\text{actuation}} , \qquad (5.33)$$

with f_n the actuation forces. The system can also be described as a system with linear parameter varying (LPV) behavior, as for which a nonparametric identification approach has been proposed in Chap. 4. Typically, nonparametric identification is an intermediate step for parametric modeling. Hence, increased accuracy of the nonparametric model leads to improved parametric modeling leading to improved estimation accuracies and robustness using model-based observers. Besides parametric modeling accuracy, variations over various systems can lead to the need of obtaining models for each system individually, which lead to the need for time-efficient approaches to obtain (non)parametric models. Many systems exhibit to a certain extent parameter dependent behavior on non-stationary parameters, e.g., position or temperature. This typically nonlinear behavior is often recast into the LPV framework [94], for which the formulation in (5.27) becomes,

$$\begin{aligned} M(\boldsymbol{\theta})\ddot q + D(\boldsymbol{\theta})\dot q + K(\boldsymbol{\theta})q &= B_0(\boldsymbol{\theta})u \\ y &= C_0(\boldsymbol{\theta})q \end{aligned} , \qquad (5.34)$$

with $\boldsymbol{\theta}$ indicating the parameters on which the formulation is depending. It should be noted that the formulation of (5.34) is used to obtain a linear approximation of (5.33). The modal state-space formulation, based on (5.34), is derived as presented in Sec. 5.4.1, and is given by

$$\begin{aligned} \dot\nu &= \begin{bmatrix} 0 & 1 \\ -\Omega^2(\boldsymbol{\theta}) & -2Z(\boldsymbol{\theta})\Omega(\boldsymbol{\theta}) \end{bmatrix}\nu + \begin{bmatrix} 0 \\ B_m(\boldsymbol{\theta}) \end{bmatrix}u, \\ y &= C_m(\boldsymbol{\theta})\nu, \end{aligned} \qquad (5.35)$$

which indicates the natural frequencies and damping constants of the system are depending on $\boldsymbol{\theta}$. For a "frozen" set of scheduling parameters, i.e., $\boldsymbol{\theta} = \boldsymbol{\theta}_\beta$ with the subscript β indicating a specific pose of the system, a linear time-invariant representation of the dynamics of the system is obtained.

For most mechanical systems, the variations in the dynamics can be described as a smooth function of $\boldsymbol{\theta}$ with static parameters, e.g., $\Omega^2(\boldsymbol{\theta}) = f(\boldsymbol{\theta})$, and $Z(\boldsymbol{\theta}) = g(\boldsymbol{\theta})$. By performing experiments for various system poses, i.e., various frozen $\boldsymbol{\theta}_\beta$, (basis)functions $f(\boldsymbol{\theta})$ can be defined describing the variations in dynamical behavior. Note that physical interpretations of the model parameters in (5.31) enable a smoothness assumption over $\boldsymbol{\theta}$ without the requirement for additional (matrix) transformations.

5.4.3 Initial parameter estimation

When a physical model is available, the model can be derived and used in the state-observer. When there is no physical model available, the modal (state-space) form can be used, however the model parameters should be obtained such that the system dynamics are approximated. For the situation where the model parameters are considered fixed, the modeling errors are desired to be as small as possible. For the situation where the model parameters are considered additional states to the observer, accurate initial estimations are important to obtain convergence of the estimations. Note that alternative adaptive approaches are available. However, since a state-observer is already required to estimate the unmeasured geometric parameters, an extension with the parameters is an intuitive approach.

The discrete Fourier transform (DFT) of a measured time-domain signal x is given by

$$X(k) = \frac{1}{\sqrt{N}} \sum_{n=0}^{N-1} x(nT_s)e^{-i2\pi nk/N}, \tag{5.36}$$

with N the measured number of samples, T_s the sample time, and k an index indicating the frequency bin. By computation of the DFT for both the excitation and measured output signal, a nonparametric frequency response functions (FRF) can be obtained, which is typically an intermediate step on which the model parameters of the models presented in Sec. 5.4.1 can be fitted.

The identification of nonparametric models, in particular frequency response functions, has been significantly advanced over the recent years, see [48] for an overview of the state-of-the-art methods. Typically, the actuator inputs are excited using a predefined signal with a desired spectrum, e.g., a band-limited white noise signal or a periodic signal where the frequency spectrum is chosen such that the frequencies where dynamics are crucial are excited. By computing the DFT of both the input and output spectra, again the transfer function can be obtained. See also chapters 3 and 4. These nonparametric models typically are considered an intermediate step in obtaining parametric models such as (5.35). By estimating the model parameters of (5.35) such that the error between the nonparametric and parametric model are minimized for fixed workpoints, individual LTI models are obtained. Using *a priori* system knowledge or basis functions, continues functions describing the change of the parameters as a function of $\boldsymbol{\theta}$ are modelled.

5.5 Experimental results

The potential of the proposed approach for geometric calibrations is illustrated in this section based on experimental results on a real imaging system.
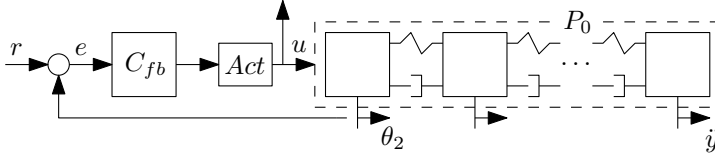
Fig. 5.3. Schematic representation of the simulation setup. The actuator dynamics, indicated by *Act* are neglected and convert the controller output, i.e., typically a current, to forces acting on the first inertia.

The system is operating in closed-loop as indicated in Fig. 5.3 where the measured outputs of P_0 are indicated in Fig. 5.4. Moreover, quasi-static effects can not be neglected as argued in Chap. 2, leading to the model,

$$\hat{P} \quad : \quad \begin{aligned} x_{k+1} &= A(x_k)x_k + B(x_k)u_k, \\ y_k &= C(x_k)x_k + M_{\mathrm{qs}}(x_k), \end{aligned} \tag{5.37}$$

where the term $M_{\mathrm{qs}}(x_k)$ represents the quasi-static and kinematic model which depends on the states x_k. In Fig. 5.5 the measured frequency response function is shown for the dynamical mappings at a single workpoint,

$$\hat{P} \quad : \quad u \mapsto \begin{bmatrix} \theta_2 \\ \ddot{y}_{\mathrm{d}} \\ y_{\mathrm{d}} \end{bmatrix}, \tag{5.38}$$

where θ_2 represents the collocated encoder measurement, $\ddot{y}_{\mathrm{d}}$ the non-collocated acceleration measurement of the y-direction of the detector, y_{d} the non-collocated position measurement of the detector as indicated in Fig. 5.4, and u the input of the plant. Information on y is only available off-line. Hence, the aim is to estimate the y-displacement of the detector during a scan where θ_2 is ranging from -90 to 90 degrees as indicated in Fig. 5.4.

Due to the availability of accurate nonparametric models for the test setup, the parametric model is assumed sufficiently close to the true system dynamics, i.e., adaptation of the parameters is not required. The parameters of the quasi-static model $M_{qs}(x_k)$ which is following the structure as presented in [102], are obtained by two approaches,

1. the parameters are obtained by computation by virtue of Gauss-Newton iterations, or any other desired optimization procedure, as proposed in [102], and

2. the quasi-static and kinematic model parameters are included in the observer as additional estimated states.

The resulting FRFs of the relevant signal mappings indicated in (5.38) are shown in Fig. 5.5 for a single workpoint, including a parametric fit based on
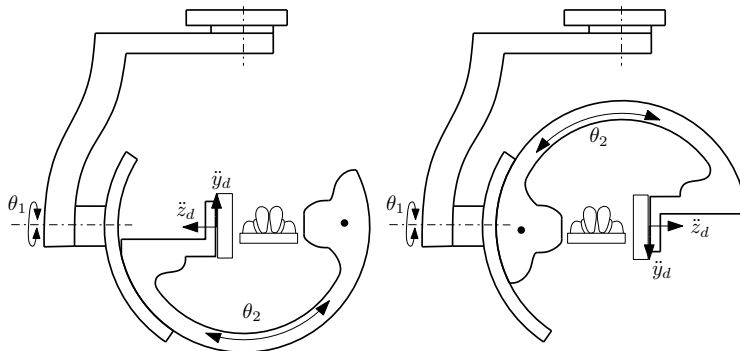
Fig. 5.4. Philips Allura Xper FD20: illustration of scan range.

Table 5.1. Identified DH-parameters of the Philips Xper Allura FD20 - *Model-Based*

	a [mm]	$\delta\theta$ [rad]	α [rad]	d [mm]	β [-]
1	-0.2314	1.5588	-1.5599	-389.0137	0.9991
2	0.6612	1.5826	1.5769	-0.1308	0.9964
3	-0.1258	1.5620	-1.5713	6.1345	0.9910
4	2.1233	3.1889	0.0110	1.8001	0.9867

$$\underline{\theta}_f = \begin{bmatrix} 3.2e^{-4}, \ 0.2e^{-4}, \ 9e^{-4}, \ 12.1e^{-4} \end{bmatrix}^T \text{[rad]}$$

Table 5.2. Identified DH-parameters of the Philips Xper Allura FD20 - *Data-Driven*

	a [mm]	$\delta\theta$ [rad]	α [rad]	d [mm]	β [-]
1	-0.2322	1.5612	-1.5713	-389.009	0.9989
2	0.6701	1.5789	1.5822	-0.1288	0.9933
3	-0.1131	1.5703	-1.5689	6.1443	0.9931
4	2.1100	3.1912	0.0201	1.8764	0.9901

$$\underline{\theta}_f = \begin{bmatrix} 3.1e^{-4}, \ -0.4e^{-4}, \ 9.1e^{-4}, \ 12.4e^{-4} \end{bmatrix}^T \text{[rad]}$$
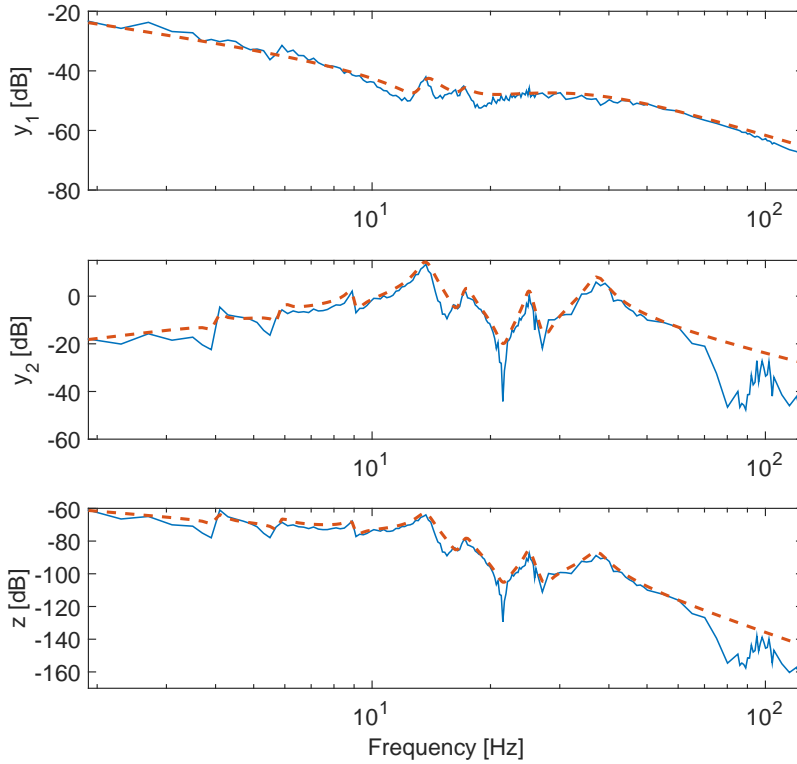
Fig. 5.5. Frequency domain representation of experimental setup: FRF (blue); parametric model (red-dashed).

the modeling structure presented in Sec. 5.4. The results of the model-based calibration approach from [102] applied on the measured data are illustrated in Table 5.1. In Table 5.2, the results of the Unscented Kalman filter approach applied on (5.37) are shown. It should be noted that the order of magnitude of the obtained DH-parameters is similar for both approaches. Note that the same initial states are obtained for both approaches. The data-driven approach however is able to estimate additional dynamical contributions, although for the currently available experimental systems these contributions are small.

In Fig. 5.6, the obtained geometric parameters using the phantom-based and the data-driven approach are shown. Since quasi-static (DH) parameter are estimated, pure acceleration measurements do not provide sufficient information. Particularly for low frequencies, acceleration sensors are subject to poor signal-to-noise ratios. For convergence of the quasi-static parameters, the phantom-

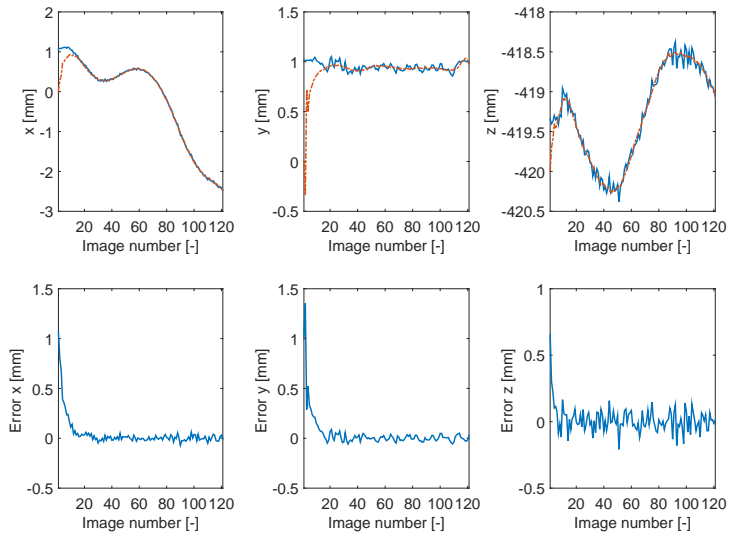**Fig. 5.6.** Calibration results including absolute (phantom) measurements: phantom-based (blue); data-driven (red-dashed).
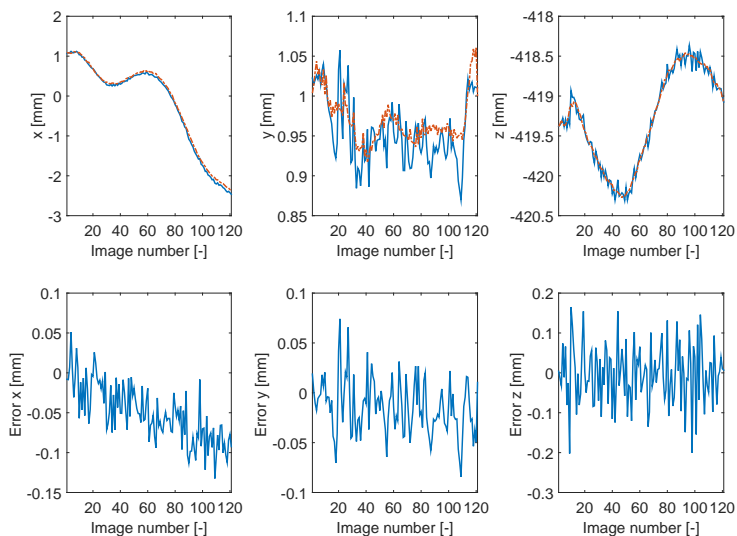

Fig. 5.7. Calibration results using accurate initial state estimations: phantom-based (blue); data-driven (red-dashed).
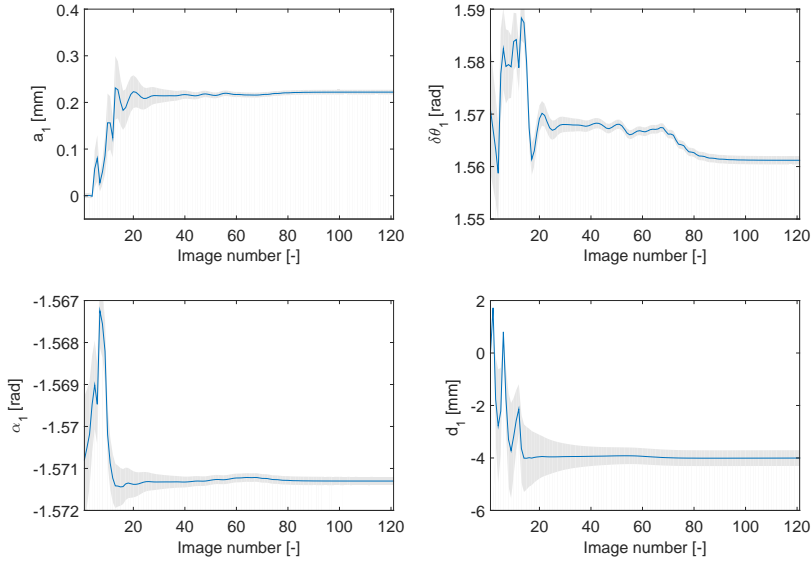
Fig. 5.8. Convergence of first four DH-parameters, indicated in Table 5.2, based on 15 consecutive measurements; mean (blue); variance (gray-shaded)

based measurements are included as additional measured output in the model (5.37), used in the observer. The images provide absolute position information, which enables the estimation of quasi-static parameters. The envisioned advantage of the proposed approach is mainly in the adaptation of the dynamical parameters, which avoids extensive experimentations to obtain parametric dynamical models with high accuracy. In sharp contrast, the identification of quasi-static parameters typically can be done using limited amounts of data as described in Chap. 2. It should be noted that after approximately 20 images the parameters are converged, see also Fig. 5.8 for the convergence of four DH-parameters indicated in Table 5.2. After the parameters are converged, the quasi-static model $M_{qs}(x_k)$ imposes a closer resemblance to the true system behavior. As a result, an improved estimation result is obtained, i.e., the geometric parameters are recovered more accurately. In Fig. 5.7, the initial states of the model are replaced with the obtained parameters in Table 5.2, and only encoder and acceleration measurements are used for estimation purposes. It should be noted that the initial estimation error is significantly smaller with respect to the results in Fig. 5.6. However, due to the use of relative measurements only, a small amount of drift can be observed.

5.6   Conclusions and recommendations

Geometric calibrations are crucial for accurate 3D reconstructions of the interior of the human body. A model-based approach to reduce required calibration times is proposed in [102] which forms the starting point for the results in this chapter. A method based on state-observers that combine measurements, e.g., encoders, acceleration sensors, and gyroscopes, with a quasi-static and dynamic model, is proposed. Due to the use of data actually measured during a scan on the patient, it is demonstrated that potentially a significant relaxation on the reproducibility condition can be obtained. In addition, it is shown that the approach can be exploited to estimate physical parameters in the models, enabling to fine-tune the parameters. Hence, slowly time-varying behavior can potentially be compensated, extending the recalibration time intervals. Typically the sample rates of the sensors are significantly higher then the imaging frame rate. Hence, an increased amount of information can be obtained, e.g., on higher frequency content.

In Sec. 5.4 dynamical models in modal form are presented that enable modeling of the system behavior. However, the proposed approach is not limited to these models. In fact, other desired modeling approach can be pursued. For the specific application on interventional X-ray systems, external flexibilities, e.g., finite stiffness in floors and ceilings on which the system is mounted, dominantly determine the quasi-static and dynamical behavior. The proposed modal form allows for an intuitive approach to obtain initial parameters on which the observer can fine-tune to obtain a global optimum.

Additional research towards improved convergence properties for the static parameters and robustness of the proposed approach is required before clinical implementations become feasible. Also, the method has the potential to compensate for non-reproducible behavior due to the use of measured data during actual operation. Although more tuning freedom is obtained by the introducing of additional states describing model parameters, experimental validation on a non-reproducible system is required.

Computational power is generally not a problem since for geometric calibration purposes the estimations are not required to be available in real-time. However, if the estimations are required for feedback purposes, deterministic observers, see, e.g., [127], can be used. For enhanced accuracy and for systems with strongly nonlinear behavior, e.g., discontinuities, particle filters [110, Chap. 9] might prove to be useful at the cost of a higher required computational power.

Chapter 6

Image-Based Measurements for Geometric Calibration

Geometric calibrations of medical imaging systems are crucial to allow for advanced (X-ray) imaging techniques. Developments in medical procedures, lightweight system design and the growing costs of health-care, lead to the desire for simpler and faster calibration approaches. The aim of this chapter is to present a novel measurement approach to enhance system calibrations for a wide range of imaging applications. The method is based on the introduction of small markers within the projection line-of-sight, by virtue of a minimal mechanical adjustment to the system. By detecting markers in the X-ray images, displacements between the systems' X-ray detector and source are in situ measured. Additionally, the approach can be used in combination with model-based and data-driven calibration approaches.

6.1   Introduction

Developments in the medical society increasingly rely on high-quality images of the interior of the human body. Minimal invasive surgeries aim at minimal collateral damage during surgery, leading to less postoperative complications and faster patient recovery times. Accurate imaging applications, e.g., high-quality three-dimensional rotational angiography (3DRA), computed tomography (CT) [5], [8], and three-dimensional (3D) roadmapping techniques [7], are critical for minimal invasive surgeries. Also, the reduction of the required X-ray and contrast fluid dose is beneficial for both the patient as well as the attending medical staff.

Interventional X-ray systems are widely applied for minimal invasive surgeries. Due to the open-kinematic structure [18], similar to robotic systems, these systems allow for easy access to the patient by the medical staff, while the system is in position to acquire images. In contrast to closed-kinematic structures, e.g., traditional CT and MRI systems, the system is relatively sensitive to external disturbances, mechanical imperfections, and inherent flexibilities. As a result, the image acquisition components, i.e., the X-ray detector and assumed point-source, do not follow the ideally described semi-circular trajectory. To avoid severe artifacts in the obtained reconstructions, deviations on the ideal trajectory imposed by the system are compensated in the reconstruction algorithm [4], which is referred to as geometric calibration [10], [21]. Hence, an ideal geometric calibration describes, for each acquired two-dimensional (2D) projection, all degrees-of-freedom (dof) of the cone-beam.

Currently available C-arc systems are typically highly reproducible, enabling an off-line calibration procedure which has to be repeated twice a year in clinical environments [128]. Typical approaches presented in literature are based on a scan of a calibration phantom of known geometry [10], [25], [19], and [40]. Various procedures are presented that enable a reduction of the number of estimated calibration parameters, see, e.g., [129] where specific degrees of freedom are neglected without significant influences on the obtained imaging qualities. Since movements of the X-ray source with respect to the detector only lead to second-order effects on the errors, a widely used assumption is that the X-ray source is fixed relative to the detector, see [102] and Sec. 2.2.2. For the current generation of X-ray systems, this assumption leads to relatively small estimation errors in the calibration parameters, i.e., a small degradation of the reconstruction quality or overlay errors. However, the numerical conditioning of the geometric calibration problem is improved leading to more reliable solutions.

The need for faster, more accurate in terms of positioning of the image acquisition components, and cheaper systems leads to lightweight system design. Due to changing ratios between inherently limited system flexibilities and masses, dynamical resonances change to lower frequencies as a result of typically decreased mechanical stiffness. For a decreased stiffness, the amplitude of the

second-order effects increases such that the influence of the neglected parameters becomes visible to the human eye in the acquired 3D reconstruction. Furthermore, the reproducibility condition required for the phantom-based geometric calibrations imposes a direct limitation on the mechanical design. Research towards online calibration approaches, i.e., performed during normal operation in a clinical environment, is often based on markers included in the patient table [26], leading to possible occlusions of relevant parts of the anatomy. More advanced approaches based on optimization of 3D reconstructions are presented in [29], [27]. Clinical results show that these approaches are sensitive to patient movements.

Model-based and data-driven calibration approaches, as proposed in Chapters 2 and 5 respectively, exploit models of the mechanics of the system in combination with available measurements, e.g., encoder signals and acceleration sensors. By using measured data from the actual performed motion, the reproducibility condition can be relaxed.

Although the model-based and data-driven approaches show promising results, the information contained within the obtained images is not fully exploited. The aim of this chapter is to present a novel measurement approach that enables a direct measurement of the relative displacements between the X-ray detector and source. In contrast to [26], where fixed markers are placed at the patient table, it is proposed to fix the markers at a predefined position with respect to the X-ray source. Thereby, it is guaranteed that the markers are never visible in the region of interest, e.g., small detection points at the edges of acquired images. The main contributions in this chapter are:

1. a novel measurement approach, based on online acquired X-ray images, enabling a measurement of the X-ray source position with respect to the detector for the low frequency region, and

2. a framework relating the image-based measurements to the data-driven approach as presented in Chap. 5.

Besides application for 3D reconstructions, the approach can also be exploited for static and 3D roadmapping applications. Errors introduced by a rotation of the detector, e.g., from portrait to landscape mode, are measured directly by the in this chapter proposed approach, which can directly be used for (overlay) calibration. Moreover, some restriction on the design of next-generation X-ray systems, particularly the rigid connection between the X-ray detector and source, are relaxed.

This chapter is structured as follows. In Sec. 6.2 the problem description and proposed approach are presented. In Sec. 6.3 some fundamentals are presented that are required for accurate marker detection within (X-ray) images. Possible (future) applications of the method are presented in Sec. 6.4, followed by experimental results based on a real X-ray system in Sec. 6.5. This chapter concludes

in Sec. 6.6 with conclusions and recommendations on future use of the proposed measurement approach.

6.2 Problem description and proposed approach

6.2.1 Problem statement

In the previous chapters, a model-based and a data-driven approach are proposed to obtain the geometric parameters defined in Sec. 2.2. By introducing additional sensors, e.g., accelerometers or gyroscopes, close to the X-ray detector and tube, information is available on the system behavior close to the performance locations, i.e., the image acquisition components. Since 3D reconstructions are based on a mapping of multiple 2D images, an intuitive choice would be to investigate whether information included within the obtained images can be used for geometric calibration purposes.

In Chap. 5 a model was introduced with the following nonlinear state-space description

$$P_0 : \quad \begin{array}{l} \dot{x} = f(x, u) \\ y = h(x, u) \end{array}, \tag{6.1}$$

where the states x are a combination of dynamical states, e.g., positions and velocities, and states describing model parameters of the dynamic and quasi-static model, see Sec. 5.2.4. Observer based approaches are used to estimate the states, followed by a (model-based) prediction of the geometric parameters, with

$$z = h_z(x, u). \tag{6.2}$$

It is well known that the excitation signals for (non)parameteric identification should be as close as possible to the true operating conditions due to nonlinear effects as presented in Chap. 3. A similar assumption holds for the proposed data-driven approach in Chap. 5. For enhanced state-estimation, measured signals should resemble the desired performance variables as close as possible to avoid propagation errors through the model.

Additional measurements can be exploited to enhance estimation qualities. Since the aim of the system is to obtain high-definition X-ray images of the object of interest, an intuitive choice is to make use of information available within the acquired images. The currently widely used phantom-based calibration approaches are a typical example of this see, e.g., [10], [11], and [39], but also approaches using markers within the line-of-sight, see also [29] and [26].

In this chapter, the objective is to enhance the model-based and data-driven approaches using images by extending the output equation in (6.1) using image-based measurements.
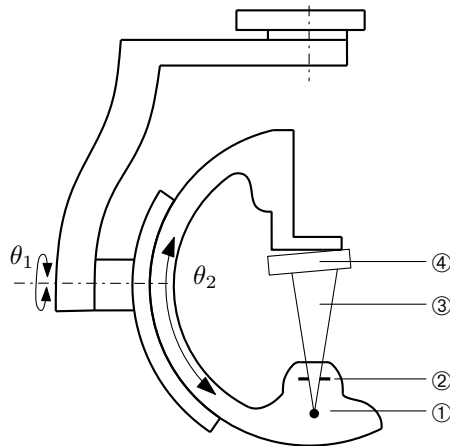
Fig. 6.1. Schematic representation of the X-ray imaging process, where ①: X-ray point source, ②: fixed marker, ③: projection beam, ④: (misaligned) X-ray detector.

6.2.2 Proposed approach

In this chapter, image-based relative displacement measurements are proposed. By introducing a mechanical marker element, i.e., a specifically designed X-ray opaque object that can be recognized in the projected 2D images, relative displacements between the X-ray source and detector are measured. In Fig. 6.1, the proposed setup is illustrated. The relative displacements between the X-ray source and detector can be used as additional geometric parameters. As introduced in Chap. 2, the relative source displacement with respect to the detector is in current approaches often neglected. In view of modern developments towards lightweight system design, the assumption that the effects of relative detector-source displacements is small, does not hold anymore. The resulting effects are at least two-fold:

1. the effect on the geometric parameters required for 3D reconstructions and 3D roadmapping overlay, see Sec. 2.2.2, will increase, leading to increased reconstruction artifacts/blur and overlay errors from 2D projections over 3D reconstructions, and

2. due to expected increasing dynamical disturbances, relative displacements become larger during the exposure time of a single X-ray image. As a result, the 2D image quality will degrade, resulting in blurred images.

Two possible cases are introduced for which the proposed measurement approach can be directly applied for (medical) imaging applications:

  I direct measurement of the relative geometric parameters, and

  II making use of detected marker points in the 2D projections as additional measurements within an observer, as introduced in Chap. 5. Hence, the output equation in (6.1) is extended.

Both cases will be presented throughout the current chapter.

6.3   Image-based marker detection

To enable accurate image-based measurements, a fundamental understanding on projective geometry is required as presented in Sec. 6.3.1. An accurate description of the projective geometry directly leads to a model that enables the estimation of the geometric parameters describing the relative detector-source displacements given an X-ray image. The design of possible markers and the detection of marker points based on line intersections is presented in sections 6.3.2 and 6.3.3.

6.3.1   Modeling approach: projective geometry

The projection of a point from 3D to 2D, i.e., the patient (3D) to a projected X-ray image (2D), is highly dependent on the image acquisition components as indicated in Fig. 6.2. An elegant framework often used to describe the projection relations is *projective geometry*, initially introduced in computer vision applications, see [104] for an extensive overview. Given a Euclidean representation of a point, e.g., $[x, \; y, \; z]$, then the point can be written in projective space $\mathbb{P}$ using so-called homogeneous coordinates by $[\lambda x, \; \lambda y, \; \lambda z, \lambda]$, where $\lambda \neq 0$ is a free scaling parameter. The extension of the Euclidean space by the parameter λ allows for linear representations of projective relations, as will be further presented throughout this section. It should be noted that the Euclidean coordinates are recovered from $\mathbb{P}$ by dividing by the last coordinate.

    The pinhole camera model is one of the simplest but widely used models to describe the projection of a 3D object on a 2D plane. In a true pinhole camera light passes through a small aperture and creates an inverted image on the image plane as indicated in Fig. 6.3a. For X-ray systems, the image is formed based on the attenuation of X-ray photons, instead of the reflection of light. An equivalent pinhole camera representation corresponding to Fig. 6.3b is required.

    The camera center, which is a well known virtual spot in projection theory, see, e.g, [104, Chap. 6], has a physical interpretation for X-ray system, namely the focal spot. The image-plane coincides with the detector plane, while the principle point, i.e., the point indicated by the central X-ray, lies typically in the center of the detection plane. A typical effect of mechanical inaccuracies, vibrations, and focal spot variations is a displacement of the principle point. In addition, the shape of the projection is varying. It should be noted that
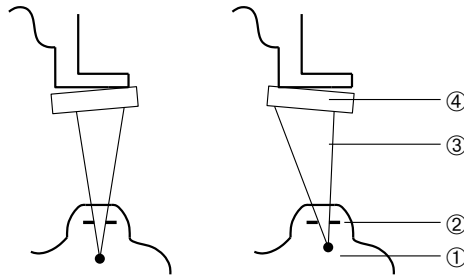
Fig. 6.2. Graphical representation of effect misalignments on projection, where ①: (misaligned) X-ray point source, ②: fixed marker, ③: projection beam, ④: (misaligned) X-ray detector.
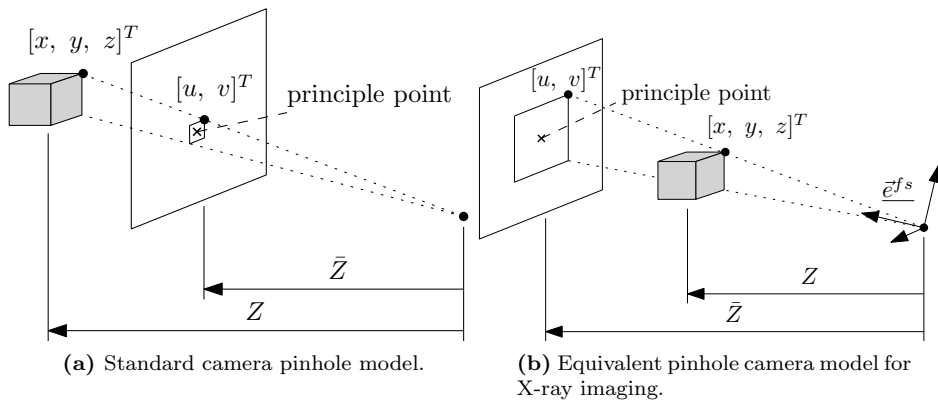

(a) Standard camera pinhole model.

(b) Equivalent pinhole camera model for X-ray imaging.

Fig. 6.3. Graphical representation of the pinhole camera model for standard cameras and X-ray imaging with $\bar{Z}$ the focal distance and Z the source-object distance.

imaging protocols also can have an effect on the principle point due to varying (dynamical) behavior of the X-ray source. The fundamental difference between normal imaging and X-ray imaging is the position of the detection plane with respect to the object of interest, leading to a magnification as a result of $\bar{Z} > Z$ in Fig. 6.3b.

An arbitrary point in 3D space within the exposure volume, expressed in a coordinate system located at the focal spot position, is described by the vector $v^{fs} = [x^{fs},\ y^{fs},\ z^{fs}]^T$. The projected point is typically described in the local detector coordinate system, where $v_p^d = [u^d,\ v^d]^T$. When an ideal situation is considered, i.e., no translational or rotational offsets of the detection plane with respect to the X-ray source, it can be derived by standard geometry that the projection of the point $[x^{fs},\ y^{fs},\ z^{fs}]^T$ is given by $[x,\ y]^T = [(x^{fs}/z^{fs})\bar{Z},\ (y^{fs}/z^{fs})\bar{Z}]^T$

with $\bar{Z}$ the focal length. By representing the same points in $\mathbb{P}$ the division, which is a nonlinear operation, is avoided,

$$\lambda \begin{bmatrix} u^d \\ v^d \\ 1 \end{bmatrix} = \begin{bmatrix} \bar{Z} & 0 & 0 & 0 \\ 0 & \bar{Z} & 0 & 0 \\ 0 & 0 & 1 & 0 \end{bmatrix} \begin{bmatrix} x^{fs} \\ y^{fs} \\ z^{fs} \\ 1 \end{bmatrix}, \tag{6.3}$$

where $[\lambda u, \ \lambda v, \ \lambda]^T$ is the projected point in homogeneous coordinates. Multiple assumptions should hold for the pinhole model to be valid [9, Sec. 4.3]:

1. the image coordinates $[u, \ v]^T$ are defined with reference to the center of the detection plane,

2. the optical center, defined as indicated in Fig. 6.3b, is projected exactly at the image center, and

3. the x and y axis of the image should be aligned with the projected x and y axis of the focal spot coordinate system.

Common extensions of the model to compensate the aforementioned effects are described in detail in, [9, Sec. 4.3], leading to the model,

$$\lambda \begin{bmatrix} u^d \\ v^d \\ 1 \end{bmatrix} = \underbrace{\begin{bmatrix} \bar{Z} & \tau & o_x + f_x & 0 \\ 0 & -\eta\bar{Z} & o_y + f_y & 0 \\ 0 & 0 & 1 & 0 \end{bmatrix}}_{P} \begin{bmatrix} x^{fs} \\ y^{fs} \\ z^{fs} \\ 1 \end{bmatrix}, \tag{6.4}$$

where τ and η define the scaling for non-square and skewed pixels, and f_x and f_y the deviations of the optical point from the center of the image. Moreover, the offsets o_x and o_y are introduced to compensate for the offset between the image center and the top left of the image in which image coordinates are usually defined. Note that o_x and o_y are based on detector specifications and usually known. Note that f_x and f_y are directly influenced by the mechanical properties of the system, e.g., relative vibrations and deformations. For the remainder of this chapter, the parameters corresponding to pure image offsets and non-square and skewed pixel sizes are neglected for clarity and not used for the presented results in this chapter.

The marker design is in detail presented in Sec. 6.3.2, however in the current section we assume that the marker includes i marker-points, i.e., recognizable elements within the projection. The marker-points are indicated by the known and static vectors $v_i^m = [x_i^m, \ y_i^m, \ z_i^m]^T, \ \forall i = 1, \ 2, \ \ldots, \ n_m$ for n_m the number of markers-points, and the superscript m indicates the local marker coordinate system.
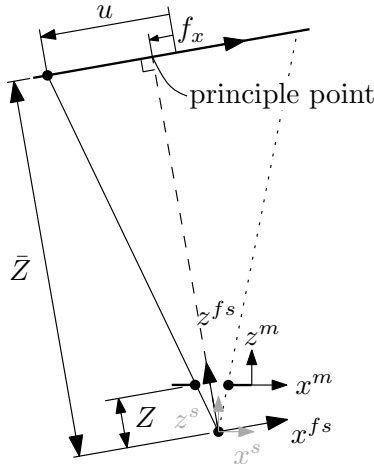
Fig. 6.4. Graphical illustration of marker projection.

The marker is placed at a known position with respect to the X-ray source as indicated in Fig. 6.4. The location of the marker-points in the source coordinate system, indicated by the superscript s, can be computed according to

$$\begin{bmatrix} v_i^s \\ 1 \end{bmatrix} = \begin{bmatrix} R & T \\ 0_3^T & 1 \end{bmatrix} \begin{bmatrix} v_i^m \\ 1 \end{bmatrix} = H_m^s \begin{bmatrix} v_i^m \\ 1 \end{bmatrix}, \tag{6.5}$$

where R is a 3×3 rotation matrix, see, e.g., [12] and Chap. 2. The vector T of dimensions 3×1 describes the translations and 0_3 is column of zeros of dimensions 3×1. A fundamental assumption for the validity of the pinhole camera model is the alignment of the coordinate system located at the focal spot with the detector coordinate system. Hence, an additional rotation is introduced, describing the angular alignment, i.e., pure rotation of the source coordinate system s to the coordinate system fs,

$$\begin{bmatrix} v_i^{fs} \\ 1 \end{bmatrix} = \begin{bmatrix} R(\theta_x, \theta_y, \theta_z) & 0_3 \\ 0_3^T & 1 \end{bmatrix} \begin{bmatrix} v_i^s \\ 1 \end{bmatrix} = H_s^{fs} \begin{bmatrix} v_i^s \\ 1 \end{bmatrix}, \tag{6.6}$$

where the angles θ_x, θ_y, and θ_z are typically unknown. The projected marker points on the detector are given by the projection matrix in (6.4), for each marker point i,

$$\lambda \begin{bmatrix} u_i^d \\ v_i^d \\ 1 \end{bmatrix} = P(\bar{Z}, f_x, f_y) \begin{bmatrix} v_i^{fs} \\ 1 \end{bmatrix}. \tag{6.7}$$

The total projection from the marker-points defined in the marker coordinate

system is given by

$$\begin{bmatrix} u_i \\ v_i \end{bmatrix} = \frac{1}{\lambda} P(\bar{Z}, f_x, f_y) H_s^{fs}(\theta_x, \theta_y, \theta_z) H_m^s \begin{bmatrix} x_i^m + \delta x^m \\ y_i^m + \delta y^m \\ 0 \end{bmatrix}, \qquad (6.8)$$

which can be described as set of typically non-convex nonlinear functions,

$$\begin{bmatrix} u_i \\ v_i \\ 1 \end{bmatrix} = h_I(\bar{Z}, f_x, f_y, \theta_x, \theta_y, \theta_z, \delta x^m, \delta y^m) \qquad (6.9)$$

where additional offsets δx^m and δy^m are introduced to describe imperfections in the marker placement. Given the measurement of a marker point, a nonlinear solver is required to estimate the unknown parameters. By increasing the number of marker-points, nonlinear least-squares approaches can be exploited to average the effects of noise.

Finally, it should be noted that the parameters f_x, f_y, and $\bar{Z}$ directly relate to the geometric parameters describing the relative detector-source displacement, as in detail presented in Sec. 2.2.1.

6.3.2   Marker design

Many constraints are imposed on marker designs for the use in X-ray applications. The marker should be made of a material which is X-ray opaque such that sufficient contrast is visible at the detector with respect to the anatomy of interest. Hence, the chosen material should have an high attenuation coefficient. Also, since the aim is to use the approach for online measurements, the marker should not compromise the region of interest, i.e., no occlusions of possible relevant tissue or anatomy may occur.

In order to contribute to geometric calibrations, the image-based measurement should provide measurements that have an accuracy of the order of magnitude of 0.1mm, however, this is highly depending on the type of imaging applications, e.g., the scan velocity and the image resolution which is directly correlated to the imaging frame rate. In order to achieve the desired measurement accuracy, subpixel accuracy is required due to scaling effects [14], e.g., if the X-ray source is moving away from the detector, the marker shift within the image is given by $\Delta u^d, v^d = \tan(\alpha)\Delta z$, with α the fan angle (angle of the cone-beam) [39].

Moreover, the placement of the marker with respect to the X-ray source heavily determines the measurement accuracy. Placement of the marker close to the X-ray source guarantees relatively large displacements of (the projection of) the markers in the detection plane. Although this is desired to achieve subpixel accuracy, X-ray specific (stochastic) disturbances heavily influence the quality of the projection. The dominant terms leading to artifacts and blurring effects are

due to X-ray scattering, Poisson noise due to the conversion of X-ray photons to detectable light within the scintillator layer of the detector, and blurring effects due to the fact that the X-ray source is in practice not a perfect point source [14]. As a result, the projection image of the markers is less disturbed when the marker is positioned close to the detector. Hence, a tradeoff between measurement accuracy and image degradations is inevitable.

The accuracy of the measurement of a single marker-point is limited by the spatial resolution of the system [5], [14, Chap. 6]. The latter being dependent on, but not limited to, the actual size of the focal spot, the source-to-image distance, used scintillator material, and the pixel pitch. It is well known that the accuracy of a measurement can be improved by multiple independent measurements [130]. By using multiple marker-points, distributed over the acquired image, an accurate relative displacement can be computed by averaging, resulting in a variance that decreases with the number of marker-points.

Two markers designs are proposed in this section. First an experimental marker that distributes marker-points on a rectilinear grid over the full image, which is an X-ray equivalent of a *checkerboard* that is often used in vision applications [104], to illustrate the potential of the approach. Second, a marker that can be used in a clinical environment is introduced, i.e., a marker with minimal disturbance to the visualization of the patients anatomy.

Experimental marker

In Fig. 6.5, the design of an experimental marker is shown. Homogeneous transformations as introduced in Sec. 6.3.1 enable the preservation of certain properties, e.g., collinearity (a line remains a line after any homogeneous transformation), intersections, and tangency [104]. These properties are exploited within the marker design. The actual marker-points are defined as the intersections of lines as indicated in Fig. 6.5.

Edges are characterized in an X-ray image by a rapid variation of the measured intensity over a limited amount of pixels. When a pixel line perpendicular to the expected edge is evaluated, it is difficult to obtain an unbiased estimation of the exact location of this "step" in measured intensity for images subject to significant noise and blur effects.

In Fig. 6.6, an photo and acquired X-ray representation of the proposed marker are depicted. The marker is produced by etching lines in a 2mm thick stainless steel alloy. The disturbing effects due to the placement close to the X-ray source are clearly visible in Fig. 6.6b. In Fig. 6.6a it can be seen that the lines are approximately symmetric in the physical marker, which is not the case for the projected X-ray image. Moreover, clear intensity variations are visible over the areas with a homogeneous material thickness and the projection is asymmetric. A typical property of X-ray scatter is that the disturbances are significantly higher around edges [70].
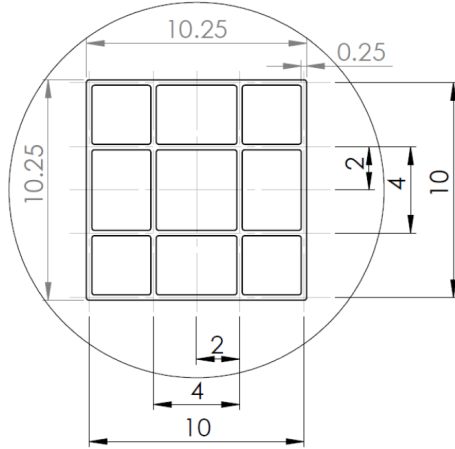
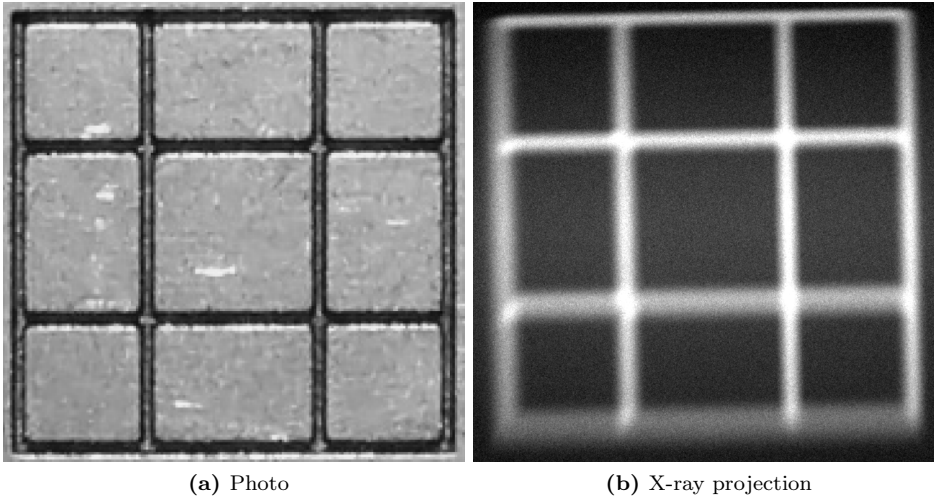**Fig. 6.5.** Design experimental marker; all units are in mm.

(a) Photo　　　　　　　　**(b)** X-ray projection

Fig. 6.6. A photographic and X-ray representation of the proposed experimental marker.
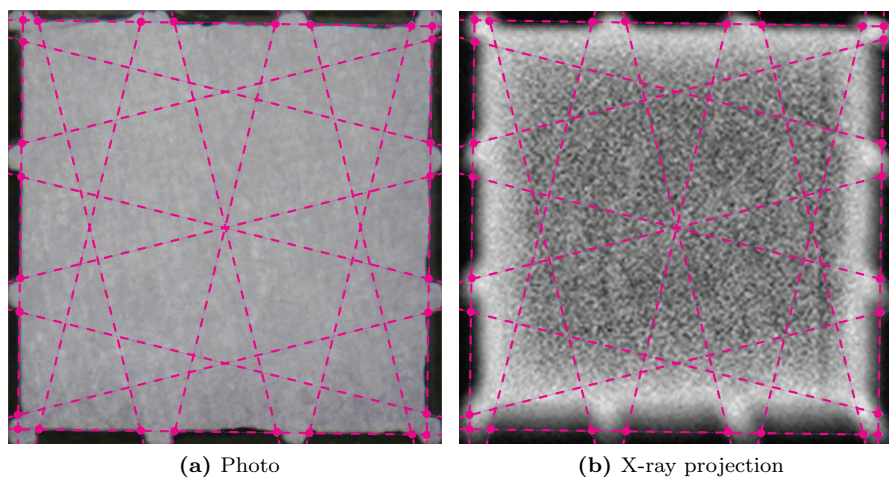
(a) Photo **(b)** X-ray projection

Fig. 6.7. A photographic and X-ray representation of the proposed clinical marker.

Design for clinical use

An alternative design, well suited for clinical usage, is depicted in Fig. 6.7. Again, the design is based on lines, where the intersections are defined as marker-points. The center of the marker is open, such that no occlusions of anatomy occur.

A photographic representation and an X-ray projection of the designed marker are given in Fig. 6.7 where again the X-ray image is significantly disturbed by scatter and noise effects. Inaccuracies in the production process of the marker, visible in 6.7a, however are hardly visible in 6.7b.

Due to imperfections in the detector and an increased effect of scatter at the edges of the detection plane, accurate estimations based on the clinical design are significantly more challenging, which is presented in more detail in the following sections.

6.3.3   Image processing: line and point detection

The fundamental step in the accurate estimation of 2D marker-points is the detection approach. Standard edge detection algorithms are characterized by the detection of the location of a discontinuity (step) in the measured intensity function (pixel values) of an image. In general, edge detection algorithms are based on the computation of local maxima in the gradient of the pixel values. Specific applications require the use of additional zero-crossings of the Laplacian, which is a second-order differential operator, see, e.g., [131] for an overview.

Edge estimation for X-ray images has additional challenges, mainly due to

the asymmetry within the projections and the effects of scatter. In the remainder of this section, three consecutive steps are presented that enable accurate automated detection of lines within the marker designs introduced in Sec. 6.3.2.

Prefiltering

The Canny edge detector, as introduced in [132], is a computationally cheap and widely used edge detector [131]. The Canny edge detector uses a convolution filter, shaped as the derivative of a Gaussian, which is optimal in the sense that it simultaneously maximizes the signal-to-noise ratio around the edge locations and minimizes the distance between the peak and the true edge [5] for Gaussian noise distributions. Although the edge preserving qualities of the Canny edge detector are desired, the presence of Poisson noise and salt-and-pepper noise (random pixel variations), [5, Sec. 5.2], and X-ray scatter degrades the performance significantly. Other edge detection algorithms are available, see, e.g., [131] and [5] for an overview. However, only for the Canny edge detector optimality in terms of edge preservation in the case of pure Gaussian noise is proven [132].

In X-ray images, the effects of X-ray scatter, Poisson, and salt-and-pepper noises can not be neglected. A typically used approach to deal with these random pixel variations in imaging applications is the use of mean or median filters, see, e.g., [5, Sec. 5.3] or morphological filters [36], [5, Chap. 9]. Mean filters replace the evaluated pixel value for the weighted average of the neighborhood of a pixel. In contrast, median filters do not compute averages but rank the values in the neighborhood of the pixel from low to high and select the median to be the new pixel value [133]. Median filters are popular in X-ray imaging applications for the excellent noise-reduction capabilities with considerably less blurring than linear smoothing filters [5, Sec. 5.3.2]. As a result, these filters have better edge preservation capabilities, which is important for the desired edge detection of the marker. The hybrid median filter (HMF), is a nonlinear filter that computes three median values based on multiple directions, i.e., a horizontal pixel line, a vertical pixel line, and a diagonal pixel line [134], [135], resulting in reduced blurring effects with respect to traditional median filters. Therefore, the HMF is used for this application. The kernel size, i.e., the evaluated pixel range, is a tuning parameter and highly depends on the amount of scatter, and the (projected) shape of the marker.

After pre-filtering the images with an HMF, the Canny edge detector can be exploited to obtain initial estimations of the edges, resulting in Fig. 6.8a. It should be noted that especially around the line intersections the corners are considerably rounded. Moreover, some residual detected edges are visible, that actually do not correspond to true edges. Hence, the true pixels corresponding to edges of the marker are detected using the linear Hough transform.
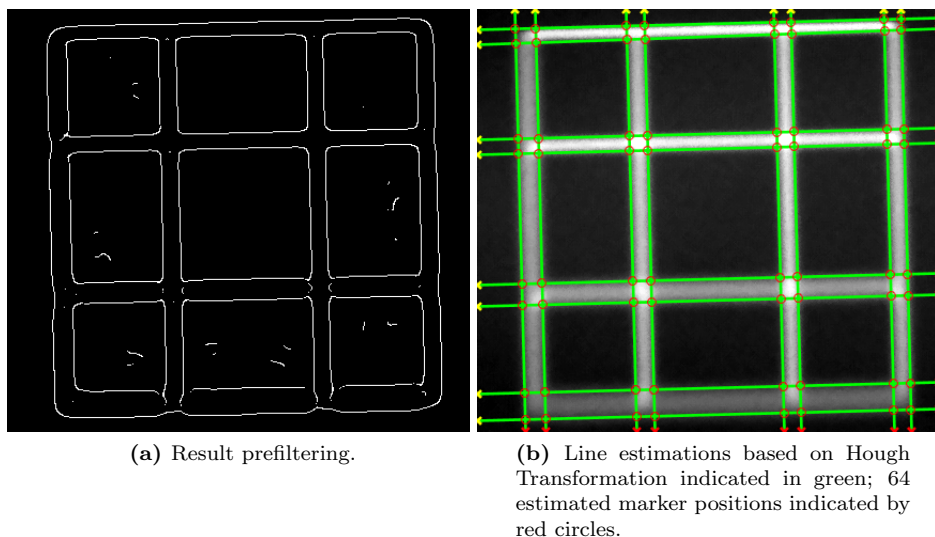
(a) Result prefiltering.

(b) Line estimations based on Hough Transformation indicated in green; 64 estimated marker positions indicated by red circles.

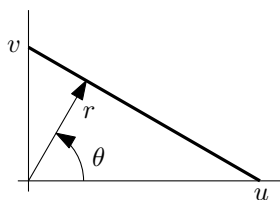**Fig. 6.8.** Initial estimation results.

Fig. 6.9. Graphical representation of line parametrization in (6.10).

Linear Hough transform

The Hough transform allows for a grouping of detected edge points, i.e., high pixel values in Fig. 6.8a, into relatively simple objects as lines, circles or ellipsoids [5, Sec. 10.2]. Since we are looking for straight lines within the projected marker image, which can be horzontal or vertical, a line parameterization is given by

$$r = u\cos(\theta) + v\sin(\theta), \tag{6.10}$$

where as a function of the image coordinates (u, v) the parameter r defines the shortest distance from the origin, $(u, v) = (0, 0)$, to the straight line, and θ is the angle between the x-axis and the line defined by r, as indicated in Fig. 6.9. It can be noted that there is a close resemblance between the Hough transform and the Radon transform introduced in Chap. 2, [136].
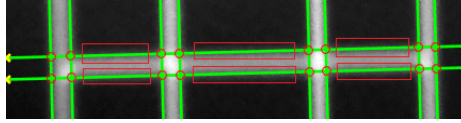
Fig. 6.10. Definition of local area used for least-squares estimation.

For each evaluated point within the image, the parameters (r, θ) which are on a discrete grid are found that correspond to the maximum number crossings with high intensity points, i.e., detected edges. By accumulating all parameters (r, θ) that corresponds to the highest number of crossings with detected edges, the parameters with the highest probability of corresponding to a true straight edge are selected. In Fig. 6.8b the resulting estimations based on the detected edges in Fig. 6.8a are shown. Based on these results, initial estimations can be made of the marker points, indicated by the circles.

Although the initial estimation describes the general shape of the marker, the desired estimation accuracy of the marker-points is not obtained yet. Due to the discrete nature of the Hough transform, only a limited accuracy can be achieved. Therefore, based on the initial estimations, a final estimation step based on a least-squares problem is proposed.

Least-Squares estimation

Based on the initial marker point estimations and *a priori* knowledge about the design of the marker, a local area is defined where the results of the Canny edge detection are considered reliable. X-ray scatter has the property to lead to increased disturbances at edges [14], leading to the rounding effects around the line intersections. By defining a relatively small area based on the estimated line based on the Hough transform and with a sufficiently large distance from the estimated marker points as indicated in Fig. 6.10, inaccurate edge estimations are excluded. By selecting only detected edges corresponding to a single line, a least-squares problem can be defined based on,

$$y_i = \begin{bmatrix} x_i & 1 \end{bmatrix} \begin{bmatrix} a \\ b \end{bmatrix}, \tag{6.11}$$

where the parameters a and b are unknown.

In Fig. 6.11 the resulting estimations for the lines and marker-points are shown. It can be seen that the estimated lines and marker-points have an improved accuracy over the results in Fig. 6.8b. Based on the obtained coordinates $[u_i, \ v_i]^T$ describing the location of marker-point i in the image, corresponding to the output of the nonlinear model (6.9) in Sec. 6.3.1. Note that similar results can be obtained for the clinical marker design, based on the straight lines indicated in Fig. 6.7.
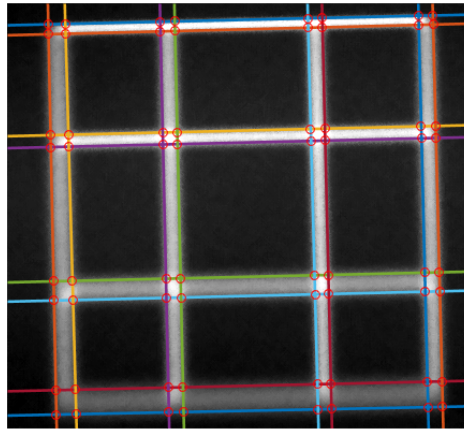
Fig. 6.11. Final result of marker point detection based on least-squares estimations

The similar approach can be applied on the clinical marker. Application of the estimated marker-points for medical imaging purposes are presented in the following section.

6.4   Application for medical imaging

The image-based measurement approach uses a marker mounted at a fixed location with respect to the X-ray source. Two possible approaches are proposed for direct application for geometric calibrations for both 3D reconstructions as well as 3D roadmapping applications.

6.4.1   Case I: direct measurement of geometric parameters

Given the nonlinear function (6.9), and the measurement of all marker-points, a nonlinear least-squares estimation problem has been formulated. The problem can be solved based on relatively simple Gauss-Newton iterations, as described in Sec. 2.3.4, however any other approach can be pursued. When the rotational errors are assumed small and can be neglected, the problem in (6.8), which is nonlinear in the unknown parameters, becomes linear in the parameters. Hence, linear least-squares approaches can be exploited from which preliminary results are available in [105].

As presented in Chap. 2, the existing approaches allow for the estimation of six out of nine parameters, where the relative displacement of the X-ray detector with respect to the X-ray source typically is neglected. The proposed measurement approach in this section provides a direct estimation of the true relative displacements. Therefore, by virtue of a minimal mechanical change, i.e., the addition of a small marker, the proposed approach has the potential to lead to enhanced reconstruction qualities. Since the currently used phantom-based calibration approaches typically are biased due to the reduced number of estimated geometric parameters, additional compensations are required in the parameter estimation process before the marker-based approach is clinically feasible.

6.4.2   Case II: proposed image-based observer

In Chap. 5, a data-driven calibration approach is proposed. Based on measurements using, e.g., encoders, accelerometers, and gyroscopes, in combination with accurate models, predictions can be obtained from the actual scan trajectories, i.e., the geometric parameters. By extending the measurements with the resulting equation in (6.8), i.e.,

$$\hat{P}: \quad \begin{bmatrix} \dot{x} \\ y \\ u_i \\ v_i \end{bmatrix} \begin{aligned} &= f(x,u) \\ &= \begin{bmatrix} h(x,u) \\ h_I(x) \end{bmatrix}. \end{aligned} \tag{6.12}$$

leading to increased measurements for the observer. The state vector x should in this case either be extended such that the additional geometric parameters are included, or the geometric parameters describing the relative X-ray detector and source displacement should be written as a combination of the model states. A typical example is the approach where additional sensors are located at both at the X-ray detector as well as the source. Independent model-based or data-driven estimations of the position can be used to describe the full nine geometric parameters. However, by introducing the additional image-based measurements, a relation between the independent models is obtained.

6.4.3   Alternative applications

The assumption that the X-ray source is located at a fixed position is widely used in medical X-ray applications. In practice however, this is not completely true due to, e.g., mechanical imperfections and heating of the filament. By activating the exposure while keeping the system at a fixed position, the source displacement can be characterized, which is an important system specification.

The accuracy of alternative geometric calibration approaches where the patient, or markers placed on the patient, are used as reference, see, e.g., [29]
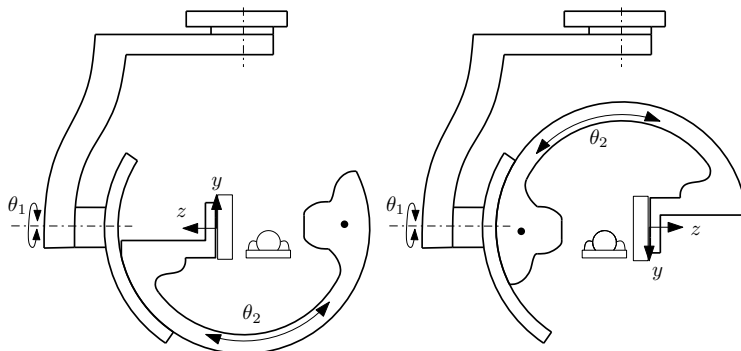
Fig. 6.12. Schematic representation of roll-scan where $\theta_2 \in [-90, \ 90]$ degrees, $\theta_1 = 0$.

and [27], degrades rapidly as a function of patient movements. The accuracy of the approach proposed in this chapter is not influenced by patient motion. However, when patient measurements are performed using the clinical marker as presented in Sec. 6.3.2, accurate detection of lines becomes more involved due to additional random disturbances introduced by, e.g., the patients anatomy, the patient table, and possibly surgical tools. Modern developments in computer vision and image processing techniques shown promising results and potentially feasible improvements of the proposed filtering approaches in this chapter, see, e.g., [5] and [9] for an overview of state-of-the-art techniques.

6.5 Experimental results

First, the relative displacements between the X-ray detector and source are measured for a standard roll-scan as indicated in Fig. 6.12. The results are shown for the x, y, and z displacement in Fig. 6.13. Since only relative measurements are performed, a reference position should be chosen, which is chosen to be the first image of the scan. The displacement during the scan in x-direction is relatively small, since this is the axis of rotation as illustrated in Fig. 6.12. The asymmetry in the y and z directions can be explained by the considerable difference in mass between the X-ray detector and source.

Note that all measurements are expressed in a local coordinate system, fixed at the center of the detector. Therefore, for an ideal system without mechanical imperfections and compliance, all values are expected to be zero during the full scan. The maximum variation can be observed in the y-direction, which is approximately 4mm. The variance on the estimations has a maximum value of approximately 0.1mm, which is in the same order of magnitude of the specifications.
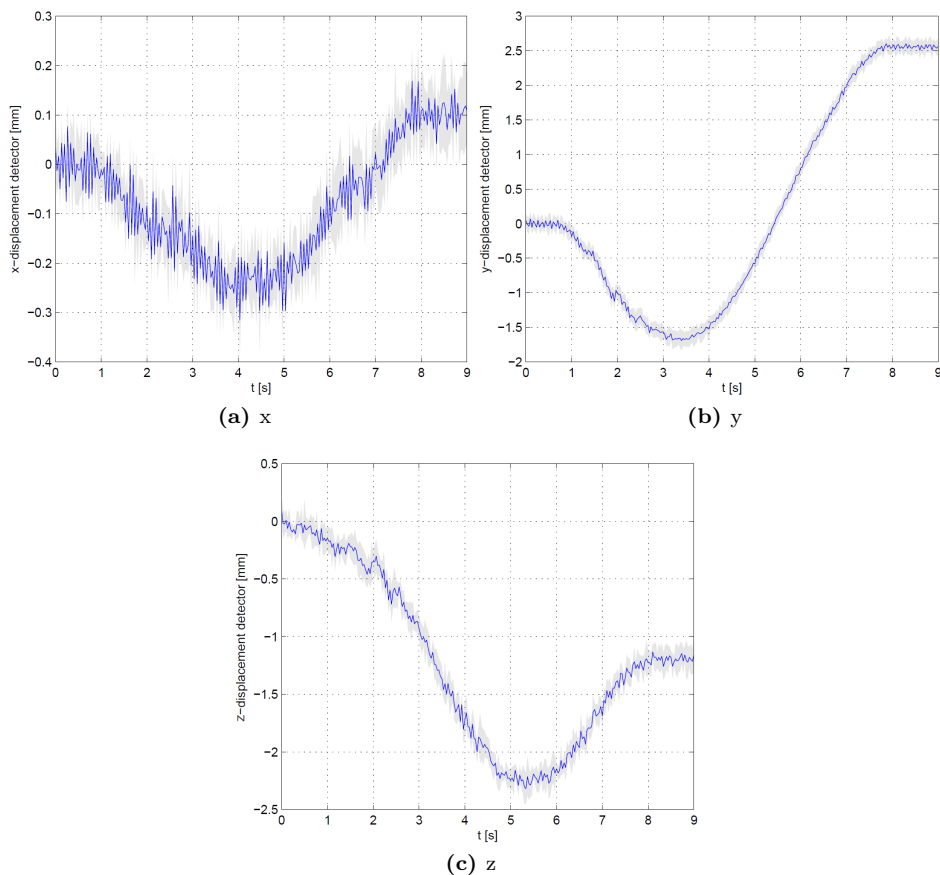
(a) x

(b) y

(c) z

Fig. 6.13. Estimation results geometric parameters for a roll scan with a maximum velocity of 30 deg/s; average over 10 consecutive scans (blue); variance (gray area).

In Fig. 6.14, the results for a propeller-scan, i.e., $\theta_1 \in [-120, 120]$ degrees and $\theta_2 = 0$, are shown for two velocities. Again the first image is used as reference for the following measurements. Since the system mechanics are symmetric over the propeller angle, the resulting measurements are also symmetric. For the high-speed scan, which requires higher accelerations, an overshoot is clearly visible.

Finally, in Fig. 6.15 the displacement of the focal spot (FS), defined as the virtual spot where the X-ray originates within the tube, as a function of time is shown. By keeping the system in a static position while projecting images, the only introduced variable is heating of the filament. The exposure time during a
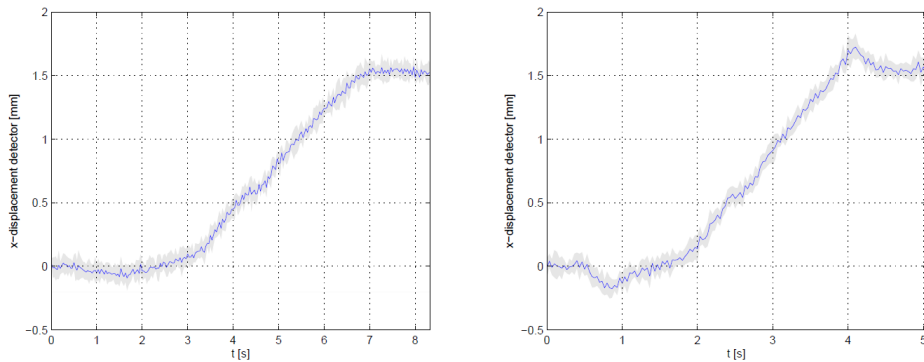
Fig. 6.14. Estimated displacement in the y direction of the detector for a propeller scan, i.e., $\theta_1 \in [-120, \ 120]$ degrees, $\theta_2 = 0$; result for a slow scan of 30 deg/s (left); result for a high-speed scan of 55 deg/s (right). The gray area indicates the variance based on ten repetitions.
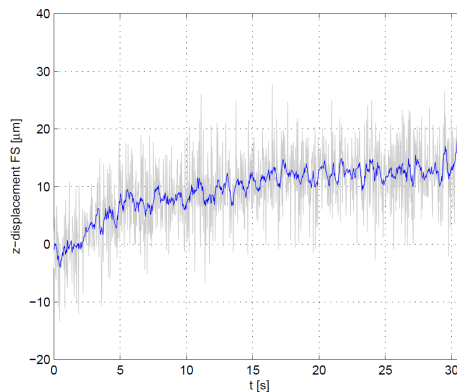
Fig. 6.15. Displacement of the focal spot (FS) in the z-direction

typical reconstruction scan is in the order of magnitude of 4 to 8 seconds, which leads to a variation of approximately $10\mu m$, however, with a significant variance. By computing the discrete Fourier transformation of the measured signal, periodicities can be identified which correspond to the rotational frequency of the source.

6.6 Conclusions and recommendations

A novel measurement approach is presented in this chapter, allowing for direct measurements between the X-ray detector and source. The approach is directly

based on obtained X-ray images and makes use of a relatively small mechanical modification of the system, i.e., the placement of a small mechanical marker. Two experimental marker designs are proposed; an experimental marker which is used to obtain the results in this chapter and a marker for clinical use which does not compromise the region of interest within the X-ray projection. By detecting multiple markers in the X-ray projection, varying disturbances over the full image, e.g., asymmetry, blur, and noises, are averaged.

Based on projective geometry, the projection of marker elements is modeled, leading to a direct relation between a subset of the geometric parameters presented in Chap. 2 and the projected marker elements. The potential of the measurements is shown based on experiments on a real X-ray system.

Although the approach seems promising and the desired estimation accuracies are achieved, various aspects required further investigation. First, the placement of the marker with respect to the X-ray source highly influences the acquired image quality, i.e., when the marker is placed close to the X-ray source accurate measurements can be obtained as a result of the magnification factor of the cone-beam at the cost of increased blur effects. Investigation towards an optimal tradeoff between increased blur and measurement accuracy might lead to improved results.

Second, the results in this work are based on a nonlinear least-squares solution of the problem as described in 6.4.1. The approach proposed in Sec. 6.4.2 requires implementation and validation.

Third, preliminary results with a clinical marker are presented in [105]. Due to X-ray scatter and increased nonlinearities of the detector near the edges of the detection surface, the image quality is degraded near the edges. As a result, further investigation is required towards clinical implementations, i.e., the mechanical marker design and advanced image processing approaches. Also, the effects of objects, e.g., a patient or surgical tools, within the line-of-sight should be investigated in more detail.

Chapter 7

Vibration Reduction Using Time-Delay Filtering

The focus of this chapter is on the development of time-delay filters to accomplish tracking of periodic signals with zero phase errors. The class of problems addressed include systems whose dynamics are characterized by lightly damped modes. A general approach for the zero phase tracking of periodic inputs is presented followed by an illustration of single harmonic tracking of under-damped second order systems with relative degree two. A general formulation of the approach is then posed for higher-order-systems and systems including zeros. The chapter concludes with the illustration of enforcing constraints to desensitize the time-delay filter to uncertainties in the location of the poles of the system and forcing frequencies. A numerical practical design case based on a medical X-ray system is used to illustrate the potential of the proposed technique.

7.1 Introduction

Modern trends in mechatronic positioning systems require faster movements and increased accuracy. Lightweight system design is motivated by the desire to achieve higher accelerations, but this is at the cost of a shift of flexible dynamical behavior to a lower frequency region. Dealing with the imposed contradiction between increased accuracy, faster movements and inherent dynamical behavior requires advanced control strategies.

To prevent motion induced residual vibrations, many control strategies are available. High performance feedback control [51], repetitive control [137] or adaptive feedback control [138] are always limited by past measurements. Feedforward based techniques, such as iterative learning control (ILC), do not suffer from the limitations imposed by feedback. However the complexity of the approaches increases significantly when robustness for, e.g., initial conditions or trajectory variations is required. When there is no direct measurement at the performance position that can be used for feedback or ILC, model-based approaches are required such as inferential control [139] or inferential ILC [140]. Input shaping or time-delay filtering (TDF) is a (practical) well established approach to reduce the dynamical effects of (lightly-damped) poles of the system by shaping the reference signal [141,142]. The approach is particularly attractive due to the ease of implementation. Most applications of TDF consider systems with point-to-point motion [143–145], with additional modifications proposed in literature such as desensitizations for model parameter variations [146] and effects of zeros in the plant [147].

In this chapter, a design approach for time-delay filters applied to systems subject to periodic motions is introduced. An example of a high-performance system subject to periodic motions is an medical X-ray system. Decreasing the residual vibrations during periodic scan motions of interventional X-ray systems directly leads to improved 3D reconstruction and/or imaging qualities [39]. Alternative applications can be found among others in periodic scan motions of wafer stages [143], printing tasks [140], repetitive robotic tasks [148] or raster grid searches of atomic force microscopes [149]. Pre-filtering of reference signals has no feedback related limitations, is easy to implement and leads to significant performance improvements.

The main contribution in this work is a harmonic time-delay filter (hTDF) design approach for systems subject to periodic motions. Additional contributions are 1) the generalization for higher-order systems and 2) a desensitization for uncertainties in model parameters as well as forcing frequency variations.

This chapter is structured as follows, first the basic design approach is illustrated in Sec. 7.2, which includes a closed form solution for a second order system and a numerical approach reducing the computational load for higher-order-systems. Extensions for systems with (non-minimum phase) zeros, systems with real-valued poles, e.g., first-order systems, desensitizations for modelling errors,
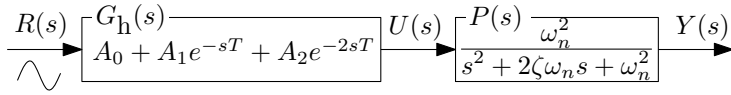
Fig. 7.1. Time-delay controlled open-loop structure of a second-order system

and non-differentiable signals are provided in Sec. 7.3. A numerical example, based on a medical X-ray system, illustrating the potential of the proposed design approach is presented in Sec. 7.4. Finally, the work is concluded with a summary and conclusions in Sec. 7.5.

7.2 Time-delay filtering for periodic movements

To illustrate the proposed design approach for time-delay filters that enable zero-phase tracking of a periodic signal, the general idea of the approach is presented in Sec. 7.2.1. Closed-form solutions are available for second-order systems and a motivating example is provided. A generalized approach for higher-order systems is described in Sec. 7.2.2. A design approach for higher-order systems, avoiding nonlinear non-convex optimizations, is provided in Sec. 7.2.3.

7.2.1 Second-order systems

A closed-form solution for tracking of a single sinusoidal reference signal using a second-order systems is derived in this section. Consider the stable lightly damped second order system,

$$P(s) = \frac{\omega_n^2}{s^2 + 2\zeta\omega_n s + \omega_n^2}, \tag{7.1}$$

with poles $p_{1,2} = -\zeta\omega_n \pm i\omega_n\sqrt{1 - \zeta^2}$. For traditional point-to-point (ptp) input shapers, the standard parametrization is given by [142],

$$G_{\text{ptp}}(s) = \frac{A}{A + 1} + \frac{1}{A + 1}e^{-sT}, \tag{7.2}$$

with,

$$T = \frac{\pi}{\omega_n\sqrt{1 - \zeta^2}}, \quad A = \exp\left(\frac{\zeta\pi}{\sqrt{1 - \zeta^2}}\right). \tag{7.3}$$

For periodic excitation signals, the following harmonic time-delay filter (hTDF) parametrization is proposed,

$$G_{\text{h}}(s) = A_0 + A_1 e^{-sT} + A_2 e^{-2sT}. \tag{7.4}$$

Substitution of the poles of the system in the proposed hTDF parametrization in (7.4), using Eulers formula and equating the real and imaginary parts to zero, leads to the constraints

$$\sum_{k=0}^{L} A_k e^{k\zeta\omega_n T} \cos(k\omega_n\sqrt{1-\zeta^2}\,T) = 0, \tag{7.5}$$

$$-\sum_{k=0}^{L} A_k e^{k\zeta\omega_n T} \sin(k\omega_n\sqrt{1-\zeta^2}\,T) = 0, \tag{7.6}$$

with $L = 2$. From (7.6) follows the closed-form solution

$$T = \frac{n\pi}{\omega_n\sqrt{1-\zeta^2}}, \quad n = 1, 2, \ldots, \infty, \tag{7.7}$$

which after substitution in (7.5) and rewriting leads to the simplification

$$A_0 = -(-1)^n A_1 e^{\zeta\omega_n T} - A_2 e^{2\zeta\omega_n T}. \tag{7.8}$$

Given Fig. 7.1 it is desired to obtain a phase shift between the input and the output of the system of 0 or a full period pi, i.e.,

$$\left(\angle G_h(s) + \angle P(s)\right)\big|_{s=i\hat{\omega}_k} = \begin{cases} 0 & \text{if } \hat{\omega}_k < \omega_n \\ \pi & \text{if } \hat{\omega}_k > \omega_n \end{cases}, \forall\hat{\omega}_k, \tag{7.9}$$

with $\hat{\omega}_k$ the frequency of the reference signal and ω_n the eigenfrequency. After the substitution of $s = i\hat{\omega}_k$ for $\hat{\omega} < \omega_n$, this phase constraint can be written as,

$$\frac{-\sum_{k=1}^{2} A_k \sin(k\hat{\omega}T)}{\sum_{k=0}^{2} A_k \cos(k\hat{\omega}T)} - \frac{2\zeta\omega_n\hat{\omega}}{-\hat{\omega}^2 + \omega_n^2} = 0. \tag{7.10}$$

Note that similar expression can be found for $\hat{\omega}_k > \omega_n$. Substitution of (7.8) in (7.10) and rewriting leads to

$$A_1 = -\underbrace{\frac{\sin(2\hat{\omega}T)(\omega_n^2 - \hat{\omega}^2) + 2\zeta\omega_n\hat{\omega}(\cos(2\hat{\omega}T) - e^{2\zeta\omega_n T})}{\sin(\hat{\omega}T)(\omega_n^2 - \hat{\omega}^2) + 2\zeta\omega_n\hat{\omega}(\cos(\hat{\omega}T) - (-1)^n e^{\zeta\omega_n T})}}_{\Phi_1} A_2. \tag{7.11}$$

Substitution of (7.11) in (7.8) leads to

$$A_0 = \underbrace{\left(-(-1)^n \Phi_1 e^{\zeta\omega_n T} - e^{2\zeta\omega_n T}\right)}_{\Phi_0} A_2. \tag{7.12}$$

Finally, substitution of (7.11) and (7.12) in the magnitude constraint,

$$\left(\|G_h(s)\| - \|P(s)\|^{-1}\right)\big|_{s=i\hat{\omega}_k} = 0, \forall\hat{\omega}_k, \tag{7.13}$$

leads to

$$A_2^2 = \frac{(\omega_n^2 - \hat{\omega}^2)^2 + (2\zeta\omega_n\hat{\omega})^2}{\omega_n^4(1 + \Phi_0^2 + \Phi_1^2 + 2\Phi_0\Phi_1\cos(\hat{\omega}T) + 2\Phi_0\cos(2\hat{\omega}T) + 2\Phi_1\cos(\hat{\omega}T))},\tag{7.14}$$

which finalizes the closed-form solution.

Note that (7.14) leads to $A_2 = \Phi_2 \ \forall \ \hat{\omega} < \omega_n$ and $A_2 = -\Phi_2 \ \forall \ \hat{\omega} > \omega_n$. When the additional $n\pi$ from (7.4) is introduced, an additional phase delay of $n\pi$ is obtained, enabling a transient reduction for periodic signals, however a gain compensation is required, i.e., $A_2 = -\Phi_2 \ \forall \ \hat{\omega} < \omega_n$ and $A_2 = \Phi_2 \ \forall \ \hat{\omega} > \omega_n$.

Example 7.1. *To illustrate the results of the proposed technique, the plant in (7.1) is considered with $\zeta = 0.02$ and $\omega_n = \sqrt{2}$, leading to the lightly damped transfer function,*

$$P(s) = \frac{2}{s^2 + 0.0566s + 2},\tag{7.15}$$

with unity DC-gain. A possible solution for the traditional (point-to-point optimized) time-delay filter of (7.2) is,

$$G_{ptp}(s) = 0.5157 + 0.4843e^{-s2.2219}\tag{7.16}$$

and for the proposed harmonic time-delay filter using a forcing frequency ($\hat{\omega} = 0.7$) $< (\omega_n = \sqrt{2})$ rad/s,

$$G_h(s) = 0.3970 - 0.0087e^{-s2.2219} - 0.3583e^{-2s2.2219}.\tag{7.17}$$

Note that the delay time T for both filters is crucial for the pole cancellation and therefore results in the same value. In Fig. 7.2 the results of both filters are shown. It can be observed that both filters cancel the dynamical effects of the lightly damped poles of the plant. The point-to-point time delay filter is not able to achieve zero-phase tracking and leads to a delayed response with respect to the desired reference and an additional gain difference. The hTDF on the other hand is able to achieve zero-phase tracking after a transient of $2T \approx 4.4$ seconds. Note that the inverse is also true, the point-to-point time delay filter will achieve better tracking results than the hTDF for a point-to-point motion. In Fig. 7.3, the filtered inputs are illustrated for both filters, i.e., the input signals $u(t)$ to the plant. It can be observed that both inputs differ significantly from the reference signal. The point-to-point TDF has only a single action at delay time T, while the hTDF also acts at delay time $2T$ which is the point where perfect tracking is obtained as shown in Fig. 7.2. In addition, both signals have a limited amplitude, which enables a practical implementation of the proposed filters.

Finally in Fig. 7.4, the frequency domain interpretations of both filters and the resulting open-loop transfer functions are illustrated. Again it can clearly be observed that the lightly damped resonance peak is compensated by both filters.
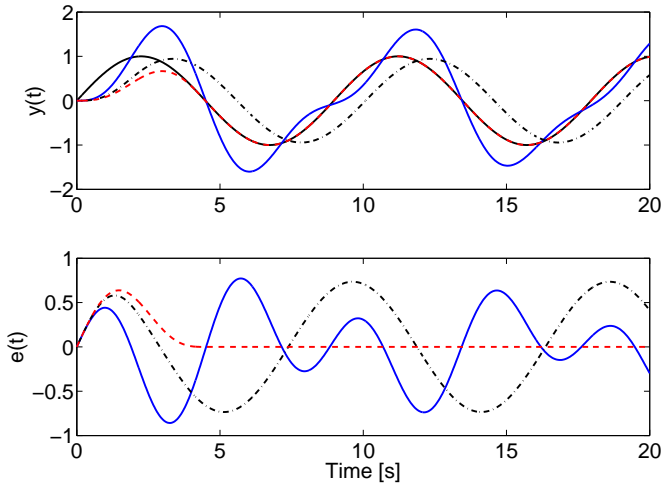
Fig. 7.2. Upper: resulting responses; reference signal (black), unshaped (plant only) (blue), point-to-point shaper (black dashed-dotted) and harmonic shaper (red dashed). Lower: resulting errors.
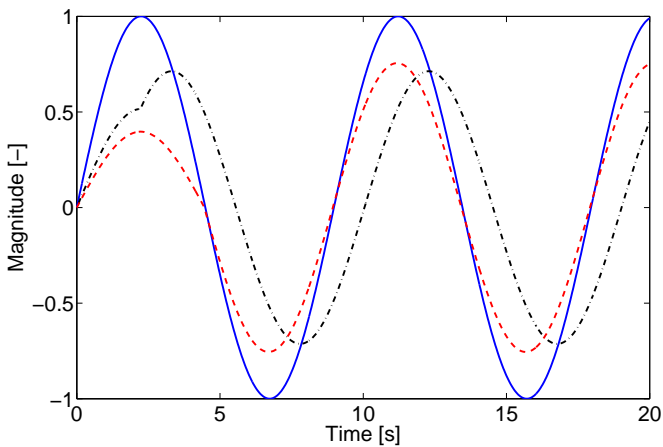
Fig. 7.3. Input signals: reference signal (blue), point-to-point shaper (black dashed-dotted) and harmonic shaper (red dashed)
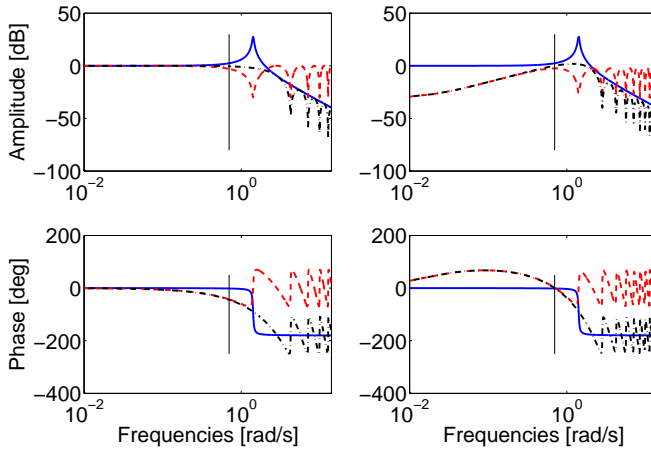
Fig. 7.4. Frequency domain representations. Left: plant $P(s)$ (blue), $G_{\mathrm{ptp}}(s)$ (red dashed) and $H_{\mathrm{ptp}}(s) = G_{\mathrm{ptp}}(s)P(s)$ (black dashed-dotted). Right: plant $P(s)$ (blue), $G_{\mathrm{h}}(s)$ (red dashed) and $H_{\mathrm{h}}(s) = G_{\mathrm{h}}(s)P(s)$ (black dashed-dotted)
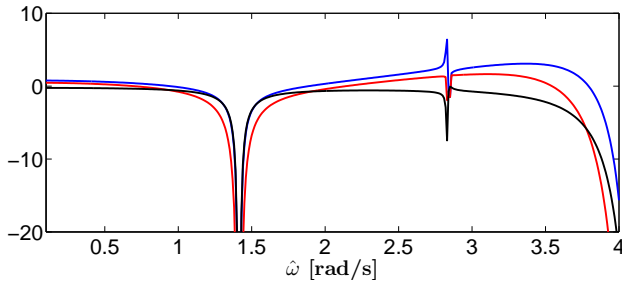
Fig. 7.5. Controller parameters: A_0 (blue), A_1 (red) and A_2 (black)

An additional compensation for the gain and phase for the forcing frequency $\hat{\omega} = 0.7$ rad/s can be observed for the hTDF.

Fig. 7.5 shows the variation of the gains A_0, A_1 and A_2 of the hTDF as a function of the forcing frequency $\hat{\omega}$. It can be observed that the solution is singular for $\hat{\omega} = n\omega_n$ with $n = 1, 3, \ldots, \infty$, which is a direct result of the placement of the zeros. By cancellation of the poles using the zeros of the hTDF, the filtered input signal for the plant as depicted in Fig. 7.3 contains only a small contribution at frequency ω_n. When choosing $\hat{\omega} = \omega_n$, infinite gains are required
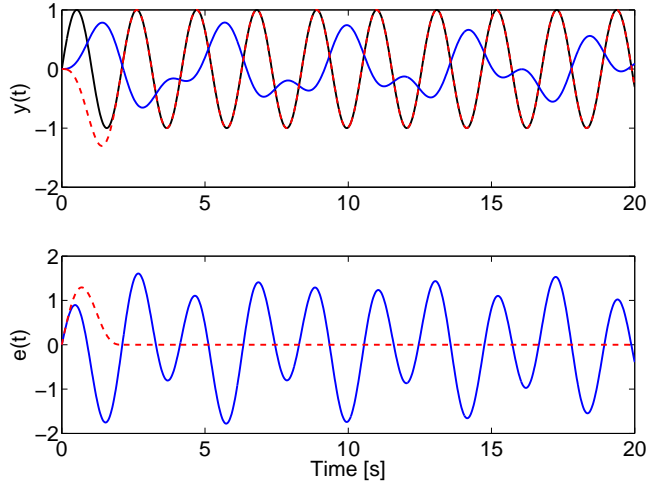
Fig. 7.6. Upper: resulting responses; reference signal (black), unshaped (plant only) (blue) and harmonic shaper (red dashed). Lower: resulting errors.

for undamped systems and large gains for lightly damped systems. ◁

Example 7.2. *Also the case where $\hat{\omega} > \omega_n$ can be considered. Although it is not required, an additional angle π can be included as introduced in (7.9) to reduce transient time. Note that a change of sign for the filter gains is required. In Fig. 7.6 the results are depicted for the same plant as introduced in (7.15) with $(\hat{\omega} = 3) > (\omega_n = \sqrt{2})$ rad/s. Note that the unshaped response of the plant is in antiphase with the reference signal as a result of the π radians phase rotation introduced by the natural frequency of the system. By compensating for this rotation, perfect tracking is again achieved.*

◁

7.2.2 General approach

A general description of a stable, possibly non-minimum phase, lightly damped system given by

$$P(s) = \frac{Y(s)}{U(s)} = \frac{\sum_{i=0}^{m} a_i s^i}{s^{N_p} + \sum_{l=0}^{N_p-1} b_l s^l} = \frac{N_s(s) N_u(s)}{D(s)}, \qquad (7.18)$$

with N_p the total number of poles of the system. The polynomials $N_s(s)$ and $N_u(s)$ describe the minimum- and non-minimum phase zeros respectively. The

fundamental idea behind input-shaping/time-delay filtering is the cancellation of the systems poles by exploiting the zeros of a prefilter $G(s)$ in an open-loop setting, such that,

$$G(s = p_j) = 0, \quad \forall p_j = \text{roots}\left(s^{N_p} + \sum_{l=0}^{N_p-1} b_l s^l\right),$$

$$= \alpha_j \pm i\beta_j. \tag{7.19}$$

In addition, for time-delay filters designed for point-to-point motion, the additional constraint on the DC gain,

$$|G_{\text{ptp}}(s = 0)| = |P(s = 0)|^{-1}, \tag{7.20}$$

should be satisfied. For systems subjected to periodic reference signals modifications are required and additional constraints should be satisfied. According to the Fourier series [150], any periodic signal can be denoted by

$$r(t) = \sum_{k=1}^{N_{\hat{\omega}_k}} a_k \sin(\hat{\omega}_k t + \varphi_k), \tag{7.21}$$

with $N_{\hat{\omega}_k}$ the total number of harmonics included in the signal and φ_k a phase-shift. By using, e.g., a notch-filter as inverse of the plant dynamics, cancellation of residual vibrations can be achieved, however, perfect tracking for a specific forcing frequency is not achieved, i.e., additional constraints on the gain and phase at the forcing frequency are required. Perfect tracking for periodic signals can be obtained by designing a prefilter that satisfies the constraints listed in Design Requirement 1.

Design Requirement 1. *Zero phase error tracking of periodic reference signals using a prefilter G_h in a noise and disturbance free situation, as illustrated in Fig. 7.1, can be achieved if,*

$$G_h(s = p_j) = 0, \quad \forall p_j, \tag{7.22}$$

with p_j the poles of the system as defined in (7.19), and in addition,

$$|G_h(s = i\hat{\omega}_k)| = |P(s = i\hat{\omega}_k)|^{-1}, \tag{7.23}$$

$$\angle G_h(s = i\hat{\omega}_k) + \angle P(s = i\hat{\omega}_k) = \begin{cases} 0 & \text{if } \hat{\omega}_k < \omega_n \\ \pi & \text{if } \hat{\omega}_k > \omega_n \end{cases}, \tag{7.24}$$

are satisfied $\forall \hat{\omega}_k$. Note that the equality to π in (7.24) leads to a reduced transient, see Sec. 7.2.1 for more details.

The proposed parametrization of the hTDF filter used throughout this chapter is given by

$$G_{\mathrm{h}}(s) = \sum_{k=0}^{L} A_k e^{-skT}, \qquad (7.25)$$

with,

$$L = N_p + 2N_{\hat{\omega}_k} - 2, \qquad (7.26)$$

leading to an equal number of optimization parameters as constraints in Design Requirement 1. Note that when $\hat{\omega}_k = \omega_n$, i.e., the forcing frequency is coincident with the natural frequency of the system, i.e., $\hat{\omega}_k = \omega_n$, the hTDF is undefined as a result of simultaneously satisfying (7.22) on the one hand and (7.23), (7.24) on the other hand. A nonlinear, non-convex, optimization problem leading to the shortest possible delay time T can be posed to determine the parameters of the hTDF as given in Eq. (7.27) to (7.30).

$$\min_{A_k \forall k} T \qquad (7.27)$$

subject to

$$\left. \sum_{k=0}^{L=N_p+2N_{\hat{\omega}}-2} A_k e^{-skT} \right|_{s=p_j} = 0, \quad \forall p_j \qquad (7.28)$$

$$\left. \left(|G_{\mathrm{h}}(s)| - |P(s)|^{-1} \right) \right|_{s=i\hat{\omega}_k} = 0, \quad \forall \hat{\omega}_k \qquad (7.29)$$

$$\left. \left(\angle G_{\mathrm{h}}(s) + \angle P(s) \right) \right|_{s=i\hat{\omega}_k} = \begin{cases} 0 \text{ if } \hat{\omega}_k < \omega_n \\ \pi \text{ if } \hat{\omega}_k > \omega_n \end{cases}, \ \forall \hat{\omega}_k \qquad (7.30)$$

Solving the non-linear, non-convex optimization problem in (7.27) will lead to the desired hTDF. Furthermore, it should be noted that the minimization of T in (7.27) is desired to minimize the initial transient.

In the following sections closed-form solutions for second-order systems and a sub-optimal approach for higher-order systems is presented.

7.2.3 Higher-order systems

For second-order systems, the closed-form solution can be computed as indicated in Sec. 7.2.1, however for higher-order systems an analytical solution is often hard or even impossible to find. Numerical optimization techniques can be used to optimize the parameters in the non-convex optimization problem in (7.27), provided that an accurate initial guess is available. Brute force methods such as genetic algorithms or particle-swarm optimizations [151] might lead to sufficiently accurate initial guesses for more structured numerical optimization methods.

By extending the parametrization of the hTDF in (7.25) with an additional delay-time, i.e., replacing (7.26) with $L = N_p + 2N_{\hat{\omega}_k} - 1$, the delay-time T can be chosen freely while the number of unknown parameters remains equal to the amount of equations. The new pole cancellation constraints for second-order systems are equivalent to (7.5) and (7.6). The constraints on the phase and amplitude of the filter for all $\hat{\omega}$ can be written as,

$$\left(\mathcal{R}e \left\{ G_{\mathrm{h}}(s = i\hat{\omega}) \right\} = \sum_{k=0}^{3} A_k \cos(k\hat{\omega}\,T) \right), \qquad (7.31)$$

$$\left(\mathcal{I}m \left\{ G_{\mathrm{h}}(s = i\hat{\omega}) \right\} = -\sum_{k=1}^{3} A_k \sin(k\hat{\omega}\,T) \right), \qquad (7.32)$$

with $\mathcal{R}e$ and $\mathcal{I}m$ representing the real and imaginary part respectively. Note that all four constraints are linear in the unknown delay-gains, which enables fast and reliable computations. By stacking constraints for multiple forcing frequencies and pole cancellations, the approach can be extended to higher-order systems and multiple forcing frequencies without the need for costly non-convex optimization at the cost of an increased duration of the transient with a single delay T.

Since practical implementations typically require discrete time solutions, the obtained delay-time T should correspond to an integer number of the sample-time. solving the general nonlinear optimization problem or closed-form, as described in Sec. 7.2.2 and Sec. 7.2.1, typically results in a T which is a non-integer number of samples. Hence, the selection of T improves the practical feasibility of the approach as is also argued in [147].

7.3 Extensions and special cases

The fundamentals of a TDF design for periodic reference signals is presented in the previous section. In the current section, additional extensions towards systems with (non-minimum) phase zeros, first-order systems, robustness, and dealing with non-differentiable signals are presented.

7.3.1 Systems with zeros

In [147], point-to-point input shapers are discussed where, in addition to pole cancelations, the zeros of the system are canceled, leading to enhanced tracking behavior. A similar approach holds for harmonic input shapers. Consider the system in (7.18), with both minimum and non-minimum phase zeros. The proposed extended parametrization for the hTDF filter is given by

$$G_{\mathrm{h}}(s) = \sum_{k=0}^{L-2} A_k e^{-skT} + \frac{A_{L-1}}{N_s(s) N_u^*(s)} e^{-s(L-1)T}, \qquad (7.33)$$

with $N_s(s)$ the polynomial describing the minimum phase zeros in (7.18) and $N_u^*(s)$ a stable approximation of $N_u(s)$. Note that the parametrization from (7.25) is recovered for $N_s(s = 0)$ and $N_u(s = 0)$. Recall that the proposed time-delay design according to Design Requirement 1 and (7.27), results in an approximation of the polynomial $D(s)$ in (7.18). For non-minimum phase systems, i.e., $N_u(s)$ is a polynomial leading to zeros of the plant in the right-half complex plane, multiple stable approximations can be applied. The most trivial stable solution is given by compensation of the DC-gain of the non-minimum phase part only, i.e.,

$$N_u^*(s) = N_u(s)|_{s=0}. \tag{7.34}$$

Other approximations, such as the well known zero-phase/magnitude error tracking control (ZPETC or ZMETC) [152] can be applied as stable approximation of $N_u^*(s)$, see, e.g., [153] for a detailed comparison of multiple methods for continuous time plant inverses.

7.3.2   First-order systems

First-order systems can be considered a special case since they have only a single real-valued pole. No pronounced dynamical behavior will be visible at the output of the system. The necessity of pole cancellation for this class of systems might be questioned. Using the reasoning introduced in Sec. 7.2.1, two filters can be designed, 1) including cancellation of the pole, and 2) only gain and phase compensation for $\hat{\omega}$. In Fig. 7.7 the frequency domain results are shown. In Fig. 7.8, the resulting tracking errors for variations of $\hat{\omega}$ are shown, indicating that the solution including the cancellation of the pole is more robust. This can directly be observed by the rate of change of the open-loop in Fig. 7.7.   In conclusion, by adding pole compensation, enhanced robustness is achieved. In Sec. 7.3.3 a detailed analysis on robustness for general systems is presented.

7.3.3   Robustness

Since the proposed approach heavily relies on the compensation of system poles using zeros of the hTDF (pole/zero cancellation), robustness is a key issue. Compensation of modeling errors, resulting in perturbations on the pole locations, are proposed in, e.g., [146]. By satisfying additional constraints,

$$\left.\begin{matrix} \frac{\mathrm{d}}{\mathrm{d}\omega_n}\left(\sum_{k=0}^{L} A_k e^{-\alpha_j kT}\cos(k\beta_j T)\right) = 0, \\ -\frac{\mathrm{d}}{\mathrm{d}\omega_n}\left(\sum_{k=0}^{L} A_k e^{-\alpha_j kT}\sin(k\beta_j T)\right) = 0, \end{matrix}\right\} \qquad \forall j = 1, \ldots, N_p \tag{7.35}$$

the sensitivity for pole location variations is decreased, which is consistent with the approach for repetitive control [137].
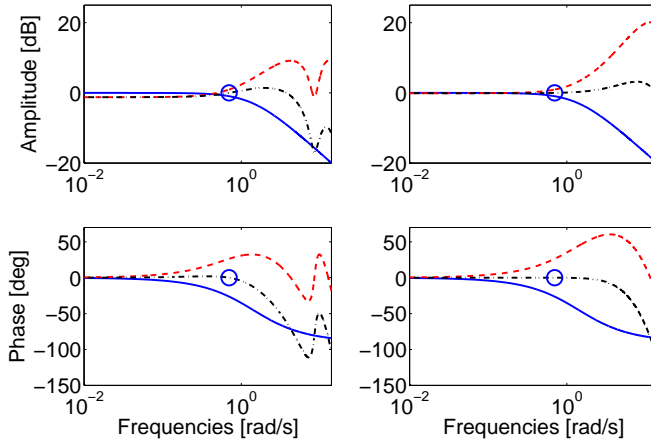
Fig. 7.7. Frequency domain representations; left: plant $P(s)$ (blue), $G_{\mathrm{np}}(s)$ (red dashed) and $H_{\mathrm{np}}(s) = G_{\mathrm{np}}(s)P(s)$ (black dashed-dotted); right: plant $P(s)$ (blue), $G_{\mathrm{h}}(s)$ (red dashed) and $H_{\mathrm{h}}(s) = G_{\mathrm{h}}(s)P(s)$ (black dashed-dotted)
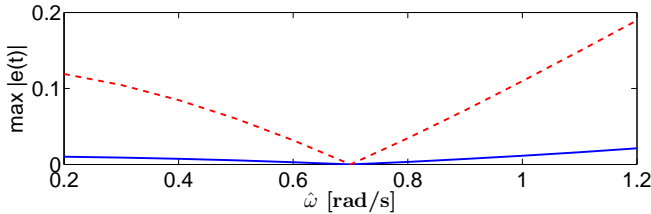
Fig. 7.8. Steady-state-errors: $G_{\mathrm{h}}(s)$ (blue) and $G_{\mathrm{np}}(s)$ (red dashed).

For robustness with respect to variations of the forcing frequencies $\hat{\omega}_k$, the additional constraints

$$\frac{\mathrm{d}H(s)}{\mathrm{d}\hat{\omega}_k}\bigg|_{s=i\hat{\omega}_k} = \left(\frac{\mathrm{d}P(s)}{\mathrm{d}\hat{\omega}_k}G(s) + \frac{\mathrm{d}G(s)}{\mathrm{d}\hat{\omega}_k}P(s)\right)\bigg|_{s=i\hat{\omega}_k} = 0, \qquad \forall\hat{\omega}_k, \quad (7.36)$$

should be satisfied. The order of the hTDF parametrization in (7.4), enforced by L parameters, should be extended with additional variables. As a result, $L = N_p + 4N_{\hat{\omega}} - 2$ for robustness with respect to variations in forcing frequencies only, $G_{\hat{\omega}}(s)$, and $L = 2N_p + 4N_{\hat{\omega}} - 2$ for both forcing frequency variations and desensitization for pole position variations, $G_R(s)$. In Fig. 7.9, the tracking errors

Fig. 7.9. Absolute errors due to uncertainties: $G_{\mathrm{h}}(s)$ (black), $G_\omega(s)$ (red dashed-dotted), $G_{\hat\omega}(s)$ (green dash-circles) and $G_R(s)$ (blue dashed); left: variations in $\hat\omega$; right: variations in model parameter.

as a function of variations in ω_n and $\hat\omega$ are illustrated for three parametrizations applied on the second order model (7.1).

7.3.4 Non-differentiable reference signals

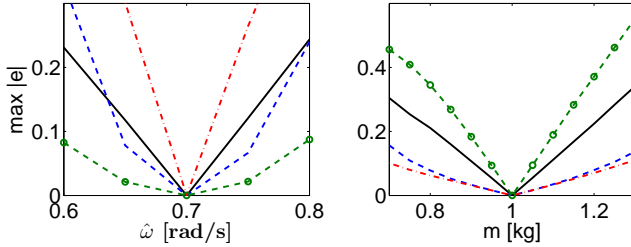According to the Fourier Series, any periodic signal can be written as a sum of N sinusoids as in (7.21). For non-differentiable signals, $N = \infty$, which makes the design of a perfect hTDF with a finite number of delay terms infeasible. However, by designing a hTDF, according to the minimization problem given by (7.27) using a limited set of harmonics, a significant tracking improvement can be achieved as demonstrated in the following numerical example.

Example 7.3. *Consider the lightly damped second order system as described in Example 1, subject to a triangular wave and block wave input signal that can be described by*

$$r_T(t) = \frac{8}{\pi^2}\sum_{k=0}^{\infty}(-1)^k\frac{\sin((2k+1)t)}{(2k+1)^2} \tag{7.37}$$

and

$$r_B(t) = \frac{4}{\pi}\sum_{k=1}^{\infty}\frac{\sin((2k-1)t)}{2k-1} \tag{7.38}$$

respectively, where $\hat\omega_k = 2k \pm 1$. By choosing a selected number of forcing frequencies, i.e., $\hat\omega_1 = 1$, $\hat\omega_2 = 3$, $\hat\omega_3 = 5$, $\hat\omega_4 = 7$, and $\hat\omega_5 = 11$, a hTDF can be designed according to the structure given by Eq. (7.25) with $L = 10$ and the parameters as given in Table 7.1. The resulting time domain responses for both signals are given in Fig. 7.10a and 7.10b, showing a significant improvement of the tracking result after an initial transient.

In the upcoming section, a practical design case is introduced showing the potential of the proposed theory. ◁

Table 7.1. Controller parameters.

A_0	-0.1774	A_4	-3.4102	A_8	-2.1592
A_1	-1.8344	A_5	-2.8815	A_9	-2.2547
A_2	-1.1593	A_6	-3.0575	A_{10}	-0.7430
A_3	-1.7812	A_7	-2.4794	T	1.0910
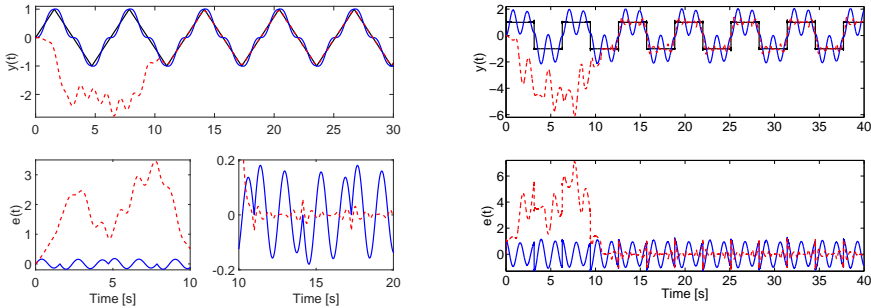
(a) Tracking of triangular-wave; lower left: error for time 0 to 10 seconds; lower right: error for time 10 to 20 seconds (zoomed).

(b) Tracking of block-wave

Fig. 7.10. Upper: resulting responses; reference signal (black), unshaped (plant only) (blue) and harmonic shaper (red dashed). Lower: resulting tracking errors.

7.4 Practical design case

The stable, underdamped sixth-order system model,

$$T_z(s) = (s^2 + \alpha s + \beta) \prod_{k=1}^{3} \frac{\omega_k^2}{s^2 + 2\zeta_k \omega_k s + \omega_k^2} \qquad (7.39)$$

with $\omega_1 = \sqrt{2}$, $\omega_2 = 3$, $\omega_3 = 4$ [rad/s], $\zeta_1 = 0.02$, $\zeta_2 = 0.05$, $\zeta_3 = 0.03$, $\alpha = 5e^{-4}$ and $\beta = 1.7$, is an approximation of the closed-loop behavior of a C-arc based X-ray system, depicted in Fig. 7.11. A graphical frequency domain representation is given in Fig. 7.14. The design goal for the filter $G_h(s)$ is to achieve $z(t) = r(t)$ where,

$$r(t) = \sin(\hat{\omega}_1 t) - 1.2 \sin(\hat{\omega}_2 t) + 1.9 \sin(\hat{\omega}_3 t), \qquad (7.40)$$

with $\hat{\omega}_1 = 0.7$, $\hat{\omega}_2 = 1.7$ and $\hat{\omega}_3 = 2.2$ [rad/s]. It should be noted that $\omega_1 < \hat{\omega}_3 < \omega_2$, which implies a phase correction is desired. The parametrization for the hTDF in (7.33) in combination with the linear computational approach for
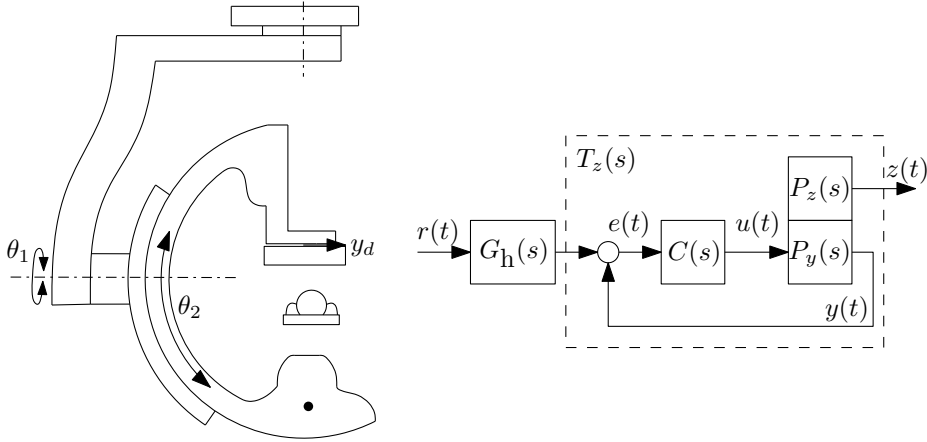
Fig. 7.11. Control setup of Philips Xper Allura FD20 system and implemented control scheme.

higher-order systems as described in Sec. 7.2.3 are used to derive the hTDF. The poles of the filter are chosen as $N_s(s) = \omega_1^2 \omega_2^2 \omega_3^2 (s^2 + \alpha s + \beta)$, with $N_u^*(s) = 1$, i.e., there are no non-minimum phase zeros. The order of the parametrization is given by $L = 12$, leading to a transient of LT seconds as indicated at the left two figures in Fig. 7.13. A second controller $G_R(s)$ is designed where the superscript R indicates robustness for pole variations in ω_2 and forcing frequency variations in $\hat{\omega}_3$. The computed filter gains for various delay times are illustrated in Fig. 7.12, from which a delay-time of 0.75 s is chosen as a feasible solution, i.e., all filter gains have feasible values for the normal and robust hTDF implementation. In Table 7.2 the corresponding filter gains are given for both the normal and the robust parametrization as introduced in Sec. 7.3.3 with $L = 16$.

Table 7.2. Controller parameters A for $T = 0.75$ s.

i	A_i	A_i^R	i	A_i	A_i^R	i	A_i	A_i^R
0	0.202	0.687	6	0.384	6.999	12	-	1.536
1	−0.175	−0.976	7	−0.513	−6.608	13	-	−0.470
2	0.377	2.623	8	0.238	6.494	14	-	0.235
3	−0.486	−3.442	9	−0.187	−4.838	15	-	−0.004
4	0.469	5.328	10	0.099	4.113			
5	−0.627	−5.967	11	1.008	−2.194			

In Fig. 7.13, the resulting time-domain responses are shown for the signal in (7.40). It can be observed that for the ideal plant, both filters are able to
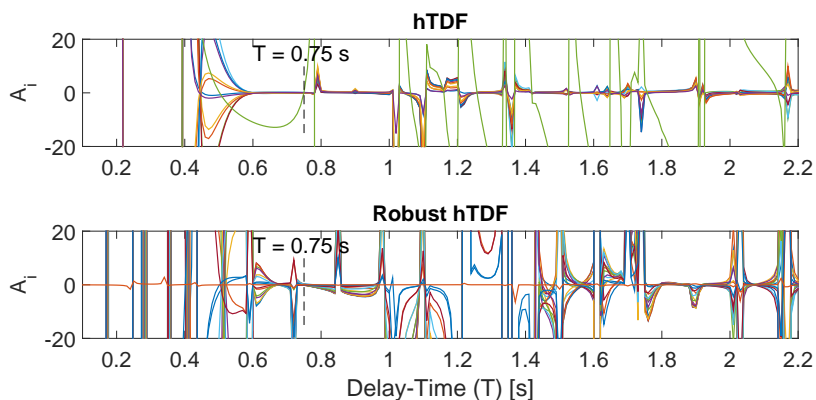
Fig. 7.12. Resulting gains A_i $\forall i = 1, \ldots, L$ given T; upper: normal hTDF; lower Robust hTDF.

achieve perfect tracking. However, for a 10% variation of both ω_2 and $\hat{\omega}_3$, the worst case error, indicated by the grey area, is reduced significantly for the robust implementation at the cost of a larger absolute error and duration of the transient. In Fig. 7.14, the frequency domain representations are given for the plant and $H(s) = G_\mathrm{h}(s)T_z(s)$ for both the normal and robust hTDF. The rate of change of the openloop $H(s)$ as a function of $\hat{\omega}_3$ is clearly smaller for the robust design, leading to a decreased sensitivity in forcing frequency variations while the gain of $H(s)$ around ω_2 is significantly smaller.

7.5 Conclusions

Time-delay control of lightly damped systems subject to periodic reference signals is considered. The theory is applicable to higher-order systems, systems with (non)minimum phase zeros and desensitization approaches for modeling errors leading to shifts in pole locations as well as variations in forcing frequencies are addressed. The filter enables zero-phase tracking of periodic reference signals. The proposed technique is illustrated in a practical design example of a sixth-order approximation of a medical X-ray system. More detailed analysis on the effect of choice for approximation methods to deal with non-minimum phase zeros should be performed to improve the tracking behavior during the transient. Advantages of the proposed approach with respect to, e.g., adaptive feedback control or ILC, are mainly in the ease of implementation and the fact that no online measurements or estimations at the performance locations are required.
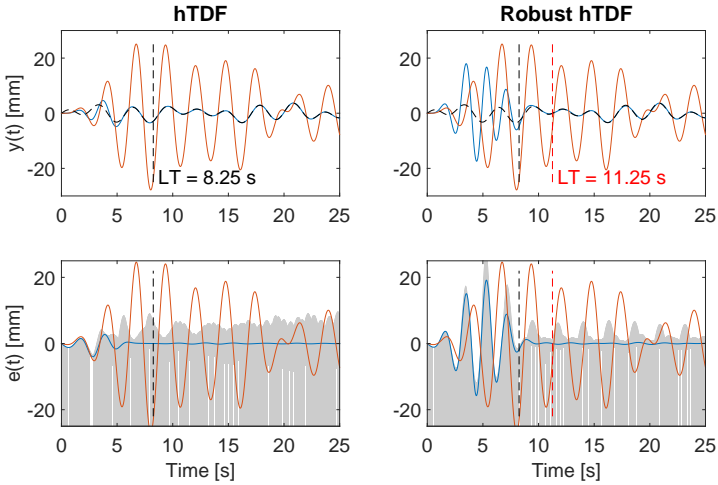
Fig. 7.13. Upper: resulting time-domain responses; reference signal (black dashed), unshaped (plant only) (red), shaped results (blue); lower: Corresponding error signals. Left: Normal hTDF (L = 12); right: Robust hTDF (L = 16). Grey area: worst-case uncertainty bound for ±10% variations.
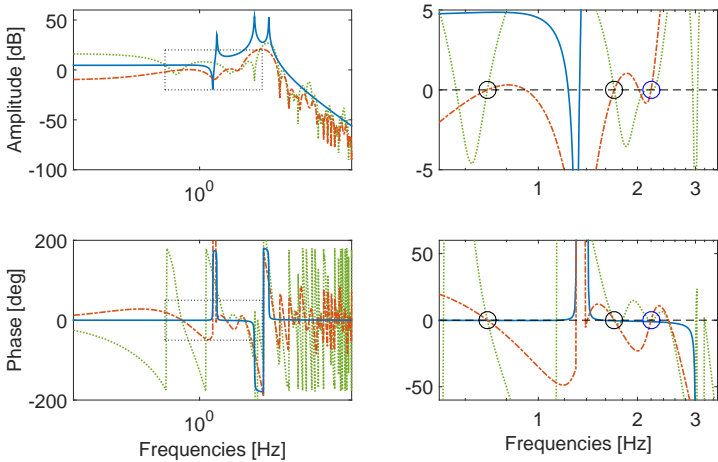
Fig. 7.14. Frequency domain representations; left: plant $P(s)$ (blue), $H(s) = P(s)G_{\mathrm{h}}(s)$ (red dashed-dotted), $H(s) = P(s)G_{\mathrm{h}}^{R}(s)$ (green dotted); right: zoomed.

Ongoing research focuses on improved tracking behavior during the transient period, on which no constraints are imposed in the results in this chapter. Moreover, the use of time-delay filters for alternative (non-periodic) reference signals is investigated.

Chapter 8

Conclusions and Recommendations

8.1 Conclusions

In this thesis, the geometric calibration problem for medical imaging systems is considered. The main contributions in this work are based on modeling and estimation approaches, overcoming imposed limitations by existing methods. A novel, model-based calibration approach for system imperfections that leads to quasi-static offsets from the ideal pose of the image acquisition components is proposed, which forms the fundamental of this thesis. For the next-generation interventional X-ray systems, it is expected that dynamical effects become significant, as is presented in Chap. 1. To deal with (increased) system dynamics, two approaches are followed. First dynamic models are obtained, which are used in a data-driven approach for geometric systems calibrations. By extending the quasi-static model with a dynamic model and using additional measured data during the patient scan itself, the true reconstruction scan is identified. In addition to the novel data-driven calibration approach, where measurements are used close to the performance locations, i.e., the X-ray detector and source, an image-based measurement approach is proposed that enables relative measurements directly at the desired performance locations. Second, the dynamical effects on the image quality can be reduced by exploitation of advanced motion control strategies. In addition to the proposed reference shaping technique, advanced adaptive control strategies are feasible for the reduction of the vibrations in the system. In fact, learning control strategies might enable a relaxation of the reproducibility condition and allow for the compensation of slowly time-varying behavior, e.g., wear of the system. The feasibility of the proposed approaches in

this work is demonstrated extensively through experiments on real-life interventional medical X-ray systems. The conclusions in this chapter are aligned with the research challenges as formulated in Chap. 1.

Research Challenge I

Chapter 2 forms the foundation of the thesis. The current generation of interventional X-ray systems require twice a year recalibration to deal with (time-varying) structural imperfections. These calibrations are typically time-consuming and, depending on the available options, can take up to four hours for each system. The novel model-based approach exploits the predictive properties of a physical model to extrapolate information within a limited set of measurements, to the full system operating space. Essentially, the calibration problem is recast in a parameter identification problem leading to a reduction of calibration times with a factor 10 to 15. The proposed approach is validated experimentally for the reconstruction of high-definition 3D objects using dynamic scans and static operation for 3D roadmapping applications. The results in Chap. 2 lead to Contribution I.

Research Challenge II

An intuitive extension of the quasi-static model-based approach presented in Chap. 2 is the extension towards the inclusion of dynamic models. The derivation of a physical model for complex high-performance motion systems is a challenging tasks. For high-performance motion systems, parametric models are often obtained based on measured data. A typical intermediate step is the measurement of nonparametric frequency response functions. In Chap. 3 a number of the current state-of-the-art nonparametric approaches is applied on an interventional medical X-ray system. The main difficulties are imposed by strong (geometric) nonlinearities, e.g., gravitational influences, friction, and play. Additionally, many motion systems show time or parameter varying behavior to a certain extend. The geometric nonlinearities of the X-ray systems can be approximated by linear parameter varying models. In Chap. 4, local parametric approaches are exploited for accurate and fast identification of LPV systems. Experimental validations of the approaches are available. The results in Chap. 3 and 4 lead to Contribution II.

Modern developments in industrial robotic systems exploit high-quality models in combination with sensor fusion techniques, e.g., Kalman and particle filters, to estimate dynamical behavior at unmeasured performance locations. For medical X-ray applications, which operate typically in crowded clinical environments, absolute (external) measurements, e.g., cameras or lasers, are infeasible. Using acceleration measurements, located at the X-ray detector and source, in combination with extended models and (nonlinear) Kalman-based filter techniques, a data-driven geometric calibration approach is proposed in Chap. 5. Due to the use of real-time measured data, the reproducibility condition imposed by

existing phantom-based approaches and the model-based approach presented in Chap. 1 can be relaxed. In addition, the proposed filters are exploited to enable fine-tuning of the model parameters, which potentially allows for an online compensation of slowly time-varying behavior of the system, e.g., wear of bearing and guidings. The results in Chap. 5 lead to Contribution III.

Image-quality is an important performance measure for medical X-ray systems. In Chap. 6, an image-based measurement approach is presented. By virtue of a minimal mechanical adjustment to the system, direct measurements of three (out of nine) geometric parameters can be performed. These additional measurements can be used to increase the calibration quality for existing approaches where they are typically neglected. Alternatively, it is shown how future developments might exploit these measurements to achieve enhanced state-estimations as presented in Chap. 5. The results in Chap. 6 lead to Contribution IV.

Research Challenge III
Finally, an input-shaping approach is presented in Chap. 7 to deal with motion induced vibrations. The main goal is to minimize the dynamical (motion induced) disturbances on the image acquisition components, enabling higher-accelerations and faster motions. This is in sharp contrast to the approach proposed in Chap. 5 where the dynamics are estimated. To design an effective input-shaper, knowledge about the system dynamics obtained in Chap. 3 and 4 is crucial. The main focus in Chap. 7 is on the design of input-shapers that enable tracking of periodic excitation signals. The results in Chap. 7 are a first step towards the use of advanced feedback/feedforward techniques, leading to Contribution V. Moreover, preliminary research results are presented in [37] where the use of iterative learning control (ILC) is proposed.

To conclude, in line with the general research goal defined in Chap. 1, a framework is developed based on modeling, estimation, and control approaches that allow for time-efficient geometric system calibrations. The proposed approaches are validated using experimental results.

8.2 Recommendations for ongoing research

The developments in this thesis show the potential of modeling, estimation, and control approaches to deal with geometric system calibration. Based on the obtained results, new insights are developed, leading to recommendations for ongoing research.

Parametrization and order selection for nD-LPM/LRM
Although the presented nD local polynomial method (LPM) and local rational method (LRM) approaches in Chap. 4 show promising results, alternative parameterizations leading to a close resemblance of the true system behavior for the local models should be investigated. Moreover, order-selection for the lo-

cal parameterizations remains a challenge. Automated order selections would be valuable for both the standard LPM/LRM approaches as for the nD-LPM/LRM. Preliminary results on advanced local parameterizations and automated order selections are reported in [154] for the LPM/LRM applied on LTI systems.

Parametric models for data-driven calibration
The results in Chap. 5 are based on a model in the modal form representation. Although this form is insightful, alternative, more efficient models are available in literature for LPV systems, see, e.g., [83] for an overview. A further investigation of more efficient models, particularly in MIMO situations, is recommended.

Parameter convergence
The results in Chap. 5 show that (adaptive) parameter convergence is achieved, however, no monotonic convergence is obtained. Although the feasibility of the data-driven approach in terms of accuracy is demonstrated, global (monotonic) convergence of the parameters is not guaranteed. The use of alternative adaptive approaches and a thorough robustness analysis are required before clinical application.

Using images in observer
In Chap. 6 it is proposed to use the detected marker-points as additional measurements in the observer proposed in Chap. 5. By using additional data, enhanced state-estimations might be obtained. Practical implementations of this proposal require additional experimentation. In addition, the filtering approaches required to obtain accurate marker-point detection impose a significant computational load. For the use in geometric calibrations for 3D reconstructions, additional research is required towards enhanced image-processing tools in terms of computation time.

Effects dynamics on 2D projections
In Chap. 6, marker-point detections are proposed within images. The image quality highly influences the variance on these estimations. Based on the expected developments towards lightweight systems and faster motions, the image quality is degrading. Ongoing research focuses on the use of obtained images, to determine the effects of dynamics on the obtained 2D projections in terms of variances. Note that reduced quality in 2D projections propagates to a reduced 3D reconstruction quality. The variances on the marker-point estimations based on the mechanical (clinical) markers as proposed in Chap. 6 can be exploited for online image-quality monitoring.

Tunable mass-damper elements Research towards vibration reduction using tunable mass-damper systems shows promising results, see, e.g., [155]. Input-shaping techniques as presented in Chap. 7 enable a reduction of motion induced

vibrations. However, due to nonlinear internal effects, e.g., play and friction, additional disturbances exciting the system are present. Tunable mass-damper systems might be exploited to minimize these effects. In [155] it is shown how a broadband reduction of lightly damped resonances can be achieved, which is a good start for future research for the application on medical X-ray systems.

Appendix A

Overview: Philips Allura X-ray Systems

In this appendix, a graphical overview of the systems under consideration in this work is provided. In Fig. A.1, the main components are indicated. In Figs. A.2 and A.3 the propellor and roll motions are indicated respectively. Finally, in Fig. A.4 is a floor based system shown.
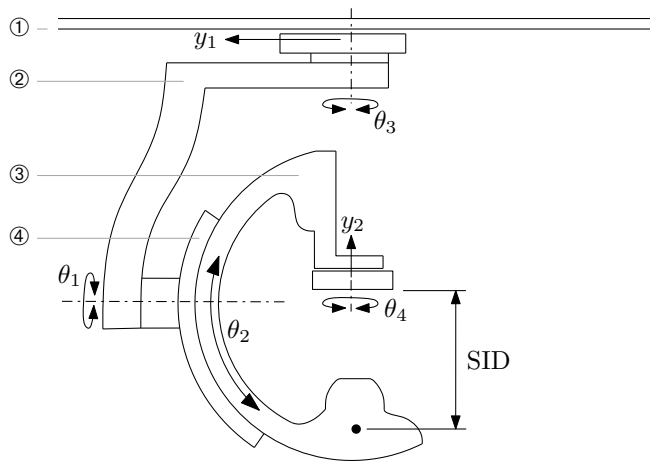
Fig. A.1. Philips Xper Allura FD20 ceiling mounted; ① ceiling mounted support rail, ② support arm, ③ C-arc, and ④ guidence sleeve.
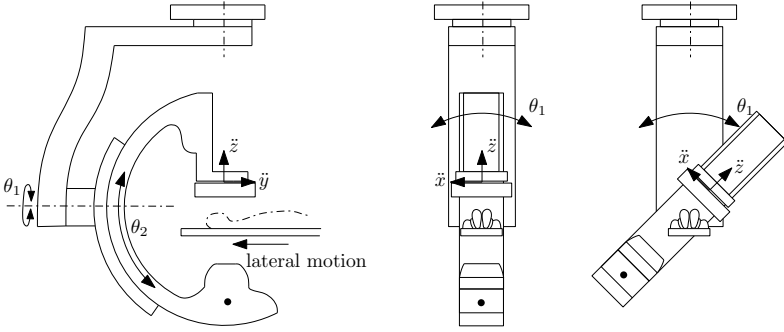
Fig. A.2. Philips Xper Allura FD20; Propeller motion
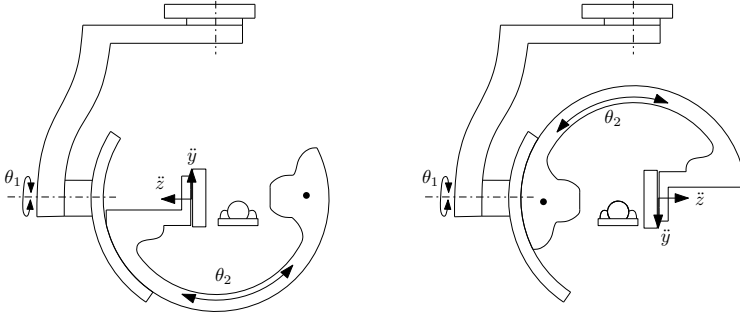
Fig. A.3. Philips Xper Allura FD20; Roll motion
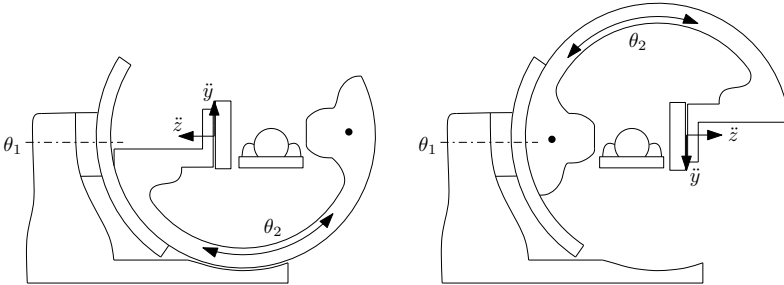
Fig. A.4. Philips Allura Centron FD15; Roll motion

3D Reconstruction Theory: Radon Transformation

As a starting point for the discussion on 3D image reconstruction, some fundamental calculations are discussed for 2D image reconstructions, based on *filtered backprojections.* These equations will be extended for the 3D reconstruction in a
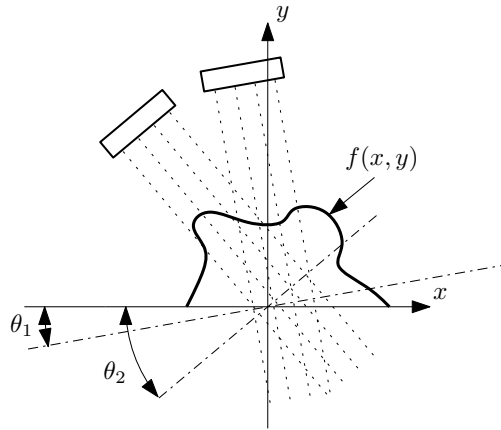
Fig. B.1. 2D Projection with parallel X-ray beam

similar fashion. To simplify the problem, some assumptions are made. The main assumption is that the X-ray beam is considered to be parallel as depicted in Figure B.1. In practice however, the source of the beam is better approximated by a spot that radiates in all directions. Furthermore, it is considered that the optimal radiation level is used and that the receiving area remains constant over

time and can be considered ideal, e.g., no (external) electronic or magnetic disturbances.

A schematic representation of a 2D image reconstruction is shown in Figure B.1. Consider a 2D function, $f(x, y)$, that bounds a surface that is desired to be reconstructed. The surface should be positioned within the circle that can be described by the detector and source, which means each point of the reconstructed object should be visible for the system from each position.
Next, a vector is defined that describes the perpendicular distance between the origin, defined as the center or rotation of the system and a single radiation beam, given a rotation, θ_k,

$$\rho_j = \begin{bmatrix} x \\ y \end{bmatrix}^T \begin{bmatrix} \cos(\theta_k) \\ \sin(\theta_k) \end{bmatrix}, \tag{B.1}$$

as shown in Figure B.2. The projection on the detecting surface for a beam, $L(\rho_j, \theta_k)$, can be given by the 2D Radon transform, see e.g., [4], which is defined as a line integral over $L(\rho_j, \theta_k)$,

$$p(\rho_j, \theta_k) = \int\limits_{-\infty}^{\infty} g(\rho_j, \theta_k) \, \mathrm{d}y. \tag{B.2}$$

with,

$$g(\rho_j, \theta_k) = \\ \int\limits_{-\infty}^{\infty} f(x, y)\delta\left(\rho_j - \begin{bmatrix} x \\ y \end{bmatrix}^T \begin{bmatrix} \cos(\theta_k) \\ \sin(\theta_k) \end{bmatrix}\right) \, \mathrm{d}x, \tag{B.3}$$

where δ is a so called dirac function, which is infinite for argument zero. By definition, the integral of a dirac function is equal to one. The complete projection for a fixed angle is given by $p(\theta_k, \rho)$ and for all angles it can be generalized to $p(\theta, \rho)$. Several definitions of the Radon transform exists, but the currently stated version is widely used in imaging applications. A similar, identical widely used expression, is given by,

$$p(\rho_j, \theta_k) = \int\limits_{-\infty}^{\infty} f(\rho_j \cos(\theta_k) - a_j \sin(\theta_k), \dots \\ \dots \rho_j \sin(\theta_k) + a_j \cos(\theta_k)) \, \mathrm{d}a_j, \tag{B.4}$$

and is called the *backprojection*, where a_j is the vector perpendicular to ρ_j and together span the vector from the origin to the function value $f(x, y)$, intersected by $L(\rho_j, \theta_k)$, as shown in Figure B.2. As a result, the detected value on

the detection line increases when the beam detects a thick part of the object, under the assumption that the object is made of a homogeneous material. A linear continuation coefficient can be defined, see, e.g., [5], that describes the permeability of the material. Depending on this coefficient, the detected value changes. Given the previously described procedures, the question still remains;
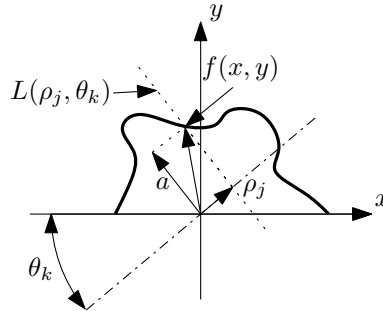
Fig. B.2. Vector definitions with $L(\rho_j, \theta_k)$ denoting a single X-ray beam.

how to reconstruct an actual object. By integrating the results of the Radon transform, over the angle θ, the so-called backprojection is obtained,

$$f(x,y) = \int\limits_0^\pi p(\rho, \theta) \mathrm{d}\theta. \tag{B.5}$$

Note that only half the rotation is required for the reconstruction due to redundant information, which is obtained for $\theta > \pi$. Practical limitations result in a finite number of angles that can be evaluated,

$$f(x,y) = \sum_{k=1}^n p(\rho, \theta_k), \tag{B.6}$$

which is equal to (B.5) for $n = \infty$. Due to the limitation on the number of evaluated 2D images ($n \approx 100 - 150$ for a normal reconstruction, $n \approx 600$ for a high resolution reconstruction), imperfections in the reconstructions are inevitable, which should be corrected by a filtering operation, the so called *filtered backprojection*.

The filtered backprojection (or sometimes in literature referred to as backsmear-

ing, [156]), of the projections are represented by,

$$f(x, y) = \int\limits_{0}^{\pi} \int\limits_{-\infty}^{\infty} p(\tau, \theta) h(\rho - \tau) \mathrm{d}\tau \mathrm{d}\theta, \tag{B.7}$$

$$= \int\limits_{0}^{\pi} p(\rho, \theta) * h(\rho) \mathrm{d}\theta, \tag{B.8}$$

with ρ defined as in (B.1), which is used to reconstruct $f(x, y)$. Note that the inner integral represents a convolution. The filter is added to improve the image quality. A more complete discussion on the convolution is given in, e.g., [157], and the filter selection with applications in medical imaging is discussed in e.g., [158].

Solving a convolution is computationally very expensive and can easily be solved by transforming the Radon transform and the filter to the spatial frequency domain using the Fourier transform. The Fourier transforms of the Radon transform and the filter are given as,

$$P(\omega, \theta) = \int\limits_{-\infty}^{\infty} p(\rho, \theta) e^{-j2\pi\omega\rho} \mathrm{d}\rho, \tag{B.9}$$

$$H(\omega) = \int\limits_{-\infty}^{\infty} h(\rho) e^{-j2\pi\omega\rho} \mathrm{d}\rho \tag{B.10}$$

which reduces (B.7) to,

$$f(x, y) = \int\limits_{0}^{\pi} \int\limits_{-\infty}^{\infty} P(\omega, \theta) H(\omega) e^{j2\pi\omega\rho} \mathrm{d}\omega \mathrm{d}\theta,$$

$$= \int\limits_{0}^{\pi} \mathcal{F}^{-1} \left[P(\omega, \theta) H(\omega) \right] \mathrm{d}\theta, \tag{B.11}$$

with $\mathcal{F}^{-1}$ defined as the inverse Fourier transform. For imaging purposes, the filter is typically defined as a ramp filter, $H(\omega) = |\omega|$. Using this result, the function $f(x, y)$ can be reconstructed using the filtered backprojections $p(\rho, \theta)$. Crucial for this relation is the parallel beam assumption for (B.2). Unfortunately, X-ray sources produce typically a (nearly) point-size source. This implies that a correction is required on (B.11) to compensate for non-parallel rays on a flat detection surface, see e.g., [6]. The theory discussed up to this point is necessary for an understanding of the relevance of calibration. However, for completeness,

a summary of the non-parallel beam situation is added.

It is assumed that the source and detector are rigidly connected, and both rotate around a fixed center, $(x_0, y_0) = (0,0)$, where the source trajectory is described by $(x_s, y_s) = (s\cos(\theta), s\sin(\theta))$, with s denoting the distance from the source to the origin.

In Figure B.3 is shown how the projection line on the virtual projection plane
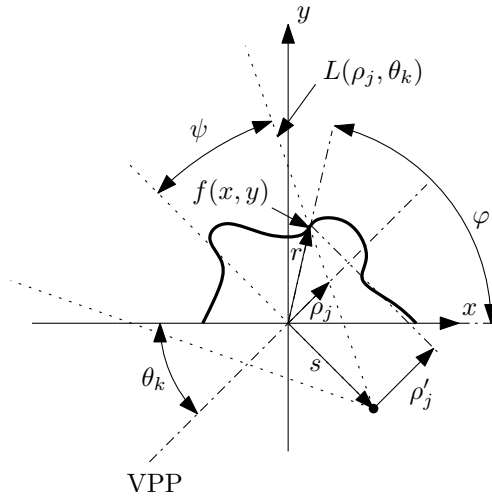
Fig. B.3. Non-parallel X-ray beam projection in a cartesian and polar coordinate system, $f(x,y) = f(r,\varphi)$.

(VPP), defined in (B.1), differs in a situation where the beams are not parallel. An additional vector ρ' is defined. Observe that,

$$\varphi = \theta + \psi, \tag{B.12}$$

and,

$$p_j = s\sin(\psi), \tag{B.13}$$

where s is the distance from the origin to the source. Note that, without loss of generality, the focus is bounded within a circular area of radius, ρ_{max} around the origin. Then, $p(\rho, \theta) = 0$, $\quad \forall \ |\rho| > \rho_{max}$, which reduces (B.7) to the form,

$$f(x,y) = \frac{1}{2} \int\limits_{0}^{\pi} \int\limits_{-\rho_{max}}^{\rho_{max}} p(\rho, \theta) \dots$$

$$\dots h(x\cos(\theta) + y\sin(\theta) - \rho)\mathrm{d}\rho\mathrm{d}\theta, \tag{B.14}$$

with $h(x\cos(\theta) + y\sin(\theta) - \rho)$ the result of the inverse Fourier transform of $H(\omega) = |\omega|$. Also note that the fact is used that projections with angle π apart are mirror images of each other.

In the case of non-parallel beams, an interesting result is found after integration of (B.14) with respect to θ and ψ. To facilitate this operation, the system is first translated to a poler coordinate representation, (r, φ), with $x = r\cos(\varphi)$ and $y = r\sin(\varphi)$. This results in,

$$f(r, \varphi) = \frac{1}{2} \int_0^{2\pi} \int_{-\rho_{max}}^{\rho_{max}} p(\theta, \rho) \ldots$$
$$\ldots h(r\cos(\theta - \varphi) - \rho)\mathrm{d}\rho\mathrm{d}\theta, \tag{B.15}$$

where,

$$r\cos(\theta - \varphi) = r\cos(\varphi)\cos(\theta) + r\sin(\varphi)\sin(\theta),$$
$$= x\cos(\theta) + y\sin(\theta). \tag{B.16}$$

After translation to the polar coordinate system, an additional coordinate transformation is required to enable the integration over the variables θ and ψ using (B.12) and (B.13). After various simplification steps, which are not within the scope of this thesis, see e.g., [5, p. 383 - 385], the final expression,

$$f(t, \varphi) = \int_0^{2\pi} \frac{1}{R^2} \left[\int_{-\psi_m}^{\psi_m} p(\psi, \theta)s\cos(\psi)h(\psi' - \psi)\mathrm{d}\psi \right] \mathrm{d}\theta, \tag{B.17}$$

is obtained, with,

$$R = \sqrt{s^2 + r^2}, \tag{B.18}$$

and,

$$h(\psi) = \frac{1}{2}\left(\frac{\psi}{\sin(\psi)}\right)^2 s(\psi). \tag{B.19}$$

So far, a 2D reconstruction can be obtained using the projections of various angles. The equations introduced in the previous part can be extended such that 3D reconstructions for semicircular orbits can be generated. For an exact reconstruction of a 3D volume, a full sphere should be described by the detection surface. However, for most medical imaging systems, mechanical limitations impose that only a semicircular orbit can be described. This results in inexactness of the reconstruction which should compensated for, see, e.g., [3] for more information.

Appendix C

Various Notations and Clarifications

C.1 Sample variance

The (co)variance of a signal is defined in Definition C.1.

Definition C.1. *The covariance over the P periods of the signal $x(k) \in \mathbb{C}^{n_x}$, with n_x the number of measured signals, is defined by,*

$$C_x(k) = \text{cov}\{x(k)\} = \mathbb{E}\left((x^{[p]}(k) - \bar{x}(k))(x^{[p]}(k) - \bar{x}(k))^H\right), \qquad \text{(C.1)}$$

with $x^{[p]}$ indicating a single period, k the evaluated frequency bin, $\bar{x}$ indicating the mean of the signal over the periods and the superscript H indicating the Hermitian transpose. The variance is defined by

$$\sigma_x^2(k) = diag\{C_x(k)\}. \qquad \text{(C.2)}$$

When only a finite number of periods is measured, the sample covariance is considered, as defined in the Definition C.2.

Definition C.2. *The sample covariance is defined by,*

$$\hat{C}_x(k) = \frac{1}{P-1} \sum_{p=1}^{P} (x^{[p]}(k) - \bar{x}(k))(x^{[p]}(k) - \bar{x}(k))^H. \qquad \text{(C.3)}$$

The covariance on an averaged signal $\bar{x}(k)$ is given by,

$$\hat{C}_{\bar{x}}(k) = \text{cov}\left\{\frac{1}{P} \sum_{p=1}^{P} x^{[p]}(k)\right\}. \qquad \text{(C.4)}$$

According to [159], the covariance of a summation is equal to the summation of the covariance, i.e.,

$$
\begin{aligned}
\hat{C}_{\bar{x}}(k) &= \text{cov}\left\{ \frac{1}{P} \sum_{p=1}^{P} x^{[p]}(k) \right\} = \frac{1}{P}\text{cov}\{x(k)\} = \frac{1}{P}\hat{C}_x(k), \\
&= \frac{1}{P(P-1)} \sum_{p=1}^{P} (x^{[p]}(k) - \bar{x}(k))(x^{[p]}(k) - \bar{x}(k))^H
\end{aligned}
\tag{C.5}
$$

with $\hat{C}_x(k)$ as in Definition C.2.

C.2   Derivation Kalman gain

The covariance of the estimated state is defined by,

$$
P_{k|k} = \text{cov}(x_k - \hat{x}_{k|k}),
\tag{C.6}
$$

where the state estimation is given by,

$$
\hat{x}_{k|k} = \hat{x}_{k|k-1} + K_k(z_k - H_k \hat{x}_{k|k-1}).
\tag{C.7}
$$

Assuming no modeling errors, the measurement can be described by, $z_k = H_k x_k + v_k$, leading to,

$$
P_{k|k} = \text{cov}\left((I - K_k H_k)(x_k - x_{k|\hat{k}-1}) - K_k v_k \right),
\tag{C.8}
$$

which, since the measurement noise is uncorrelated to the state estimation errors, can be written as,

$$
P_{k|k} = \text{cov}\left((I - K_k H_k)(x_k - x_{k|\hat{k}-1}) \right) + \text{cov}\left(K_k v_k \right),
\tag{C.9}
$$

$$
= (I - K_k H_k)\text{cov}\left((x_k - x_{k|\hat{k}-1}) \right)(I - K_k H_k)^T + K_k \text{cov}\left(v_k \right)K_k^T,
\tag{C.10}
$$

$$
= (I - K_k H_k)P_{k|k-1}(I - K_k H_k)^T + K_k R_k K_k^T.
\tag{C.11}
$$

The aim of the Kalman gain is the minimization of the state-estimation error, i.e.,

$$
\mathbb{E}\left\{ \|x_k - \hat{x}_{k|k}\|^2 \right\},
\tag{C.12}
$$

which is equivalent to the minimization of the trace of the state-covariance matrix $P_{k|k}$ as described in (C.11), which can be rewritten as,

$$
P_{k|k} = P_{k|k-1} - K_k H_k P_{k|k-1} - P_{k|k-1}H_k^T K_k^T + K_k S_k K_k^T.
\tag{C.13}
$$

with $S_k = H_k P_{k|k-1} H_k^T + R_k$. The trace of $P_{k|k}$ is minimized when the derivative of the $Tr(P_{k|k})$ with respect to K_k is equated to zero,

$$
\frac{\mathrm{d}Tr(P_{k|k})}{\mathrm{d}K_k} = -2(H_k P_{k|k-1})^T + 2K_k S_k = 0.
\tag{C.14}
$$

By exploiting the symmetry of $P_{k|k-1}$,

$$K_k S_k = (H_k P_{k|k-1})^T = P_{k|k-1} H_k^T, \tag{C.15}$$

leading to the Kalman gain,

$$K_k = P_{k|k-1} H_k^T S_k^{-1}. \tag{C.16}$$

Bibliography

[1] W. C. Röntgen, "Ueber eine neue Art von Strahlen. Fortsetzung," *Sitzungsberichte der Würzburger Physik.-medic. Gesellschaft*, pp. 1 – 9, 1896.

[2] United Nations Scientific Committee, "Report of the united nations scientific committee on the effects of atomic radiation to the general assembly," vol. 1, 2000.

[3] P. Suetens, *Fundamentals of Medical Imaging*, 2nd ed. New York: Cambridge University Press, 2009.

[4] J. Radon, "On the Determination of Functions From Their Integral Values Along Certain Manifolds," *IEEE Trans. on Medical Imaging*, vol. 5, no. 4, pp. 170–176, 1986.

[5] R. C. Gonzalez and R. E. Woods, *Digital Image Processing*, 3rd ed. Upper Saddle River, New Jersey, USA: Pearson Education Inc., 2008.

[6] A. Kak and M. Slaney, *Principles of Computerized Tomographic Imaging*. IEEE Press, 1988. [Online]. Available: http://www.slaney.org/pct/pct-toc.html

[7] M. Söderman, D. Babic, R. Homan, and T. Andersson, "3D roadmap in neuroangiography: technique and clinical interest," *Neuroradiology*, vol. 47, no. 10, pp. 735 – 740, 2005.

[8] J. Schwartz, A. Neubauer, T. Fagan, N. Noordhoek, M. Grass, and J. Carroll, "Potential role of three-dimensional rotational angiography and C-arm CT for valvular repair and implementation," *Int. J. of Cardiovascular Imaging*, vol. 27, pp. 1205 – 1222, 2011.

[9] C. Papalazarou, "3D object reconstruction in image-guided interventions using multi-view X-ray," PhD - Thesis, Eindhoven University of Technology, 2012.

[10] F. Noo, R. Clackdoyle, C. Mennessier, T. A. White, and T. J. Roney, "Analytic method based on identification of ellipse parameters for scanner calibration in cone-beam tomography," *Physics in Medicine and Biology*, vol. 45, pp. 3489 – 3508, 2000.

[11] Y. Cho, D. Moseley, J. Siewerdsen, and D. Jaffray, "Accurate Technique for Complete Geometric Calibration of Cone-Beam Computed Tomography Systems," *Medical Physics*, vol. 32, no. 4, pp. 968 – 983, 2005.

[12] B. Siciliano, L. Sciavicco, L. Villani, and G. Oriolo, *Robotics Modeling, Planning and Control*.   London, UK: Springer, 2010.

[13] A. Baert, M. Knauth, and K. Sartor, *Multislice CT*, 3rd ed., M. Reiser, C. Becker, K. Nikolaou, and G. Glazer, Eds.   Berlin Heidelberg: Springer-Verlag, 2009.

[14] R. Snoeren, "Physics-Based Optimization of Image Quality in 3D X-ray Flat-Panel Cone-Beam Imaging," PhD - Thesis, Eindhoven University of Technology, 2012.

[15] J. Hsieh, "Three-Dimensional Artifact Induced by Projection Weighting and Misalignment," *IEEE Trans. on Medical Imaging*, vol. 18, no. 4, pp. 364 – 368, dec 1999.

[16] W. A. Kalender and Y. Kyriakou, "Flat-detector computed tomography (FD-CT)," *European Radiology*, vol. 17, no. 11, pp. 2767–79, dec 2007.

[17] J. Hsieh, *Computed Tomography, Second Edition: Principles, Design, Artifacts, and Recent Advances*, 2nd ed.   Hoboken, New Jersey: John Wiley & Sons, Inc., 2009.

[18] N. K. Strobel, B. Heigl, T. M. Brunner, O. Schuetz, M. M. Mitschke, K. Wiesent, and T. Mertelmeier, "Improving 3D image quality of x-ray C-arm imaging systems by using properly designed pose determination systems for calibrating the projection geometry," in *Proc. of SPIE in Medical Imaging*, 2003, pp. 943 – 954.

[19] S. Hoppe, F. Noo, F. Dennerlein, G. Lauritsch, and J. Hornegger, "Geometric Calibration of the Circle-Plus-Arc Trajectory," *Physics in medicine and biology*, vol. 52, no. 23, pp. 6943–6960, dec 2007.

[20] C. Mennessier, R. Clackdoyle, and F. Noo, "Direct determination of geometric alignment parameters for cone-beam scanners," *Physics in medicine and biology*, vol. 54, no. 6, pp. 1633 – 1660, mar 2009.

[21] K. Wiesent, K. Barth, N. Navab, P. Durlak, T. Brunner, O. Schuetz, and W. Seissler, "Enhanced 3-D-reconstruction algorithm for C-arm systems suitable for interventional procedures." *IEEE Trans. on Medical Imaging*, vol. 19, no. 5, pp. 391 – 403, may 2000.

[22] G. T. Gullberg, B. M. Tsui, C. R. Crawford, J. G. Ballard, and J. T. Hagius, "Estimation of geometrical parameters and collimator evaluation for cone beam tomography," *Medical Physics*, vol. 17, pp. 264 – 272, 1990.

[23] A. Rougée, C. Picard, C. Ponchut, and Y. Trousset, "Geometrical Calibration of X-ray Imaging Chains for Three-Dimensional Reconstruction," *Computerized medical imaging and graphics*, vol. 17, no. 4/5, pp. 295–300, 1993.

[24] M. Daly, J. Siewerdsen, Y. Cho, D. Jaffray, and J. Irish, "Geometric Calibration of a Mobile C-arm for Intraoperative Cone-Beam CT," *Medical Physics*, vol. 35, no. 5, p. 2124, 2008.

[25] K. Yang, A. L. Kwan, D. F. Miller, and J. M. Boone, "A geometric calibration method for cone beam CT systems," *Medical Physics*, vol. 33, no. 6, pp. 1695 – 1706, 2006.

[26] D. Gross, U. Heil, R. Schulze, E. Schoemer, and U. Schwanecke, "Auto calibration of a cone-beam-CT," *Medical Physics*, vol. 39, no. 10, 2012.

[27] J. Cates, Y. Pan, V. Battle, and R. Whitaker, "Cone-beam CT data-driven pose correction for analytic reconstruction methods," in *Proc. of SPIE in Medical Imaging*, 2011.

[28] J. Wicklein, H. Kunze, W. A. Kalender, and Y. Kyriakou, "Image Features for Misalignment Correction in Medical Flat-Detector CT," *Medical Physics*, vol. 39, no. 8, pp. 4918 – 4931, 2012.

[29] Y. Kyriakou, R. Lapp, L. Hillebrand, D. Ertel, and W. Kalender, "Simultaneous misalignment correction for approximate circular cone-beam computed tomography," *Physics in Medicine and Biology*, vol. 53, pp. 6267 – 6289, nov 2008.

[30] C. Gong, J. Yuan, and J. Ni, "Nongeometric Error Identification and Compensation for Robotic System by Inverse Calibration," *Int. J. of Machine Tools and Manufacture*, vol. 40, pp. 2119 – 2137, 2000.

[31] A. Klimchik, A. Pashkevich, Y. Wu, S. Caro, and B. Furet, "Design of Calibration Experiments for Identification of Manipulator Elastostatic Parameters," *J. of Mechanics Engineering and Automation*, vol. 2, pp. 531 – 542, 2012.

[32] B. Gao, Y. Liu, N. Xi, and Y. Shen, "Developing an Efficient Calibration System for Joint Offset of Industrial Robots," *J. of Applied Mathematics*, vol. 2014, 2014.

[33] R. Toth, *Modeling and Identification of Linear Parameter-Varying Systems*, P. S. Heuberger and P. M. Van den Hof, Eds. Berlin: Springer-Verlag, 2010.

[34] J. Schoukens, G. Vandersteen, K. Barbé, and R. Pintelon, "Nonparametric Preprocessing in System Identification: A Powerful Tool," *European Journal of Control*, vol. 15, no. 3-4, pp. 1–21, 2009.

[35] T. Mckelvey and G. Guérin, "Non-parametric Frequency Response Estimation Using a Local Rational Model," in *16th IFAC Sym. on System Identification*, no. 1, 2012, pp. 49–54.

[36] R. Gaasbeek, R. van der Maas, M. den Hartog, and B. de Jager, "Improved Automatic Exposure Control using Morphology-Based Disturbance Recognition," in *IEEE Int. Sym. on Biomedical Imaging*, Beijing, China, 2014, pp. 1271 – 1274.

[37] W. Eijsermans, "Inferential Norm-Optimal ILC for Parameter Varying Systems: Application for Medical X-ray Systems," MSc - Thesis, Eindhoven University of Technology, 2015.

[38] B. Sleegers, "X-ray Image-Based Pose Estimation and Identification for Geometric System Calibration," MSc - Thesis, Eindhoven University of Technology, 2015.

[39] D. Jaffray, J. Siewerdsen, J. Wong, and A. Martinez, "Flat-panel cone-beam computed tomography for image-guided radiation therapy." *Int. J. of Radiation Oncology, Biology, Physics*, vol. 53, no. 5, pp. 1337 – 1349, aug 2002.

[40] L. von Smekal, M. Kachelrieß, E. Stepina, and W. A. Kalender, "Geometric misalignment and calibration in cone-beam tomography," *Medical Physics*, vol. 31, no. 12, pp. 3242 – 3266, 2004.

[41] M. Spong, S. Hutchinson, and M. Vidyasagar, *Robot Modeling and Control*, 1st ed. New York, NY, USA: John Wiley & Sons, Inc., 2005.

[42] R. Clackdoyle and M. Defrise, "Overview of reconstruction algorithms for exact cone-beam tomography," in *SPIE Mathematical Methods in Medical Imaging III*, 1994, pp. 230 – 241.

[43] R. Henriksson, M. Norrlöf, S. Moberg, E. Wernholt, and T. Schön, "Experimental Comparison of Observers for Tool Position Estimation of Industrial Robots," in *Joint 48th Conference on Decision and Control and 28th Chinese Control Conference*, 2009, pp. 8065–8070.

[44] D. Kostic, B. de Jager, M. Steinbuch, and R. Hensen, "Modeling and Identification for High-Performance Robot Control : An RRR-Robotic Arm Case Study," *IEEE Trans. on Control Systems Technology*, vol. 12, no. 6, pp. 904 – 919, 2004.

[45] G. Alici and B. Shirinzadeh, "Enhanced Stiffness Modeling Identification and Characterization for Robot Manipulators," *IEEE Trans. on Robotics*, vol. 21, no. 4, pp. 554 – 564, 2005.

[46] N. Bompos, P. K. Artemiadis, A. S. Oikonomopoulos, and K. J. Kyriakopoulos, "Modeling, Full Identification and Control of the Mitsubishi PA-10 Robot Arm," in *IEEE/ASME Int. Conf. on Advanced Intelligent Mechatronics*, Zurich, CH, 2007, pp. 1 – 6.

[47] W. Khalil and S. Besnard, "Geometric Calibration of Robots with Flexible Joints and Links," *J. of Intelligent and Robotic Systems*, vol. 34, pp. 357 – 379, 2002.

[48] R. Pintelon and J. Schoukens, *System Identification: A Frequency Domain Approach*, 2nd ed. Piscataway, New Jersey, USA: IEEE Press, 2012.

[49] J. Swevers, C. Ganseman, J. De Schutter, and H. Van Brussel, "Experimental Robot Identification Using Optimised Periodic Trajectories," *Mechanical Systems and Signal Processing*, vol. 10, no. 5, pp. 561–577, 1996.

[50] R. Munnig Schmidt, G. Schitter, A. Rankers, and J. Van Eijk, *The Design of High Performance Mechatronics*, 2nd ed. IOS Press, 2014.

[51] M. van de Wal, G. van Baars, F. Sperling, and O. Bosgra, "Multivariable $\mathcal{H}_\infty$ /μ feedback control design for high-precision wafer stage motion," *Control Engineering Practice*, vol. 10, pp. 739–755, 2002.

[52] M. Steinbuch and M. Norg, "Advanced Motion Control : An Industrial Perspective," *European Journal of Control*, pp. 278–293, 1998.

[53] S. Skogestad and I. Postlethwaite, *Multivariable Feedback Control, Analysis and Design.* Chichester, England: John Wiley & Sons, Ltd., 2005.

[54] J. Wallén, I. Dressler, A. Robertsson, M. Norrlöf, and S. Gunnarsson, "Observer-Based ILC Applied to the Gantry-Tau Parallel Kinematic Robot - Modelling, Design and Experiments," in *IFAC Trenniel World Congress*, Milano, Italy, 2010, pp. 992 – 998.

[55] L. Ljung, *System Identification: Theory for the User*, 2nd ed. Upper Saddle River, New Jersey: Prentice Hall Inc., 1999.

[56] S. Moberg, J. Öhr, and S. Gunnarsson, "A Benchmark Problem for Robust Control of a Multivariable Nonlinear Flexible Manipulator," Linköping University, Tech. Rep., 2008.

[57] M. Östring, S. Gunnarsson, and M. Norrlöf, "Closed-Loop Identification of an Industrial Robot Containing Flexibilities," *Control Engineering Practice*, vol. 11, no. 3, pp. 291–300, mar 2003.

[58] B. Bamieh and L. Giarré, "Identification of linear parameter varying models," *Int. J. of Robust and Nonlinear Control*, vol. 12, no. 9, pp. 841–853, 2002.

[59] J. Goos, J. Lataire, and R. Pintelon, "Estimation of Linear Parameter-Varying affine State Space Models using Synchronized Periodic Input and Scheduling Signals," in *American Control Conference*, no. 1, 2014, pp. 3754–3759.

[60] R. Toth, F. Felici, P. S. C. Heuberger, and P. M. J. Van den Hof, "Discrete time LPV I/O and state space representations, differences of behavior and pitfalls of interpolation," in *Proc. of the European Control Conference*, 2007, pp. 5418–5425.

[61] M. Groot Wassink, M. van de Wal, C. Scherer, and O. Bosgra, "LPV control for a wafer stage: Beyond the theoretical solution," *Control Engineering Practice*, vol. 13, pp. 231–245, 2005.

[62] E. Wernholt and S. Moberg, "Nonlinear gray-box identification using local models applied to industrial robots," *Automatica*, vol. 47, no. 4, pp. 650–660, apr 2011.

[63] R. Pintelon, J. Schoukens, G. Vandersteen, and K. Barbé, "Estimation of Nonparametric Noise and FRF Models for Multivariable Systems - Part I: Theory," *Mechanical Systems and Signal Processing*, vol. 24, pp. 573–595, 2010.

[64] E. Geerardyn, T. Oomen, and J. Schoukens, "Enhanced $\mathcal{H}_\infty$ norm estimation using local LPM/RPM modeling: Applied to an AVIS," in *Proc. IFAC 19th Triennial World Congres*, Cape Town, South-Africa, 2014, pp. 10 856 – 10 861.

[65] E. Wernholt and S. Gunnarsson, "Estimation of Nonlinear Effects in Frequency Domain Identification of Industrial Robots," *IEEE Trans. on Instrumentation and Measurement*, vol. 57, no. 4, pp. 856–863, apr 2008.

[66] R. Voorhoeve, A. van Rietschoten, E. Geerardyn, and T. Oomen, "Identification of High-Tech Motion Systems : An Active Vibration Isolation Benchmark," in *Sym. on System Identification*, Beijing, China, 2015.

[67] R. Pintelon and J. Schoukens, "Measurement of Frequency Response Functions Using Periodic Excitations , Corrupted by Correlated Input / Output Errors," *IEEE Trans. on Instrumentation and Measurement*, vol. 50, no. 6, pp. 1753–1760, 2001.

[68] T. P. Dobrowiecki, J. Schoukens, and P. Guillaume, "Optimized excitation signals for MIMO frequency response function measurements," *IEEE Trans. on Instrumentation and Measurement*, vol. 55, no. 6, pp. 2072–2079, 2006.

[69] B. Sanchez, J. Schoukens, R. Bragos, and G. Vandersteen, "Novel estimation of the electrical bioimpedance using the local polynomial method. Application to in vivo real-time myocardium tissue impedance characterization during the cardiac cycle," *IEEE Trans. on Biomedical Engineering*, vol. 58, no. 12, pp. 3376–3385, 2011.

[70] R. Snoeren, J. Kroon, and P. de With, "Image quality analysis of vibration effects in C-arm flat panel X-ray imaging," *2011 Int. Congress on Image and Signal Processing*, pp. 1716–1722, oct 2011.

[71] J. Schoukens, G. Vandersteen, R. Pintelon, Z. Emedi, and Y. Rolain, "Bounding the Polynomial Approximation Errors of Frequency Response Functions," *IEEE Trans. on Instrumentation and Measurement*, vol. 62, no. 5, pp. 1346–1353, 2013.

[72] D. J. Leith and W. E. Leithead, "Survey of gain-scheduling analysis and design," *Int. J. of Control*, vol. 73, no. 11, pp. 1001–1025, 2000.

[73] W. J. Rugh and J. S. Shamma, "Research on gain scheduling," *Automatica*, vol. 36, pp. 1401–1425, 2000.

[74] M. Steinbuch, R. van de Molengraft, and A. van der Voort, "Experimental modelling and LPV control of a motion system," *American Control Conference*, vol. 2, no. 1, pp. 1374–1379, 2003.

[75] A. Forrai, T. Ueda, and T. Yumura, "Electromagnetic actuator control: A linear parameter-varying (LPV) approach," *IEEE Trans. on Industrial Electronics*, vol. 54, no. 3, pp. 1430 – 1441, 2007.

[76] J. Jayender, R. Patel, S. Nikumb, and M. Ostojic, "Modelling and gain scheduled control of shape memory alloy actuators," in *Proc. IEEE Conference on Control Applications, 2005*, 2005, pp. 767 – 772.

[77] M. Jung and K. Glover, "Calibratable linear parameter-varying control of a turbocharged diesel engine," *IEEE Trans. on Control Systems Technology*, vol. 14, no. 1, pp. 45–62, 2006.

[78] J.-W. van Wingerden, "Control of wind turbines with 'Smart' rotors: proof of concept & LPV subspace identification," PhD - Thesis, Delft University of Technology, 2008.

[79] L. Lee and K. Poolla, "Identification of linear parameter-varying systems using nonlinear programming," *J. of Dynamic System, Measurement, and Control*, vol. 121, no. 1, pp. 71 – 78, 1999.

[80] P. Lopes dos Santos, T. Paula Azevedo Perdicoúlis, C. Novara, J. A. Ramos, and D. E. Rivera, *Linear Parameter-Varying System Identification: New Developments and Trends.* Singapore: World Scientific Publishing Co. Pte. Ltd., 2011.

[81] M. Lovera, C. Novara, P. Lopes dos Santos, and D. Rivera, "Guest Editorial Special Issue on Applied LPV Modelling and Identification," *IEEE Trans. on Control Systems Technology*, vol. 19, no. 1, pp. 1–4, 2011.

[82] F. Felici, J. W. van Wingerden, and M. Verhaegen, "Subspace identification of MIMO LPV systems using a periodic scheduling sequence," *Automatica*, vol. 43, pp. 1684–1697, 2007.

[83] J. De Caigny, R. Pintelon, J. F. Camino, and J. Swevers, "Interpolated Modeling of LPV Systems," *IEEE Trans. on Control Systems Technology*, vol. 22, no. 6, pp. 2232–2246, 2014.

[84] B. Paijmans, W. Symens, H. Van Brussel, and J. Swevers, "Identification of Interpolating Affine LPV Models for Mechatronic Systems with one Varying Parameter," *European Journal of Control*, vol. 1, pp. 16–29, 2008.

[85] D. Vizer, G. Mercère, O. Prot, and J. Ramos, "A local approach framework for black-box and gray-box LPV system identification," in *European Control Conference*, 2013, pp. 1916–1921.

[86] Y. Zhu, *Multivariable System Identification for Process Control.* Elsevier Science & Technology Books, 2001.

[87] P. Hägg, H. Hjalmarsson, and B. Wahlberg, "A least squares approach to direct frequency response estimation," *IEEE Conference on Decision and Control and European Control Conference*, vol. 1, pp. 2160–2165, 2011.

[88] R. Pintelon, G. Vandersteen, J. Schoukens, and Y. Rolain, "Improved (non-)parametric identification of dynamic systems excited by periodic signals - The multivariate case," *Mechanical Systems and Signal Processing*, vol. 25, no. 8, pp. 2892–2922, 2011.

[89] A. J. Fleming and S. O. Reza Moheimani, "Spatial System Identification of a Simply Supported Beam and a Trapezoidal Cantilever Plate," *IEEE Trans. on Control Systems Technology*, vol. 11, no. 5, pp. 726–736, 2003.

[90] R. Scholte, I. Lopez Arteaga, N. Roozen, and H. Nijmeijer, "Truncated Aperture Extrapolation for Fourier-Based Near-Field Acoustic Holography by Means of Border-Padding," *J. of the Acoustical Society of America*, vol. 125, no. 6, pp. 3844–3854, 2009.

[91] J. Lataire, R. Pintelon, and E. Louarroudi, "Non-parametric estimate of the system function of a time-varying system," *Automatica*, vol. 48, no. 4, pp. 666–672, 2012.

[92] R. Pintelon, E. Louarroudi, and J. Lataire, "Nonparametric time-variant frequency response function estimates using arbitrary excitations," *Automatica*, vol. 51, pp. 308–317, 2015.

[93] P. Z. Csurcsia, J. Schoukens, I. Kollár, and J. Lataire, "Nonparametric Time-Domain Identification of Linear Slowly Time-Variant Systems Using B-Splines," *IEEE Trans. on Instrumentation and Measurement*, vol. 64, no. 1, pp. 252–262, 2015.

[94] J. Mohammadpour and C. W. Scherer, *Control of Linear Parameter Varying Systems with Applications.* New York, NY, USA: Springer, 2012.

[95] R. van der Maas, A. van der Maas, and T. Oomen, "Accurate Frequency Response Function Identification of LPV Systems : A 2D Local Parametric Modeling Approach," in *IEEE Conference on Decision and Control*, Osaka, Japan, 2015, pp. –.

[96] R. Pintelon, K. Barbé, G. Vandersteen, and J. Schoukens, "Improved (non-) parametric identification of dynamic systems excited by periodic signals," *Mechanical Systems and Signal Processing*, vol. 25, pp. 2683–2704, 2011.

[97] K. Köningsberger, *Analysis 2.* Berlin: Springer, 2004.

[98] A. van der Maas, R. van der Maas, R. Voorhoeve, and T. Oomen, "Frequency Response Function Identification of LPV Systems : A 2D-LRM Approach with Application to a Medical X-ray System," in *American Control Conference*, Boston, Massachusetts, USA, 2016, pp. –.

[99] M. Gevers, P. Hägg, H. Hjalmarsson, R. Pintelon, and J. Schoukens, "The Transient Impulse Response Modeling Method and the Local Polynomial Method for nonparametric system identification," in *IFAC Symp. on System Identification*, 2012, pp. 55 – 60.

[100] W. Widanage, N. Omar, J. Schoukens, and J. Van Mierlo, "Estimating the frequency response of a system in the presence of an integrator," *Control Engineering Practice*, vol. 35, pp. 1–11, 2015.

[101] D. Wang, W. Strugnell, G. Cowin, D. M. Doddrell, and R. Slaughter, "Geometric distortion in clinical MRI systems Part I: evaluation using a 3D phantom," *Magnetic Resonance Imaging*, vol. 22, no. 9, pp. 1211–1221, 2004.

[102] R. van der Maas, B. de Jager, M. Steinbuch, and J. Dries, "Model-based geometric calibration for medical x-ray systems," *Medical Physics*, vol. 42, no. 11, pp. 6170 – 6181, 2015.

[103] R. Kalman, "A New Approach to Linear Filtering and Prediction Problems," *J. of Basic Engineering*, vol. 82, no. Series D, pp. 35–45, 1960.

[104] E. I. Hartley and A. Zisserman, *Multiple View Geomery in Computer Vision*, 2nd ed.   New York, NY, USA: Cambridge University Press, 2004.

[105] R. Gaasbeek, R. van der Maas, M. den Hartog, and B. de Jager, "Image-Based Estimation and Nonparametric Modeling: Towards Enhanced Geometric Calibration of an X-ray System," in *IEEE Multi-Conference on Systems and Control*, 2015, pp. 21 – 23.

[106] J. Xu and B. M. Tsui, "A Graphical Method for Determining the In-Plane Rotation Angle in Geometric Calibration of Circular Cone-Beam CT Systems." *Trans. on Medical Imaging*, vol. 31, no. 3, pp. 825–33, mar 2012.

[107] L. Ljung, "Asymptotic Behavior of the Extended Kalman Filter as a Parameter Estimator for Linear Systems," *IEEE Trans. on Automatic Control*, vol. 24, no. 1, pp. 36–50, 1979.

[108] S. Julier, J. Uhlmann, and H. Durrant-Whyte, "A New Approach for Filtering Nonlinear Systems," in *American Control Conference*, Seattle, Washington, USA, 1995, pp. 1628 – 1632.

[109] E. Wan and R. Van Der Merwe, "The Unscented Kalman Filter for Nonlinear Estimation," in *Adaptive Systems for Signal Processing, Communications, and Control Symposium*, 2000, pp. 153–158.

[110] F. Gustafsson, *Statistical Sensor Fusion*, 2nd ed.   Lund: Studentlitteratur AB, 2012.

[111] B. A. Francis and W. M. Wonham, "The internal model principle for linear multivariable regulators," *Applied Mathematics & Optimization*, vol. 2, no. 2, pp. 170–194, 1975.

[112] S. Cooper and H. Durrant-Whyte, "A Kalman filter model for GPS navigation of land vehicles," in *IEEE/RSJ Int. Conf. on Intelligent Robots and Systems*, vol. 1, 1994, pp. 157 – 163.

[113] S. Julier and J. Uhlmann, "A General Method for Approximating Nonlinear Transformations of Probability Distributions," University of Oxford, Tech. Rep., 1996.

[114] M. Gautier and P. Poignet, "Extended Kalman filtering and weighted least squares dynamic identification of robot," *Control Engineering Practice*, vol. 9, no. 12, pp. 1361–1372, 2001.

[115] S. Julier, J. Uhlmann, and H. F. Durrant-Whyte, "A New Method for the Nonlinear Transformation of Means and Covariances in Filters and Estimators," *IEEE Trans. on Automatic Control*, vol. 45, no. 3, pp. 477 – 482, 2000.

[116] S. J. Julier and J. K. Uhlmann, "Unscented Filtering and Nonlinear Estimation," *Proc. of the IEEE*, vol. 92, no. 3, pp. 401–422, 2004.

[117] N. Adurthi, P. Singla, and T. Singh, "The Conjugate Unscented Transform - An Approach to Evaluate Multi-Dimensional Expectation Integrals," in *American Control Conference*, 2012, pp. 5556 – 5561.

[118] W. Gawronski, *Advanced Structural Dynamics and Active Control of Structures*, ser. Mechanical Engineering Series. New York, NY, USA: Springer, 2004.

[119] K. Glover and J. Willems, "Parametrizations of linear dynamical systems: Canonical forms and identifiability," *IEEE Trans. on Automatic Control*, vol. 19, no. 6, pp. 640–646, 1974.

[120] M. Gevers and V. Wertz, "Parametrizations for Multivariable Linear Systems *," *Automatica*, vol. 20, no. 3, pp. 333–347, 1984.

[121] G. Mercère and L. Bako, "Parameterization and identification of multivariable state-space systems: A canonical approach," *Automatica*, vol. 47, no. 8, pp. 1547–1555, 2011.

[122] M. Lovera and G. Mercère, "Identification for gain-scheduling: A balanced subspace approach," in *American Control Conference*, no. 2, 2007, pp. 858–863.

[123] M. Steinbuch, R. Merry, M. Boerlage, M. Ronde, and M. van de Molengraft, "Advanced Motion Control Design," in *Control System Applications*, 2010.

[124] R. Craig and A. Kurdila, *Fundamentals of Structural Dynamics*, 2nd ed. New York: John Wiley & Sons, 2006.

[125] K. Kozlowski, *Modeling and Identification in Robotics.* New York: Springer-Verlag, 1998.

[126] W. Khalil and E. Dombre, *Modeling, Identification and Control of Robots.* Elsevier Ltd, 2004.

[127] A. De Luca, D. Schröder, and M. Thümmel, "An acceleration- based state observer for robot manipulators with elastic joints," in *IEEE Int. Conf. on Robotics and Automation*, Roma, Italy, 2007, pp. 3817 – 3823.

[128] R. Fahrig and D. Holdsworth, "Three-dimensional computed tomographic reconstruction using a C-arm mounted XRII: image-based correction of gantry motion nonidealities," *Medical Physics*, vol. 27, no. 1, pp. 30 – 38, 2000.

[129] P. Rizo, P. Grangeat, and R. Guillemaud, "Geometric calibration method for multiple-head cone-beam SPECT system," *IEEE Trans. on Nuclear Science*, vol. 41, no. 6, pp. 2748–2757, 1994.

[130] J. L. Bucher, *The Metrology Handbook*, Second, Ed. Milwaukee, Wisconsin: ASQ Quality Press, 2012.

[131] V. Torre and T. A. Poggio, "On Edge Detection," *IEEE Trans. on Pattern Analysis and Machine Intelligence*, vol. 8, no. 2, pp. 147–163, 1986.

[132] J. Canny, "A computational approach to edge detection." *IEEE Trans. on Pattern Analysis and Machine Intelligence*, vol. 8, no. 6, pp. 679–698, 1986.

[133] E. Davies, *Computer & Vision Machine Vision: Theory, Algorithms, Practicalities.* New York, NY, USA: Academic Press, 2012.

[134] A. Taguchi and Y. Murata, "The Median and Mean Hybrid Filters," in *IEEE Int. Symp. Circuits and Systems*, 1991, pp. 93 – 96.

[135] M. Muneyasy, K. Hotta, T. Hinamoto, and A. Taguchi, "Edge-preserving Smoothing using Median Mean Neural Hybrid Filters," *J. Franklin Inst.*, vol. 335B, no. 6, pp. 1145 – 1156, 1998.

[136] M. van Ginkel, C. Luengo Hendriks, and L. van Vliet, "A short introduction to the Radon and Hough transforms and how they relate to each other," Delft University of Technology, Tech. Rep., 2004.

[137] M. Steinbuch, S. Weiland, and T. Singh, "Design of noise and period-time robust high-order repetitive control, with application to optical storage," *Automatica*, vol. 43, no. 12, pp. 2086–2095, dec 2007.

[138] M. Bodson and S. C. Douglas, "Adaptive Algorithms for the Rejection of Sinusoidal Disturbances with Unknown Frequency," *Automatica*, vol. 33, no. 12, pp. 2213–2221, 1997.

[139] T. Oomen, E. Grassens, and F. Hendriks, "Inferential Motion Control : Identification and Robust Control Framework for Positioning an Unmeasurable Point of Interest," *IEEE Trans. on Control Systems Technology*, vol. 23, no. 4, pp. 1602 – 1610, 2014.

[140] J. Bolder, T. Oomen, and M. Steinbuch, "On Inferential Iterative Learning Control : with Example to a Printing System," in *American Control Conference*, 2014, pp. 1827 – 1832.

[141] N. Singer and W. Seering, "Preshaping Command Inputs to Reduce System Vibration," *J. of Dynamic Systems, Measurement, and Control*, vol. 112, pp. 76 –82, 1990.

[142] T. Singh, *Optimal Reference Shaping for Dynamical Systems: Theory and Applications.* Taylor & Francis, 2009.

[143] D. de Roover and F. Sperling, "Point-to-Point Control of a High Accuracy Positioning Mechanism," in *American Control Conference*, no. June, Albuquerque, New Mexico, 1997, pp. 1350–1354.

[144] B. Dijkstra, N. Rambaratsingh, C. Scherer, O. Bosgra, M. Steinbuch, and S. Kerssemakers, "Input Design for Optimal Discrete Time Point-to-Point Motion of an Industrial XY-Positioning Table," in *IEEE Conference on Decision and Control*, vol. 1, 2000, pp. 901 – 906.

[145] T. Singh and S. Vadali, "Input-Shaped Control of Three-Dimensional Maneuvers of Flexible Spacecraft," *J. of Guidance, Control and Dynamics*, vol. 16, no. 6, pp. 1061 – 1068, 1993.

[146] ——, "Robust Time-Delay Control," *J. of Dynamic Systems, Measurement, and Control*, vol. 115, no. June, pp. 303 – 306, 1993.

[147] T. Singh, "Pole-Zero, Zero-Pole Canceling Input Shapers," *J. of Dynamic Systems, Measurement, and Control*, vol. 134, no. 1, p. 011015, 2012.

[148] M. M. Zain, M. Tokhi, and Z. Mohamed, "Hybrid learning control schemes with input shaping of a flexible manipulator system," *Mechatronics*, vol. 16, no. 3-4, pp. 209–219, apr 2006.

[149] P. Chang, P. Huang, J. Maeng, and S. Andersson, "Local raster scanning for high-speed imaging of biopolymers in atomic force microscopy." *Review of scientific instruments*, vol. 82, no. 6, p. 063703, jun 2011.

[150] T. Körner, *Fourier Analysis.* Cambridge University Press, 1990.

[151] T.-H. Kim, I. Maruta, and T. Sugie, "Robust PID controller tuning based on the constrained particle swarm optimization," *Automatica*, vol. 44, no. 4, pp. 1104–1110, apr 2008.

[152] M. Tomizuka, "Zero Phase Error Tracking Algorithm for Digital Control," *J. of Dynamic Systems, Measurement, and Control*, vol. 109, no. March, pp. 65–68, 1987.

[153] M. Al-Numay, "Unified Approximate Tracking Control of Linear Systems with Unacceptable Zeros," *J. of King Saud University*, vol. 19, no. 2, pp. 239 – 251, 2007.

[154] A. van Rietschoten, T. Singh, and R. van der Maas, "State Estimations for Application in Diabetes Control," in *American Control Conference*, no. 2, Chicago, IL, USA, 2015, pp. 5122 – 5127.

[155] K. Verbaan, "Robust Mass Damper Design for Bandwidth Increase of Motion Stages," PhD - Thesis, Eindhoven University of Technology, 2015.

[156] M. Grass, R. Koppe, E. Klotz, R. Proksa, M. Kuhn, H. Aerts, J. Op de Beek, and R. Kemkers, "Three-Dimensional Reconstruction of High Contrast Objects Using C-arm Image Intensifier Projection Data." *Computerized Medical Imaging and Graphics*, vol. 23, no. 6, pp. 311 – 321, 1999.

[157] B. Girod, R. Rabenstein, and A. Stenger, *Signals and Systems*. New York, NY, USA: John Wiley & Sons Ltd, 2001.

[158] J. Jackson, C. Meyer, D. Nishimura, and A. Macovski, "Selection of a Convolution Function for Fourier Inversion Using Gridding," *IEEE Trans. on Medical Imaging*, vol. 10, no. 3, pp. 473 – 478, 1991.

[159] M. Loève, "Probability Theory I," in *Elementary Probability Theory*. New York, NY, USA: Springer-Verlag, 1977, pp. 1 – 52.

Societal Summary

With the discovery of X-ray by Wilhelm Conrad Röntgen in 1895, the medical society has undergone fundamental changes. From the evaluation of bone-structures, medical imaging has emerged to an indispensable tool for modern advances in healthcare. Modern (interventional) X-ray systems are capable to generate digital high-definition 2D images and 3D reconstructions of the interior of the human body, enabling progress in virtually every medical discipline.

With the rise of minimal invasive surgeries, the amount of post-operative complications and patient recovery times has been reduced significantly. In contrast to traditional computed tomography (CT) and magnetic resonance (MR) systems, interventional X-ray systems are specifically designed for use while providing access to the patient for the physician. In the near future, a rise of minimal invasive surgeries is envisioned in combination with new imaging applications.

The generation of high-definition 3D reconstruction is technologically a challenging task. The system has to move with a high velocity in a semicircular motion around the patient, while the positions for each exposure should be known with high accuracy. Due to the large mass of the system, imperfections in the manufacturing process and external disturbances, extensive time-consuming, (geometric) system calibrations are required. In addition, due to the close proximity of the patient, physician, and supporting staff, safety is critical.

New developments in high-performance mechatronic systems, such as medical X-ray systems, tend to lightweight system design leading to a tradeoff between increased scan velocities, enhanced safety, and reduced costs against typically decreased imaging qualities. In this research, advanced modeling, estimation, and control techniques are presented to meet (future) technological and societal demands. Advanced modeling techniques are employed to reduce the consumed time for geometric calibrations, enabling a significant cost reduction. Estimation and control approaches are used to overcome the limitations imposed by future lightweight systems. The theoretical and experimental results in this thesis are a first step forward to a new generation of future X-ray systems.

Summary

Advanced Geometric Calibration and Control for Medical X-ray Systems

Advancing techniques in the medical society increasingly rely on high quality images of the interior of the human body. Developments in minimal invasive surgery that aim at reduced collateral damage during interventions, leading to less postoperative complications and faster patient recovery times, are typically demanding from an imaging perspective. Hence, accurate imaging is key for minimal invasive surgery. X-ray Computed Tomography (CT) and 3D Rotional Angiography (3DRA) enable the generation of high quality 3D reconstructions based on a large number of 2D X-ray images, each taken from a different perspective with respect to the patient. In addition, clinical interest in 3D roadmapping applications, where real-time 2D fluoroscopy images are projected on a pre-generated 3D reconstruction, is increasing.

Interventional C-arm based X-ray systems are well suited for the described imaging applications. Due to the combination of the open kinematic structure of the system and a finite stiffness of the systems mechanical components, the performance is significantly influenced by internal and external disturbances, e.g., gravitational and Coriolis forces, leading to position dependent, quasi-static deformations and inherent (nonlinear) multivariable behavior. Assuming quasi-reproducible (repetitive) behavior of the system, external geometric calibrations have to be repeated every six months.

Although the currently applied calibration approaches lead to high quality 3D reconstructions for the present generation of X-ray systems, the procedure is time-consuming and might take up to four hours, i.e., a further increase in calibration times is not desired, limiting the addition of novel imaging options that lead to additional geometric calibrations. Additionally, driven by cost reductions, construction limitations, e.g., limitations imposed by the floor or ceiling on which the system will be mounted, and safety issues, the next generation X-

ray systems are tending towards a lightweight design, resulting in an increased sensitivity for internal and external disturbances. Hence, the reproducibility condition cannot be guaranteed.

The key elements of this research are 1) to develop a geometric calibration approach that leads to reduced calibration times, and 2) the development of a calibration and/or control strategy that enables dealing with non-collocated dynamical system behavior, i.e., enabling the use of (future) systems that violate the reproducibility condition. In this thesis, multiple approaches are proposed that enable fast calibrations and/or that can be used on systems that do not satisfy the reproducibility condition.

The first main contribution, which forms a basis of the approaches proposed in this thesis, is the model-based geometric calibration approach. The dominant physical phenomena leading to the need for geometric calibrations, e.g., misalignments and deformations due to finite stiffness of mechanical components, are included in a quasi-static physical model of the system. Based on a single identification experiment, where the system follows a predefined trajectory, the physical model parameters are identified. By exploiting the predictive properties of the model, the limited data obtained during the parameter identification experiment can be extrapolated to other desired chosen scan types and velocities. Hence, a significant reduction in calibration times is achieved for reproducible systems. By extending the proposed quasi-static physical model with a model that includes dynamical behavior, more complex system behavior can be estimated, still assuming reproducibility of the system.

The second contribution is the acquisition of a nonparametric dynamical model, which typically is an intermediate step in obtaining parametric models that can be used for predictions of dynamical behavior. Various academic approaches are applied to a real system, enabling a comparison in terms of required measurement times and obtained accuracies. Since the X-ray system shows a close resemblance to (industrial) manipulators, the system exhibits strong position dependent behavior. Local parametric approaches such as the Local Polynomial Method (LPM) and Local Rational Method (LRM), based on a local Taylor series expansion, are extended to parameter varying systems using an nD-Taylor series expansion. Hence, a novel preprocessing framework leading to fast and accurate nonparametric models of parameter varying systems is developed.

Although a (dynamical) model-based approach for the current generation of X-ray systems might lead to a reduction in calibration times, an extensive modeling procedure is required. The calibrations are typically repeated for each individual system every six months, leading to the third contribution; an observer-based approach for geometric calibrations. Using additional absolute measurements, e.g., acceleration measurements or gyroscopes, at the performance location (detector and source), observers, e.g., Kalman filters, can be exploited to estimate the true trajectory of the system, relaxing the reproducibility condition.

The fourth contribution is an image-based measurement approach that en-

ables an additional measurement taken directly from the X-ray images with only a minimal mechanical adjustment to the system. Relative positions and orientations of the detector with respect to the X-ray source can be measured, that can be used in the observer to achieve an increased estimation accuracy and additional information on relative detector-source misalignments.

The fifth and final contribution is an input- or reference shaping approach that reduces the effect of motion induced vibrations by a modification of the reference signal. The main focus in this chapter is on point-to-point and periodic motions, with the main aim to reduce disturbing effects leading to increased 2D image and 3D reconstruction qualities.

The approaches and results introduced in this thesis are a definite step toward the application of advanced modeling, identification, estimation and control for medical imaging systems and other (industrial) manipulators. As such, this thesis should be of interest to a broad readership, from an academic, medical and engineering perspective.

Samenvatting

Advanced Geometric Calibration and Control for Medical X-ray Systems

Vernieuwende technieken in de medische wereld vertrouwen in steeds grotere mate op hoge kwaliteit beelden van het inwendige van het menselijk lichaam. Ontwikkelingen in minimaal invasive procedures, die zich richten op het reduceren van gevolg schade gedurende interventies wat leidt to minder post-operatieve complicaties en kortere patient herstel tijden, leiden typisch tot hoge eisen aan de beeldvorming. Daarom is het verkrijgen van accurate beelden cruciaal voor minimaal invasive operaties. X-ray Computed Tomography (CT) en 3D Rotational Angiography (3DRA) maken het mogelijk om hoge kwaliteit 3D reconstructions te genereren, gebaseerd op een groot aantal 2D röntgen projecties elk verkregen vanuit een ander perspectief ten opzichte van de patient. Daarbij neemt ook de klinische interesse in 3D roadmapping toepassingen verder toe, waarin real-time 2D fluoroscopie projecties worden geprojecteerd op een vooraf gegenereerde 3D reconstructie.

Interventionele C-arm gebaseerde röntgen systemen zijn zeer geschikt voor de hierboven beschreven beeldvormende toepassingen. Door de combinatie van de open kinematische structuur van het systeem en de eindige stijfheid van de mechanische componenten, wordt de prestatie significant beïnvloed door interne en externe verstoringen. Voorbeelden van dergelijke verstoringen zijn zwaartekracht effecten en Coriolis krachten, welke leiden tot positie afhankelijke quasi-statische deformaties en van nature (niet-lineare) multivariabel dynamisch gedrag. Wanneer wordt aangenomen dat het systeem zich quasi-reproduceerbaar (herhalend) gedraagt worden er externe geometrische kalibraties uitgevoerd welke iedere zes maanden herhaalt worden.

Ondanks dat de huidig toegepaste kalibratie procedures leiden tot hoge kwaliteit 3D reconstructies voor de huidige generatie röntgen systemen, kost de procedure erg veel tijd en kan tot vier uur duren. Dientengevolge is het niet

gewenst om de kalibratie tijden verder op te laten lopen wat typisch een limiterende factor is bij het toevoegen van nieuwe opties die kunnen leiden tot extra kalibraties. Gedreven door kosten reducering, limitaties in het ontwerp opgelegd door bijvoorbeeld de vloer of plafond aan welke het systeem bevestigd zal worden, en veiligheids overwegingen, zullen de ontwikkelingen voor de volgende generatie röntgen system richting lichtgewicht ontwerpen gaan. Dientengevolge zullen de systemen in een toenemende mate gevoeligheid voor interne en externe verstoringen vertonen. Hierdoor kan de reproduceerbaarheid van het systeem niet meer gegarandeerd worden.

De kenmerkende elementen van dit onderzoek zijn 1) het ontwikkelen van een geometrische kalibratie aanpak wat leidt tot gereduceerde kalibratie tijden, en 2) het ontwikkelen van een kalibratie en/of control strategie die het mogelijk maakt om te gaan met dynamisch systeem gedrag. Een voorbeeld van dit laatste element het mogelijk maken om gebruik te maken van (toekomstige) systemen die niet voldoen aan de reproduceerbaarheids eis. In dit proefschrift zijn meerdere aanpakken voorgesteld die het mogelijk maken om snelle kalibraties uit te voeren en/of die gebruikt kunnen worden voor systemen met een gereduceerde reproduceerbaarheid.

De eerste bijdrage in dit werk, welke een basis vormt voor de overige aanpakken die voorgesteld worden in dit proefschrift, is een model-gebaseerde geometrische kalibratie aanpak. Het dominante fysische fenomeen wat leidt tot de noodzaak tot geometrische kalibraties, bijvoorbeeld uitlijningsfouten en vervormingen door de eindige stijfheid van de mechanische componenten, zijn toegevoegd in een quasi-statisch fysisch model van het systeem. Gebaseerd op een enkel identificatie experiment, waarbij het systeem een voorgeschreven traject aflegt, worden de fysische model parameters bepaald. Door gebruik te maken van de voorspellende eigenschappen van een model kan de gelimiteerde data set verkregen uit het identificatie experiment geëxtrapoleerd worden naar andere gewenste scan types en snelheden. Als gevolg is een significante reducering van kalibratie tijden verwezenlijkt voor reproducerende systemen. Door het voorgestelde quasi-statische model uit te breiden met een model welke ook dynamisch gedrag bevat kan meer complex system gedrag voorspeld worden, echter de reproduceerbaarheid van het systeem blijft noodzakelijk.

De tweede bijdrage is het verkrijgen van een niet-parametrisch dynamisch model, wat typisch een tussenstap is voor het verkrijgen van parametrische modellen welke gebruikt kunnen worden voor het voorspellen van het dynamisch gedrag. Meerdere academische aanpakken zijn toegepast op een fysisch systeem, waarmee een vergelijking mogelijk is gemaakt in termen van de benodigde meettijden en verkregen nauwkeurigheden. De beschreven röntgen systemen sterk gerelateerd zijn aan (industriële) manipulators, en laten dan ook vergelijkbaar sterk positie afhankelijk gedrag zien. Lokale parametrische aanpakken zoals de Local Polynomial Method (LPM) en Local Rational Method (LRM), gebaseerd op een lokale Taylorreeks ontwikkeling, zijn uitgebreid voor parameter variërende

systemen gebruik makend van een nD-Taylorreeks ontwikkeling. Hiermee is een nieuwe voorbereidingsstrategie die leidt tot snelle en accurate niet-parametrische modellen van parameter variërende systemen ontwikkeld.

Ondanks dat een (dynamisch) model gebaseerde aanpak voor de huidige generatie X-ray systemen leidt tot een reductie in kalibratie tijden, is een uitgebreide modelerings procedure noodzakelijk, welke herhaald moet worden voor ieder individueel systeem, wat leidt tot de derde contributie, een observer gebaseerde aanpak voor geometrische kalibraties. Gebruik makend van additionele absolute metingen, bijvoorbeeld acceleratie metingen of gyroscopen op de lokatie waar de presentatie behaald dient te worden (detector en röntgen bron), is het mogelijk om middels algoritmes zoals Kalman filters schattingen te verkrijgen van het werkelijk afgelegde trajectory. Als gevolg kan de reproduceerbaarheids eis afgezwakt kan worden.

De vierde bijdrage is een op röntgen beelden gebaseerde methode die het mogelijk maakt om additionele metingen te verkrijgen direct vanuit de beelden met slechts een minimale mechanische aanpassing aan het systeem. Relatieve posities en oriëtaties van de detector ten opzichte van de röntgen bron kunnen op deze manier gemeten worden, wat vervolgens gebruikt kan worden in de data-gebaseerde methode om de schattings nauwkeurigheid te verhogen.

De vijfde en laatste bijdrage is een ingangs- of referentie design aanpak wat het effect van door bewegingen geïntroduceerde dynamica reduceert middels een aanpassing van het referentie traject. De voornaamste focus in dit hoofdstuk is op punt-naar-punt bewegingen en periodieke bewegingen, waarbij het doel is om verstoringen te reduceren wat leidt tot een verbeterde 2D beeld en 3D reconstructie kwaliteit.

De aanpakken en resultaten die geïntroduceerd zijn in dit proefschrift vormen een duidelijke stap richting het toepassen van geavanceerde modellering, identificatie, schattingen en regeltechniek voor medische beeldvormende systemen, maar ook andere (industriële) manipulatoren. Als zodanig, is dit proefschrift van belang voor een breed publiek, vanuit een academisch, medisch en technisch perspectief.

Dankwoord

Tijdens de vlucht vanaf (helaas) mijn laatste conferentie terug naar Nederland, heb ik mooi de tijd gehad om de afgelopen vier jaar eens goed te overdenken. Dit boekje is het resultaat van een hectisch maar toch ook ontzettend leuk promotie traject. Ondanks dat er maar een naam op de voorkant staat, hebben een aantal mensen een grote bijdrage geleverd.

Ten eerste wil ik mijn promotor Maarten Steinbuch bedanken voor de mogelijkheid om binnen zijn groep aan dit onderzoek te werken. Maarten, bedankt dat je mij aan een project gekoppeld hebt wat voor mij precies de juiste balans heeft gehad tussen toepassing en theorie. Je aanstekelijke enthousiasme heeft er zeker toe geleid dat ik, ook op momenten dat ik zelf niet goed wist waar het onderzoek naartoe ging, weer energie kreeg. Ook wil ik je bedanken dat je Annemiek en mij de mogelijkheid hebt geboden om samen gedurende drie maanden een fantastische ervaring in de Verenigde Staten op te doen.

Voor de dagelijkse begeleiding wil ik mijn copromotor, Bram de Jager, bedanken. Bram, jouw kritische blik op het werk heeft dit proefschrift zeker naar een hoger niveau gebracht. Ook jouw nuchtere blik op problemen heeft er voor gezorgd dat ik gedwongen werd om terug te grijpen naar de basis, waardoor ik vaak snel weer op het juiste spoor beland ben. Ondanks dat we een totaal andere mening toegedaan zijn op het gebied van sportiviteit en met name fietsen, hoop ik dat ik je toch een beetje "trots" heb gemaakt door (bijna) dagelijks tussen Helmond naar Eindhoven te fietsen.

Ook wil ik Tom Oomen bedanken voor de prettige samenwerking die eigenlijk al tijdens mijn afstuderen is begonnen. Tom, in mijn ogen ben je een soort onoffiële tweede copromotor geweest en heb je een significante bijdrage geleverd aan dit werk. Jouw enthousiasme en vooruitziende blik hebben in mijn ogen uiteindelijk tot de belangrijkste theoretische bijdrage in dit boekje geleid.

Gedurende mijn promotie heb ik er naar gestreefd om het systeem en de bijbehorende problematiek centraal te laten staan. Hierbij heb ik veel tijd doorgebracht bij Philips Healthcare. Hiervoor wil ik mijn directe Philips collega's

bedanken, met name Johan Dries en Mark den Hartog. Johan, jouw diepgaande kennis van het systeem is voor mij cruciaal geweest om dit onderzoek tot een goed einde te brengen. Jouw scherpe blik tijdens ons wekelijks overleg heeft een enorme bijdrage geleverd aan de resultaten in dit proefschrift. Zonder jouw ondersteuning in het uitvoeren van experimenten zou dit werk niet mogelijk geweest zijn. Hiernaast heb ik ook altijd de koffie pauzes erg gewaardeerd, waarin je gepassioneerd kon vertellen over de "basket", karate en natuurlijk de Belgische bieren. Mark, jouw onuitputtelijke enthousiasme heeft me meerdere malen geholpen wanneer mijn onderzoek wat stroef liep. Het is voor mij erg leuk en leerzaam geweest om met jou te sparren en om te zien hoe problemen vanuit de fysica aangepakt worden (en vaak tot vergelijkbare resultaten te komen). Verder wil ik van binnen de Philips organisatie Rob van Loon, Rob Gielen, Piet Schakenraad, Wil Baaten en Rens Schoones bedanken voor hun bijdragen.

During my research I was given the opportunity to spend some time at the SUNY at Buffalo in collaboration with Tarunraj Singh. Tarun, thank you for the opportunity to be in your group for three months. Your enthusiasm and critical views on the results has led to a significant part of this thesis. Spending some time in a new environment seems to be very stimulating and I would advice it to all PhD candidates. Finally, I would like to thank you, and of course all other members, for being part of my committee.

Dit boekje had nooit zo dik kunnen worden zonder bijdragen van alle studenten die ik de afgelopen vier jaar heb mogen begeleiden. In het bijzonder wil ik Rolf bedanken voor zijn grote bijdrage die geresulteerd heeft in een aantal publicaties en een hoofdstuk in dit proefschrift. Ook vind ik het fijn om te weten dat je toch nog niet helemaal zonder mij kon en vervolgens mijn kantoorgenoot bent geworden. Dit brengt mij ook gelijk bij alle andere mensen waarmee ik het genoegen heb gehad om een kantoor te mogen delen: David, Sinan, Frank, Robbert Voorhoeve, Robbert van Herpen (kort maar krachtig zullen we maar zeggen), Irmak, Rolf en Jurgen, bedankt! Frank, ook voor jou een speciale dank dat je mijn getuige op mijn bruiloft hebt willen zijn! Natuurlijk wil ik ook alle andere collega's bedanken voor alle zin en onzin van de afgelopen jaren.

Ik wil mijn dankwoord afsluiten met een aantal speciale mensen die persoonlijk het dichtst bij mij staan. En especial, quiero agradecer a mis buenos amigos Angélica, Lucas, Alexandra y Daniel por su amistad y apoyo durante un período difícil para mí. Además, las buenas conversaciones, la deliciosa comida (mexicana) y las agradables excursiones que me proporcionaron la distracción necesaria. Este libro no habría sido posible sin todos ustedes!

Ook wil ik mijn (schoon)familie bedanken voor alle steun en liefde. Tenslotte wil ik de belangrijkste persoon in mijn leven bedanken. Annemiek, bedankt voor je onvoorwaardelijke liefde en steun. Je hebt me geholpen tijdens de leuke en minder leuke perioden van het promoveren, zowel op het persoonlijke vlak als op academisch gebied. Mijn werk van de afgelopen jaren is iets waar ik trots op ben, jij maakt me echt gelukkig!

List of publications

Peer-reviewed journal articles

- R. van der Maas, J. Dries, and B. de Jager, *Observer-Based Geometric Calibration for Medical X-ray Systems*, Medical Physics, 2015, *ready for submission*

- R. van der Maas, R. Gaasbeek, M. den Hartog, and B. de Jager, *Image-Based Estimation and Nonparametric Modeling: an Enhanced Geometric Calibration Approach of an X-ray System*, Control Engineering Practice, 2015, *ready for submission*

- R. van der Maas, A. van der Maas, R. Voorhoeve, and T. Oomen, *Accurate FRF Identification of LPV Systems: nD-LPM with Application to a Medical X-Ray System*, Transactions on Control Systems Technology, 2015, *under review*

- R. van der Maas, T. Singh, and M. Steinbuch, *Periodic Signal Tracking for Lightly Damped Systems*, ASME Journal on Dynamic Systems, Measurement, and Control, 2016, *under review*

- R. van der Maas, A. van der Maas, J. Dries, and B. de Jager, *Efficient Nonparametric Identification of Multi-Axis Medical X-ray Systems*, Control Engineering Practice, 2015, *under review*

- R. van der Maas, J. Dries, B. de Jager, and M. Steinbuch, *Model-Based Geometric Calibration for Medical X-ray Systems*, Medical Physics, vol. 42(11), pp. 6171 - 6181, 2015

Peer-reviewed articles in conference proceedings

- A. van der Maas, R. van der Maas, R. Voorhoeve, and T. Oomen, *Frequency Response Function Identification of LPV Systems: 2D-LRM Approach with Application to a Medical X-ray System*, American Control Conference, 6 - 8 July 2016, Boston, Massachusetts, USA, *Submitted for review.*

- R. van der Maas, A. van der Maas, and T. Oomen, *Accurate Frequency Response Function Identification of LPV Systems: a 2D Local Parametric Approach*, IEEE Conference on Decision and Control, pp. - - -, 15 - 18 December 2015, Osaka, Japan, *Accepted.*

- R. Gaasbeek, R. van der Maas, M. den Hartog, and B. de Jager, *Image-Based Estimation and Nonparametric Modeling: Towards Enhanced Geometric Calibration of an X-ray System*, IEEE Multiconference on Systems and Control, pp. 1063 - 1068, 21 - 23 September 2015, Sydney, Australia.

- R. van der Maas, T. Singh, and M. Steinbuch, *Time-Delay Pre-Filter Design for Vibration Free Tracking of Periodic Reference Signals*, American Control Conference, pp. 2167 - 2172, 1 - 3 July 2015, Chicago, Illinois, USA.

- A. van Rietschoten, T. Singh, and R. van der Maas, *State Estimations for Application in Diabetes Control*, American Control Conference, pp. 5122 - 5127, 1 - 3 July 2015, Chicago, Illinois, USA.

- R. van der Maas, T. Singh, and M. Steinbuch, *Application of a Time-Delay Pre-Filter Design for Periodic Signal Tracking of Lightly-Damped Multivariable Systems*, IFAC Workshop on Time-Delay Systems, pp. 1271 - 1274, 28 - 30 June 2015, Ann Arbor, Michigan, USA.

- R. Gaasbeek, R. van der Maas, M. den Hartog, and B. de Jager, *Improved Automatic Exposure Control Using Morphology-Based Disturbance Recognition*, IEEE International Symposium on Biomedical Imaging, pp. 1271 - 1274, 29 April - 2 May 2014, Beijing, China.

- R. van der Maas, J. Dries, B. de Jager, and M. Steinbuch, *Model-Based Approach to Minimize System Calibrations for 3D Reconstruction Quality of a Cone-Beam CT System*, IEEE Multiconference on Systems and Control, pp. 140 - 145, 28-30 August 2013, Hyderabad, India.

Other publications

- T. Oomen, R. van der Maas, C.R. Rojas, and H. Hjalmarsson *Iterative Data-Driven $\mathcal{H}_{\infty}$-norm Estimation of Multivariable Systems with Application to Robust Active Vibration Isolation*, IEEE Trans. on Control Systems Technology, vol. 22(6), pp. 2247 - 2260, 2014

- R. van der Maas, and T. Oomen, *Robust Active Vibration Isolation: A Multivariable Data-Driven Approach*, IFAC Triennial World Congress, pp. 4754 - 4759, 24-29 August 2014, Cape Town, South Africa.

- T. Oomen, R. van der Maas, C.R. Rojas, and H. Hjalmarsson, *Iteratively Learning the $\mathcal{H}_\infty$-norm of Multivariable Systems Applied to Model-Error-Modeling of a Vibration Isolation System*, American Control Conference, pp. 6703 - 6708, 17-19 June 2013, Washington, D.C., USA.

- R. van der Maas, J. Dries, and M. Steinbuch, *Model-Based Calibrations for Medical 3D Reconstructions*, DSPE Conference, pp. 57-62, 2-3 September 2014, Sint Michielsgestel, the Netherlands

Curriculum vitae

Rick van der Maas was born on February 7, 1985 in Vlissingen, the Netherlands. In 2002 he finished his secondary education at the Nehalennia in Middelburg. Subsequently, he studied Mechanical Engineering at the Avans University of Applied Sciences in Breda, the Netherlands, where he obtained his Bachelor's degree in 2007 followed by the Master's degree Mechanical Engineering from the Eindhoven University of Technology in 2011. His master's thesis was entitled "Multivariable Data-Based $\mathcal{H}_\infty$-norm Estimation for Achieving Robust Performance on an AVIS" and was carried out under the supervision of Tom Oomen and Okko Bosgra.

Since March 2012, Rick has been working as a Ph.D. student in the Control Systems Technology Group of Maarten Steinbuch at the Eindhoven University of Technology. During this period, Rick was supervised by Bram de Jager and Maarten Steinbuch from the Eindhoven University of Technology and Johan Dries from Philips Healthcare. The research is part of the joint Philips Healthcare / Eindhoven University of Technology Mechatronics in X-ray Systems (MIxR) project which received funding from the Dutch Ministry of Economic affairs. In the period May-August 2014, Rick was a visiting researcher at the State University of New York (SUNY) at Buffalo, New York, USA, as part of a collaboration with Tarunraj Singh.

The research focus in the MiXR project is on advanced identification, modeling and control approaches, with the goal to minimize time-consuming geometric system calibrations while maintaining the same performance for the next-generation imaging systems. The main results of this research are presented in this thesis.